

## DOCTOR OF PHILOSOPHY

### Development of a non-industrial waste water heat recovery unit using PCMs

Mazhar, Abdur Rehman

*Award date:*  
2020

*Awarding institution:*  
Coventry University

[Link to publication](#)

#### **General rights**

Copyright and moral rights for the publications made accessible in the public portal are retained by the authors and/or other copyright owners and it is a condition of accessing publications that users recognise and abide by the legal requirements associated with these rights.

- Users may download and print one copy of this thesis for personal non-commercial research or study
- This thesis cannot be reproduced or quoted extensively from without first obtaining permission from the copyright holder(s)
- You may not further distribute the material or use it for any profit-making activity or commercial gain
- You may freely distribute the URL identifying the publication in the public portal

#### **Take down policy**

If you believe that this document breaches copyright please contact us providing details, and we will remove access to the work immediately and investigate your claim.

# **Development of a non-industrial waste water heat recovery unit using PCMs**

**By**

**Abdur Rehman Mazhar**

**PhD**

**September 2019**



# **Development of a non-industrial waste water heat recovery unit using PCMs**

By

**Abdur Rehman Mazhar**

September 2019



*A thesis submitted in partial fulfilment of the University's requirements for the Degree  
of Doctor of Philosophy*

## **Library declaration and deposit agreement**

---

Content removed on data protection grounds



## Ethics approval certificate



### Certificate of Ethical Approval

Applicant:

Abdur Mazhar

Project Title:

Design and development of a non-industrial waste water heat recovery unit using  
Phase Change Materials (PCMs)

This is to certify that the above named applicant has completed the Coventry University Ethical Approval process and their project has been confirmed and approved as Medium Risk

Date of approval:

11 July 2018

Project Reference Number:

P72957

## **Abstract**

The harnessing of heat from waste water in non-industrial buildings is of utmost importance to balance the demands of space with those of hot water heating in order to make future buildings more energy efficient, to increment the share of third generation renewable technologies in the energy consumption of buildings and to potentially make future buildings both a source and sink of decentralised heat in low temperature fourth generation district heating (DH) networks.

This research develops a methodology to design a waste water heat harnessing exchanger for non-industrial setups, incorporating phase change materials (PCMs). In this thesis, the methodology is applied to waste water heat harnessing in residential buildings' appliances, with the associated boundary conditions. Heat is stored from the incoming waste water into the PCM and transferred back to cold water (CW). Such a heat exchanger (HE) decouples demand and supply by providing high-density latent thermal storage whilst incorporating heat recovery and storage in a single unit. This passive technique has considerable advantages over the commercially available technologies in terms of energy efficiency, economic and environmental benefits, as highlighted in the literature review. The boundary conditions and flow patterns of waste water flow in residential buildings are also established with an extensive literature review as the basis for the subsequent research. At the same time, the applications of PCMs used in passive waste heat harnessing applications are also put forward.

This research was divided into three main phases. Initially, the PCM having the optimum thermal characteristics and melt temperature with regard to the boundary conditions of this application was selected using a Particle Swarm Optimisation (PSO) algorithm coupled with the classical 2-phase analytical solution, developed in MATLAB. Secondly, the optimal geometric parameters of a corrugated pipe were selected to enhance heat extraction internal to the pipe for the flowing fluids. A Computational Fluid Dynamics (CFD) simulation developed in Star-CCM was validated based on an experimental setup to carry out a parametric study to select such a corrugated pipe. Finally, to propagate the heat fully into the PCM, an external thermal conductivity enhancement technique using high conductive fins was selected in a similar CFD and experimental setup. Based on the outcome of these three research

phases, a full scale HE was developed and assessed for usage in conjunction with conventional appliances in residential buildings.

In residential appliances, the average outgoing waste or grey water (GW) is at about 325K (51.85°C) while the incoming fresh CW is at 285K (11.85°C), both at a mass-flow rate of 0.1kg/s. Based on these boundary conditions, in the first part of the research, a PCM with a melt temperature of 298K (24.85°C) was chosen to provide the optimal thermal performance both in terms of melting and freezing. In the second part of the research, a corrugated pipe having a rib height 'e' of 4.5mm with a pitch 'p' of 30mm was selected to provide the best enhancement in terms of internal heat transfer. Finally, based on the third part of the research, 1mm thick copper fins with a pitch of 10mm and dimensions of 40×90mm provided the best external heat transfer enhancement within the PCM. The design was based on the bottleneck case of PCM freezing, which is about 60-70% more-time consuming than melting for the same amount of heat transfer. Based on this configuration, the highest possible increment in CW temperature was achieved with a complete PCM phase change resulting in the maximum amount of latent heat transfer for both melting and freezing. Additionally, the holistic design of a HE with three multi-cascaded PCMs is predicted to increment the CW temperature by 15K. In a typical four-member household, this device would save 4,687kWh of energy annually with a payback time on the investment of 4.77 years in lieu of present-day gas prices.

Based on the outcomes of this research, the design of such a HE for any non-industrial building can be established, especially for commercial ones that have a higher potential of heat harnessing. Additionally, usage of the harnessed heat has versatility in its potential applications that are not limited to CW heating, as in this thesis.

## **Acknowledgments**

First of all I am extremely thankful to Prof. Shuli Liu and Dr. Ashish Shukla for their continuous support and supervision throughout this research project. As a researcher, I will always be indebted to their technical assistance and mentoring. Throughout the course of this research, their guidance has always been top-notch.

Secondly, I would like to thank Mr. Ian Breakwell of the Hydraulics lab for his comprehensive assistance in my experimental work. In spite of his hectic schedule and commitments, he was always there to fully support me. I am very thankful to him for constructing a state of the art heat exchanger in a basic laboratory without any automated machines, solely based on his sheer excellent craftsmanship. Without his backing in the experimental setup, this project would have been futile as it would not have been validated.

Finally I would like to thank all my friends at the 'Centre for the Built and Natural Environment' for their valuable support and advice throughout the duration of my research. In particular I would like to thank Mr. Arpit Goyal, Mr. Adil Idrees Khan and Mr. Shamir Tahir for their unseen yet priceless support in making this project fruitful.

I would also like to thank my family, especially my parents for their continual support and comfort during these years. I could not have accomplished anything without their unfaltering support, encouragement and inspiration.

## Table of Contents

Library declaration and deposit agreement.....	i
Ethics approval certificate .....	ii
Abstract .....	iii
Acknowledgments.....	v
Abbreviations .....	ix
Nomenclature .....	ix
Subscripts .....	x
List of Figures .....	xi
List of Tables.....	xiv
Chapter 1 - Introduction .....	1
1.1. Overview.....	1
1.2. Problem statement.....	2
1.3. Constraints and proposal.....	5
1.4. Aim and objectives .....	8
1.5. Research methodology.....	9
Chapter 2 - Literature review .....	15
2.1. Overview.....	15
2.2. Characteristics of GW .....	16
2.2.1. Production data .....	16
2.2.2. Production patterns .....	20
2.2.3. Potential of harnessing.....	27
2.3. Commercial GW heat harnessing technologies .....	30
2.3.1. Heat exchangers (HE).....	33
2.3.2. Heat pumps (HP) .....	43
2.3.3. Hybrid systems .....	50
2.4. PCMs in waste heat harnessing applications.....	52
2.5. Outcome.....	58
Chapter 3 - PCM selection .....	59
3.1. Overview.....	59
3.2. Background and mathematical models .....	64
3.2.1. The Stefan problem and the classical 2-phase analytical solution.....	64
3.2.2. Particle swarm optimiser (PSO) .....	76
3.3. Methodology and algorithms .....	83
3.4. Results.....	89
3.4.1. Variation in PSO parameters .....	93
3.4.2. Variation in the parameters of the classical 2-phase analytical solution .....	95
3.5. Outcome.....	96
Chapter 4 - Internal heat transfer enhancement .....	98
4.1. Overview.....	98
4.2. Internal heat transfer enhancement techniques .....	100
4.2.1. Vortex generators .....	101

4.2.2.	Corrugated/fluted pipes .....	102
4.2.3.	Tape/wire inserts.....	102
4.2.4.	Internally finned/baffled .....	103
4.2.5.	Grooved/dimpled .....	103
4.2.6.	Increased surface roughness/coating .....	104
4.3.	Rationale for usage of corrugated GW/CW pipes.....	107
4.4.	Experimental model .....	109
4.5.	Numerical model.....	112
4.5.1.	Governing equations.....	112
4.5.2.	Geometry .....	114
4.5.3.	Mesh .....	116
4.5.4.	Boundary conditions and solvers.....	117
4.5.5.	Verification and calibration .....	120
4.5.6.	Validation .....	120
4.5.7.	Results .....	124
4.6.	Outcome .....	142
Chapter 5 - External heat transfer enhancement .....		143
5.1.	Overview.....	143
5.2.	Heat transfer enhancement techniques for PCMs .....	147
5.2.1.	Thermal conductivity.....	147
5.2.2.	Area of contact .....	150
5.2.3.	Flow conditions .....	151
5.3.	Rationale for fin usage .....	156
5.4.	Experimental model .....	157
5.4.1.	Equipment.....	157
5.4.2.	Procedure.....	165
5.4.3.	Results .....	167
5.5.	Numerical model.....	182
5.5.1.	Geometry, mesh and solvers.....	182
5.5.2.	Validation .....	184
5.5.3.	Results .....	186
5.6.	Outcome .....	198
Chapter 6 - Design of the holistic heat exchanger (HE) .....		199
6.1.	Overview.....	199
6.2.	Design methodology .....	201
6.3.	Performance of the HE.....	207
6.3.1.	Thermal performance .....	207
6.3.2.	Multi-cascaded PCMs.....	210
6.4.	Case study .....	214
6.5.	Outcome .....	217
Chapter 7 - Conclusion and recommendations .....		218
7.1.	Summary .....	218

7.2. Recommendations.....	220
References.....	222
Appendix A – Data sheets of PCMs.....	231
Appendix B – Experimental results of all thermocouples in the finned heat exchanger of section 5.4.3.....	233
Appendix C – Publications.....	239

## Abbreviations

ASHP	Air source heat pump
BW	Black water
CFD	Computational fluid dynamics
CFR	Critical flow rate
COP	Coefficient of performance
CW	Cold water
DC	District cooling
DH	District heating
$e$	Rib height
$f$	Friction factor
GW	Grey water
HAF	Heat absorbing fluid
HE	Heat exchanger
HP	Heat pump
HPC	High performance computer
HTC	Heat transfer coefficient
HTF	Heat transfer fluid
LHS	Left-hand side
Nu	Nusselt
$p$	Pitch
PCM	Phase change material
PSO	Particle swarm optimiser
PV	Photovoltaic
Re	Reynolds
RHS	Right-hand side
TPF	Thermal performance factor
TRL	Technology readiness level
WWTP	Waste water treatment plant
$\varepsilon$ -NTU	Effective - Number of transfer units

## Nomenclature

$C_{\mu}, \sigma_k, \sigma_{\varepsilon}, C_{1\varepsilon}, C_{2\varepsilon}$	Constants dependent on iterations and conditions
$E_{ij}$	Component of the rate of deformation
$N_t$	Number of points
$\dot{V}$	Volume flow rate in $\text{m}^3/\text{s}$
$\dot{m}$	Mass-flow rate in $\text{kg}/\text{s}$
$\dot{q}$	Heat in W
$y^+$	Dimensionless wall treatment height
$\infty$	Infinity
$a$	Ratio of the under root of the thermal diffusivities
$A$	Area in $\text{m}^2$
$c$	Specific heat in $\text{kJ}/(\text{kg}\cdot\text{K})$
$D$	Diameter in m
$E$	Energy in J
erf	Error function
erfc	Complementary error function
$g$	Acceleration due to gravity in $\text{m}/\text{s}^2$
$H$	Enthalpy in J



h	Heat transfer coefficient due to convection in W/ (m <sup>2</sup> K).
j <sub>1</sub>	Cognitive learning rate
j <sub>2</sub>	Social learning rate
k/K	Thermal conductivity of liquid phase W/(m.K)
L	Latent heat kJ/kg
l	Length in m
m	Mass in kg
η	Efficiency
P	Pressure in Pa
pBest	Particle best vector of the PSO
q/Q	Heat in J
r	Random variable between 0 -1
R	Thermal resistance in K/W
r	Radius in m
sBest	Swarm best vector of the PSO
St	Stefan number
T	Temperature in K
t	Time in s
U	Overall heat transfer coefficient in W/ (m <sup>2</sup> .K)
v	Velocity in m/s
w	Inertia weight of the particle
x	Position in m
y	First cell height from wall in mm
Δ	Delta or change
λ	Root of the transcendental equation
ρ	Density in kg/m <sup>3</sup>
f(x)	Fitness function for the PSO
α	Thermal diffusivity in m <sup>2</sup> /s
μ	Dynamic viscosity in Pa.s

### Subscripts

abs	Absolute
b	Boundary
eff	Effective
Exp	Experimental
f	Freezing
i/0	Initial
in	Interface
L	Liquid region
l	Liquidus
Lat	Latent heat
m	Melting
n	Nominal
S	Solid region
s	Solidus
Sens	Sensible heat
Sim	Simulation
v	Volumetric

## List of Figures

Figure 1-1: Imbalance in energy demand for space heating and hot water [6].....	2
Figure 1-2: Replacement of second with third generation renewable technologies for heating .....	3
Figure 1-3: Requirement of decentralised heat sources and sinks in fourth generation DH grids.....	4
Figure 1-4: Convergence of the research objective towards GW heat harnessing .....	5
Figure 1-5: Proposed concept of GW heat harnessing using PCMs .....	8
Figure 1-6: Summary of research methodology .....	13
Figure 2-1: Layout of the water drainage architecture in a conventional residential building [20].....	17
Figure 2-2: Production patterns as per appliances of GW over a day in residential buildings [15].....	21
Figure 2-3: Distribution of GW temperatures in conventional residential buildings in the UK [14] .....	21
Figure 2-4: Region wise daily GW production per person .....	22
Figure 2-5: Distribution of the source of GW in a conventional residential building [30].....	22
Figure 2-6: Typical showering statistics in the UK a) average shower times b) shower head types [30] ..	23
Figure 2-7: Distribution of the temperature settings for washing machines [30] .....	25
Figure 2-8: GW output profile of a typical commercial spa in China [33].....	26
Figure 2-9: Sankey diagram of the energy distribution in conventional residential appliances .....	29
Figure 2-10: Sankey diagram of the potential energy savings with GW heat harnessing in conventional residential appliances .....	31
Figure 2-11: Flow of GW in a) horizontally oriented b) vertically oriented piped HEs [52] .....	39
Figure 2-12: Proposed configuration to improve the efficiency of horizontally oriented piped HEs [52] ..	39
Figure 2-13: Operation strategies of HEs for GW heat harnessing at a building level a) balanced with a storage option b) unbalanced c) balanced without a storage option [50].....	42
Figure 2-14: Schematic of the operation of a HP linked with GW heat harnessing [38].....	44
Figure 2-15: Harnessing thermal heat from sewage lines used as a source of a) DC b) DH grids in Bern, Switzerland [12] .....	57
Figure 3-1: Basic layout of GW heat harnessing with PCM linked to incoming CW .....	59
Figure 3-2: Techniques to solve the Stefan problem for PCMs.....	65
Figure 3-3: Boundary and initial conditions to solve the Stefan problem using the classical 2-phase analytical.....	69
Figure 3-4: Neighbourhood topologies to determine the sBest in the PSO algorithm [126] .....	82
Figure 3-5: Overall algorithm for the classical 2-phase analytical solution based melting-freezing PSO algorithm – where grey is the PSO, red is melting and blue is freezing .....	83
Figure 3-6: Synoptic algorithm for melting and freezing using the classical 2-phase analytical solution..	84
Figure 3-7: Temperature profiles at the position $x = 5.4\text{mm}$ from the boundary of the layout, for both melting and freezing .....	90
Figure 3-8: Propagation of the phase change fronts from the boundary of the layout.....	91
Figure 3-9: Heat flux distributions at the optimum $T_m = 295.5\text{K}$ ( $22.35^\circ\text{C}$ ), for both melting and freezing .....	92
Figure 3-10: Convergence of the fitness function i.e. the total absolute heat transferred.....	92
Figure 3-11: Convergence of the optimum melt temperature ' $T_m$ ' .....	93
Figure 3-12: Variation of the specific latent heat capacity and optimised melt temperature as the output of the algorithm .....	95
Figure 4-1: Techniques to enhance internal heat transfer in pipes .....	101
Figure 4-2: Geometric parameters of a corrugated pipe ' $D_n$ ' = nominal diameter, $e$ = rib height, $p$ = pitch, $t$ = thickness.....	108
Figure 4-3: Schematic of the experimental setup to assess corrugated pipes .....	109
Figure 4-4: Experimental test rig to assess corrugated pipes.....	110
Figure 4-5: Layout of the geometric model with three domains: fluid flow, corrugated copper pipe and the PCM .....	115
Figure 4-6: Structure of the mesh for the geometry.....	117
Figure 4-7: Layout of the corrugated pipe with an ' $e$ ' = $0.7\text{mm}$ , ' $p$ ' = $5\text{mm}$ for the experimental and numerical models with thermocouples positioned at the red dots .....	121
Figure 4-8: Inlet and outlet temperature differential of the GW flow of both datasets.....	122
Figure 4-9: Average pipe temperature of both datasets .....	122
Figure 4-10: PCM temperature at $100\text{mm}$ from the GW inlet and $2\text{mm}$ from the edge of the pipe, for both datasets .....	123
Figure 4-11: Parametric study of the corrugated pipes with varying ' $e$ ' and ' $p$ ' values .....	125
Figure 4-12: TPF1 for both melting (GW flow) and freezing (CW flow) .....	127
Figure 4-13: Variations in the ratios of ' $D_v$ ' and ' $v$ ', compared to a plane pipe (Case 10) .....	128
Figure 4-14: TPF2 for a) melting (GW flow) b) freezing (CW flow) .....	129

Figure 4-15: Amount of a) melted PCM b) frozen PCM, for all cases .....	130
Figure 4-16: Pressure drop ratios for both melting (GW flow) and freezing (CW flow), compared to a plane pipe (Case 10) .....	131
Figure 4-17: Friction factor 'f' ratios for both melting (GW flow) and freezing (CW flow), compared to a plane pipe (Case 10) .....	132
Figure 4-18: Volume averaged vorticity ratios for both melting (GW flow) and freezing (CW flow), compared to a plane pipe (Case 10).....	133
Figure 4-19: Vorticity contours for a) (e4.5p30 mm) Case 9 b) (plane pipe) Case 10, at a mass-flow rate of 0.02 kg/s .....	134
Figure 4-20: Volume averaged helicity ratios for both melting (GW flow) and freezing (CW flow), compared to a plane pipe (Case 10).....	135
Figure 4-21: Streamlines of the fluid pathway of a) (e4.5p30 mm) Case 9 b) (plane pipe) Case 10, at a mass-flow rate of 0.02 kg/s .....	135
Figure 4-22: High definition streamlines of the fluid pathway for the first 0.5m of all cases .....	136
Figure 4-23: Nusselt 'Nu' number ratios for both melting (GW flow) and freezing (CW flow), compared to a plane pipe (Case 10) .....	137
Figure 4-24: Heat transfer ratios at the pipe-fluid interface for a) melting (GW flow) b) freezing (CW flow), compared to a plane pipe (Case 10) .....	137
Figure 4-25: Geometrical parameter ratios compared to a plane pipe (Case 10).....	138
Figure 4-26: Area averaged outlet temperatures for a) GW in melting b) CW in freezing .....	139
Figure 4-27: Fluid outlet temperature for (e4.5p30 mm) Case 9 and (plane pipe) Case 10, for a) melting (GW flow) b) freezing (CW flow).....	139
Figure 4-28: Temperature contours for a) melting of (e4.5p30 mm) Case 9 b) melting of (plane pipe) Case 10 c) freezing of Case 9 d) freezing of Case 10, at a mass-flow rate of 0.02 kg/s.....	140
Figure 4-29: Solid volume fractions of a PCM for a) melting of (e4.5p30 mm) Case 9 b) melting of (plane pipe) Case 10 c) freezing of Case 9 d) freezing of Case 10, at a mass-flow rate of 0.02 kg/s.....	141
Figure 4-30: Layout of the optimum corrugated pipe with 'e' of 4.5mm and 'p' of 30mm .....	142
Figure 5-1: Techniques to enhance heat transfer in PCMs .....	147
Figure 5-2: Experimental test rig to assess the HE with fins .....	157
Figure 5-3: Schematic of the experimental setup to assess the HE with fins .....	158
Figure 5-4: Layout of the copper pipe of the GW and CW flows with a 12.7mm diameter.....	159
Figure 5-5: Counter-flow arrangement of the vertically cascaded GW and CW pipes .....	160
Figure 5-6: Layout of the fins installed on the counter-flow pipes.....	161
Figure 5-7: Layout of the assembled HE with the copper pipes and fins .....	161
Figure 5-8: Surface contact between the fins and pipes, fabricated using a mechanical jig .....	162
Figure 5-9: Layout of the mild-steel container of the HE.....	163
Figure 5-10: Layout of the assembled HE labelled with the thermocouple positions .....	164
Figure 5-11: Procedure for the experimental sensitivity analysis to assess the HE with fins.....	165
Figure 5-12: Temperature variation for the odd-numbered thermocouples in the solo-flow strategy .....	169
Figure 5-13: Heat transferred a) from the GW b) to the CW flows, in the solo-flow strategy .....	172
Figure 5-14: Average temperature of the fins in the solo-flow strategy .....	173
Figure 5-15: Temperature variation for the odd-numbered thermocouples in the dual-flow strategy .....	176
Figure 5-16: Heat transferred a) from the GW b) to the CW flows in the dual-flow strategy .....	177
Figure 5-17: Average temperature of the fins in the dual-flow strategy .....	178
Figure 5-18: Retention of a) temperature b) phase, for both the PCMs.....	180
Figure 5-19: Shrinkage of volume and air bubble formation, due to ullage after the freezing of the PCM .....	181
Figure 5-20: Pitting on the surface of the mild steel container and copper fins .....	182
Figure 5-21: Layout of the geometric model with four domains: GW fluid flow, CW fluid flow, corrugated copper pipe and the PCM .....	183
Figure 5-22: Configuration of the fins to be optimised .....	186
Figure 5-23: Solid volume fractions at line probes a) perpendicular to the fin (z-axis) b) adjacent to the horizontal edge of the fin (y-axis) c) parallel to the fin width offset by 15mm (x-axis), for freezing .....	187
Figure 5-24: Assessment of the fin height based on the temperature gradient for a) melting b) freezing of the PCM.....	188
Figure 5-25: Thermal resistance diagram of the finned and non-finned configurations.....	191
Figure 5-26: Temperature profile of the fin for the optimised geometry for a) melting b) freezing of the PCM .....	192
Figure 5-27: Cross-sectional view of the temperature profile of the a) finned b) non-finned configurations for melting .....	193

Figure 5-28: Cross-sectional view of the temperature profile of the a) finned b) non-finned configurations for freezing .....	194
Figure 5-29: Phase change profile for a) melting b) freezing, of the PCM .....	195
Figure 5-30: Cross-sectional view of the velocity profile of the a) finned b) non-finned configurations .....	196
Figure 5-31: Propagation of natural convection vortices in the a) finned b) non-finned configuration ...	196
Figure 5-32: Outlet temperature profile for the a) GW b) CW flows .....	197
Figure 6-1: Configuration of a unit-volume of the designed HE.....	204
Figure 6-2: Procedure of the iterative scheme to model a holistic HE, based on a unit-volume .....	205
Figure 6-3: a) Average temperature of the PCM after complete melting b) Solid volume fraction of the PCM after freezing .....	208
Figure 6-4: Heat a) absorbed into the PCM during GW flow b) released from the PCM during CW flow .....	209
Figure 6-5: Temperature profiles for a) GW outlet during PCM melting b) CW outlet during PCM freezing.....	209
Figure 6-6: PCM a) heat absorbed vs $\Delta(T_{GW} - T_{melt\_PCM})$ b) heat released vs $\Delta(T_{melt\_PCM} - T_{CW})$ .....	210
Figure 6-7: Fluid flow vs the fluid outlet-PCM, temperature differentials for a) GW b) CW flow .....	211
Figure 6-8: Temperature profiles with a) single b) three-cascaded c) two-cascaded PCMs.....	212
Figure 6-9: Layout of the holistic HE having three-cascaded PCMs with a piping length of 9m .....	213
Figure 6-10: Overview of applicability of the holistic HE in typical residential appliances .....	214
Figure B-1: Temperature variations for the lower tier of thermocouples in the solo-flow strategy .....	233
Figure B-2: Temperature variations for the middle tier of thermocouples in the solo-flow strategy .....	234
Figure B-3: Temperature variations for the upper tier of thermocouples in the solo-flow strategy .....	235
Figure B-4: Temperature variations for the lower tier of thermocouples in the dual-flow strategy .....	236
Figure B-5: Temperature variations for the middle tier of thermocouples in the dual-flow strategy .....	237
Figure B-6: Temperature variations for the upper tier of thermocouples in the dual-flow strategy .....	238

## List of Tables

Table 1-1: Comparison of conventional GW heat harnessing with the proposed technique	6
Table 1-2: Research strategy based on the constraints of GW heat harnessing with PCMs	7
Table 2-1: Classification of residential waste water	16
Table 2-2: Different levels of waste water heat harnessing	31
Table 2-3: Summary of the different types of HEs used in GW heat harnessing	37
Table 2-4: Literature review of the usage of PCMs to harness waste thermal energy	54
Table 3-1: Advantages and disadvantages of the most common evolutionary optimising algorithms	77
Table 3-2: Range of the thermal parameters of commercially manufactured PCMs for a phase change temperature at 295-325K (21.85-51.85°C)	86
Table 3-3: Optimisable variables with their range of the search space for the algorithm	86
Table 3-4: Input variables to the algorithm having fixed values	87
Table 3-5: Results of the optimum variables of the algorithm	89
Table 3-6: Results of the variation in the PSO parameters	94
Table 3-7: Difference in thermal parameters of the algorithm recommended and the commercially available PCM	97
Table 4-1: Summary of the techniques of internal heat transfer enhancement	105
Table 4-2: Thermal parameters of RT-25	110
Table 4-3: Specifications of the experimental equipment	111
Table 4-4: Boundary conditions and solvers for the three regions of the numerical simulation, M = melting, F = freezing	117
Table 4-5: Difference between the numerical and experimental results to assess corrugated pipes	123
Table 4-6: Performance results of the optimal corrugated pipe at a mass-flow rate of 0.1kg/s	142
Table 5-1: Summary of the techniques of heat transfer enhancement of PCMs	153
Table 5-2: Thermal parameters of RT-42	166
Table 5-3: Heat transfer regimes of melting and freezing in PCMs	172
Table 5-4: Thermal performance for the solo-flow operation strategy	173
Table 5-5: Thermal performance for the dual-flow operation strategy	178
Table 5-6: Difference between the numerical and experimental results to assess the HE with fins	184
Table 5-7: Optimised geometric parameters of the fins with respect to the HE	189
Table 5-8: Performance results of the optimal fin configuration at a mass-flow rate of 0.1kg/s	198
Table 6-1: Summary of the results of the three-phase research methodology to harness GW heat for usage in CW in residential appliances	202
Table 6-2: Adaptability of typical methods for holistic HE analysis to this application	205
Table 6-3: Distribution of costs for the holistic HE	215
Table 6-4: Economic feasibility of the HE	216
Table 6-5: Performance results of the holistic HE	217

# Chapter 1 - Introduction

## 1.1. Overview

The population of the earth is increasing at an exponential rate, approaching about 7.9 billion by the end of this year. This has especially put extra strain on the environment and energy resources. Concurrent to this exponential growth, the number of buildings is increasing simultaneously. It is estimated that in the next 30 years, the demand for buildings for housing will increase by 67% and for commercial buildings, 300% [1]. At the moment, buildings consume about one third of the final global energy consumption and approximately half of this consumption is accounted for by hot water and heating/cooling requirements [1]. It is clear that to develop an overall sustainable energy system, the transformation of the building sector should play an integral role. At the same time, this issue is at the core of energy summits and policies worldwide.

At the 2015 United Nations Climate Change Conference COP-21 in Paris, the goal of a comprehensive agreement on mitigating climate change with all the nations of the world was reached. Most of the approved pacts included the concept of developing green buildings with zero-carbon technologies [2]. Furthermore, the whole of the fourth day of this summit was dedicated to improving overall building energy efficiencies. It was concluded that by 2050, about 50EJ of energy could be saved globally, reducing about 2Gt of carbon emissions, by improving policies aimed at buildings [3]. As a consequence of this summit, most global policies to transform the building sector revolve around three objectives:

- Reduction of energy demand by technological improvements and retrofitting the structure (secured energy).
- Sourcing the required energy from renewable and sustainable sources (sustainability).
- Making heating/cooling more energy efficient along with the overall energy demand of the building (competitiveness).

## 1.2. Problem statement

Based on the first objective for future buildings, the concept of passive houses was developed to reduce the energy demand of non-industrial buildings. These types of buildings originated in the early 1990s with the objective of consuming minimal amounts of energy whilst maintaining indoor comfort. Their main focus is on using passive technologies whilst being robust under all environmental conditions and maintaining the architectural integrity of a building [4]. Passive houses can be built at an extra cost of about 5-10% while consuming about 80-90% less energy in comparison with conventional buildings. Presently, there are more than 25,000 such buildings in Europe only, with considerable research in this domain to ultimately transform these houses into near zero external energy consuming structures [5]. However, most past and present research on passive houses is aimed at reducing the space heating demand. Consequently, a reduction in the energy consumption demand for hot water has usually been overlooked and is a relatively unexplored research domain. In conventional buildings, the energy consumption for space heating is about 40-50% of the total energy demand, while water heating consumes about 10-20%. However, with extensive research and improvements in passive house designs, the consumption for space heating is less than 10%, while that of water heating is about 50% [6]. This imbalance is depicted in Figure 1-1:

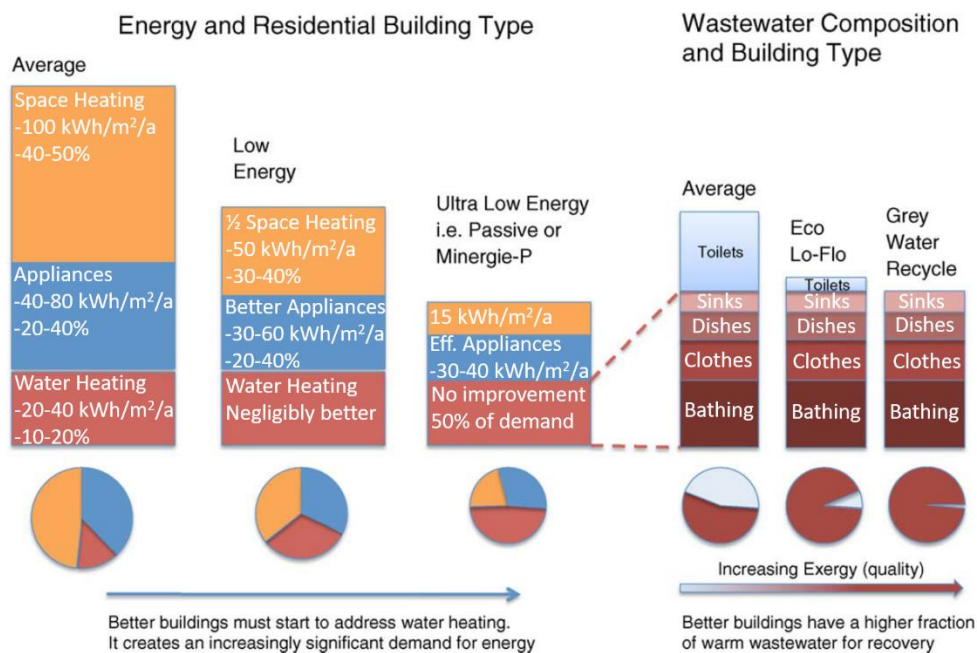


Figure 1-1: Imbalance in energy demand for space heating and hot water [6]

Evidently, the sub-divisions of energy consumption in passive houses are extremely disproportionately distributed. Normally, the space heating demand is less than 15kWh/m<sup>2</sup> while the water heating demand is about 50kWh/m<sup>2</sup>. Although the temperatures of the consumption of hot water cannot be reduced due to human comfort requirements, the efficiency of its utilisation can be improved. The waste water from all sources apart from toilets has a high thermal exergy (maximum useful work) content, which is normally flushed down the drain. Clearly, this source of low temperature waste water or grey water (GW) is a major source of inefficiency and must be addressed in non-industrial buildings.

Considering the second point outlined in section 1.1, it is envisioned that the source of energy in future buildings should be renewable for sustainability. In densely urban populations, it is almost impossible to harness energy via second generation renewable technologies including large scale wind turbines, solar panels and bio-fuels [7]. This is due to limited space, sensitive surroundings and most of all, the unpredictable generation potentials. For this reason, energy harnessing/harvesting techniques have been in the limelight, especially with a focus on dense urban centres. Conventional renewable technologies for heating can be replaced with more flexible sources of energy to be scavenged into useful thermal output, as displayed in Figure 1-2:

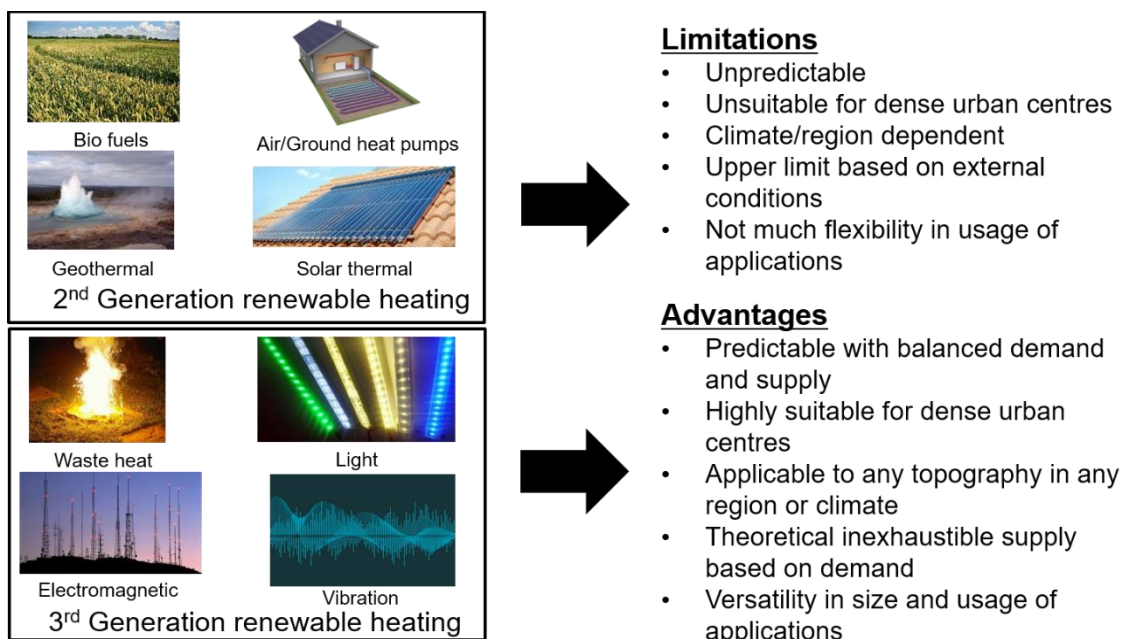


Figure 1-2: Replacement of second with third generation renewable technologies for heating



As per the second law of thermodynamics, all energy conversion processes have an upper limit. Therefore, there is an abundant supply of waste non-industrial heat with GW having the highest exergy potential which has usually been overlooked, due to the low energy efficiency and the economic feasibility of recovery. At the same time, there is an inexhaustible supply of other forms of man-made waste energy that has the potential of being thermally harvested [8]. In this sense, harnessing the thermal energy from GW is considered as a third generation renewable technique, complying with the overall objective of increasing the share of renewables in future buildings [9]. As per the third objective in section 1.1, district heating/cooling (DH)(DC) is considered as the most efficient mechanism to meet the demands of buildings, especially in dense urban centres [10]. In fact, most urban centres in Europe are already transforming to low temperature fourth generation DH grids [11]. Normally, these grids operate at relatively low temperatures of 313-333K (39.85-59.85°C) with several decentralised and centralised sources along with sinks of heat, as illustrated in Figure 1-3:

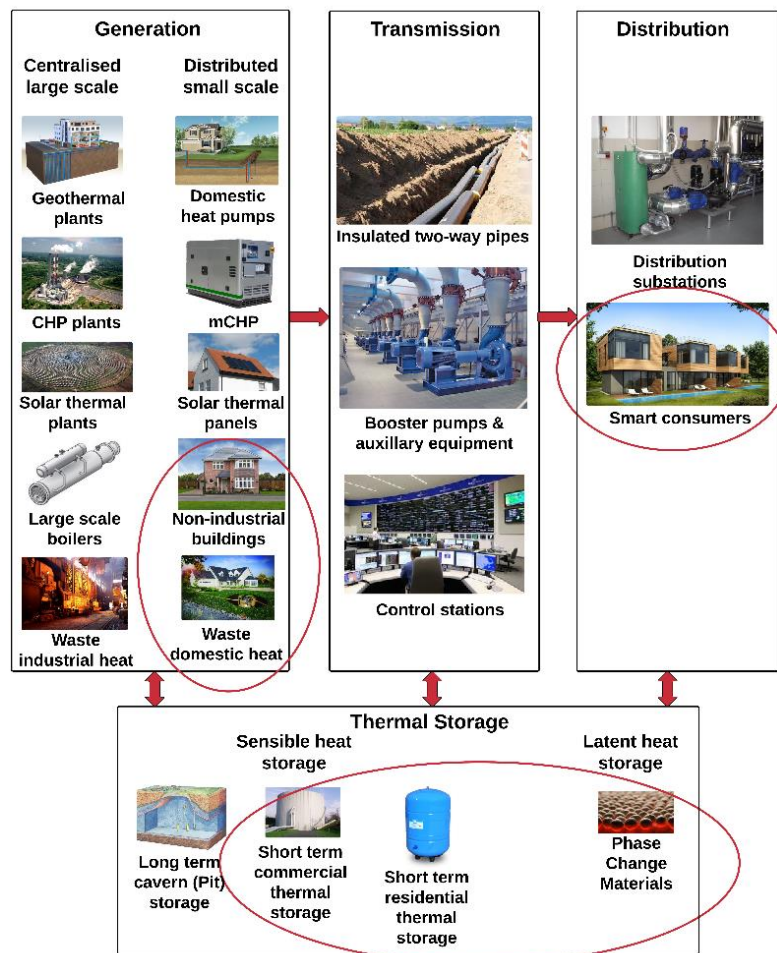


Figure 1-3: Requirement of decentralised heat sources and sinks in fourth generation DH grids

To realise this concept to its maximum potential, there is a requirement for integrating decentralised sources and sinks with efficient thermal storage and smarter distribution networks in a unified approach, as encircled in red. This decentralisation must be available at both a district and a national scale, requiring non-industrial buildings to simultaneously act as a source and sink of heat with the capability of high-density thermal storage. The most viable option to achieve this is once again through GW heat harnessing.

A summary of the motivation and problem statement, which is inclined towards the harnessing of GW heat, is presented in Figure 1-4:

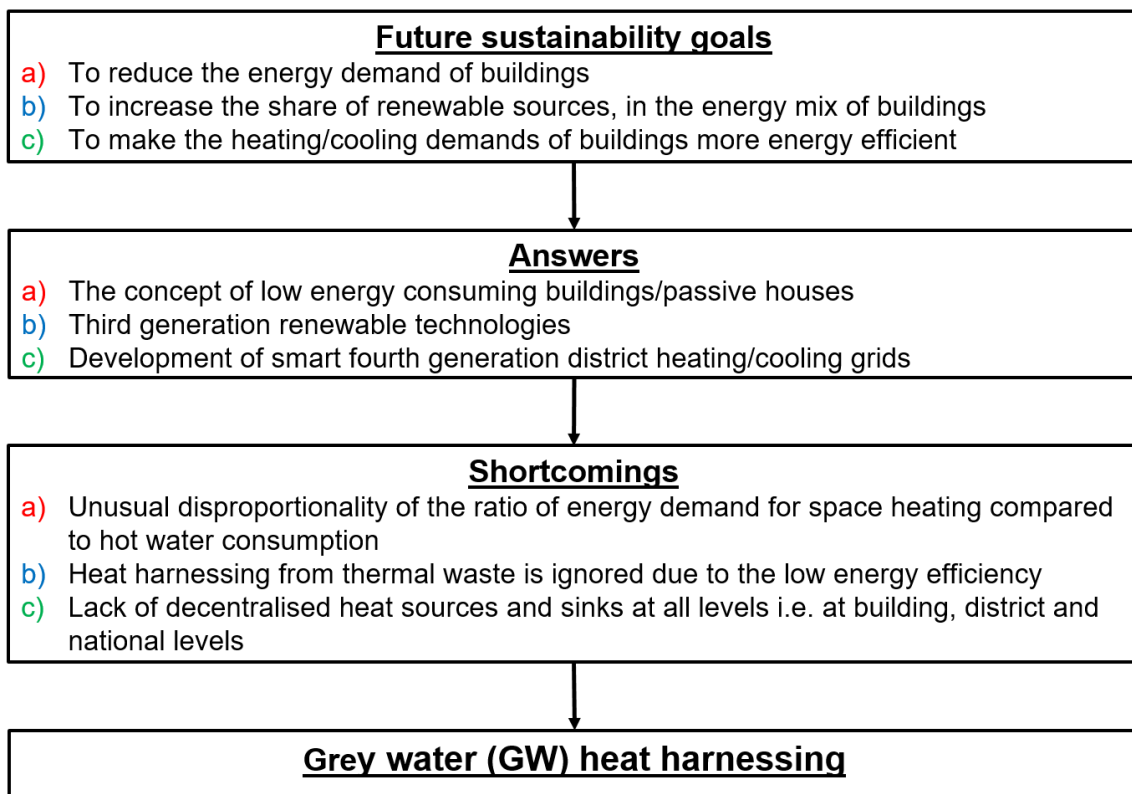


Figure 1-4: Convergence of the research objective towards GW heat harnessing

### 1.3. Constraints and proposal

Energy savings from harnessing heat from GW are tremendous. At the same time, many commercial technologies are already available for this purpose including simple counter-flow heat exchangers (HEs) and heat pumps (HPs), as will be detailed in section 2.3. Nevertheless, this idea still has not become mainstream and is yet to become an integral part of every building. According to a study [12], some decisive

factors determining the mass commercialisation of GW heat harnessing devices are as follows:

- Feasible capital costs, savings and payback times of the device especially compared to conventional fossil-fuel powered technologies.
- The size of harnessing and linkage to viable heating networks.
- The decoupling of the demand and supply of heat.
- Enhancement in the thermal storage density of these devices.

The commercial technologies used at present lack all these aforementioned domains [3]. For this reason, it is obvious that a better harnessing device to remedy these shortcomings should be proposed. A basic requirement of such a device is that it must be a passive technology with reasonable harnessing efficiencies capable of being integrated at all levels of the waste water system. An overview of the shortcomings of conventional technologies and the remedies required in the proposed device are presented in Table 1-1:

*Table 1-1: Comparison of conventional GW heat harnessing with the proposed technique*

<b>Conventional heat harnessing</b>	<b>Proposed schema</b>
Usually appropriate for a single-appliance or specific building	Flexibility to be utilised with any appliance, or building even at a district level
Potential to harness GW on a large scale is quite rare	Buildings could be exploited as decentralised heat sources/sinks on a district level conforming with the overall concept of smart energy grids
Exergetic efficiencies are low	Higher heat extraction potential to increase exergetic efficiency
Only increases the energy efficiency of a building	Has the potential to be utilised in a dynamic manner on a large scale within a smart energy system to optimise the its use based on a range of criteria
Mechanically moving parts with high maintenance costs	Simple robust parts having a higher reliability
High capital costs	Mediocre costs expected to reduce with research advancements in the future
Supply and demand coupled together since cold water (CW) must be heated when GW flows	Decoupled demand and supply, to store the heat of the GW without the need to immediately transfer it
Limited demand side management and optimisation techniques to reduce heating demands	Stored thermal energy could be utilised by efficiently managing several resources

	at once since the constraint of time is removed
Heat recovery and storage is usually done separately	Integration of heat recovery and storage into a single unit
Usually, thermal storage is only applicable to sensible heat storage at a small-scale level	Usage of high-density latent heat storage, so heat could be transferred to any secondary source at any level increasing the versatility of usage in multiple applications
Must be custom designed based on application and topography	Applicable to a range of conditions with only minor changes

Based on these deficiencies in conventional devices, the most obvious outcome is that high-density latent heat storage must be utilised. This would integrate recovery and storage into a single unit, decouple demand and supply and at the same time make the unit applicable to a range of applications, even at a district level. The usage of Phase Change Materials (PCMs) in this application is a novel, innovative and extremely promising approach as it has not been investigated before. It would be particularly insightful to see how a custom designed multi-flow PCM HE could harness waste heat at multiple levels without any mechanically moving parts, both in the short and the long term. Consequently, the usage of PCMs with this application has many constraints which would be tackled in three phases of this research, as outlined in Table 1-2:

*Table 1-2: Research strategy based on the constraints of GW heat harnessing with PCMs*

	<b>Constraint</b>	<b>Implication</b>	<b>Research strategy</b>
<b>1</b>	Intermittent supply and demand patterns	Using a PCM optimised for this application to maximise robustness	Heat storage – Phase 1 – Selection of the PCM
<b>2</b>	Space constraints	Making the HE compact and maintenance free, using a high-density PCM with appropriate thermal characteristics	
<b>3</b>	High flow rates for low time durations	Enhancement of the heat transfer coefficient (HTC) of the fluids involved	Heat extraction – Phase 2 – Enhancement of heat transfer of the flow internal to the pipes
<b>4</b>	High potential of deposits of biological impurities & fouling	Flow without constrictions through streamlined pipes	
<b>5</b>	Low pressure of incoming water flows	Streamline flow path without abrupt bends or turns to avoid fluid backflow	

<b>6</b>	Low thermal conductivity of PCMs	Enhance the thermal conductivity external to the pipe flows	Heat transfer – Phase 3 – Enhancement of heat transfer external to the flow in the pipes
----------	----------------------------------	---	--

The structure of this thesis is presented accordingly. A summary of the constraints and the proposal in this section is presented in Figure 1-5:

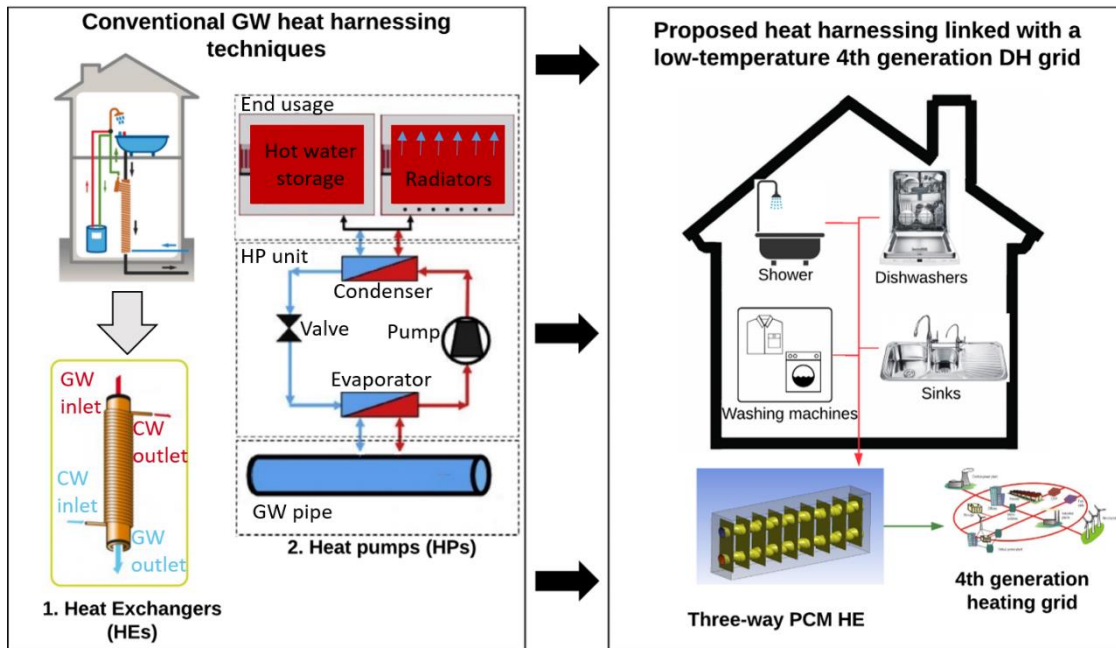


Figure 1-5: Proposed concept of GW heat harnessing using PCMs

## 1.4. Aim and objectives

The aim of this study is to formulate a methodology to develop a PCM HE capable of extracting waste heat from non-industrial GW, to comply with the initial goals and fulfil the shortcomings of conventional devices as outlined in the last two sections.

This formulated methodology to develop a PCM HE would be specifically applied as an example of harnessing heat from GW in conventional appliances in residential buildings. Although the extracted heat stored in the PCM could be used in any heating application, this study will focus on heating incoming mains CW. Consequently, the research is based on the following underlined objectives accompanied with the specific research questions:

- A literature review of the different aspects of GW heat harnessing.  
*What is GW and its parameters in non-industrial setups? Which technologies exist commercially? Are PCMs a viable solution?*
- Selection of a PCM with optimum thermal performance based on the constraints of this application.  
*What is the background and the requirements of this phase of research? Which techniques are used to model PCMs? Which optimisation techniques are used? What are the best PCM thermal behaviour and optimisation models? Which methodology is to be used for the development of an integrated algorithm?*
- Enhance the internal heat transfer of the flow of GW and CW in the pipes of the HE.  
*What is the background and the requirements of this phase of research? Which mechanisms are used to enhance internal heat transfer? Which technique is appropriate for this phase of research? Which methodology is to be used for the selection of the best parameters?*
- Enhance the external heat transfer into the PCM.  
*What is the background and the requirements of this phase of research? Which mechanisms are used to enhance heat transfer in the PCM? Which technique is appropriate for this phase of research? Which methodology is to be used for the selection of the best parameters?*
- Develop the thermal performance of the complete HE based on the outcomes of the last three objectives.  
*How would the holistic HE be developed? What methods are used to thermally analyse HEs? What is the thermal performance of the developed HE? What influence does a multi-cascaded PCM arrangement have?*
- Establishing the economic viability linked with usage in residential appliances.  
*What is the economic viability of the developed HE in a residential building?*

### **1.5. Research methodology**

The approach in this thesis is applied research, categorised as being quantitative with both analysis and synthesis. It is a systematic scientific investigation of design and performance based on a combination of mathematical, experimental and computational techniques. For this reason, it is also be considered as a triangulation approach. Based

on experimental techniques, the numerical and mathematical models are validated to conduct optimisation studies in order to select the best set of design parameters. A case study of a residential building is investigated to establish the holistic performance of the HE. An overview of the contents in the chapters of this thesis, based on the hypotheses of the research questions in each phase with the associated methodology, as per the outlined objectives is as follows:

### Chapter 2 - Literature review

- a) An overview of the characteristics of GW, its composition, GW piping in conventional non-industrial buildings, techniques for gathering GW production data, characteristics of the GW produced based on different residential appliances and in typical commercial buildings and the potential of GW heat harnessing both in terms of energy and exergy.
- b) An overview of the technical parameters of different stages of GW heat harnessing, types and performance of conventional HE recovery units, types and performance of conventional HP recovery units, drawbacks of both technologies, an overview of hybrid combinations of both techniques used with renewable applications and an overview of decentralised heat sinks/sources.
- c) Performance and categorisation of PCMs used in waste heat harnessing applications.

### Chapter 3 - PCM selection

- a) A literature review of PCM modelling and optimisation strategies. The constraints and objectives concerned with the selection of the PCM.
- b) An overview of the mathematical models and mechanisms to predict the thermal behaviour of PCMs for the selection of an appropriate model.
- c) An overview of the most appropriate optimisation algorithms with the selection of a suitable technique.
- d) Background and mathematical formulation of both the appropriate PCM and optimisation models to determine the maximum amount of heat absorbed and released by the PCM.

- e) Development of the algorithm suitably linking both models to select the PCM with optimum thermal performance with regard to the boundary conditions of GW heat harnessing for residential appliances.
- f) A parametric study to investigate the influence of the variables in both the PCM and optimiser model, for the selection of a commercially available PCM with the most suitable thermal properties.

#### Chapter 4 - Internal heat transfer enhancement

- a) A literature review of internal flow enhancement techniques along with the objectives concerned with its selection for this application.
- b) An overview of the pros and cons of commonly used internal heat transfer enhancement techniques.
- c) Selection of the best enhancement technique with regard to the constraints of the GW heat harnessing application and an overview of the important parameters of the selected technique.
- d) An overview of the experimental rig to practically test the selected technique and the development of a numerical model, validation of the numerical model based on experimental data to conduct a parametric study for the selection of the optimum configuration.
- e) Analysis of the internal flow and thermal performance characteristics of the enhancement technique based on the parametric study to select the best geometric parameters of the configuration. Analysis of the overall performance linked with GW heat harnessing using the selected PCM.

#### Chapter 5 - External heat transfer enhancement

- a) A literature review of PCM heat transfer enhancement techniques along with the objectives concerned with its selection for this application.
- b) An overview of the viable options to enhance the external heat transfer with the pros and cons of each method.
- c) Selection of the best enhancement technique with regard to the boundary conditions of the GW heat harnessing application and an overview of the important parameters of the selected technique.
- d) An overview of the extension of the experimental test rig to practically test the selected technique and the development of a numerical model. Validation of the numerical model based on experimental data to conduct an optimisation study for the selection of the best layout.



- e) Analysis of enhancement in PCM heat transfer compared to a layout without enhancement in the GW-PCM application. A comparison of the important parameters and overall thermal performance to select the best geometric parameters of the configuration.

#### Chapter 6 – Design of the holistic HE

- a) An overview of numerical techniques to model holistic HEs and the selection of an appropriate method after integrating the outcomes of all three previous phases of the research.
- b) A literature review of methods to holistically analyse HEs, the pros and cons of each technique and the selection of an appropriate method.
- c) Define and formulate the important evaluation criteria to assess the thermal performance of the HE.
- d) Regression analysis of the data to develop a generic equation of the performance of the holistic HE. A parametric study of the thermal analysis of different cascaded combinations.
- e) Costs, payback times and practicality of the developed model to formulate an economic feasibility study.

#### Chapter 7 - Conclusion and recommendations

- a) An overview of the developed HE.
- b) Shortcomings, concerns and recommendations to further develop and commercialise the designed HE to different GW heat harnessing applications.

A summary of this methodology is presented in Figure 1-6:

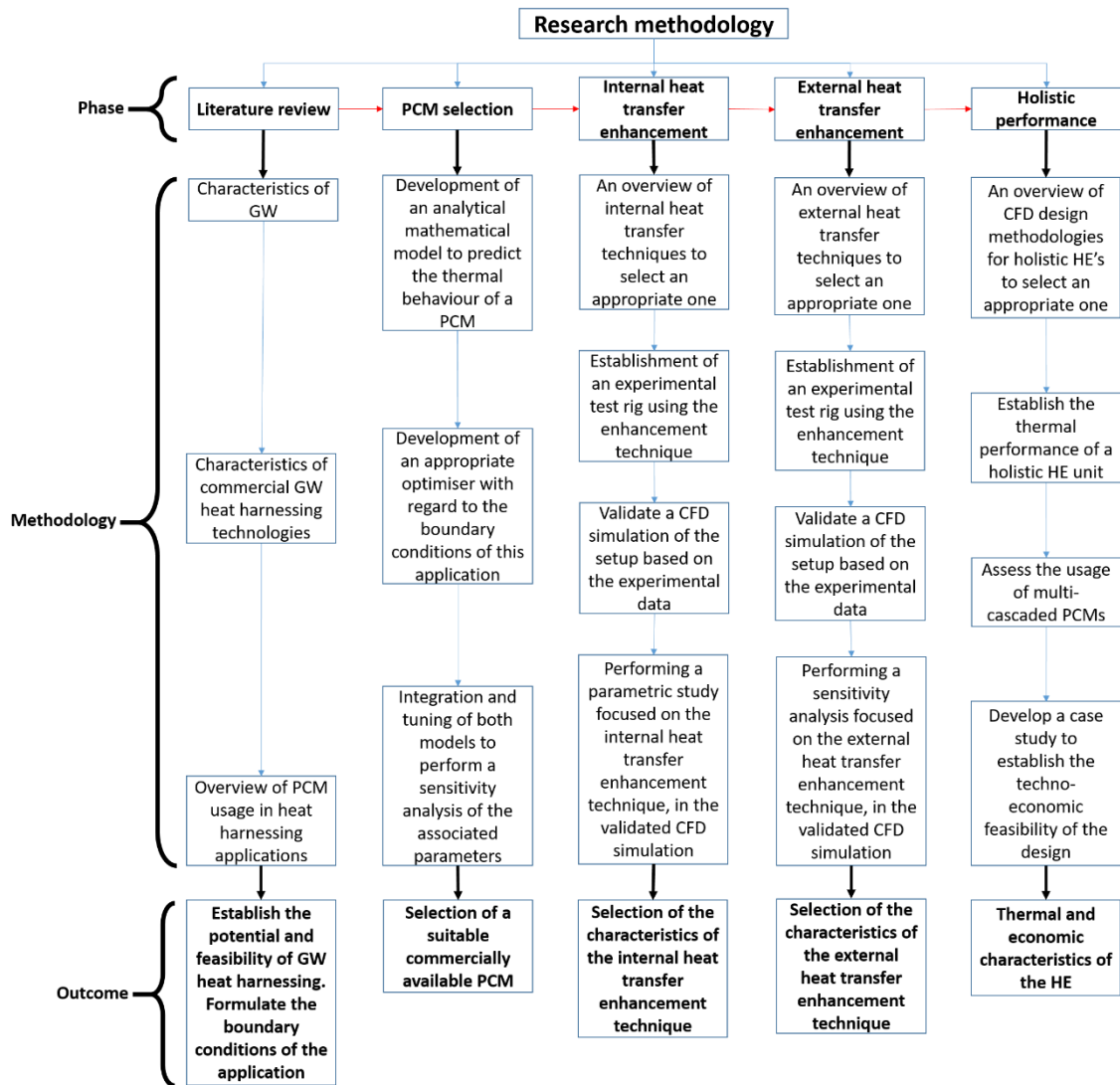


Figure 1-6: Summary of research methodology

The temperature, mass-flow rate and flow duration for both GW and CW in domestic appliances was established, based on the outcome of the literature review. Using these boundary conditions in MATLAB, the classical 2-phase analytical solution to predict the PCM's thermal behaviour was merged with the Particle Swarm Optimisation (PSO) technique to select the PCM for this application. The algorithm predicted the usage of a commercially available organic PCM to perform optimally, named RT-25 and manufactured by Rubitherm. In the next phase using RT-25, an experimental test rig with a commercially available corrugated pipe was used to validate a Computational Fluid Dynamics (CFD) simulation of a similar setup, in Star-CCM. A parametric study was conducted on nine different corrugated pipe configurations in the CFD environment at three plausible mass-flow rates to select a copper corrugated pipe to perform the best.

The optimum pipe was with a rib height of 4.5mm and a pitch of 30mm. In the final step of this three-phase methodology, an appropriate external heat transfer enhancement technique was selected. The experimental setup was extended, but instead of using the selected corrugated pipe from the previous phase, a plane pipe was used in the experiment due to manufacturing constraints. Additionally, as a comprehensive comparative assessment between different flow conditions the experiment was performed for a longer time duration with two different mass-flow rates and two different operation strategies of the HE. At the same time, to validate the selection of RT-25 as the PCM in the first phase of this research, this stage of the experimental setup compared the performance with RT-42. Nevertheless, the corrugated pipe version was used in the validated CFD simulation to carry out a sensitivity analysis to select 40×90mm rectangular copper fins with a pitch of 10mm, to perform the best. Finally, a unit-volume of the designed HE based on the outcomes of this three-phase methodology was simulated to derive empirical correlations of the thermal performance of a holistic HE. Consequently, a three stage multi-cascaded PCM was shown to increment the incoming CW by 15K whilst having a payback time of about 4.77 years, for typical domestic houses in the UK.

As an alternative to this three-phase methodology, an approach based either completely on an experimental or on a simulation analysis was a possibility. However, due to resource and especially manufacturing constraints, a complete experimental analysis was not viable. Hence, in this three-phase methodology, the experiments were designed only to validate the simulation which became the basis of an in-depth study. Similarly, a complete simulation using a holistic software e.g. (Modelica, Dymola, TRNSYS, Revit, IES) or a thermodynamic modelling approach in a programming language etc., was also not viable. Primarily this was because the number of unknown variables in such a singular approach were high, making it impossible to compute a satisfactory solution. At the same time, most of these platforms lack the capability to both explicitly design the individual components of the HE along with testing it in a case study. This is especially a concern when modelling PCMs, as they have unpredictable characteristics, lacking a complete mathematical model. For this reason, simultaneously using both experimental and simulation approaches along with subdividing the design into three different phases to comprehensively study each component of the HE was considered the most feasible option in this situation.

## **Chapter 2 - Literature review**

To formulate the design of this GW heat harnessing application for domestic buildings, the boundary conditions of the flow had to be determined based on the production patterns along with establishing the potential of heat harnessing. The shortcomings of commercially available technologies also had to be investigated in order to be rectified when using GW heat harnessing with PCMs. At the same time, the feasibility of using PCMs in similar waste heat harnessing applications had to be potentially examined.

### **2.1. Overview**

As mentioned above, limited research has been carried out within the domain of GW heat harnessing. Research has been inadequate and lacks a holistic picture, whether it is the collection of GW data [13,14] or the analysis of technologies to capture this waste heat [15,16]. This is primarily due to the fact that very low energies are involved in a harnessing technology, making it economical unviable in comparison to current fossil-fuel powered technologies. However, it is only recently, with fluctuating fuel prices and environmental awareness, that researchers have been exploring the possibility to tap this source of energy. This section presents a complete picture of all the elements involved in GW heat harnessing. In particular, the following objectives are researched, to give a holistic overview of the past and the future:

- The various output patterns of GW and conventional methods used to source this data.
- Commercially mature GW heat harnessing technologies used at different levels along sewage lines.
- An analysis of the shortcomings of these commercial technologies with the underlying hurdles in making them mainstream in conventional buildings.
- Investigating the potential of PCMs coupled with GW heat harnessing based on similar applications.

## 2.2. Characteristics of GW

Initially, the most important criteria to be established are determining the availability of GW production data, the sources and characteristics of GW output patterns in non-industrial buildings and assessing the potential of heat harnessing.

### 2.2.1. Production data

GW has been at the centre of many research studies due to global water shortages. However, this is not from the perspective of heat harnessing but for reclamation purposes [17]. For this reason, production data is scarce, especially in terms of the thermal characteristics [6]. In typical residential buildings, GW can be classified into the three categories [15,18–20], presented in Table 2-1:

*Table 2-1: Classification of residential waste water*

<b>Type</b>	<b>Source</b>	<b>Contents</b>
Low/light-load GW	Showers, bathtubs, WC basins	Shampoo, soap, hair, bacteria, organic particles, etc.
Heavy/dark-load GW	Dishwashers, kitchen sinks, washing machines	Surfactants, detergents, phosphates, heavy metals, suspended solids, organic particles, oil, grease, higher pH-bacteria, etc.
Black water (BW)	Toilets, bidets	Faeces, urine, toilet paper, etc.

Heat harnessing of light GW is the easiest and has the highest potential, while that of dark GW requires additional grease traps, strainers and sludge removal equipment [18]. These impurities tend to clog the HE, eventually reducing the thermal efficiency to a great extent. BW is unsuitable for harnessing due to its higher waste contents and lower temperature [15].

Another important reason for the scarcity of GW production data is due to the piping architecture in conventional buildings. The separation of the three classes of water outlined in Table 2-1 is usually non-existent [18]. Normally, most houses have a single stack where the wastewater of the entire building is dejected, irrespective of its class and re-usage potential. Due to this, not only is the possibility of gathering essential data

eliminated, but the possibility to harness heat at the building's level is also low. For this reason, most buildings of the future would have different stacks for each class of water. However, GW heat harnessing in buildings at an appliance level is more practical with a higher technical feasibility. An overview of the plumbing system of a conventional residential building is illustrated in Figure 2-1:

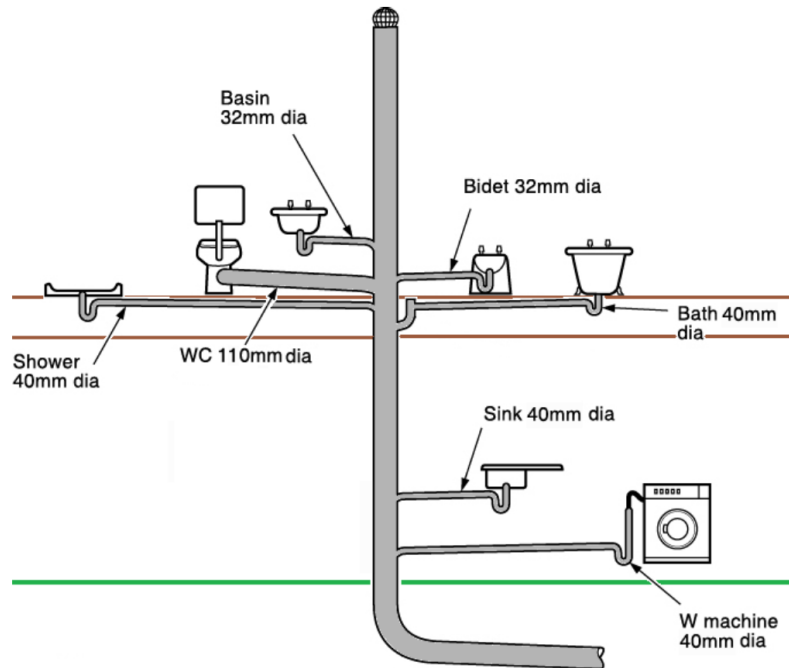


Figure 2-1: Layout of the water drainage architecture in a conventional residential building [20]

The stack is a large pipe positioned vertically through the building with a trap at the top in order to minimise clogging and smells caused by the congestion of water. With every appliance, there is a requirement to install a P-trap to avoid clogging followed by downward sloped piping. The P-trap is an essential component as part of building regulations [21]. However, this limits the flexibility of installing a heat harnessing device, let alone a data capturing unit. Similarly, due to the slightly sloped pipe, the flow of waste water is caused only by gravity with limited pressures. This puts a constraint on harnessing waste heat with minimal pressure losses. For this reason, the use of intrusive techniques inside the pipe's diameter cannot be carried out. Finally, most of the GW piping architecture in buildings is buried beneath concrete floors. The hardest pipes to access are beneath baths and showers due to an additional layer of hard ceramic tiles [19]. Therefore, the potential of gathering production data and heat harnessing is quite limited without a major retrofitting of the piping architecture in conventional buildings [18]. These physical constraints coupled with economic

unfeasibility are the main reasons for the scarcity of GW production data. However, the layout of passive houses and future buildings is more versatile with an increased possibility of both GW heat harnessing and reclamation.

Typically, production data in non-industrial buildings can either be collected in a field study [13] or through theoretical techniques [15], irrespective of the position of measurement in the piping architecture.

#### I. Experimental/Field data

This method is more genuine, although considerable fluctuations in the data are present. It must be noted that GW production data is quite erratic as it is greatly dependent on the mood and location of the user. Based on data [13], collected in 25 houses in the UK, the water usage varied by a factor of seven in spite of similar building designs and specifications. The three important parameters for the purpose of GW heat harnessing are the outlet temperatures, flow rates and duration of flow from the various appliances and/or sewage lines in a building [22]. The outlet data has to be collected after GW discharges from an appliance, since measured data from the stack would be inaccurate as it would contain BW [19]. Three components must be installed onto the specified pipeline to measure real-time data via a field study:

- Instrument

The physical constraints of a GW heat harnessing application put a limit on obstructing the flow due to increased pressure losses and the vulnerability of biofilm deposits. For this reason, non-intrusive and non-invasive devices are recommended on the outer diameter of the pipe to collect data. In order to measure the mass-flow rate, ultra-sonic flow meters that function based on the Doppler effect are more commonly used compared to magnetic induction meters [23]. Clamp-on ultrasonic meters usually cost between £500-2,000 with almost no maintenance requirements. Although they must be regularly calibrated, this can easily be done manually by using the timed volume measurement technique [22]. Both these devices produce pulses as an output where the frequencies of these pulses are proportional to the flow rate [13].

Similarly, to measure the temperature of the GW production data, a non-intrusive and non-invasive strategy has to be used. The chances of error with clamped sensors are much greater due to the effects of the ambient temperature in case the device is not securely fastened onto the pipe [24]. Probe-type sensors can usually be used at pipe junctions without considerable retrofitting requirements, although with less installation flexibility. Thermocouples and resistance-based semiconductors are the most commonly used, with prices ranging between £10-500 [25]. The physical principles behind their operations are the Seebeck effect and Ohms law, respectively. Since clamps and self-adhesives may not provide a firm contact point over the long term, the chances of error can be quite high, especially if the pipe has GW flow in its lower circumference [26]. Infrared (based on the principle of radiation) and fibre-optic sensors (based on the Raman Effect) are more accurate, with online prices in the range of £100-2,000.

- Power Source

There are usually three options to power instruments: firstly, with an externally powered direct current battery in the range of 0-30V; secondly, the instrument can be plugged into a conventional alternating current socket of a building; thirdly, using rechargeable internal batteries, charged via the connected data logger or the data transmitting source. The applicability of each technique depends on the instrument and the accessibility.

- Data transmitter

Long term real-time GW data is usually desirable, hence the need for an external data storage to be coupled instead of a simple LED display on conventional instruments [19]. The transmission of data can be wireless or via Modbus, Ethernet, or USB devices, etc. The most common method is the transmission of the data onto an external hard disk via an interconnected data logger [22]. Depending on the location in the piping architecture and the data storage capacity, the frequency of the transmission of recording values can range between 1-600s [13]. Nevertheless, a cleaning method is usually required to eliminate noise in the acquired data [19].



## II. Theoretical data

This probabilistic method has gained popularity over the years with advancements in artificial intelligence-based computer algorithms [27]. The inflow of water from the mains connection of a building or the outflow from a boiler is measured in this technique. Following this, programming techniques are used to compute the production and characteristics of GW at different points in the piping architecture [15]. This general technique is known as a flow trace analysis, although different variations exist [28]. Using data from field studies, this technique has been validated with several developed models having the ability to predict with a 90% accuracy [27]. These tools can be adjusted based on building types and regions, making them quite versatile along with being extremely economical compared to data collected via field studies. Similar techniques are also used for forecasting GW data for the future, essential for demand side management techniques [29]. At the same time, regression analysis and extrapolation techniques based on field data are used to predict future production data for GW [13]. An example of such a statistical prediction model was developed by the American Water Works Association based on data collected from a million users [15]. At the same time, a water consumption calculator was launched in the UK based on a regional survey [30]. The origin of this calculator is a statistical algorithm based on questions on usage patterns from a million survey takers. Ultimately, a smart water meter is in the making to efficiently perform demand side management techniques, where users can monitor their real-time usage linked with heating.

### **2.2.2. Production patterns**

As an estimate, approximately 16 million cubic meters of water are handled by the UK sewage system on a daily basis from non-industrial buildings [30], which is increasing at an annual rate of 0.5-1% [22]. For this reason, it is vital to understand the characteristics of the patterns of production in both residential and commercial buildings before assessing the potential of heat harnessing.

#### I. Residential buildings

In residential buildings, the highest production of GW is normally before and after local working hours, as depicted in Figure 2-2:

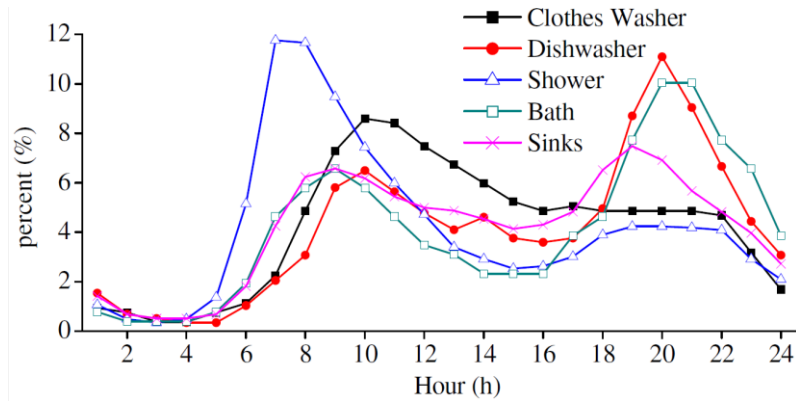


Figure 2-2: Production patterns as per appliances of GW over a day in residential buildings [15]

The usage profile of each appliance throughout the day is represented as a time percentage over its total daily use. This pattern is consistent throughout the year without the influence of external weather conditions. However, the contents of the outflowing GW vary considerably and are highly dependent on the occupancy statistics of the building. The second most important feature in terms of GW heat harnessing is the temperature profile. Based on a field study [14], of 124 dwellings in the UK, the typical production temperatures with an average of 324.9K (51.75°C) are illustrated in Figure 2-3:

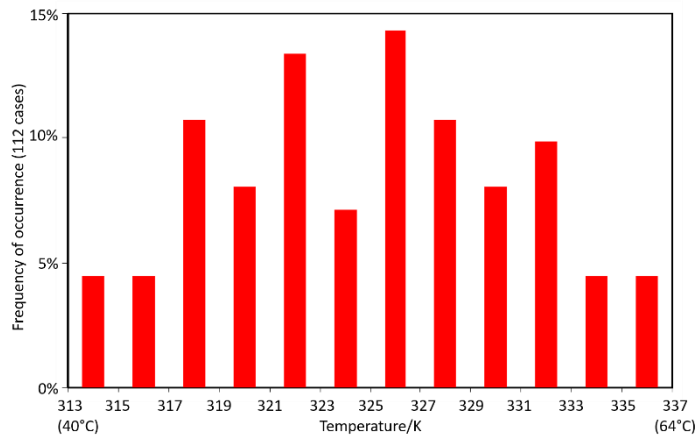


Figure 2-3: Distribution of GW temperatures in conventional residential buildings in the UK [14]

Finally, the amount of GW produced per person is also quite variant in terms of region, environment and economics [31]. An approximate overview of the typical production of GW per person on a daily basis is presented in Figure 2-4:

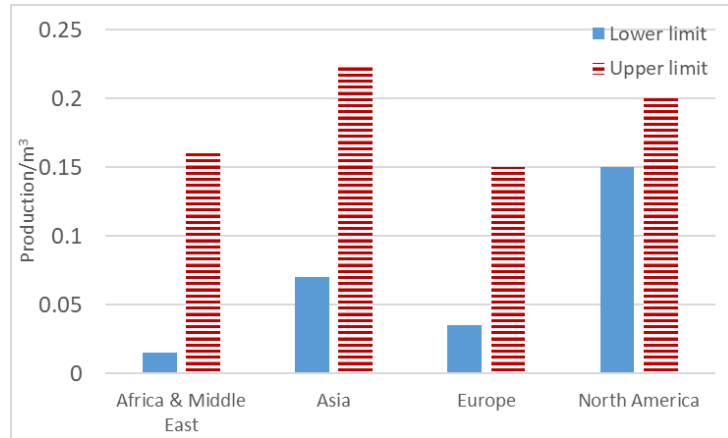


Figure 2-4: Region wise daily GW production per person

Based on these figures, a single person produces about 0.14-0.15m<sup>3</sup> of GW per day. As a cross-verification, a similar study by the Oak Ridge National Lab estimated that an average person produces 0.136m<sup>3</sup> per day [32]. In terms of the division of this amount, Figure 2-5 illustrates that showers produce the highest amount of GW:

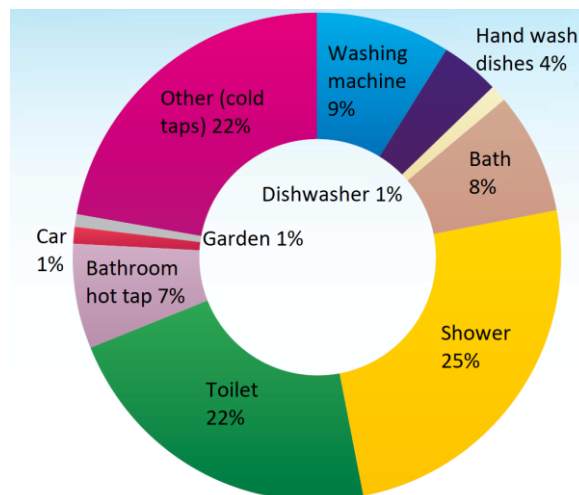


Figure 2-5: Distribution of the source of GW in a conventional residential building [30]

Of all the waste water production in a conventional residential building, about 64% of the output is GW. Similarly, a more optimistic study [32], estimated that 41-91% of the total waste water production can be classified as GW, having a high potential of harnessing heat.

Based on Figure 2-2, there are three main areas in a residential building contributing to the production of GW: a) washroom b) kitchen and c) washing machine. Additionally, both washrooms and kitchens have basins/sinks, making a total of five appliances potentially applicable for GW heat harnessing.

- Showers/baths and washroom basins

Hot showers cost about £2.3 billion annually in the UK [30]. Statistically, a person showers 0.7 times a day for an average duration of about 8.2 minutes. The average flow rate of old shower heads is about 0.2kg/s. This corresponds to about 70kg of GW generated from the shower on a daily basis. Comparatively, about 80kg of GW is produced if a water bath is used [30]. The average temperature of the GW produced in a shower is between 313-323K (39.85-49.85°C), depending on the user and the region [28]. An overview of the statistics of showers is presented in Figure 2-6:

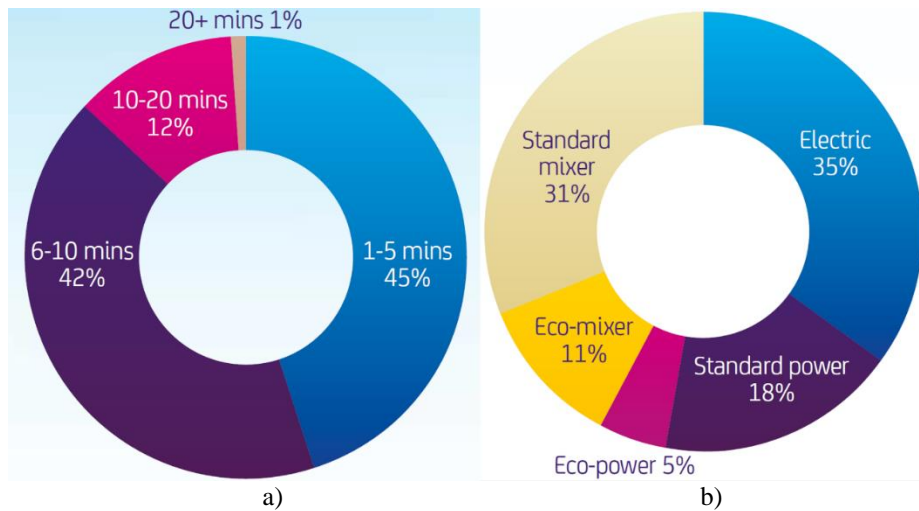


Figure 2-6: Typical showering statistics in the UK a) average shower times b) shower head types [30]

Standard power shower heads producing about 0.20-0.25kg/s have mostly been replaced with standard mixer shower heads in the UK, having an average flow rate of 0.13kg/s. Eco-mixers and electric showers are considered low flow, having an average flow rate of 0.1kg/s. These mixers usually have aerated showerheads drawing in air along with water at higher pressures in a strategy to minimise consumption.

Similarly, the average temperature of GW produced in washroom basins can be between 313-333K (39.85-59.85°C) [20]. On average, a person produces about 50-60kg per week with flow rates from basin taps being at about 0.03kg/s.

- Dishwashers and kitchen sinks

An average of about £1.6 billion worth of electricity is consumed annually to heat water for dishwashers and washing machines in the UK [30]. Similar to washroom usage, kitchen GW production can be divided into dishwashers and sink usage. The larger the household and the more developed the region, the higher the probability of ownership of a dishwasher. In developed countries, about 41% of all households have a dishwasher [30]. Compared to washing dishes in a kitchen sink, recently developed eco-friendly dishwashers have better water usage and energy consumption statistics. A typical dishwasher produces about 10-25kg of GW per wash at a temperature between 333-358K (59.85-84.85°C) [25]. In typical dishwashers, water is drawn in and flushed in three different cycles, with a single wash lasting about an hour.

Washing in kitchen sinks can be done via two main mechanisms. Some users prefer filling the entire bowl of the sink only once to wash all the dishes while others use a constantly running tap without clogging the sink outlet. About 86% users in the UK use the first method with separate sinks for washing and rinsing. This sink filling mechanism consumes about 8kg of water compared to about 20-30kg in the running tap method. The output temperature of the GW in both mechanisms is in the range of 313-333K (39.85-59.85°C). A single person uses a dishwasher approximately once a week or normally washes the dishes by hand at about 3-7 times a week [30]. However, these statistics are subject to high variability depending on the household size. With bigger households, the average production per person lowers as the kitchen usage of water becomes more economical.

- Washing machines

In developed countries, 97% of the population use washing machines while in developing countries, most use the old fashioned way of using a hot water tub to wash clothes by hand [30]. A single wash in a washing machine produces about 30-50kg of water without the influence of whether the machine is fully or partially loaded. In most washing machines, water flows in and drains out in two different cycles, with a single wash lasting at least an hour. A conventional household uses a washing machine 2-4.7 times a week or 1-2 times a week for a single person, normally at a temperature above

303K (29.85°C). The distribution of washing machine temperatures based on statistics in the UK is presented in Figure 2-7:

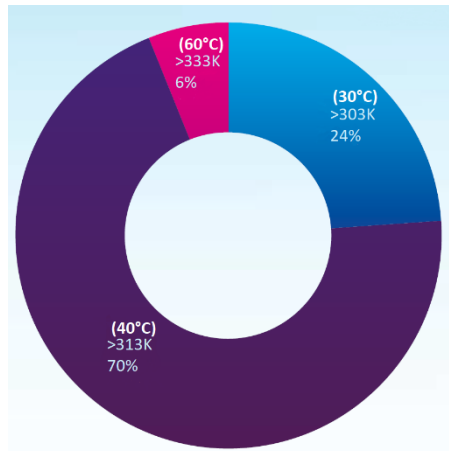


Figure 2-7: Distribution of the temperature settings for washing machines [30]

For showers and basins/sinks there is a concurrent production of GW and demand for CW to be heated. The time gap between both is non-existent, making heat transfer by conventional harnessing devices ineffective without the usage of thermal storage. On the other hand, the demand with supply in washing machines and dishwashers is not simultaneous as there are different cycles of inlet and outlet flow, necessitating thermal storage for continuous operation. Hence, both cases advocate in favour of the use of a high-density thermal storage to decouple demand and supply to improve thermal efficiencies.

## II. Commercial buildings

Harnessing heat from GW in commercial buildings has a much higher potential. This is because the output patterns are much more consistent and predictable compared with residential buildings, while the flow rates and durations of flow are much higher as well. However, due to the versatility in types of commercial buildings, a harnessing unit based on the boundary conditions has to be specifically designed for each one. A major undesirable aspect is the fact that in most commercial buildings, GW can be only harnessed during working hours on weekdays [33]. Figure 2-8 illustrates the consistent nature of the output profile of GW production in a commercial hotel and Spa in Shenzhen, China:

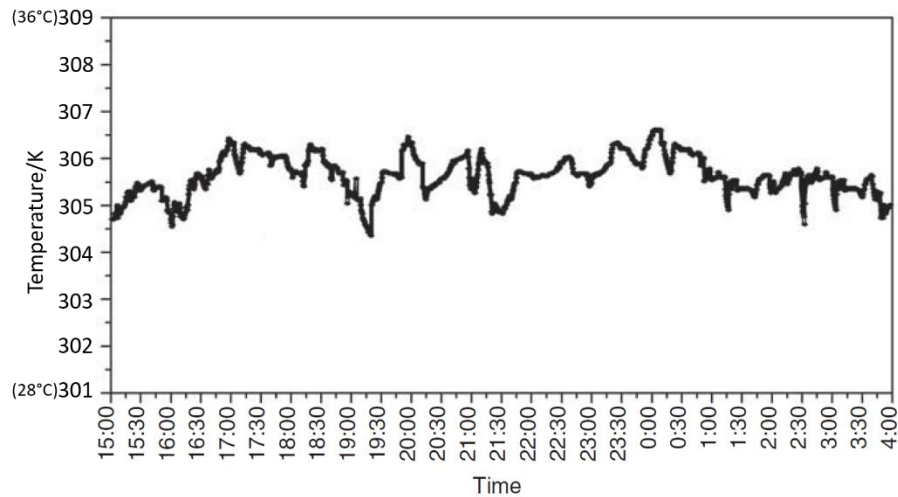


Figure 2-8: GW output profile of a typical commercial spa in China [33]

The mean temperature is about 306K (32.85°C) with GW produced only during the spa's operating times. At the same time, the readings were recorded in summer when the output temperatures are comparatively less compared to conventional values.

In another research [32], the commercial washroom and dining facilities of an army barracks were investigated in terms of GW heat harnessing potential. In terms of the shower facilities, a cadet used an estimated 50kg of water a day. There were about 600 cadets in a standard army barracks which corresponded to an output of about 30,600kg of GW a day. Once again, the average output temperature was in the range of about 303-323K (29.85-49.85°C), depending on the ambient temperature. The dining halls of such a barracks had at least two dishwashers operating for about 10.5 hours a day. This corresponded to an output of 0.18kg/s of GW at a temperature of 333-353K (59.85-79.85°C).

In another study [19], the potential of installing low temperature heat harnessing devices in a primary school in Kuwait was investigated. Although only 3-16kg per student was dejected during school hours, the potential is still quite large. This is because most was sourced from basins with a consistent output pattern that had almost no impurities.

Similarly, the potential to harness heat from GW in large residential apartments is tremendous. In a case study [34], a 41 apartment building in Berlin with 100 tenants produced approximately 3,000kg of light GW daily. At the same time, a 330 room student dorm in Berlin was estimated to have the potential to harness 917kWh worth of

heat from GW in the main sewage line on a daily basis [35]. However, the highest potential of harnessing in terms of commercial buildings is in public swimming pools and water parks [26]. In a typical Olympic-sized swimming pool, about 3 million kg of water at a temperature of about 303-308K (29.85-34.85°C) is flushed out at least once a week. Similarly, a hotel room produces about 184kg of GW while a hospital bed produces 327kg on a daily basis [36].

Based on these studies, similar statistics for commercial showers in gyms, dining facilities in hotels and dorms in universities etc. would portray an optimistic potential for GW heat harnessing.

### **2.2.3. Potential of harnessing**

The US Department of Energy has estimated that 350TWh worth of energy ends up in the USA sewage system on an annual basis [37]. It was concluded in this study that if every household had a simple harnessing device with 40% energy efficiency, at least 140TWh of this energy could be recovered. This would save 30-50% of the fuel used for heating water. It was also put forward that when water is converted to GW, it loses only 10-20% of its thermal energy. In another study [38], it was estimated that the GW produced in Germany and Switzerland had the potential to heat 3% of the buildings within these countries. Similarly, about 1,928 million m<sup>3</sup> of GW is produced annually in Holland, being at least 20K higher than the ambient temperature. At the same time, 60TWh worth of heat has the potential to be recovered from the sewage system in Switzerland [12].

Although there are several constraints in GW heat harnessing, the potential advantages outnumber the disadvantages:

- Harnessing GW heat would make buildings more energy efficient, increase the share of renewables in the energy mix and at the same time increase the possibility of having decentralised sources of heat in a fourth generation DH grid, as outlined in section 1.2.



- The output and temperature profiles of GW production are consistent throughout the year and are independent of weather conditions. This ensures production reliability and predictability of this potential heat source.
- As outlined, the quantity and the potential are also quite large, especially in commercial buildings.
- The possibility of using the harnessed heat in a variety of applications makes this source quite versatile. At the same time, integrating harnessing devices in the plumbing systems of future buildings can be done with minimal costs and effort.
- GW heat harnessing can easily be done at low costs and maintained using passive technologies.
- In residential buildings, these devices are known to extend the life of boilers and enhance their performance as their usage decreases [37].
- In countries with warm climates, the reverse of a harnessing cycle can be developed. Incoming water can be cooled down by injecting heat to the GW. In fact, such co-generation technologies are considerably more practical and economical, based on past experiences [24].

As an example, if only 1K of heat from 1m<sup>3</sup> of GW was extracted, this would save 1.17kWh of energy. As mentioned, an average person produces 140-150kg of GW on a daily basis. As an optimistic estimate, if 20K could be transferred from the GW to the incoming CW, a total of 3.5kWh would be saved. When this is amplified to a national level for the 65 million population of the UK, it amounts to a saving of 228GWh worth of energy. A conventional boiler would consume 0.4m<sup>3</sup> of gas to produce this 3.5kWh of thermal energy. This corresponds to an annual consumption of 145m<sup>3</sup> of gas which would save 320kg of CO<sub>2</sub> if it was not burned [39]. This is estimated based on the 80% energy efficiency of a conventional boiler in the UK [40]. 6% of the overall CO<sub>2</sub> emissions in the UK are contributed due to heating water which could be reduced to about half this value with heat harnessing technologies [30]. The average price of gas in the UK is about 2.8p/kWh, hence a GW heat harnessing device would save £45 in annual gas bills for a single person. This corresponds to an estimated 20% savings on energy bills. A summary of the potential of GW heat harnessing is presented in the Sankey diagram in Figure 2-9:

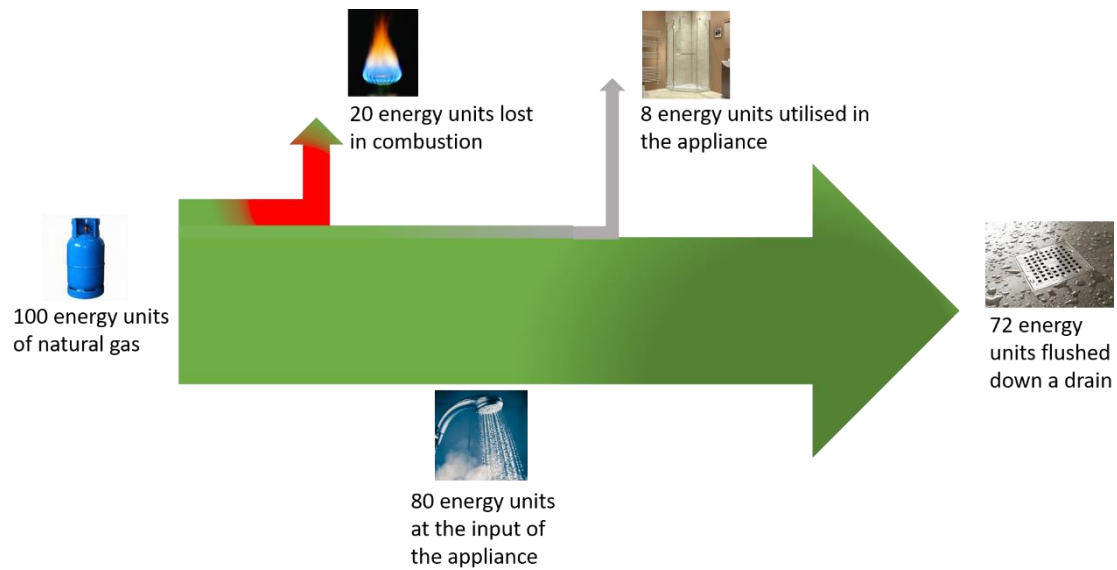


Figure 2-9: Sankey diagram of the energy distribution in conventional residential appliances

A similar analysis can be performed based on exergy to determine the quality of the GW heat [6]. The exergy potential of GW is calculated compared to the average incoming temperature of CW of about 285K (11.85°C), taken as the dead state [14]. As highlighted in Figure 2-3, the average GW temperature is 325K (51.85°C) for 150kg produced daily per person. This corresponds to an annual exergy content of 2,465kWh per person. If this exergy content was converted into mechanical energy, the exergetic potential would only be about 151kWh with more than 90% destroyed as anergy due to the irreversibility in the conversion process. This proves that the heat from GW is best suited to be stored thermally for later use instead of being converted into electricity, primarily due to the fact that it is a low-grade energy source [39]. Only thermal to thermal recovery is the best approach to extract this energy. Additionally, the harnessed heat is not sufficient to be operated in a Rankine cycle or a similar work output cycle. Nevertheless, thermoelectric generators that directly convert thermal energy to electricity without any mechanical parts are also quite famous as an alternative option [41]. These generators operate on the Seebeck principle similar to the functioning of Photovoltaic (PV) cells. However, they would have an extremely low energy efficiency with regard to this application.

Unfortunately, as presented in section 2.3, conventional GW heat harnessing devices are only capable of extracting 20-50% of this exergy content. This is yet another reason to develop a more efficient heat harnessing device. In general, the incoming CW in a conventional buildings needs to be heated by about 40-60K before being consumed. If

most of this required temperature increment is provided by GW, both the improvement in exergetic and energetic efficiency would significantly enhance the building's competence [14]. The usage of latent heat storage linked with this application is a novel and an unexplored approach. For this reason, this approach can be categorised as having a Technology Readiness Level (TRL) of 3/4. Having proved its feasibility, considerable upgrades would be expected to demonstrate the technology in actual operating conditions. At the same time, linking this source of harnessed heat with a fourth generation DH grid is a concept at a TRL-1 stage, especially in non-Scandinavian countries [10].

### **2.3. Commercial GW heat harnessing technologies**

Harnessing the thermal energy from GW is a concept that has existed for several decades. Consequently, HEs and HPs or a combination of both, are mature technologies available in the market to harness GW heat [42]. Comparatively, HEs have lower investment and operational costs as they are much simpler compared to HPs. For this reason, the energy efficiencies of HEs are lower with less operational flexibility in comparison with HPs. However, HPs have the disadvantage of higher installation and maintenance costs due to having mechanically moving parts, i.e. the pump. HPs require an external source of energy classifying them as non-passive devices. Harnessing GW heat while investing additional energy defies the concept of low-energy passive houses and makes the whole process economically unfeasible. At the same time, HPs are more suited to larger sewage pipes and are not applicable for single appliances primarily due to space constraints. Hybrid combinations of both are frequently used to amplify the advantages of both technologies and minimise the disadvantages. As an extension of Figure 2-9, if a typical heat harnessing device is used in conjunction with an appliance, it would recover 60% of the thermal content of the flushed GW (72 energy units). Only 46 energy units of fuel would be needed instead of the original 100 energy units. This would save 54% of the original 100 units of fuel consumption, as illustrated in the Sankey diagram in Figure 2-10:

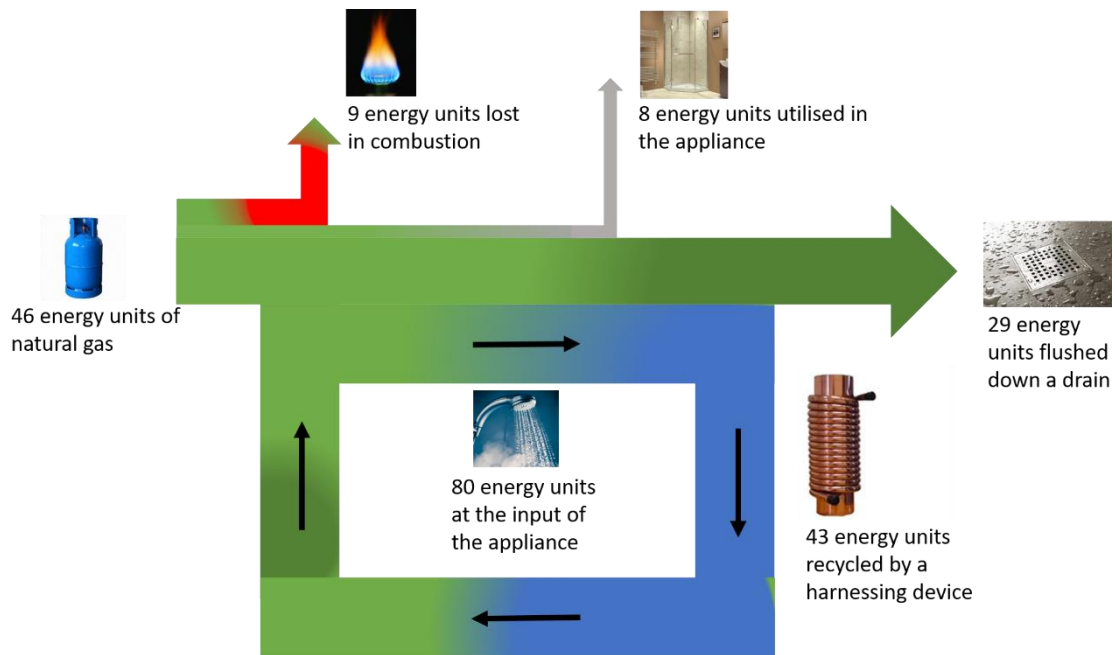


Figure 2-10: Sankey diagram of the potential energy savings with GW heat harnessing in conventional residential appliances

Harnessing heat from waste water can be done at three different levels [34,35,42,43], as highlighted in Table 2-2:

Table 2-2: Different levels of waste water heat harnessing

Level	Temperatures/K	Mass-flow rates/kgs <sup>-1</sup>	Technologies	Possible recovery
At a building level, instantly after the GW enters the drain of an appliance	313–337 (39.85–63.85°C)	0.03-0.33	HE and HPs	70–90% of the initial energy content
At a larger district level, when the GW arrives at the main sewage lines	288-303 (14.85–29.85°C)	166.67 > depending on the location and pipe diameter	Both in-line (plate HEs) and out-line (HEs & HPs) having additional pressure pumps	A higher content of contaminants resulting in recovery of 40–50% of the original energy content
At a waste water treatment plant (WWTP), before the purification process	283-293 (9.85–19.85°C)	166.67 <	HPs to transport the large quantities over distance	10–30% of energy recovery depending on the purification process

Harnessing at the second and third levels cannot only be done on GW without massive infrastructure changes to the conventional sewage system. At this level, GW and BW are mixed with sludge and sometimes industrial waste water as well. As the waste water propagates through the sewage system from a building to a WWTP, it loses its temperature and gains more impurities, typically in the form of more sludge. Additional pumps are normally required to keep this higher density wastewater moving through the piping grid [40]. An advantage of harnessing at the WWTP level is that after treatment, the water can be directly used in a HP cycle without the need of an intermediate circuit. Although the temperatures of the wastewater in the last two levels are lower, probably about 1-10K can be recovered compared to a recovery of about 10-30K at a building level, but the flow rates and volume of water involved at these last two levels is so high that the potential to harness it is still quite extraordinary [34]. Harnessing heat at a building level is relatively easier in terms of the legal requirements as the owners are the only stakeholders. However, at the other two levels, harnessing would be a district-initiated project. Additionally, there are stringent legal requirements for the quality and minimum allowable temperature of the wastewater in sewage lines which puts an upper limit on the harnessing potential [43]. One reason for this is that there is a possibility that the sludge would freeze in the sewage lines if heat harnessing was performed below a minimum temperature, making it impossible to get it transferred to the WWTP. At the same time, if the temperature of the wastewater fell below 283K (9.85°C) [24], it would be extremely difficult to purify the water in the WWTP during the nitrification stage [12]. Additionally, there is a need for a temperature cushion as the waste water loses an additional 5-10K in the purification process [42]. If the GW heat is harnessed beyond this limit, there would be an additional requirement to heat the sludge during purification which would defy the concept of harnessing the heat passively to save energy. Another issue with WWTP level harnessing is the distance between consumption and recovery, requiring additional pumps and auxiliary equipment. WWTPs are generally on the outskirts of urban centres; in fact only specific points in the sewage lines can be accessed even for level two harnessing. Harnessing at the second and third level is generally large-scale, acting as a centralised source of heat. However, the realisation for fourth generation DH requires decentralised heat sources instead of large centralised sources. In some circumstances, the harnessed heat can be utilised within the WWTP at the third level (e.g. at the digester tank or to dry the sludge in the later processes of purification) [12]. In general, recovery at the sewage level has

the best rate of return, especially in providing heat at district levels [35]. However, the temperatures involved are lower, eventually resulting in the destruction of more exergy. It is estimated that at the second or third level, about 4,000 MWh of energy could be recovered at a regional level [44].

### **2.3.1. Heat exchangers (HE)**

HEs are the most commonly used passive heat harnessing technique; transferring heat without contact between fluids with no external energy input and minimal maintenance requirements. About 40-80% of the thermal energy in the GW can usually be recovered with the possibility to recover even more using longer cascaded arrangements. The rate of recovery is highly dependent on the flow characteristics of the fluids involved and the HE design [16]. In some circumstances, external pumps are used to enhance the HTC with forced convection and turbulent flow conditions [34]. Pumps are also usually used at level two or three harnessing systems in Table 2-2 [35]. HEs do not decouple supply with demand as there must always be a CW inflow when the GW heat is being harnessed. For this reason, it is important that the pipes in the HE have double layers to avoid contamination or leakages into the incoming CW. At the same time, the GW drain line should be vented to avoid any foul smells and clogging.

Most commercial HEs are usually advertised and designed for residential showers. However, they can be equally beneficial when used with other residential appliances or commercial drain lines as well. In a field study [45], a commercial HE was successfully demonstrated to harness GW heat from basins/sinks in a multi-storey building, showers in a student dorm, dishwashers in a restaurant and washing machines in a laundry facility. The best results were achieved when the HE was used in conjunction with the dishwashers, since the incoming GW temperature was greater than 333K (59.85°C). The payback period for most HEs used with residential appliances is usually between 2.5-5 years. However, when constructing a residential building, their investment is less than 0.1% of the total cost making it a good investment over the long term [46]. In general, HEs for GW heat harnessing can be divided into five main categories:

- Type
- Orientation

- Location of installation
- Anti-fouling mechanism
- Operation strategy

Consequently, each main category has several subcategories as illustrated:

#### I. Type

A further division of four main types of commercial HEs is possible:

- Shell and tube

Along with plate HEs, this type is considered the best for liquid-to-liquid heat transfer applications. When used for GW heat harnessing, both these types of HEs have a high vulnerability to fouling and biofilm deposits. Normally, a large GW storage shell contains spirally arranged CW tubes within [32]. The CW tubes can be arranged within the shell along its circumference to avoid biofilm deposits on their external surfaces. This HE is different due to the fact that the GW is retained in the shell over a longer duration. This leads to convection along with conduction as the sources of heat transfer, enhancing the energy efficiency. The capacity of the shell is usually designed at 90kg per person [47]. The shell is insulated from the outside with several possible connections as it can be linked with more than one appliance at the same time. Considerable pressure losses in the CW tubes limit the overall transfer of heat with efficiencies in the range of 40-50%.

- Concentric pipe

Also known as the tube-in-tube HE, it is the most economical and the simplest of all methods to harness GW heat. Typically, a smaller diameter pipe is inserted into a larger diameter pipe with a small gap between them both. Normally, GW flows along the circumference of the internal pipe with support from surface tension and gravity while CW flows in a counter-flow direction along the external pipe. An impermeable lining is usually necessary on the outer circumference of the internal pipe to minimise the risk of contamination and leakages. The efficiencies of these HEs are less than 60% with the advantage that there are almost no pressure losses and fouling possibilities [48]. Also, the start-up time is only a few minutes before steady-state conditions are achieved. A

drawback is that this HE can only be installed in a vertical orientation. These HEs have the least energy efficiency in comparison, due to their low contact time and the surface area of contact between the fluids [49].

- Falling/Gravity film

This type of HE is the most commonly used with the greatest number of manufacturers, having had about ten patents since the 1980s [47]. With the assistance of gravity and surface tension, the GW falls along the circumference of a vertical pipe with smaller CW tubes looped around the external circumference [50]. This HE is also referred to as the gravity-film exchanger (GFX) due to its gravity assisted operation. The flow of the GW is considered turbulent, having more than 1mm of velocity boundary layer thickness. Although there is no pressure loss in the GW flow, there are considerable losses in the CW tubes of between 7-15kPa, depending on the flow conditions and design of the HE. An important limitation for these HEs is their lack of performance at high GW flow rates. In this circumstance, most of the GW falls through the centre of the vertical pipe without much contact with the circumference, resulting in almost negligible heat transfer [25,51]. The material of the pipe and tube in the HE ranges from aluminium, copper and plastic with lengths of about 1-1.5m [52]. Nevertheless, cascaded combinations of more than one HE can be used, keeping in mind an optimum balance between the length and the performance. Beyond the optimum length, the small additional performance is not worth the extra investments. There can usually be about 0.5-3m of vertical installation capacity in the drain pipes of a residential appliance. The energy transfer efficiency of the falling film HEs is the highest at about 60-70%. In an interesting study [26], to enhance the performance of these HEs, a layer of water jacket was used to cover the outer CW tubes. Water has a higher thermal conductivity in comparison to air, which reduces the thermal resistance between the GW and the outer tubes. It was concluded that the smaller the gaps between the outer tubes and the inner vertical pipe, the better the performance. Consequently, it was proposed to use square outer tubes instead of circular ones, to minimise this gap and increase the surface area of contact. In these types of HE, the vertical GW pipe is about 50-150mm in diameter while the CW tube is about 12-25mm. Since these are the oldest HEs to harness GW heat, they have evolved over three generations [26]. In the first generation, the flow of both fluids was counter-flow with the CW having only a single point of entry in the



tubes, resulting in high pressure losses. In the second generation, the CW had multiple entry points in several tubes arranged in parallel. This resulted in lower pressure losses, but most HEs developed in this generation were not counter-flow. In the latest third generation, thin squared CW tubes with multiple parallel entries and a counter-flow arrangement with the GW were developed. This reduced the CW pressure losses whilst maintaining a high heat transfer rate [37]. However, a noticeable drawback in the third generation is the deposition of lime due to calcium carbonate in the CW flow, primarily due to the thin square tubes being prone to fouling.

- Plate


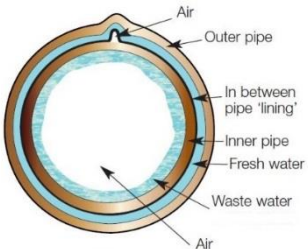

Plate HEs are normally used to harness GW heat at a sewage level along with a building level. In building installations, horizontal plate HEs are placed directly beneath the slabs or floor tiles. This type is most commonly used in conjunction with residential showers, due to their ease of installation. Normally, the slab or platform is integrated with footplate HEs or a multi-layer unit is placed horizontally underneath the drain [47]. Although it is not common, this HE can also be placed on top of shower slabs, as in a case study [53], where an integrated lattice type plate HE recovered 50% of the thermal energy of the GW. Such a unit consists of alternate flow channels of the GW and CW, with a series of plates combined together in a cascaded arrangement. Adjacent layers of the plates with the same flow fluid are linked together with a manifold at either end. The flow of the fluids (GW and CW) can either be counter or cross-flow. An additional chamber usually exists vertical to the HE to temporarily store and guide the GW through [54]. These types of HEs have the advantage of an increased surface area of contact whilst having average pressure losses, but are vulnerable to fouling. The energy efficiency is usually below 50%, but several cascaded units can recover up to 90% of the thermal content of the GW. The material for the plates is normally stainless steel to avoid corrosion over the long term.

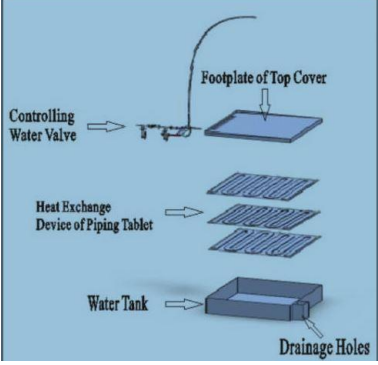


Plate HEs are also commonly used in large sewage lines. They are usually embedded within pipelines by being placed on the surface of the lower circumference of the pipe [38]. However, due to the sludge and sediment formations on the surface, regular maintenance is required and the energy efficiency is considerably lower. Consequently, the use of outline HEs in conjunction with sewage lines is proposed to tackle this

obstacle [43]. However, the requirements of additional pumps and filtration systems increase the investment and operational costs, making it impractical without major infrastructure refurbishments.

A summary of the different types of HEs with details of commercial manufacturers and costs [32,37,47], are in Table 2-3:

Table 2-3: Summary of the different types of HEs used in GW heat harnessing

Type	Manufacturers	Cost	Images
Shell and tube	<ul style="list-style-type: none"> <li>• OSO Hotwater AS</li> </ul>	£1,150	
Concentric pipe	<ul style="list-style-type: none"> <li>• Wavin</li> <li>• Hei-tech B.V.</li> <li>• BRIES Energietechnik</li> </ul>	£250–600	
Falling/Gravity film	<ul style="list-style-type: none"> <li>• Power Pipe</li> <li>• Retherm</li> <li>• Waterfilm Energy Inc.</li> <li>• EcoInnovation Technologies Inc.</li> <li>• Watercycles Energy Recovery Inc.</li> </ul>	£300–925	

<p>Plate - (footplate at building level)</p>	<ul style="list-style-type: none"> <li>• Redi</li> <li>• Ecodrain</li> <li>• Hei-tech B.V.</li> <li>• BRIES Energietechnik</li> <li>• SUP Technology</li> </ul>	<p>£300– 2,000</p>	
<p>Plate - (in-line at sewage level)</p>	<ul style="list-style-type: none"> <li>• Rabtherm</li> <li>• KASAG</li> <li>• Pressurepipe</li> <li>• Uhrig therm-liner</li> <li>• BB heatliner</li> </ul>	<p>£750– 1,700 per kW</p>	
<p>Out-line (sewage level)</p>	<ul style="list-style-type: none"> <li>• DDI Cube</li> <li>• SHARC Energy Systems</li> <li>• Huber</li> </ul>	<p>£5,000 &lt;</p>	

## II. Orientation

The thermal performance of the described commercial HEs is better in vertical orientation compared to horizontal installations which have only about 20-50% energy efficiency [52]. The primary reason for installing horizontal orientation HEs is the lack of vertical space in the drains of residential appliances. In an experimental study [52], vertical installations of different HEs were compared to horizontal orientations. The energy efficiencies were in the range of 30-75% for low flow rates in a vertical

orientation, while the same devices were between 5-20% efficient in a horizontal orientation. Hence, the same HEs would have to be oversized for horizontal orientations which would eventually increase their payback period from 3 to 15 years. The outlying reason for this major difference in efficiency is portrayed in Figure 2-11:

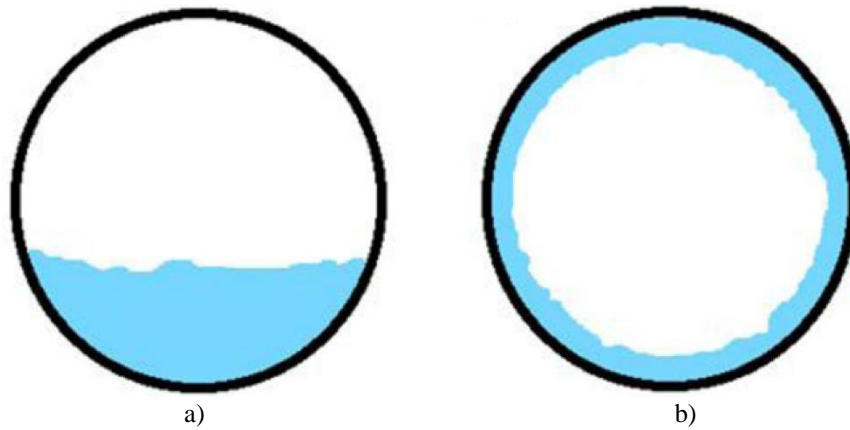


Figure 2-11: Flow of GW in a) horizontally oriented b) vertically oriented piped HEs [52]

In a horizontal orientation, only the lower circumference of a pipe is in contact with the flowing fluid. Comparatively, the entire circumference is in contact in vertical orientation which considerably enhances the heat transfer rate. The increase in the surface area of contact is more than double for the vertical orientation, which is the prime reason for the difference in efficiencies. Additionally, an alternative configuration was proposed for horizontal installations in this study to enhance the area of contact, as illustrated in Figure 2-12:

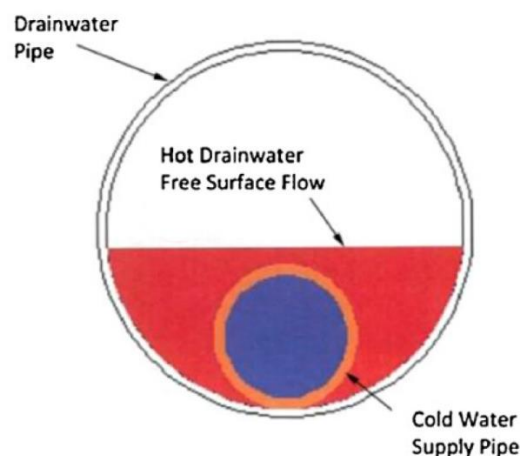


Figure 2-12: Proposed configuration to improve the efficiency of horizontally oriented piped HEs [52]

The energy efficiency was 45% in this counter-flow concentric pipe configuration. This is still lower compared to the vertical installation but considerably better than typical

horizontal orientations. Additionally, it was concluded that falling film HEs lose 4% in energy efficiency when tilted by 2° from the vertical. This relationship is not linear but quadratic, with a maximum allowable angle of tilt of 15° prescribed by manufacturers [53].

### III. Location of installation

HEs can be used at either a building or a sewage level when installed in solo operation. However, they can be used at any level when combined in hybrid with HPs. In this case, they can either act as a preheater for the HP or provide last-stage additional heating after the HP cycle.

The installation of HEs in sewage lines has two options; either in-line or out-line with additional pumping and filtration systems [43]. To efficiently utilise in-line HEs, it is recommended that the sewage lines have a diameter greater than 800mm with a minimum flow rate of 30kg/s with waste water covering at least 0.8m<sup>2</sup> of surface on the bed of the sewage pipe [12]. There are two further options for in-line installations, as highlighted in Table 2-3. Either the HE can be embedded into the lower bed of the sewage pipe or a plate HE can be placed on this bed [55]. Embedding a HE into a sewage line is only possible in new installations, as the refurbishment of existing lines would be extremely expensive and challenging.

Typically, out-line installations of HEs are coupled in hybrid with HPs to enhance energy efficiency. However, additional pumps and filtration devices are needed, especially when pumping sewage water over long distances. There is usually an opening at the lower end of the sewage pipe, from which the waste water is filtered and pumped into an intermediate HE followed by a HP circuit. About fifty different facilities of this type are present in Switzerland with some having hybrid HE-HP combinations [24]. At the same time, only three such facilities in the city of Zurich have the capacity to recover 5MW of waste heat. Similarly, a facility installed in Oslo, Norway can heat an entire district of the city during peak hours.

#### IV. Anti-fouling mechanism

There is always a high vulnerability to fouling in HEs, especially in conjunction with GW heat harnessing where biofilm deposits are inevitable, especially in the long term. There are two techniques to tackle this problem; either actively or passively. Passive techniques are usually used in simple HEs, while both methods can be used simultaneously in the evaporators and condensers of HPs. It is a more critical concern in HPs, since it affects the performance of all the associated machinery. At the same time, the clogging of the evaporator and condenser can even lead to the choking of the HP. For this reason, active anti-fouling techniques are elaborated in section 2.3.2. The most common passive strategy for simple HEs is dipping and baking the surface of the pipes with chemical coatings. This averts corrosion and fouling at the cost of reduced thermal conductivity. For small HEs in residential applications, the easiest and most practical approach is prevention. The most economical and effective method is regular cleaning and flushing the pipes with appropriate detergents. For larger biological impurities, the use of strainers and filters at the cost of additional pressure losses is recommended. In an interesting approach [38], the use of low-cost plastic pipes for HEs in GW heat harnessing was investigated. Although fouling was reduced to a certain extent; the long-term durability of the HEs was also reduced, especially at higher flow temperatures.

#### V. Operation strategy

When harnessing GW heat at a building level, three options of installing HEs exist, as displayed in Figure 2-13:

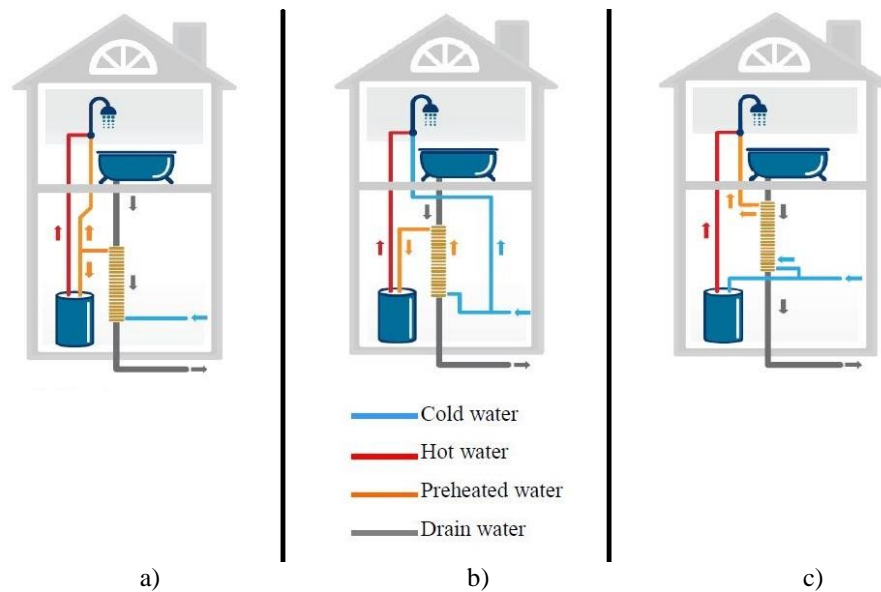


Figure 2-13: Operation strategies of HEs for GW heat harnessing at a building level a) balanced with a storage option b) unbalanced c) balanced without a storage option [50]

- a) preheated water flows to both the storage and the appliance—balanced condition.
- b) preheated water flows only to the storage—unbalanced condition.
- c) preheated water flows only to the appliance—balanced condition.

The cylindrical drum is a heater with the possibility of storing water. In options a) and c), both the flow rates of the demand and supply of water are equal, therefore it is regarded as the balanced condition. However, a) has more flexibility with the additional option of storing preheated water in the drum. HEs are known to perform best in balanced flow conditions when the flow rate of the demand is exactly equal to the supply. In such circumstances, the temperature lost by the GW is equal in units to that gained by the CW. For this reason, option a) is the most preferred amongst the three as it also has the highest energy efficiency and the best rate of return on investment [46]. However, in real conditions, the fluid flow is not exactly balanced due to its transient nature [16]. In unbalanced conditions, the HE is used as a preheater, to store warm water in the drum, or both. Energy efficiencies in the balanced flow mode are usually greater than 50% but are less for an unbalanced flow [37].

In a study [25], an analysis was performed on five different HEs to determine the importance of GW flow rate in comparison to temperature. It was determined that the flow rate was more important. However, only an optimum value gave the best

performance [13]. The energy efficiency of a HE is proportional to the flow rate up until an optimum Critical Flow Rate (CFR). After this value, the efficiency is constant or may decrease with higher flow rates. The CFR of a HE operating with GW is dependent on a number of flow, metallurgical and geometrical characteristics. The CFR is between 0.07-0.13kg/s based on experimental data for pipes having a diameter between 5-10cm [56]. At the same time, a HE operating at the CFR value reaches the quickest steady-state operation. It is estimated to take a maximum of 300s for a HE pipe to warm up and reach steady-state conditions with GW flow [25]. The associated pressure losses cannot be ignored whilst considering the harnessing of GW heat through HEs. Since the GW flows only with the pull of gravity, the margin for pressure losses are quite low, as explained. These losses are proportional to the square of the velocity of the fluid and the length of the pipe whilst being inversely proportional to the diameter of the pipe, according to the Darcy-Weisbach formulation [39]. In a falling film HE with the GW having a flow rate of 0.17kg/s, the pressure drop can be in the range of 200-1,750Pa/m [25].

### **2.3.2. Heat pumps (HP)**

The flow of heat in a HE is from a high temperature to a lower temperature source. However, a HP is capable of transmitting heat in the opposite direction with an external input of energy in the form of electricity in a vapour-compression cycle, or heat in an absorption cycle. The main components of a HP are an evaporator, a compressor, a condenser and a throttling valve; operating in this specific order. A working fluid transfers net thermal energy when operating in a closed cycle HP. Initially, it evaporates by gaining heat in the evaporator to be compressed and transported to the condenser where it loses heat to be eventually throttled back to the evaporator. The working fluid changes phase from being a gas in the evaporator to a liquid in the condenser [39]. This net transfer of energy is based on the phase change of the working fluid, which is governed by the latent instead of the sensible heat. For this reason, HPs are capable of transferring large amounts of heat compared to HEs that operate on the physics of sensible heat transfer. However, the evaporator and condenser of a HP are both HEs in principle. Although the association of HPs with GW heat harnessing is not that old, in



general the technology is. The operation of a HP cycle linked with GW heat harnessing is illustrated in Figure 2-14:

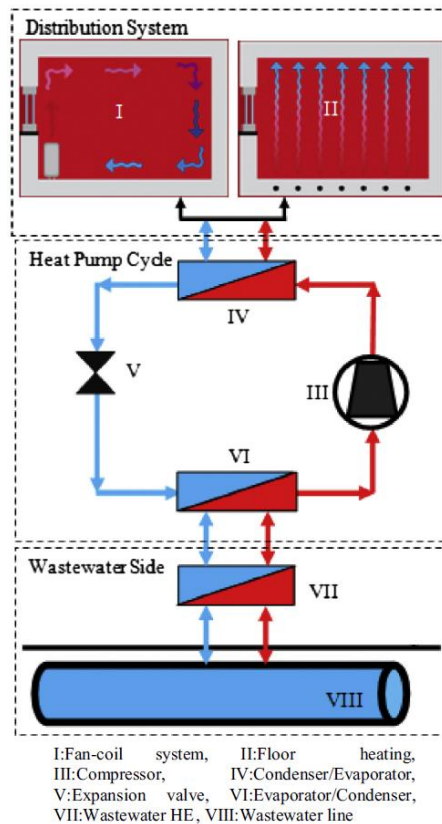


Figure 2-14: Schematic of the operation of a HP linked with GW heat harnessing [38]

In this specific application, the thermal energy of the GW is harnessed via a HP to be used for space heating, where fan coils blow air over the condenser of the HP acting as a cross-flow radiator from the floor of a building. Unlike HEs that can only be used to heat CW, the output of a HP can be used in many versatile applications after harnessing the GW heat. Additionally, HPs are estimated to have higher energy efficiencies of about 80-90% [16]. The main drawback of HPs for GW heat harnessing is that once again, supply and demand are coupled as the HP must deliver output heat whenever there is a flow of GW. At the same time, this is not a passive technology as it requires an input of external energy. In the event that a HP is used to heat incoming CW to a predefined level whilst simultaneously harnessing GW heat, the sizing of the HP increases substantially. For this reason, it is mostly relevant in large scale harnessing applications (level two and three) and not at a building level. Additionally, there are space constraints for the installation of HPs at building levels, whilst being economically unfeasible due to maintenance and input energy requirements. Another

drawback is that the performance of a HP is more sensitive to the GW characteristics being less reliable compared to HEs [33]. In general, GW heat harnessing HPs can be distinguished based on the following five categories:

- Type
- Type of HE used in the evaporator/condenser
- Working fluid
- Location of installation
- Reversibility

Similar to HEs, each main category has several subcategories as illustrated:

#### I. Type

The major differences based on the type of HP cycle are:

- Vapour-compression cycle

This is the more commonly used type, where the input energy to the compressor is in the form of electricity. As mentioned, the compressor is used to increase the pressure of the working fluid to enable it to release heat to the condenser [39]. As a rule of thumb, centrifugal compressors are preferred compared to reciprocating compressors when the working fluid has a large specific volume and low evaporator pressures are involved, as for this application of GW heat harnessing. Additionally, in recent energy efficient HPs, a variable speed compressor combined with an electronic throttling valve are used to enhance the economics of usage and flexibility in operation [6]. A typical centrifugal compressor draws about 5-6A of current at a voltage rating of 220-240V.

- Absorption cycle

The difference between an absorption and vapour-compression cycle is the mechanism, in which the pressure of the working fluid is increased. In an absorption cycle, the pressure is enhanced by absorbing the working fluid into another soluble liquid and pumping it to a higher pressure. Since a pump is used in comparison to a compressor, the input energy required is comparatively less [39]. However, in order to make the working fluid soluble into the absorption medium, an external source of heat is also

required. In most cycles, ammonia is the working fluid while water is the absorbent. The Coefficient of Performance (COP) of absorption cycle HPs is lower than that of vapour-compression cycles, since both heat and electricity are inputs [57]. At the same time, compressing a liquid can considerably increase pressure compared to pumping. In most non-industrial building legislations, it is required that vapour-compression cycles have a COP of at least 2, while absorption cycle HPs are of at least 1 before they can be installed to supply heat [57].

## II. Type of HE used in the evaporator/condenser

Unlike the versatility in the types of HEs, only two types are used as the evaporator/condenser in a HP: a) plate and b) shell-tube type [44].

The evaporator is usually of the shell-tube type while the condenser is of the plate type. This is due to the difference in the boundary conditions on both sides, including the temperatures and pressures involved. However, in large scale applications including harnessing heat in WWTPs, both the evaporator and condenser are of the shell and tube type [38]. The shell usually contains the GW/waste water with copper tubes inserted into it containing the HP cycle's working fluid [6].

The biggest concern with HP evaporators is their vulnerability to fouling, especially as GW is in direct contact at this point in the cycle. It is estimated that if no maintenance is done, biofilm layers of up to 1mm deposit on the external sides of the tubes of the shell-tube HE within the first five months of operation. This reduces the overall COP of the HP by about 20% [33]. There are three main types of fouling in the evaporators in this application of GW heat harnessing: a) biological (biofilm deposits) b) corrosion and c) precipitation [33]. The chemistry of the formation of each type is dependent on the flow conditions, geometric features, HE design and operating times, etc. However, as mentioned, the removal of these fouling conditions can be done actively or passively. The magnitude of the fouling problem is much more intense in levels two and three of waste water heat harnessing setups with large-scale HPs, necessitating active techniques. In an interesting study [33], a vibrating anti-fouling clean-up system based on an automatic electronic control mechanism was developed for a large HP. It was concluded that such a technology was only suitable for commercial systems since a

significant amount of energy input was required. If used for residential GW heat harnessing applications, it would require a net energy input to defy the approach of lowering the energy demand. Similarly, most large scale HPs have built-in pneumatically controlled automatic fouling removal mechanisms [58]. In such a system, automated rubber balls are circulated and brushed in a HP evaporator operating after fixed workload hours. Similarly, passive techniques on large-scale HP evaporators have also been analysed. In a unique device, a manually controlled external screw attached to rotating rubber baffles located inside the evaporator was used to clean-up biofilm deposits whenever required. This manual strategy was effective, economical and flexible, yet zero-energy consuming. Based on an estimation, the convective HTC in HP evaporators for sewage heat harnessing is 40% less compared to normal HP applications due to fouling and sludge deposition [38].

### III. Working fluid

The working fluid is primarily selected based on the temperature differentials between the evaporator and the condenser, which depend on the heat output application after GW heat harnessing. Additionally, the phase change temperatures along with several other thermal and physical parameters of the working fluid are important as well [39]. In the case of GW heat harnessing, the temperature of all three levels of harnessing is 283-333K (9.85-59.85°C) in the shell-side of the evaporator. The working fluid in the tubes of the evaporator usually operates at a temperature 5-10K lower than this, to more easily facilitate heat transfer as per the first law of thermodynamics. Additionally, the working fluid is selected so that it can change phase by evaporating at an appropriate pressure without considerable input energy requirements. The use of fluorinated hydrocarbons (HFCs) is now more common due to the role of controversial chlorofluorocarbons (CFCs) in ozone layer depletion [57]. Based on the temperature range of GW heat harnessing, the most appropriate working fluids for a HP are R-134a, R-404a, R-407c and R-410a [39]. Similarly, for non-industrial applications of HPs, the use of R-134a and R-410a are the most common working fluids [33]. Normally, the working fluids for absorption cycle HPs are air, ammonia, carbon dioxide and water [38]. However, compared to the many options in vapour-compression systems, the choice of working fluids for absorption HPs is limited due to the solubility requirement into an appropriate absorbent.

#### IV. Location of installation

As mentioned, HPs are best suited for level two or three large-scale heat harnessing of waste water. However, they have been tested at all three levels.

The temperature lift is defined as the difference between the temperature of the heat source at the evaporator and that of the deliverable source at the condenser. The COP of a HP is inversely proportional to the temperature lift [6]. Values of the COP as high as 10 have been recorded in cases where the temperature lift is within 20K. Based on this, the highest potential for heat harnessing is at a building level, when the GW has the maximum temperature. When using HPs at a building level with appliances, it is normally an out-line arrangement with major changes in the conventional drainage architecture [16]. Unlike HEs, this is due to space constraints and the requirement of an additional input energy source. Using HPs in this arrangement has produced a COP in the range of 5-6 [16]. Typically, these HPs for heat harnessing at a building level have capacities in the range of 0.8-10kW. In a field study [6], a HP linked with the GW outputs from a bathroom recovered 2,400kWh of heat annually with only a 410kWh energy input into the compressor. In a similar study [59], the use of cascaded HPs harnessed a comparatively higher amount of energy, as two serially connected HPs were used to recover GW heat to be transferred into CW for commercial washing machines. Using plate type HEs in the condenser, the incoming CW was heated from 287K (13.85°C) to 328K (54.85°C). Similarly, the shell-tube type evaporator cooled the outgoing GW from 322K (48.85°C) to 287K (13.85°C). The unit had a balanced operation strategy in which the mass-flow rates of both the GW and CW were equal. This resulted in an overall COP of six for both the serially connected units. In this cascaded combination, both HPs had different working fluids to suit the varying GW and CW temperatures as they flowed through the arrangement. The HP operating at a higher GW temperature used R134a while the lower temperature HP in the cascaded combination used R407c. Consequently, about 85% of the required input energy for heating CW in a washing machine was reclaimed through these HPs.

Although the temperatures at a building level are much higher, the flow rates are lower. At the sewage level, both are intermediate and by economies of scale, is considered as the best point for harnessing heat by a HP, as the recorded COPs range from 1.77 to

10.63 [38]. The heating capacity of most units at this level range between 10-20,000kW. The most important criteria when designing a sewage level HP is the predictability of temperature along the flow line, so that it does not drop below the legal limit. In such a study [24], a mathematical model was developed to predict the sewage temperature along the length of the line. The temperature is dependent on the flow conditions, the geometric properties of the line and the properties of the soil around the pipe. This model had the flexibility to be adapted to different locations around the globe and was validated based on a field study in Switzerland. In a pilot test [12], a shell-tube evaporator of a 30kW HP was used to harness waste water heat by installation in a pit linked to the sewage line external to a commercial 100-bed hospital, at an average COP of 3.8.

When harnessing heat at the third level, several cascaded combinations of both HPs and HEs are usually used. Nevertheless, there are recorded cases of solo operations of HPs with WWTPs. In Switzerland and Scandinavia, over 100 such HPs are in operation with ratings of up to 70,000kW [35]. In Lucerne, Switzerland there is a 50MW HP installed in solo operation. Similarly, a HP with a rating of 9kW is used to heat the underground train stations in Glasgow using sewage water, having a COP between 2.5-3 [60]. Additionally, there are over 500 such HPs operational worldwide [12].

## V. Reversibility

By using a reversible throttling valve as in Figure 2-14, a HP cycle can be used as a refrigeration cycle to provide cooling instead of heating. Normally, in the case of cooling, the GW temperature is lower than the ambient [32]. This is extremely useful in countries where both cooling and heating are desirable; especially in the Middle East or tropical countries where daytime temperatures require cooling while night time conditions need heating. The COP of reversible HPs operating in a cooling mode is between 2.23-5.35 [38].

The most prominent manufacturers of level two and three HPs are Friotherm AG (Frauenfeld, Switzerland), TECSIR (Quintana Roo, México), Nova Thermal Energy (Philadelphia, USA) and Viessmann (Allendorf, Germany). The prices of a unit vary considerably, being dependent on the size, whether the components are sold separately

or as a whole unit, the level of control required in the HP, the reversibility requirement and the desirable thermal performance. The installation of HPs at a building level is more flexible, as smaller units with dissociated components are usually available. For waste water heat harnessing at level two and three, the units are sold as a whole, normally in a bulk casing.

### **2.3.3. Hybrid systems**

#### **I. HE/HPs with renewable and conventional heating technologies**

In most circumstances, heat harnessed from GW is incapable of providing the full-load heat demand for the end-user. It can only partially fulfil the demand and needs to be topped up with other sources of heat. It is most commonly used in conjunction with conventional boilers and electric heaters to provide the remaining full-load heat demand [36]. This also enhances flexibility and reliability, where the conventional heating technologies can only be used as a back-up source during peak-load hours. In such a field study [36], a 24kW HP was used as a preheater in a student dorm to heat incoming CW from the initial 285K (11.85°C) to 318K (44.85°C). Following this, a traditional gas boiler was used to further heat the water to the required 333K (59.85°C). In this case, the HP reduced about 68% of the gas consumed by the boiler in normal circumstances.

Since GW heat harnessing is considered as a third-generation renewable source [10], linking it with second-generation renewable sources has been widely researched. In a field study [15], a HP harnessing GW heat was coupled with an air source heat pump (ASHP) to fulfil both the hot water and space heating demands of a residential apartment building in New York. In all combinations of operation, the COP of the system was greater than 4 and a minimum energy saving of 34% was recorded. Combining harnessing technologies with solar thermal heat is most commonly researched within this domain of GW heat harnessing, especially the cascaded combination of solar heat-HP-HE, in spite of the high capital costs. Normally, a dark flat plate solar thermal collector is installed on the roof of a conventional building [61]. The working fluid that gains heat through the absorbers of the solar thermal collectors is usually water and an anti-freeze agent, eventually releasing this heat to a primary

heating circuit. GW heat is harnessed by the cascaded HE/HP system with the same essential features discussed previously, although it has more complicated control equipment due to the complexity of integration. Usually, the HP/HE combination is used to preheat the CW prior to it gaining heat from the solar thermal collectors and may also require additional boilers in case the desired temperature is higher [62]. Data from such systems show annual energy savings of up to 90%. In a study [62], the hybrid combination of a HE-HP system combined with solar thermal collectors was tested to heat water in a public showering facility. In this serially connected cascaded chain, the solar collectors were the first in the circuit followed by the HE and eventually the HP. The ecoMax manufactured by the firm Eco Hybrid Solar (Stamford, USA) is a commercially sold unit for residential and commercial buildings that integrates solar thermal energy with GW heat recovery.

## II. HE/HP combinations

Although this combination exists at all levels of heat harnessing, it is most common in the second and third levels of Table 2-2. In most circumstances, the HE is the preheater for the incoming CW followed by a serially connected HP. To prove its viability even at a small-scale, an integrated HE-HP was installed in the drain of a shower [63]. In this investigation of a relatively small single-family house, the harnessed heat from the GW was initially used to preheat CW in a shell-tube HE, after which it was used to heat the CW in an evaporator of a small HP. Initially, the temperature of entry of the GW at the first HE was 305K (31.85°C) reducing to 300K (26.85°C) before leaving this preheater. It was finally discharged after the HP cycle at 288K (14.85°C). The source of the GW was a member of the household showering at 315K (41.85°C) for 900s, with an average flow rate of 0.1kg/s. The evaporator of this unit had a capacity of 2.70kW, while the compressor had an input of 0.60kW. During most modes of operation, the HP had a COP between 2.19 to 3.21. The CW heated by this hybrid combination was stored in a 60kg storage tank for this three-member household. Eventually, this system saved about 60-70% in fuel usage. In a similar study [64], a robust all weather resistant HE-HP duo was used to recover heat from a shower GW. The secondary circuit of the HE was the regenerator while that of the HP was the evaporator in the central heating system, using the GW heat source for space heating. The HP had a condenser and evaporator



temperature of 284.83K (11.68°C) and 324.65K (51.50°C), respectively, giving an overall COP of 4.97.

Since harnessing GW heat at the second and third level is a major infrastructure project, the induced complexities are high because of its large scale. At these levels it is most important to have appropriate control strategies, especially to manage variations in supply and demand. The margin for error is relatively low and the safety requirements are more stringent. A prominent out-line HE-HP system exists in a 900mm sewage line at a college campus in Galashiels, Scotland [65]. Using pumps and a mechanical filtration system, the first step is to divert and filter the waste water into the out-line system. The pumps further move the waste water into a series of 400kW cascaded HE-HP arrangements. The COP of the HPs are 4.8, while the overall system provides 1.9GWh of heat annually for preheating CW on the college premises.

## **2.4. PCMs in waste heat harnessing applications**

With the objectives outlined in section 1.4 along with the constraints to the heat harnessing problem of section 1.3, the use of PCMs is proposed to harness GW heat.

Sensible heat storage linked with HEs and HPs is a mature yet comparatively inefficient technique. In comparison, latent heat storage via PCMs is a new higher density storage option. When a material goes through a phase change, it absorbs or releases heat at a constant temperature. Normally, this phase change or latent heat of a material is much larger than the specific heat capacity making latent heat storage higher in density compared to sensible heat storage. A material usually absorbs heat (endothermic) to melt while releasing (exothermic) it to solidify again. PCMs are available in several phase types but the most commercially used are the solid-liquid type. This is due to many favourable thermal factors, including a larger latent heat of fusion over a narrow temperature range along with having minimal changes in volume during the phase changes [66]. The use of latent heat storage has been widely researched in numerous studies involving passive heating and cooling applications [67]. However, there are only a handful of studies in the literature where PCMs are used to harness waste thermal energy. At the same time, there are no studies focused on harnessing GW heat using PCMs. Table 2-4 proves that if PCMs can effectively be integrated into similar waste

heat harnessing systems, then they have a favourable prospect of being effectively utilised with this GW heat harnessing application. Current research in conjunction with PCMs and waste heat harnessing applications in the literature are summarised in Table 2-4:

Table 2-4: Literature review of the usage of PCMs to harness waste thermal energy

Application	Reference	Overview	Results
Waste industrial heat at 500K (226.85°C)	[68,69]	<p>An experimental research was conducted to mimic the actual circumstances on a large scale, where PCMs were used to recover and transfer heat from industrial waste at a temperature of over 500K (226.85°C). Experiments were conducted for encapsulated PCMs and the packed bed configurations. The characteristics of six different PCMs were ranked according to different thermodynamic, chemical and economic considerations.</p>	<p>The metallic encapsulated design showed better heat transfer rates. While con-current flow of the fluids involved, compared with counter-flow strategies, provided better heat transfer rates.</p>
Waste heat from a steel plant to a chemical plant	[70]	<p>In this theoretical study, the feasibility of using PCMs to transfer heat, at over 573K (299.85°C), from one industrial setup to another, was analysed. NaOH was used as the PCM, having a melting temperature of 593K (319.85°C). The feasibility analysis was done in terms of energy savings, exergy potential improvements, carbon emissions and economic aspects. Theoretically transferring 8.15GJ of heat was analysed, with different parameters and characteristics in comparison with conventional sensible heat storage mechanisms.</p>	<p>Compared to a sensible storage mechanism, about 2.76 times more energy was transferred. Comparatively this approach consumed only 8.6% of the energy, had 38% more exergy efficiency and 18% more carbon savings than a conventional system.</p>
Recovering waste heat in dishwashers/washing machines	[71,72]	<p>In this experimental analysis, four different PCMs were used to preheat the CW in a second cycle from the waste heat of the first cycle in a washing machine and dishwasher. Thermal cycling was also investigated by testing the PCM in 1000 thermal cycles.</p>	<p>A temperature increase of 13.4K was achieved in the second cycle. The PCMs remained chemically stable with a loss of only 10% of the latent heat capacity.</p>
Simple waste fluid HE	[73]	<p>In this published patent, a coaxial HE with two cylindrical pipes was designed. The inner cylinder stored heat from a waste fluid to the PCM while the second cylinder contained the fluid, to which it transferred the heat.</p>	<p>Although the HE could be used in a wide range of applications, the patent intended its use for waste heat recovery applications.</p>

Waste heat from cooking stoves	[74]	This was a simulative study, in which a design was proposed for commercial stove tops to limit convective heat losses from the top. After storage of this otherwise wasted heat in the PCM, it can be discharged in other useful applications. The stove top was numerically analysed to assess the temperature and thermodynamic performance.	It was only feasible to use this stove top in commercial applications, since efficiencies were too low in domestic conditions.
Exhaust heat from an air-conditioning unit	[75–78]	In this research, a PCM was used to capture the waste heat ejected from the condenser of an air-conditioning unit to heat incoming CW. Analysis was focused on using a finned tube PCM-HE to capture the waste heat, with different variations. An experimental test rig with the different configurations investigated this phenomenon.	Results showed that a spiral finned double tube HE in vertical orientation was best suited for this application. The PCM also had graphite embedded in it to enhance conductivity. COP of the air-conditioner was enhanced as well.
Waste heat recovery from engine exhaust	[79–81]	About 30% of the heat of combustion leaves a diesel engine via the exhaust. In this experimental study, a PCM HE integrated with a storage tank was used to extract this exhaust heat, with different loading conditions. A similar analysis was done for normal IC engines, varying the parameters and conditions in experimental and numerical studies.	About 10–15% of the heat of combustion was recovered, which is about 7% of the fuel energy, corresponding to about 86.45 kg/kJ of energy. Results show that the flow rate of the exhaust gas was a bottleneck yet to be addressed effectively.
Automobile coolant waste heat recovery	[82]	In this experimental study, two important criteria; the heat transfer rate and time required to store energy from an engine coolant to a fin and tube HE filled with a PCM was analysed. The recovered heat by this PCM could be used to heat the engine during start-up. A PCM with a melting temperature of about 373K (99.85°C) was selected.	The warm-up time of an engine was decreased by 34% using 4.2kg of PCM by extracting heat from approximately 6kg of coolant.
Waste heat from a fuel-cell	[83]	A PCM was experimentally tested and analysed for use to harness waste heat from a fuel-cell, normally between 333–373K (59.85-99.85°C). The addition of additives was	Magnesium nitrate hexahydrate was analysed as the PCM for this specific application with several additives. Such

		also analysed to enhance the thermal and chemical properties of the PCM. The effects of 1000 cycles on the long-term stability of the PCM was also analysed.	additives made the PCM extremely suitable to the application, having all the desired properties.
Waste heat recovery from industrial air compressors	[84]	The performance of a small-scale plate heat exchanging evaporator (2–5kW) to recover waste heat from a compressor using an organic PCM was experimentally tested. With a numerical method, multiple conditions were simulated and analysed for this specific application. The PCM was also part of an organic Rankine cycle to eventually convert the harnessed heat to electrical energy.	Although the concept was feasible, proper control strategies varying with external conditions must be ensured for smooth operation, due to the unstable thermodynamics of the PCM.
Waste heat recovery from residential refrigerators	[85]	A PCM slab was experimentally added on the outside surface of the evaporator of a common residential refrigerator. The PCM would be capable of extracting the waste heat from the refrigerator and sharing the load with the evaporator. At times of low peak, this energy was released back from the PCM, hence ensuring that the loads and performance of the refrigeration cycle were consistent.	Such enhancement techniques by the addition of a PCM enhanced the heat transfer rate allowing a higher evaporating temperature of the refrigerator. This allowed the operation in hot environmental conditions unlike before. An increase in 5–15% of the COP was also witnessed.

In spite of the fact that PCMs have been used to harness waste heat in different recovery applications, their usage with regard to GW heat harnessing at multiple levels is almost non-existent. Nevertheless, this literature review proves the fact that if the constraints outlined in section 1.3 are overcome, it is a possible solution. The integration of PCMs with GW heat harnessing would also pave the way for an integrated heating grid based on waste heat sources [36]. The usage of buildings as decentralised sources of heat along with larger centralised sources based on level two and three heat harnessing would make fourth generation DH a reality, resembling a smart electricity grid [44]. Fourth generation DH grids are operating at a low temperature of about 313-323K (39.85-49.85°C), making such a grid perfect to accommodate low-grade waste thermal heat [11]. There have already been several pilot studies on such grids in Denmark. At the moment, residential buildings act only as heat sinks, but commercial buildings and sewage systems are already sources of decentralised heat. The WWTP in Bern, Switzerland is capable of generating 30MW of thermal energy recovered from waste water. This facility annually supplies 5GWh of heat to the city's local DH grid [12]. At the same time, this DH grid in Bern has the capability to further condition the heat supplied as per the demands of different users via an extra heating station. Additionally, it acts as a DC grid in summer by supplying chilled water at 280-290K (6.85-16.85°C), using a reverse absorption HP cycle. A schematic of this facility in Bern is illustrated in Figure 2-15:

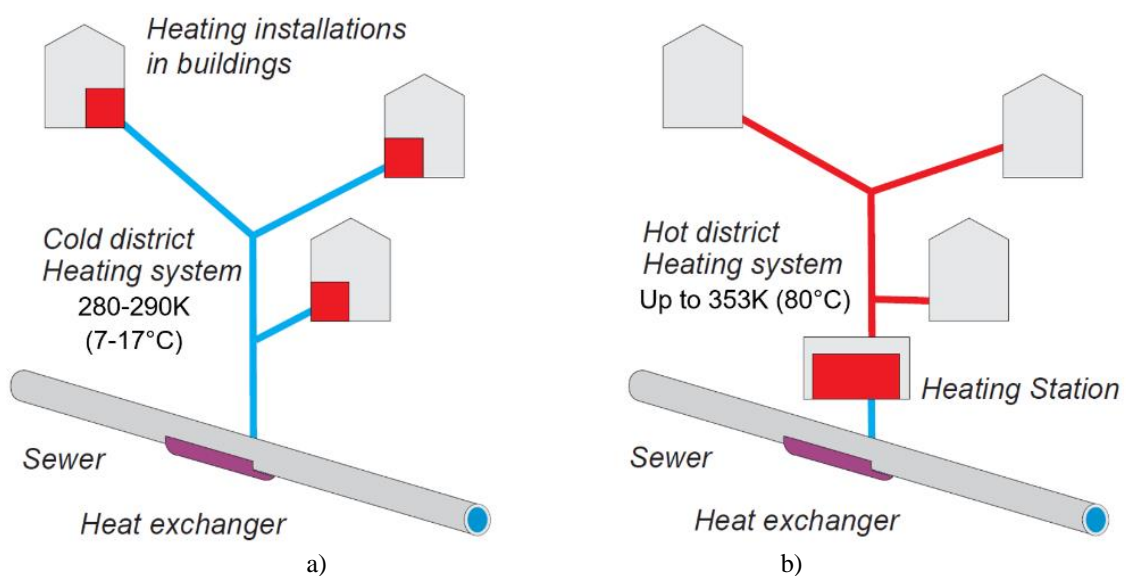


Figure 2-15: Harnessed thermal heat from sewer lines used as a source of a) DC b) DH grids in Bern, Switzerland [12]

## 2.5. Outcome

The three important parameters for the design of the HE in the forthcoming sections to be determined from this literature review are:

- Temperature: Typically, the GW temperature from an appliance is about 5-10K lower than the inflow water temperature [15]. There is a wide disparity in production temperatures with washing machines and dishwashers consuming at relatively higher temperatures. Nevertheless, the average GW production temperature of 325K (51.85°C) will be used in the design for a PCM HE for appliances [14]. Similarly, the average incoming temperature of the CW is taken as 285K (11.85°C).
- Mass-flow rate: Once again there is a great disparity in flow rates, with showers producing GW at a higher rate compared to other appliances. Nevertheless the flow rates of the GW from each appliance can be controlled by varying pipe diameters, having temporary storage openings or using electronic actuating valves operated by controllers [26]. Generally in the piping architecture of conventional buildings, the inlet pipes (25mm) to appliances are thinner compared to the outlet drainage pipes (40mm) in order to maintain steady flow rates and pressure at the inlet while avoiding clogging at the outlet [20]. An average estimate of GW flow rates is between 0.2-0.1kg/s with 0.1kg/s more frequent in showers, dishwashers and washing machines used for this design [30]. Correspondingly the inflow of CW is at a similar flow rate.
- Duration of flow: As mentioned, the average duration of showers is 8.2 minutes, while multiple 5 minute cycles occur in dishwashers and washing machines. Additionally, the cumulative usage of basins/sinks is more than 30 minutes a day. In this design, the average flow duration per appliance is taken as 15 minutes. Additionally, the inflow of the CW is for the same duration of time to the appliance.

At the same time, it can be concluded that the usage of PCMs in this application is viable, as they have been successfully demonstrated in heat harnessing application from the literature sources.

## Chapter 3 - PCM selection

As per Table 1-2, the first phase of this research was to select an appropriate PCM within the prescribed boundary conditions, to harness GW heat and transfer it back to the incoming CW, for residential appliances. The selection of a PCM with optimal thermal characteristics suited for this application was required before a detailed design of the remaining components of the three-way HE.

### 3.1. Overview

Although the extracted GW heat can be used in many applications, in this phase the focus was on demonstrating heating CW for residential appliances. With different boundary conditions, this methodology, can be extended to any similar application [86]. In a basic preliminary layout, an orthodox GW pipe was linked to the mains CW pipe via a PCM in an enclosed container forming a three-way HE, as displayed in Figure 3-1:

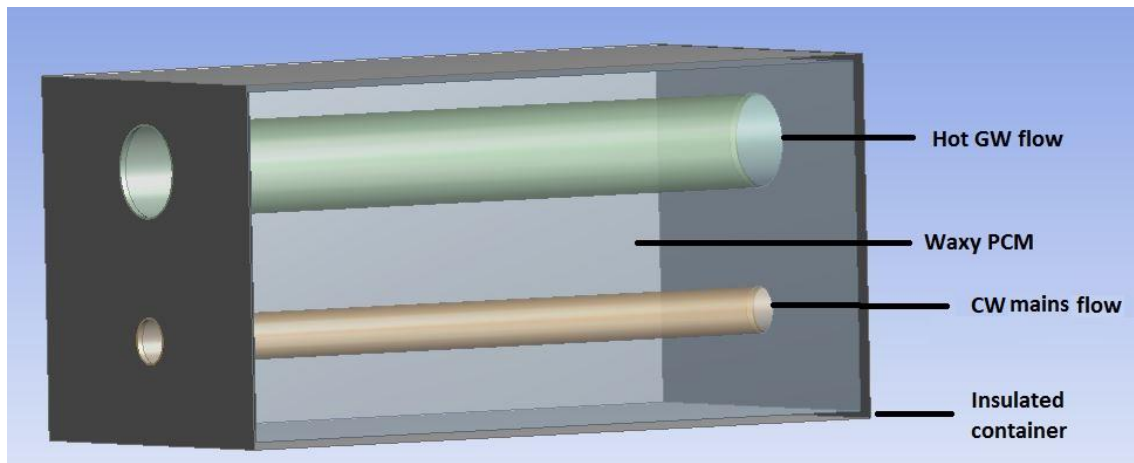


Figure 3-1: Basic layout of GW heat harnessing with PCM linked to incoming CW

As mentioned in section 2.2.2, the incoming CW pipe is normally smaller in diameter compared to the outgoing drain pipe of the GW. As per Figure 2-3, the incoming GW is at 313-337K (39.85-63.85°C) at an average temperature of 325K (51.85°C). In this HE, the GW gives away its thermal energy to the surrounding PCM. The PCM melts, and upon an incoming flow of CW at 278-288K (4.85-14.85°C) with an average temperature of 285K (11.85°C), it freezes back to release the stored energy to the CW. Several configuration improvements were made to this simple design in Figure 3-1, but the only concern for the current chapter was selecting the optimum PCM that provided the best heat transfer behaviour.



Numerous researches have focused on PCMs over the last few decades due to the popularity of high-density latent thermal storage. Many theoretical studies have been conducted to evaluate an idea in order to carry out a basic system design. Gu et al. [76], theoretically calculated the energy savings of using PCMs to harness waste heat from air-conditioners. Mousa et al. [87], conducted an analysis of using PCMs to store heat from solar irradiation for use in buildings during the night-time. In another study [68], evaluated the possibility of utilising PCMs for waste industrial heat and a theoretical analysis was conducted. Nomura et al. [70], investigated the practicability of transporting waste heat from chemical plants over long distances using PCMs. Similarly, simulation softwares have also been used in conjunction with PCMs to study their interaction with other sub-systems. In a study [88], a solar heating tank linked with a PCM was modelled in relation to a building in Lhasa, Tibet for an entire season. Ihm et al.[89], modelled an ice-based PCM storage unit in EnergyPlus using direct data from an actual building. Finally, after these two phases of independently brainstorming an idea and then conjoining it with sub-systems, there comes the stage of a thorough feasibility analysis. In a study [90], the feasibility was conducted in terms of an exergy analysis for a solar desalination unit combined with PCM heat storage. Similarly, an initial integration idea of using PCMs in a thermoelectric generator on the exhaust of an automotive unit followed by a proof of concept analysis led to the development of a specially created prototype [80]. Based on this, an analysis of the potential energy savings along with the performance of the PCM-equipped thermoelectric generator was calculated. Shon et al. [82], used PCMs to store heat from an automobile's coolant waste using a fin-tube HE. The transient heat transfer rate was theoretically analysed to assess the feasibility of the concept. Fadaei et al. [91], conducted a small-scale experiment to analyse the feasibility of using a solar chimney with PCMs. Furthermore, the performance of the most important parameters in specific PCM applications have been the focus of many parametric and optimisation studies. Bilgin et al. [92], focused on optimising the economic rate of return based on the geometric layout of a PCM system used as a coolant for PV panels. In another study [93], a PCM was used to cool lithium-ion batteries by filling a layer of the cylindrical battery. The design was optimised based on the geometric layout of the hollow PCM filled cylinder. In other studies [94,95], a sensitivity analysis was performed to optimise various parameters of PCM filled concrete and simple wooden walls for natural passive cooling over different seasons. Li et al. [96], optimised the melting of a PCM filled horizontal annulus and

concluded that the boundary temperature was the most important parameter in the study. Most of these optimisation studies were experimentally demonstrated within controlled laboratory conditions. In an experimental setup [79], the performance of a HE linked with latent heat storage for an exhaust gas recovery system of an automobile was investigated under different load conditions. Similarly, an experimental analysis [97], tested the thermo-physical performance of liquid metal laden in an organic PCM for thermal storage. The thermal cycles after long-term usage of the PCMs, along with the energy storage performance were thoroughly tested. Zhang et al. [75], experimentally tested the harnessing of waste heat into PCMs from the evaporator outlets in air-conditioning units to the point where the water in the outlet air condensed. In another experimental study [83], different PCMs were assessed for the thermal storage of urban waste heat from emerging co-generation systems. Comparative to experimental testing, the use of numerical simulations in PCM studies has become more widespread with technological advancements over the years. Along with being economical, less time consuming and simple, these numerical simulations can effectively mimic experimental studies. Most numerical models for PCMs are basic variations of the enthalpy and effective heat capacity method, derived using finite-volume techniques. Additionally, most simulations in literature are simplified in terms of symmetry or are 2D due to computational limitations. The most common commercial softwares to independently model PCMs include ANSYS, Star-CCM, Comsol, OpenFoam, Modelica and MATLAB, etc. Li et al. [98], studied the physical phenomena of PCM melting inside a sphere-shaped container, in the ANSYS Fluent platform. Park et al. [99], used a 1D numerical analysis of a PCM-based heat storage system in Modelica, to reduce engine warm-up times for a vehicle. Bhagat et al. [100], analysed the transient response of a PCM storage system linked with an organic Rankine cycle-based solar thermal power plant in ANSYS using user-defined scalar equations. In most studies, an experimental analysis is integral to validate the numerical simulation before conducting a sensitivity analysis. Joulin et al. [101], validated a 2D Fortran-ANSYS Fluent-based simulation using experimental results for a PCM mixed with construction materials in a building envelope, to be used as passive solar walls. Lamberg et al. [102], used PCMs to compensate for temperature peaks in telecommunication electronics. A numerical model was constructed in FEMLAB before being validated by experimental data. Furthermore, both the melting and freezing of a PCM are governed by different physical and thermodynamic aspects. Most studies focus only on one of them. Dadollahi et al. [103],

studied only the melting of ten different PCMs in three configurations inside a closed container. Similarly, Gracia et al. [104], investigated only the freezing of a domestic electrical hot water heating cylinder linked with PCMs for different performance cycles. Nevertheless, only a handful of studies focus on both aspects; melting and freezing. In a study [105], a PCM storage tank linked with solar thermal heat was assessed both in terms of melting and freezing. In a similar manner, [106], numerically analysed both the melting and freezing of a portable electronic device using a PCM-based heat sink.

Most literature is either dedicated to preliminary feasibility studies or to a detailed design analysis with regard to specific applications. There is an absence of a methodology to describe a strategy in the initial design phase to select a PCM based on the temperature boundary conditions. At the same time, such a strategy with regard to GW heat harnessing is non-existent. The majority of the published literature on PCM applications is limited to the cooling of batteries/electronics, solar thermal energy, passive heating/cooling technologies with air as the medium, usage in passive building walls, waste heat harnessing in automotive applications and enhancing the energy efficiency of existing thermal storage units. Similarly, in terms of optimisation strategies, most research has been performed without a specific technique by simply testing discrete variants of a design, either experimentally or numerically. Also, most studies focus on solving the mathematical models of PCMs either numerically or by empirical prediction through experimental testing. Based on this overview, it can be observed that there is a lack of research focusing on the analytical solution of the Stefan problem. Additionally, only the partial behaviour of either melting or freezing is considered in most research, depending on the requirement of the application.

The selection of a PCM for an initial design that considers both freezing and melting based on an analytical solution in conjunction with an evolutionary optimiser for GW heat harnessing was not to be found in the literature. The goal was to select the phase change temperature and various other thermal parameters of the PCM so that:

- Maximum heat is extracted while melting, with the GW flow.
- Maximum heat is inserted while freezing, with the CW flow.

This was not possible using numerical techniques in CFD softwares due to computational constraints, as the method in this application required the integration of a basic optimisation algorithm to select a PCM based on a range of thermal parameters.

Comparatively, the classical 2-phase analytical solution of the Stefan problem was best suited for this optimisation analysis to select the thermal parameters of the PCM for this GW heat harnessing application. Using this method, the net heat flux was computed during both melting and freezing with reference to a specific phase change temperature, which was also to be optimised. The PSO was used in conjunction, since it has minimal requirements and guarantees fast convergence of an array of variables within specified ranges [107]. This is a class of well-known optimisers imitating social behaviour using artificial intelligence techniques. The PSO algorithm has been commonly used with various heat transfer-related applications [108–112]. In fact, to improve the robustness of the PSO-algorithm with specific thermodynamic applications, various custom-built versions have been built to make this optimiser extremely flexible and adaptable to this application as well. These algorithms include the Bare-bones PSO [108], quantum PSO [109], Gaussian kernel PSO [111] and the repulsive PSO [110,112].

This phase of the research has the following objectives:

- Formulation of a classical 2-phase analytical solution based on the thermal parameters of the PCM, for both melting and freezing.
- Integrating a PSO algorithm with this solution based on the predefined boundary conditions of the GW heat harnessing application.
- Optimisation of the parameters for both the solution and the optimiser, with the aim of maximising the net heat flux into the PCM.
- Performing a sensitivity analysis of the main parameters affecting the outcome of the solution.
- Selecting a viable commercial PCM to be used in this application based on the outcome of the algorithm.

## 3.2. Background and mathematical models

Both the Stefan problem and optimisation algorithms have an old historical background. A basic phase change process can be described using Stefan's approach. This was brought into the limelight in the late nineteenth century and was also previously highlighted by Lamé and Clapeyron. There are many solutions depending on the accuracy and simplifications of the problem. Similarly, optimisation is the selection of the best choice in a set of alternatives, analogous to finding the maxima or minima of a defined function in calculus. Optimisation theory and techniques have always constituted a large portion of applied mathematics. Many optimisation algorithms exist suited for different problems which can be appropriately modified or used in hybrid.

A brief background is presented in this section, along with the mathematical models of the classical 2-phase analytical solution to the Stefan problem and the PSO algorithm [86].

### 3.2.1. The Stefan problem and the classical 2-phase analytical solution

#### I. Background of the Stefan problem

The Stefan problem models melting and freezing phenomena, or more commonly a phase change, at a macroscopic level. This problem is non-linear and the greatest difficulty lies in the fact that unknown variables exist in a region which is yet to be solved, e.g. the to-be liquid region in a melting model of an initial solid. This problem is mathematically categorised as a 'moving boundary problem', due to its dependency on the phase change front and its variation with time. Phase change is interdisciplinary, involving theoretical concepts from heat transfer, mass transfer, materials sciences, fluid dynamics and thermodynamics. Hence, there are many variant methods of the solution to the Stefan problem summarised in Figure 3-2, depending on the simplifications and accuracy required:

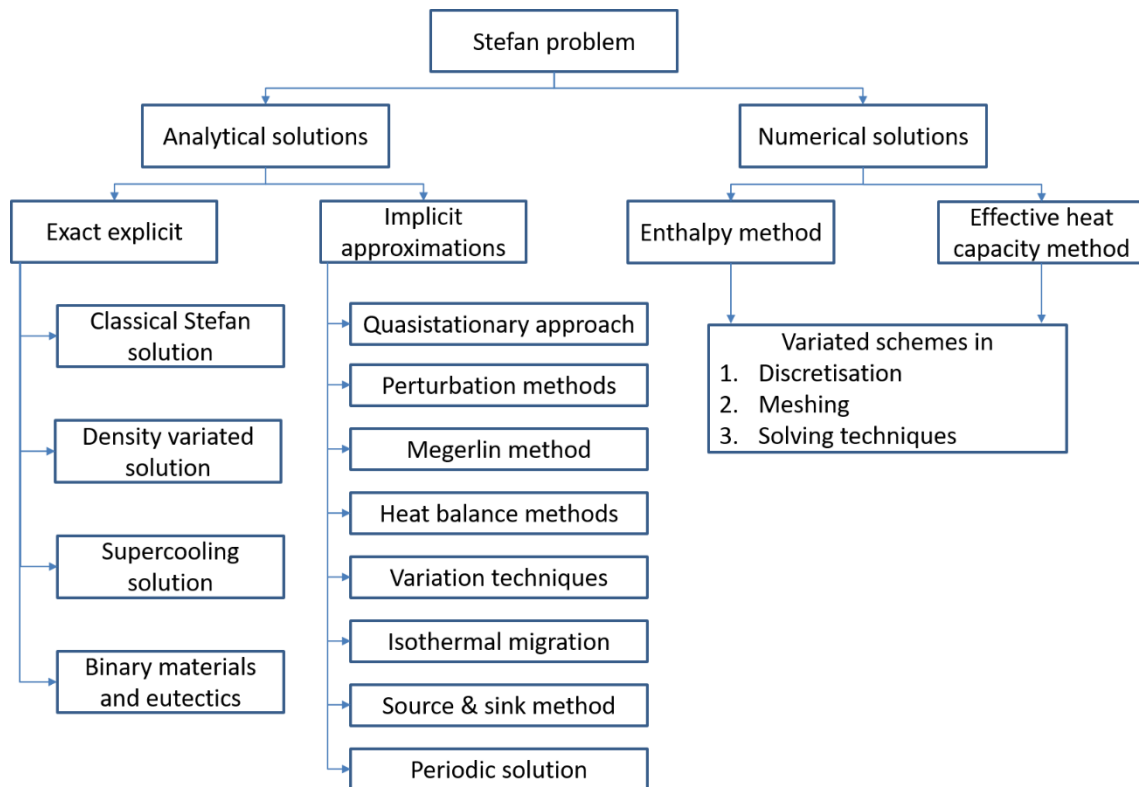


Figure 3-2: Techniques to solve the Stefan problem for PCMs

The exact explicit solutions are recognised as the analytical solutions solved with the Neumann approach, but usually contain many simplifications and are typically 1D. However, they are the foundations of understanding the different thermal parameters involved in a phase change phenomenon and can be a reasonable estimate of real scenarios [113]. At the same time, various 3D applications can also be accurately simplified using this analytical 1D approach [114]. On the other hand, implicit approximations are also based on numerous simplifications and assumptions, but reasonably model practical examples [66]. Generally, they are used as an initial estimate or rough approximations of a practical setup. Validation of these analytical solutions is necessary either through experimentation or via a numerical analysis, as in many studies [115,116]. Finally, numerical methods are more accurate, at the cost of more computation time and resources. Many variants to this method exist and it is a wide field in CFD analysis [117]. Variants range from different discretisation schemes, meshing methods and solving criteria [118,119].

The direct formulation of implicit approximations was not possible at this stage of the design process, since the complete layout of the HE had not been established. Similarly, most numerical solutions are performed in CFD platforms as mentioned, without the

possibility to integrate a custom-built optimisation algorithm to select a PCM. At the same time, they are also used for a holistic analysis of the complete HE. For this reason, the usage of the classical solution was most appropriate at this stage of the research. The formulation used in this model was based on a semi-infinite 2-phase analytical solution of a 1D slab. Although the case of a slab is different from the HE configuration of Figure 3-1, it is a good approximation of a comparative assessment of selecting an appropriate PCM based on the boundary conditions of melting and freezing. Unless the pipe radius is very small, the freezing or melting around a pipe is thermodynamically slab-like, which is reasonable in this case [114]. Additionally, the slow conduction heat transfer and the transition in phase is a reasonable approximation of a semi-infinite slab to that of a real finite slab. Also, in the case where a finite slab has no boundary condition or is insulated at its other end, semi-infinite approach is reasonable. In the GW case, the HE was insulated using Styrofoam, making it a reasonable approximation.

The most common PCM used in practical applications is the solid-liquid type [66]. Before a solid can melt, it must acquire a specific amount of energy to overcome the bonding forces within it or similarly, a liquid must release this energy for transition to a solid. This energy is called the latent heat capacity 'L', representing the difference in enthalpy levels between a liquid and solid at similar conditions, also known as the Stefan condition at the phase change interface. Phase transition happens at a specific temperature or at a temperature range known as the melt temperature ' $T_m$ '. This temperature is dependent on pressure and most thermo-physical properties of a material undergo abrupt changes after phase transition in a discontinuities manner, further complicating the moving boundary problem. Density ' $\rho$ ' is the most likely to change with differences of about 5-30% of its numerical value in both phases [114]. Most PCMs have higher densities when solid, ' $\rho_s > \rho_L$ ' so they expand when melting. Due to the density changes in both phases, buoyant forces cause convection to become a predominant mode of transfer while melting. Typically, the thermal conductivity ' $k_s$ ' of solids is higher than that of liquids ' $k_L$ '. However, the specific heat capacity, ' $c_L$ ' for liquids is usually higher than that of solids ' $c_s$ '.

The classical 2-phase analytical solution is the simplest solution to the Stefan problem, based upon which more complex solutions can be derived [117]. The basic assumptions of this model to be used are as follows:

- The PCM has constant thermal parameters for both phases. All parameters have no discontinuity and are smooth functions.
- Heat transfer is only by conduction in both melting and freezing. The heat flow is normal to the boundary of the slab and is uni-directional. To account for convection heat transfer, the liquid thermal conductivity is assumed to be higher than that of the solid phase.
- The phase change interface is sharp, planar, has zero-thickness, is straight and occurs only at the isothermal phase change temperature. There is only one phase change front with multiple cycles having no impact.
- No internal heat source or sink is present within the PCM. The slab is adiabatic with no heat loss to the surroundings.
- There is no decline in the temperature of a point within the modelled domain which is continually rising or is constant, for melting; vice versa for freezing.
- Nucleation, supercooling, surface effects and curvature effects are neglected.

The heat equation expresses the conservation of heat locally in a material and predicts the temperature distribution in terms of position and time. It is derived from Fourier's law of conduction and the conservation of energy. It is a parabolic differential equation presented in Cartesian coordinates as:

$$\rho c_p \frac{\partial T}{\partial t} = k \left( \frac{\partial^2 T}{\partial x^2} + \frac{\partial^2 T}{\partial y^2} + \frac{\partial^2 T}{\partial z^2} \right) + \dot{q} \quad (3-1)$$

The term on the left-hand-side (LHS) represents the thermal energy stored within the body over time; the first term on the right-hand side (RHS) is the heat flux transferred through conduction within the coordinate system of the body. The second term on the RHS represents any heat source/sink within the body. It can be simplified in any coordinate system as:

$$\frac{\partial T}{\partial t} = \alpha \nabla^2 T + \dot{q} \quad (3-2)$$

The solid and liquid regions of a phase change problem are modelled with the heat equation, with no internal heat sink/source. As described in the forthcoming Figure 3-3



at the end of this section, the classical 2-phase analytical solution assumes that a phase changing slab is initially at a temperature ‘ $T_i$ ’, with the application of a constant temperature ‘ $T_b$ ’ at the left-hand boundary at time ‘ $t = 0s$ ’. The jump from ‘ $T_i$ ’ to the temperature ‘ $T_b$ ’ at this initial instant of time is a discontinuity in the heat equation and the resultant solution, as well. It implies that the temperature changes at an infinite rate at this initial time ‘ $t_0$ ’. Although this may seem unreasonable, the assumption in the equation is applicable for theoretical calculations in a semi-infinite domain with relatively small temperature gradients. This assumption in the analytical solving of the equation is another reason that the other boundary of the slab is insulated or considered semi-infinite, as is in this model.

From equation (3-2), the thermal diffusivity ‘ $\alpha$ ’, of a material is defined as:

$$\alpha = \frac{k}{\rho c_p} \quad (3-3)$$

It is a measure of the rate of heat transfer within a material. When there is a change in temperature within a material, the thermal diffusivity dictates the rate at which this temperature smoothens out, or the rate at which the body reaches thermal equilibrium. A higher thermal diffusivity means a low thermal inertia, implying heat moves rapidly within the material having a fast response time.

The heat equation governs the liquid and solid phases, after which the next step is modelling the phase change interface. Applying the law of conservation of energy at the interface over time, the following equation is derived:

$$(\rho e)_t + \text{div}q = 0 \quad (3-4)$$

Based upon this equation, the rate of heat transfer across the interface is equal to the net heat flux across it. Using the Rankine-Hugoniot jump relations and the fact that the enthalpy of the liquid phase is higher than the solid phase by the value of the latent heat [120], the Stefan condition can be derived to be:

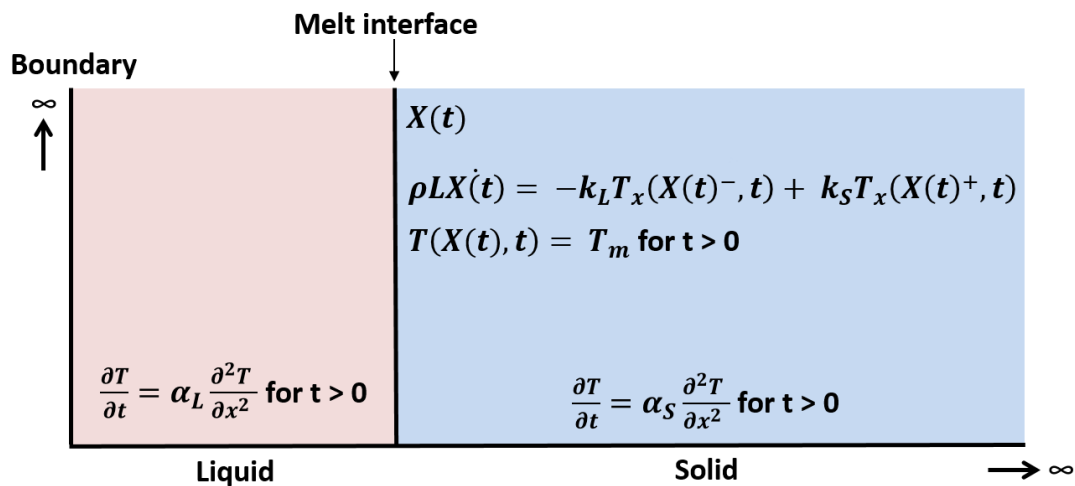
$$\rho L v = q \cdot n \quad (3-5)$$

Where ‘ $v$ ’ is the velocity of the interface and ‘ $n$ ’ is a vector normal to it.

Stefan’s condition states that the net heat flux across the interface is equal to the rate of transfer of latent heat per unit area. The enthalpy of the liquid phase is higher than the solid phase, the difference being the required heat flux across the interface for phase change [120]. The velocity of the interface is equal to the rate of change of this net heat flux. The net heat flux across the interface is nil only when the latent heat is zero or the interface is stationary. For a 1D case with the assumption that conduction is the only mode of transfer, the Stefan condition becomes:

$$\rho L X \dot{(t)} = -k_L \frac{\partial T}{\partial x}(X(t)^-, t) + k_S \frac{\partial T}{\partial x}(X(t)^+, t) \quad (3-6)$$

Where ‘ $X(t)$ ’ is the position of the melt front and the superscript, (–) denotes it is being approached from the liquid while (+) from the solid side. A summary of the applicable equations, boundary and initial conditions for a melting problem of the classical 2-phase analytical solution is in Figure 3-3, where the solid black lines represent the boundaries and the interface:



Initial conditions

$$T(x, 0) = T_i \text{ where } T_i < T_m$$

$$X(0) = 0$$

$$x > 0$$

Boundary conditions

$$T(0, t) = T_b \text{ where } T_b > T_m \text{ for } t > 0$$

$$\lim_{x \rightarrow \infty} T(x, t) = T_i$$

Figure 3-3: Boundary and initial conditions to solve the Stefan problem using the classical 2-phase analytical solution

This classical 2-phase analytical solution for the semi-infinite slab with a constant temperature boundary condition is solved via the Neumann similarity approach in the forthcoming section [120]. In real scenarios, boundary conditions can be transient and thermal properties are phase or temperature variant. The principles of superposition or separation of variables are not applicable due to these non-linearities, resulting in weak approximations or numerical solutions. For this reason, solutions to the Stefan problems in 2D or 3D do not have any exact analytical solution. However, many 3D problems can be accurately simplified to this classical 1D approach for the purposes of basic analysis [114]. To further simplify this case, it can be assumed that the solid is initially at melt temperature and that the melt (liquid phase) is instantaneously removed, resulting in a 1-phase problem.

## II. Mathematical formulation of the classical 2-phase analytical solution

Mathematical models mimic the understanding of a physical process. Based on the model, the underlying parameters, relationships and in general the behaviour of a process can be understood for better control. In this phase change problem, three important properties were of interest:

- The temperature distribution of both phases.
- The location and speed of the phase change interface.
- The amount of heat stored and released during the melting and freezing of the PCM, respectively.

As mentioned, the solving of the boundary conditions of Figure 3-3 in an explicit manner is known as the classical 2-phase analytical solution using the Neumann similarity approach [120]. Figure 3-3 models a semi-infinite slab initially at a temperature ' $T_i$ ' lower than ' $T_m$ ', with the application of a constant temperature boundary ' $T_b$ ' higher than ' $T_m$ ' at time ' $t > 0$ '.

Three common variables defining the outcome of the solution are presented in equation (3-7).

$$St_L = \frac{c_L(T_b - T_m)}{L}, \quad St_S = \frac{c_S(T_m - T_i)}{L}, \quad a = \sqrt{\frac{\alpha_L}{\alpha_S}} \quad (3-7)$$

The Stefan (St) number represents the ratio of the sensible heat to the latent heat. The number is usually small for certain waxes or organic PCMs, therefore the bulk of the heat transfer is in latent form, as in this application of GW heat harnessing. It is usually 1-10 for metals, therefore sensible heating effects cannot be neglected. Normally, it is very large for ceramics and silicates with negligible latent effects [121].

As mentioned, the solution is computed via the Neumann approach. As a result, a variable ‘ $\lambda$ ’, is defined as the root to a transcendental equation [66]. Such equations are quite common as part of solutions for parabolic differential equations with roots found via numerical methods. The transcendental equation contains a special transcendental function, as these equations generally lack a closed-form solution. A unique solution of ‘ $\lambda$ ’ exists for each value of the Stefan numbers. The uniqueness of this root implies the uniqueness of the solution resulting in a well-posed melt front and temperature solutions [122]. The value of the root ‘ $\lambda$ ’ and eventually the solution are dependent on the Stefan number.

The transcendental equation is defined as:

$$f(\lambda) = \frac{St_L}{\exp(\lambda^2) \operatorname{erf}(\lambda)} - \frac{St_S}{(a \exp(a^2 \lambda^2) \operatorname{erfc}(a\lambda))} - \lambda\sqrt{\pi} \quad (3-8)$$

The transcendental equation is solvable with the Newton-Raphson iterative method, with an initial guess [114]. The Newton-Raphson method is defined as:

$$\lambda_{t+1} = \lambda_t - \frac{f(\lambda_t)}{\dot{f}(\lambda_t)} \quad (3-9)$$

More accurate solutions to the transcendental equation may be found using Brents method [122]. The initial estimate ‘ $\lambda_0$ ’, for the Newton-Raphson iterations is:

$$\lambda_0 = 0.5 \left[ -\frac{St_S}{a\sqrt{\pi}} + \sqrt{2St_L + \left(\frac{St_S}{a\sqrt{\pi}}\right)^2} \right] \quad (3-10)$$

Based on the solution of the Newton-Raphson method, the position of the melt front can be computed as:

$$X(t) = 2\lambda\sqrt{\alpha_L t} \quad t > 0 \quad (3-11)$$

The temperature in the liquid region is defined as:

$$T(x, t) = T_b - (T_b - T_m) \frac{\operatorname{erf} \left[ \frac{x}{2\sqrt{\alpha_L t}} \right]}{\operatorname{erf} \lambda} \quad 0 < x < X(t) \text{ and } t > 0 \quad (3-12)$$

While the temperature in the solid region is:

$$T(x, t) = T_i + (T_m - T_i) \frac{\operatorname{erfc} \left[ \frac{x}{2\sqrt{\alpha_S t}} \right]}{\operatorname{erfc}(\lambda a)} \quad x > X(t) \text{ and } t > 0 \quad (3-13)$$

For the case of melting, at any time interval 't > 0', the liquid occupies the region (0, X(t)) while the solid occupies (X(t), ∞). The liquid (3-12) and solid (3-13) equations are applicable only within these zones and it is important to co-relate the equations with the position of the melt front at any time.

It is assumed that at 't<sub>0</sub>' the system is solid, having zero energy at the temperature 'T<sub>i</sub>'. Based on this, the total heat entering the system for melting is as follows:

$$Q(t) = \int_0^t q(0,t)dt = \int_0^t -k_L \frac{\partial T}{\partial x}(0,t)dt = \frac{\rho L St_L X(t)}{\sqrt{\pi} \lambda \text{erf} \lambda} \quad (3-14)$$

The surface right next to the boundary with the temperature 'T<sub>b</sub>' is always liquid, hence the usage of only the liquid thermal conductivity 'k<sub>L</sub>' term in this equation [121].

The total energy absorbed by the system is the sensible heat of both the liquid and the solid along with the latent heat. The sensible heat addition to the liquid phase is as follows:

$$Q_L^{sens}(t) = \int_0^{X(t)} \rho C_s (T_m - T_i) dx + \int_0^{X(t)} \rho C_L (T(x,t) - T_m) dx \quad (3-15)$$

After simplification it is reduced to:

$$Q_L^{sens}(t) = \rho L St_s X(t) + \rho L St_L X(t) \frac{1 - e^{-\lambda^2}}{\sqrt{\pi} \lambda \text{erf} \lambda} \quad (3-16)$$

Initially the liquid is solid and is the reason for the first expression on the RHS of this equation. The sensible heat added to the solid phase is as follows:

$$Q_S^{sens}(t) = \int_{X(t)}^{\infty} \rho C_s (T(x,t) - T_i) dx \quad (3-17)$$

After simplification it is:

$$Q_S^{sens}(t) = \rho L St_s X(t) \left[ \frac{1}{\sqrt{\pi} a \lambda e^{(a\lambda)^2} \text{erfc}(a\lambda)} - 1 \right] \quad (3-18)$$

The latent heat added to the system is:

$$Q^{lat}(t) = \rho LX(t) \quad (3-19)$$

To verify that the energy balance is satisfied within the system, the following should be valid:

$$Q_L^{sens} + Q_S^{sens} + Q^{lat} = Q \quad (3-20)$$

Heat conduction in a semi-infinite slab for the case of the freezing process where ' $T_i > T_m$ ' and ' $T_b < T_m$ ' was also modelled in this algorithm. In general, the liquid and solid subscripts are reversed in most equations, along with some basic definitions [114]. The changed variables and equations are defined, with all the other parameters remaining the same.

The Stefan numbers are:

$$St_L = \frac{c_L(T_i - T_m)}{L}, \quad St_S = \frac{c_S(T_m - T_b)}{L} \quad (3-21)$$

The transcendental function is now defined as:

$$f(\lambda) = \frac{St_S}{\exp(\lambda^2) \operatorname{erf}(\lambda)} - \frac{St_L}{(a \exp(a^2 \lambda^2) \operatorname{erfc}(a\lambda))} - \lambda\sqrt{\pi} \quad (3-22)$$

The initial estimate to the root ' $\lambda$ ' for the Newton-Raphson method is as follows:

$$\lambda_0 = 0.5 \left[ -\frac{St_L}{a\sqrt{\pi}} + \sqrt{2St_S + \left(\frac{St_L}{a\sqrt{\pi}}\right)^2} \right] \quad (3-23)$$

The position of the freezing front is now defined as:

$$X(t) = 2\lambda\sqrt{\alpha_S t} \quad t > 0 \quad (3-24)$$

The temperature in the liquid region is:

$$T(x, t) = T_i + (T_m - T_i) \frac{\operatorname{erfc} \left[ \frac{x}{2\sqrt{\alpha_L t}} \right]}{\operatorname{erfc}(\lambda a)} \quad x > X(t) \text{ and } t > 0 \quad (3-25)$$

While the temperature in the solid region is:

$$T(x, t) = T_b - (T_b - T_m) \frac{\operatorname{erf} \left[ \frac{x}{2\sqrt{\alpha_L t}} \right]}{\operatorname{erf} \lambda} \quad 0 < x < X(t) \text{ and } t > 0 \quad (3-26)$$

In the event that ' $T_i < T_m$ ', the case of pure conduction in the liquid slab is witnessed, which will be seen as a possibility in section 3.3. For this condition, the temperature profile in the non-frozen liquid PCM is:

$$T(x, t) = T_b - (T_b - T_i) \operatorname{erf} \left( \frac{x}{2\sqrt{\alpha_S t}} \right) \quad (3-27)$$

The total heat input to the system is defined as:

$$Q(t) = \frac{\rho L S t_s X(t)}{\sqrt{\pi} \lambda \operatorname{erf} \lambda} \quad (3-28)$$

The sensible heat addition to the liquid phase is:

$$Q_L^{\text{sens}}(t) = \rho L S t_L X(t) + \rho L S t_S X(t) \frac{1 - e^{-\lambda^2}}{\sqrt{\pi} \lambda \operatorname{erf} \lambda} \quad (3-29)$$

While that to the solid phase is:



$$Q_S^{sens}(t) = \rho L S t_L X(t) \left[ \frac{1}{\sqrt{\pi} a \lambda e^{(a\lambda)^2} \operatorname{erfc}(a\lambda)} - 1 \right] \quad (3-30)$$

### 3.2.2. Particle swarm optimiser (PSO)

#### I. Background of the PSO

Starting from an approximate solution, an optimiser will iteratively improve the solution based on predetermined convergence criteria. The algorithm that is used to move from the first to the final solution is what distinguishes different optimisers from each other. The optimisation of the Stefan problem for melting and freezing in GW heat harnessing is a multi-dimensional and non-linear problem requiring a not so computationally intensive optimiser, for practical purposes.

Zero-order methods are the simplest and most straightforward for this task. These methods only use values of the objective function without using the function itself or its derivatives, as compared to first-order methods. Second and third-order optimisers have their main disadvantages in their complexity and computation times [123]. At the same time, they require the problem to be well-behaved with minimal fluctuations since higher order optimisers compute the derivative of the function, which is not the case in this classical 2-phase analytical solution.

Zero-order bracketing methods could be employed, but their computation time is high with greater chances of converging to local optimas instead of global ones. On the other hand, evolutionary methods are inspired by nature from social psychology. By using artificial intelligence-based algorithms, they are used to solve non-linear, non-convex and even discontinuous problems at a reasonable speed with simple algorithms and are being more applicable in this scenario.

Although about forty different nature-inspired evolutionary methods have been defined up until now [123], the three most common methods were to be assessed. The most famous techniques that have evolved in recent years include the PSO, Ant colony optimiser and the Firefly optimisation algorithm. The PSO method was inspired by a swarm of birds flying towards their destination with the simple variables of speed and

the position of a bird leading it to the optimised point. The Ant colony method is derived from the behaviour of ants looking to find the optimised path between their colony and a food source. Variables of the position of an ant and the probability of selecting a new position based on a learning history dictate the route to the optimised point. Fireflies are unisexual insects which mate by clustering together. A firefly flashes to mate, with the brightness of this flash dictating the movement of the entire cluster. The variables in the Firefly algorithm are the brightness of a firefly and the relative distance, converging all the insects towards an optimum point.

At this stage, the objective was to have the simplest algorithm to achieve the optimised solution in the minimum computing time whilst incorporating the constraints of the GW heat harnessing application. The general pros and cons of these three evolutionary methods [124,125], are presented in Table 3-1:

Table 3-1: Advantages and disadvantages of the most common evolutionary optimising algorithms

	<b>Advantages</b>	<b>Disadvantages</b>
<b>Particle swarm method</b>	<ul style="list-style-type: none"> <li>• Applicable in a range of problems (robust)</li> <li>• Simplest of all with fewest variables</li> <li>• Fastest convergence</li> <li>• Adapts to multi-dimensions without any side effects</li> <li>• Insensitive to scaling of design variables</li> <li>• Oldest method with several custom modifications possible</li> </ul>	<ul style="list-style-type: none"> <li>• Chances of local optima are highly possible</li> <li>• Not applicable for extremely noisy problems</li> <li>• Requires a multi-dimensional coordinate system</li> <li>• Parameters for each problem require custom tuning</li> </ul>
<b>Ant colony method</b>	<ul style="list-style-type: none"> <li>• Applicable in dynamic problems</li> <li>• Inherent parallelism</li> <li>• Large parameter ranges possible</li> <li>• Closest replication to real social behavior</li> <li>• Manages external effects more efficiently</li> </ul>	<ul style="list-style-type: none"> <li>• Theoretically difficult algorithm</li> <li>• A comparatively large number of variables</li> <li>• Probabilities and chance factors must be computed for each iteration</li> <li>• Convergence time uncertain and highly dependent on initial estimate</li> </ul>
<b>Firefly algorithm</b>	<ul style="list-style-type: none"> <li>• Applicable for noisy multi-peak problems</li> <li>• Latest and newest of the evolutionary methods</li> </ul>	<ul style="list-style-type: none"> <li>• Comparatively slow convergence rates</li> <li>• Probability of the local optima trap is the greatest</li> </ul>

	<ul style="list-style-type: none"> <li>• Hybrid combinations easily possible</li> <li>• Applicable to discontinuous functions</li> </ul>	<ul style="list-style-type: none"> <li>• A high number of variables and complexities</li> <li>• Custom modification of the entire algorithm as per problem is required</li> <li>• Extra behavioural information of the problem is required</li> </ul>
--	--	---

Based on these considerations, the PSO method was implemented due to its simple algorithm, its robustness, its ability to handle large dimensions and most importantly, the fact that it has the best convergence time compared to the other two methods. At the same time, experimental research has proven it to perform in several versatile problems [126]. An extremely important advantage for this application is the fact that it can search through multidimensional space arrays without taking the derivative of the function, even if the problem is noisy, discontinuous or even irregular. However, a serious drawback is that it may sometimes lead to premature convergence and find the local optima if the parameters are not properly tuned. Nevertheless, this can be avoided by managing the parameters governing the algorithm, with multiple trials for convergence.

PSO is based on the collective behaviour of multiple, interacting particles (birds) following simple mathematical rules. Each particle can be considered as unintelligent, but the collective system of the swarm is intelligent. The self-organisation, co-evolution and learning behaviour of these particles, after every iteration of the algorithm, ensures convergence to the optimised point in a minimal amount of time. It is categorised as a generic population-based metaheuristic optimisation algorithm [127]. Several hybrid and modified versions have evolved with an increasing popularity in the field of optimisation, but the most basic is used with the classical 2-phase analytical solution, as in this algorithm.

## II. Mathematical formulation of the PSO

In the PSO algorithm, the particles evolve by social interaction with their neighbours and by learning from their own mistakes. Only the position and velocity of each particle in the swarm changes after each iteration, as the entire swarm heads towards the optimum solution [128]. Although there is no centralised control structure governing the

behaviour of the swarm, the local interactions between the particles result in the emergence of a unified behaviour. In contrast to other evolutionary methods it does not employ complexities such as crossover, mutation and probability theorems, etc. [126].

The following steps formulate a simple PSO algorithm used in this application of GW heat harnessing [126,129]:

- The set of variables to be optimised and the output value (fitness) determining the optimum is identified.
- The number of iterations and associated parameters of the PSO algorithm are defined.
- The search space for each variable is defined in a range between a maximum and a minimum. Each variable is a dimension of the PSO represented by an element in the position vector of a particle.
- The PSO is initialised with a fixed sized population (particles) of random solutions. The rule of thumb is that the number of particles should be up to four times the number of optimisable variables (dimensions). The position of any particle in an iteration in the search space is a vector of ‘n’ dimensions representing each optimisable variable, used to find the fitness function or the potential solution. As an example, the position of a particle in iteration ‘k’ is represented with ‘n’ variables ‘x’ as  $x_i(k) = (x_1, x_2 \dots x_n)$ .
- Each particle has a velocity which governs its position in the coming iteration. The velocity is a vector, like the position vector that guides the particle to move to a potentially better position. The position and velocity of each particle is updated after each iteration. The velocity of a particle is also represented by ‘n’ variables in a vector form ‘v’,  $v_i(k) = (v_1, v_2 \dots v_n)$ . In the first iteration, the velocity vector is randomised similar to the way the position vector is initialised.
- The fitness ‘ $f(x)$ ’, for each particle is computed, based on the output function defined in the first step.
- A given particle’s position in the next iteration is influenced by its own learning represented by the variable ‘pBest’, also an ‘n’ dimension vector:  $pBest_i(k) = (pBest_1, pBest_2 \dots pBest_n)$ . The best personal position discovered by the particle is updated after each iteration, as defined by the fitness value in the last step. If, in a specified iteration ‘k’, the position of the particle is better than its

previous best, it is updated for each dimension, otherwise it is kept same. In the first iteration, ‘pBest’ for each particle is initialised to the first position. For a given iteration, each dimension in ‘pBest’ is updated according to this simple logic:

$$pBest_i(k + 1) = \begin{cases} pBest_i(k) & \text{if } f(x_i(k)) \leq f(pBest_i(k)) \\ x_i(k) & \text{if } f(x_i(k)) > f(pBest_i(k)) \end{cases} \quad (3-31)$$

A ‘greater than’ sign for the fitness assumes a better condition, although the logic can vary in case a minima is the optimal solution. In this case a maxima is desired, as explained in section 3.3.

- A given particles position in the next iteration is also influenced by the best position of the entire swarm or its social network. It is represented by the variable ‘sBest’, also an ‘n’ dimension vector:  $sBest(k) = (sBest_1, sBest_2 \dots sBest_n)$ . The best personal position discovered by the swarm is updated after each iteration, as defined by the fitness value. To find the best position of the entire swarm, ‘sBest’ is compared to the ‘pBest’ of each particle in an iteration as:

$$sBest(k + 1) = \begin{cases} sBest(k) & \text{if } f(pBest_i(k)) \leq f(sBest(k)) \\ pBest_i(k) & \text{if } f(pBest_i(k)) > f(sBest(k)) \end{cases} \quad (3-32)$$

- Finally, a particles velocity determining its movement in the next iteration is updated, according to the following equation:

$$v_i(k + 1) = (w \times v_i(k)) + (j_1 \times r_1 \times (pbest_i(k) - x_i(k))) + (j_2 \times r_2 \times (sbest(k) - x_i(k))) \quad (3-33)$$

The first part of the equation is known as the momentum/memory part which ensures through the inertia constant ‘w’, that the new velocity of the particle does not change abruptly. The second part is known as the cognitive part, in which the particle learns from its own experience. The third part is known as the social part, in which the particle learns from social interactions within the swarm

[129]. A large velocity increases the convergence speed along with the chances of converging towards the boundaries of the search space. However, a small value increases the computation time but finds a global optimum as it increases the particles' ability to explore.

The random variables ( $r_1$  and  $r_2$ ) add a random component to the algorithm and prevent it from getting stuck at a local optimum. There is always a random component in the decision making in real world swarms as well. ' $j_1$ ' and ' $j_2$ ' are described in the forthcoming section 3.3. 'pBest' and 'sBest' are the quality factors of the algorithm, ensuring diversity of the particle positions [128]. If only 'sBest' (i.e. dependence on the social ability) was used, all the particles would eventually occupy the same position after a few generations and the algorithm would not evolve to the actual optimum. This is similar to real world scenarios, as decisions are not entirely based on social influences but on one's own personal experiences as well. The inertia constant 'w' ensures that these decisions are not made abruptly [128].

- Finally, the new position of a particle is updated as:

$$x_i(k + 1) = x_i(k) + v_i(k + 1) \quad (3-34)$$

- Due to the random nature of movement, after each iteration it is necessary to check that the position of every dimension of each particle is within the search space. If this is not the case, it is set equal to the closest limit of the dimension's search space. This ensures that the swarm does not explode and follows a converging path. Once again  $x_{max/min} = (x_1, x_2 \dots x_n)$  is a vector of 'n' dimensions.

$$\text{If } (x)_i > x_{max} \text{ then } (x)_i = x_{max} \quad (3-35)$$

$$\text{If } (x)_i < x_{min} \text{ then } (x)_i = x_{min}$$

Another important feature is the selection amongst the two neighbourhood topologies of the swarm defining the social interaction method to calculate 'sBest' of a particle [127].

There are two main topologies:

- The global model is known as a fully connected social network. In this topology, all the particles are interconnected to each other in terms of communication. The best position of a particle 'pBest' is known to the entire swarm, enabling each particle to compare itself with the entire swarm. However, this is rarely the case and is only possible in cases where the swarm size is small.
- The local model is known as a partial social network. Each particle is influenced only by the best performance of its neighbours, which is a subset of the swarm and not the entire swarm. The best position of a particle 'pBest' is known only to these neighbours. There are further subtype topologies to define neighbours and compute the variable 'sBest<sub>i</sub>' where 'i' denotes a specific neighbourhood, as in Figure 3-4:

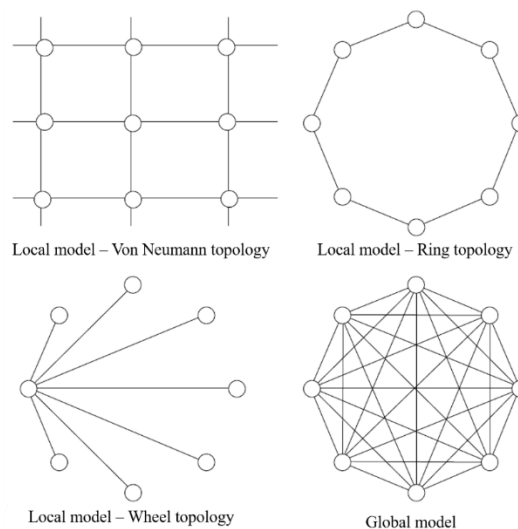


Figure 3-4: Neighbourhood topologies to determine the sBest in the PSO algorithm [126]

In the Von-Neumann sub-type, each particle is connected using a grid network to its four neighbouring particles in its vicinity. In the ring sub-type, each particle relates to two neighbours only. In the wheel sub-type, each particle is isolated from another and all the information is communicated via a focal particle.

The local model diversifies the possible solutions and is instrumental to avoid convergence to a local minimum and at the same time is more realistic. It searches the entire solution space efficiently, but at the cost of a lower convergence speed compared to the global model.

### 3.3. Methodology and algorithms

The ‘PSO-Classical 2-phase analytical solution’ algorithm was coded into MATLAB, with the objectives outlined in section 3.1. An overview of the overall structure of the algorithm is detailed in Figure 3-5:

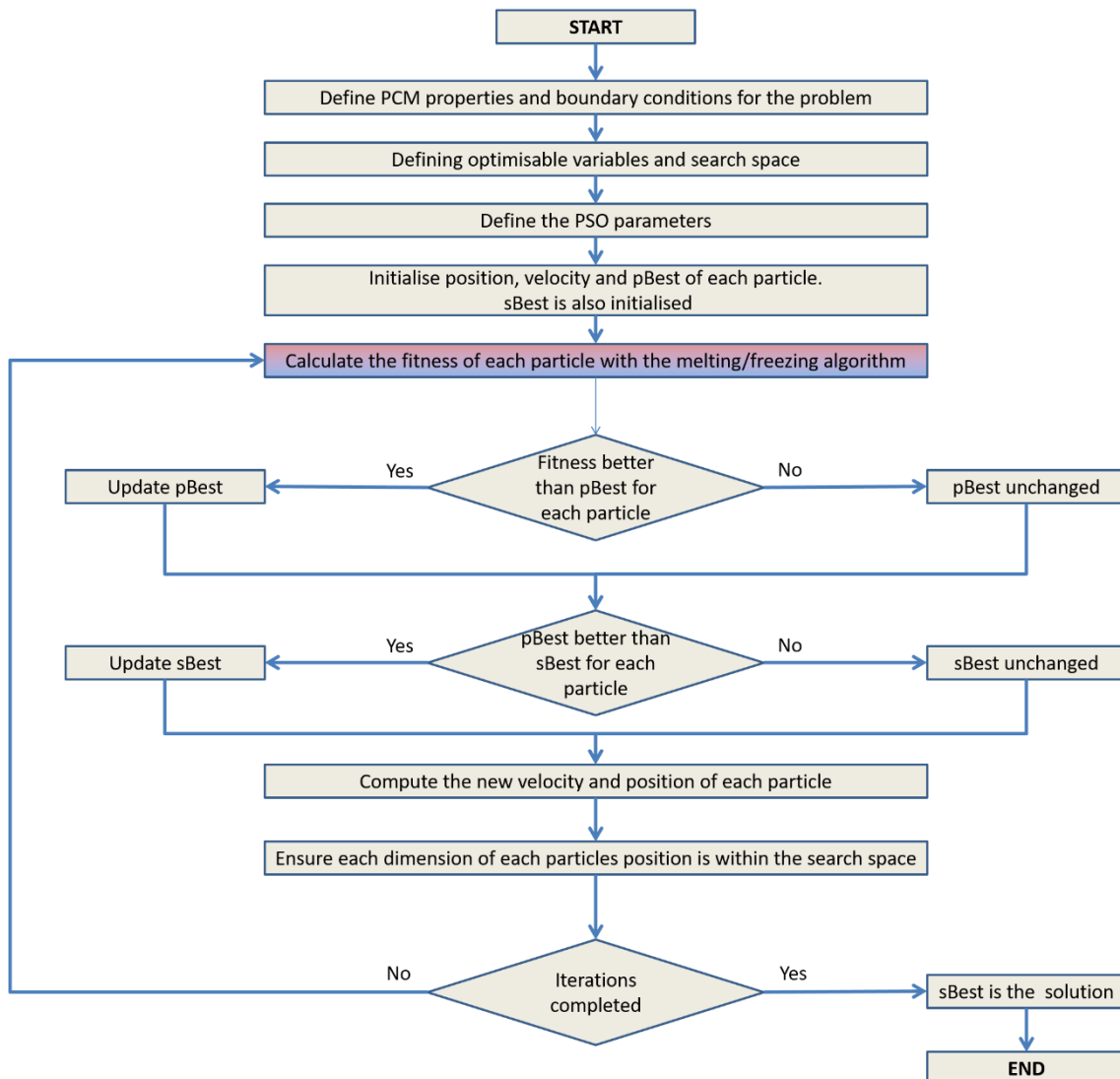


Figure 3-5: Overall algorithm for the classical 2-phase analytical solution based melting-freezing PSO algorithm – where grey is the PSO, red is melting and blue is freezing

Using the classical 2-phase analytical solution, initially the PCM was melted to store heat extracted from the GW flow. After this process, the liquid PCM was frozen to utilise this heat to be transferred into the CW flow. The algorithm for the melting and freezing is in Figure 3-6:



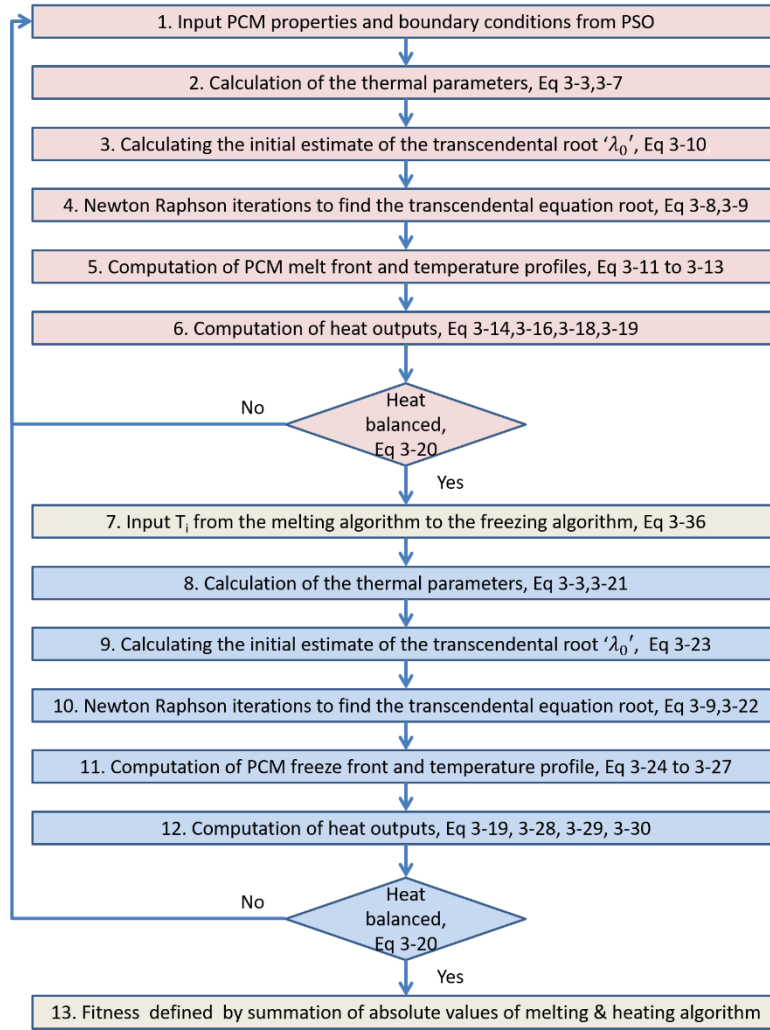


Figure 3-6: Synoptic algorithm for melting and freezing using the classical 2-phase analytical solution

The classical 2-phase analytical solution is valid for a constant initial temperature ‘ $T_i$ ’ of the semi-infinite slab. However, the slab has a non-uniform temperature profile after the melting cycle. For this reason, it was assumed that the initial temperature of the entire slab was equal to that of the mid-point of the melt-front, as the algorithm moves from the melting to the freezing processes as of point 7 of Figure 3-6, using the following equation:

$$T_i^{freezing} = T_b^{melting} - (T_b^{melting} - T_m) \frac{\operatorname{erf} \left[ \frac{\left( \frac{2\lambda^{melting} \sqrt{(\alpha_L) t}}{2} \right)}{2\sqrt{\alpha_L t}} \right]}{\operatorname{erf} \lambda^{melting}} \quad (3-36)$$

Another important point to mention is that the variable 'x', used in the equations of the temperature profiles for both melting and freezing, represents a hypothetical point of interest at any distance from the boundary of the slab. It has no involvement in the fitness function or the outcome, but is used only to visualise the temperature profiles at this specific position.

In the algorithm, a condition might occur outside the melt region, where ' $T_i < T_m$ ', is at this hypothetical distance 'x' when passing from the melting to the freezing process. In this event, equation (3-27) was used to calculate the temperature profile without a phase change occurrence. However, this algorithm takes the melt region as the area of consideration for optimisation.

As per Figure 3-5, the first step was to define the PCM properties and boundary conditions for the GW heat harnessing problem. Based on the average temperature of the GW and CW stated previously, ' $T_b$ ' for melting was defined at 325K (51.85°C) and for freezing at 285K (11.85°C). The initial temperature ' $T_i$ ' for the melting algorithm was taken as the ambient temperature of 295K (21.85°C). Ambient indoor temperatures based on thermal comfort are dependent on a range of characteristics and can be calculated based on commonly used standards including the ISO 7730 and ANSI/ASHRAE Standard 55. Typically, based on these standards, indoor environments are in the range of 291-295K (17.85-21.85°C). A PCM with a melt temperature below the ambient would always be in the liquid phase, making heat addition unviable. Hence, the PCM properties were defined based on a collection of data compiled for organic PCMs in the range of 295-325K (21.85-51.85°C), from various commercial manufacturers including Pluss, PureTemp, Honeywell, Rubitherm, PlusICE, SavenRG, Microtek and Croda International Plc. Organic PCMs are more preferable in building applications due to their lower cost, stability and suitable phase change temperature ranges. A summary of the thermal parameters derived from the dataset is in Table 3-2:

Table 3-2: Range of the thermal parameters of commercially manufactured PCMs for a phase change temperature at 295-325K (21.85-51.85°C)

	<b>Specific latent heat capacity 'L' in kJ/kg</b>	<b>Density 'ρ' in kg/m<sup>3</sup></b>	<b>Solid thermal conductivity 'k<sub>s</sub>' in W/(m.K)</b>	<b>Liquid thermal conductivity 'k<sub>L</sub>' in W/(m.K)</b>	<b>Solid specific heat capacity 'C<sub>s</sub>' in kJ/(kg.K)</b>	<b>Liquid specific heat capacity 'C<sub>L</sub>' in kJ/(kg.K)</b>
<b>Max</b>	340	2,100	0.59	32	3.51	4.19
<b>Min</b>	37	735	0.1	0.14	1.15	1.39
<b>Average</b>	187.5	1,092.5	0.27	0.65	2.15	2.47
<b>Standard deviation</b>	50.5	310.2	0.19	2.84	0.35	0.62

The next step was to differentiate between the constant variables and optimisable variables used in the algorithm for the PCMs. The following four variables in Table 3-3 were optimised through the PSO algorithm within the specified range. The specific latent and heat capacities were selected as optimisable variables, to judge whether the algorithm prefers latent or sensible heat transfer. The range was selected based on the differences between the average values and standard deviations, as presented in Table 3-2. The thermal conductivities and density of the PCM were taken as constants, also based on average values from Table 3-2. The main optimisable variable of interest was the melt temperature 'T<sub>m</sub>', with the range selected based on the boundary conditions of the GW problem.

Table 3-3: Optimisable variables with their range of the search space for the algorithm

<b>Variable</b>	<b>Interpretation</b>	<b>Range</b>
C <sub>p</sub> liquid	Liquid specific heat capacity in kJ/(kg.K)	1.9 – 3.1
C <sub>p</sub> solid	Solid specific heat capacity in kJ/(kg.K)	1.8-2.5
L	Specific latent heat capacity for the PCM in kJ/kg	137-238
T <sub>m</sub>	Melt temperature of the PCM in K	295-325 (21.85-51.85°C)

Consequently, each particle of the PSO would have four dimensions based on the optimisable variables, with a defined search space of Table 3-3. The fitness of a particle was assessed on the basis of the absolute values of the heat absorbed and released by the

PCM during the melting (equation (3-14)) and freezing (equation (3-28)) processes, respectively, as per the following equation.

$$f(x_i(t)) = Q_{abs} = |Q_{melt}(t)| + |Q_{freeze}(t)| \quad (3-37)$$

The highest value of this fitness function or maxima was desired in this application. The total time set for the simulation was 1,800s. Equal times of 900s were predefined for both the melting and freezing processes. This was based on the average time of flowing for GW in residential appliances, as defined in section 2.5 [3].

Finally, the parameters for the PSO algorithm were defined after several test trials. The number of particles in the swarm was set to be 8. The optimisable variables were 4 and as mentioned, the rule of thumb was to select up to four times the number of particles based on the optimisable variables. A much larger number of particles would however result in faster convergence with a chance of finding a local maxima, as will be discussed in section 3.4. The number of iterations for this algorithm was set to be 100. Since the search space in this application was not as vast compared to typical PSO algorithms, the solution converged quite quickly in the 100 iterations. Additionally, as the number of particles in the swarm was not as high, the global topology method of Figure 3-4 was selected to update the ‘sBest’ variable. As mentioned, the variables of equation (3-33) also have to be manually tuned after several test trials, as done for each PSO application. It had to be ensured that a global maxima was reached with complete convergence of all the particles by the end of the iterations. After this tuning, the three important variables of equation (33) ( $w$ ,  $j_1$  and  $j_2$ ) were assigned with values of 0.6, 0.5 and 0.4, respectively. Additionally, all the other constant variables in the model are summarised in Table 3-4:

*Table 3-4: Input variables to the algorithm having fixed values*

<b>Variable</b>	<b>Interpretation</b>	<b>Value</b>
T <sub>b</sub> Melting	Boundary temperature i.e. GW pipe temperature for the melting algorithm in K	325 (51.85°C)
T <sub>b</sub> Freezing	Boundary temperature i.e. CW pipe temperature for the freezing algorithm in K	285 (11.85°C)

$T_i$ Melting	Initial temperature for the melting algorithm in K	295 (21.85°C)
$k_L$	Thermal conductivity of liquid phase in W/(m.K)	0.65
$k_S$	Thermal conductivity of solid phase in W/(m.K)	0.27
$\rho$	Phase-independent density in kg/m <sup>3</sup>	1092.5
Time	Time for both melting and freezing, in seconds. Equal division of time between both algorithms	1800
Particles	Number of PSO particles	8
Dimensions	Number of optimisable variables defining the rows in $x_i$ , $v_i$ , $pBest_i$ , $sBest$ vectors of the PSO algorithm	4
Iterations	Number of iterations in the PSO algorithm	100
$w$	Inertia weight of the particles	0.6
$j_1$	Cognitive learning rate	0.5
$j_2$	Social learning rate	0.4

' $w$ ' is a sensitive variable to control the exploration of the search space for a particle in each dimension and it greatly influences the algorithm's computation time. A large value allows a particle to move with a greater velocity, enabling it to find the optimum in a minimum amount of time. However, a very large value will make the particle explore only around the edges of the search space. A small value can narrow the particles' search space, to find a local optimum in a larger amount of computation time. It is obvious that this value cannot be greater than one, since in this case the swarm would explode. Selection was based on a delicate balance of the range of the search space and the chances of finding a local maxima compared to a global one. Based on research, the value of ' $w$ ' should be between 0.1 to 0.9 to balance exploration and exploitation [130]. Since the range of the search space in this application was not as vast, a mid-range value of the variable ' $w$ ' ensured convergence to a global maxima. The movement of each particle in the swarm was controlled by the acceleration constants ' $j_1$ ' and ' $j_2$ '. For simplicity, most guidelines treat the sum of the two constants as the variable to be adjusted. The frequency of oscillations about the optimum increases as this summed variable increases. However, the trajectory explodes to infinity for values greater than four [130]. The trajectory of a particle is extremely long and highly damped for small values of this summed variable. Normally, it is not recommended to equalise the two variables ' $j_1$ ' and ' $j_2$ ', as the learning curve of a bird in a swarm is rarely based equally on both personal and social behaviour. Usually, these

variables are initially set at large values decaying over time. However, since the complexity of the fitness function and variables in this model was low, it used constant values with reasonable accuracy and convergence times.

The developed model for the classical 2-phase analytical solution was validated with examples from Alexiades et al. [114], using Glauber’s salt, as per section 2.2 of the reference. Additionally, the validation was further extended by ensuring the energy balance of equation (3-20) for both melting and freezing after every iteration. For the PSO algorithm, there was no benchmark for validation as each application differed. However the behaviour of the swarm was assessed over several trials to ensure no abnormalities existed. It was made certain that the entire search space for each dimension was explored by plots similar to Figure 3-11, as the parameters were finely tuned. The outcome was intuitively assessed for its credibility and seemed reasonable.

### 3.4. Results

Using the defined search spaces and parameters, Table 3-5 summarises the optimum results obtained:

*Table 3-5: Results of the optimum variables of the algorithm*

<b>Variable</b>	<b>Interpretation</b>	<b>Value</b>
$C_p$ liquid	Liquid specific heat capacity in kJ/(kg.K)	3.1
$C_p$ solid	Solid specific heat capacity in kJ/(kg.K)	2.5
L	Specific latent heat capacity for the PCM in kJ/kg	238
$T_m$	Melt temperature of the PCM in K	295.5 (22.35°C)
$Q_{abs}$	Total heat absorbed and inserted in kJ	5.023
$\lambda_{melting}$	Root of the transcendental equation for melting	0.4121
$\lambda_{freezing}$	Root of the transcendental equation for freezing	0.1646

The first four variables correspond to the 4-dimensioned ‘sBest’ after the 100 iterations, based on the algorithm illustrated in Figure 3-5. From the results of Table 3-5, the maximum values of the upper limit of the set range of Table 3-3 were preferred for the sensible and latent heat parameters. Similarly, the temperature differential of the optimum melt temperature was much greater with the ‘ $T_b$ ’ for melting or GW flow

compared to freezing or the CW flow. The temperature profiles at the midpoint of the phase change front at 5.4 mm from the boundary of the slab for both melting and freezing are presented in Figure 3-7:

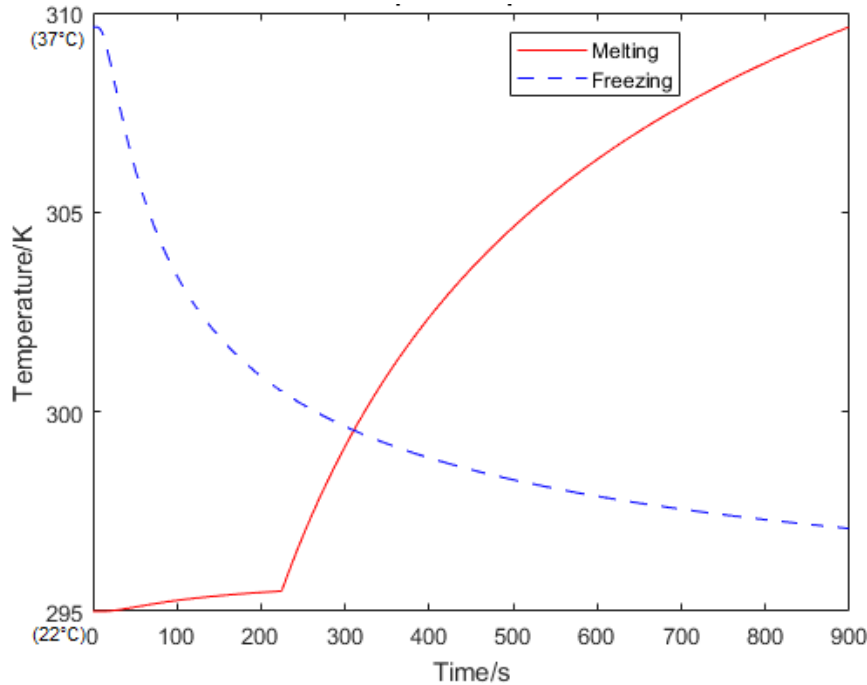


Figure 3-7: Temperature profiles at the position  $x = 5.4\text{mm}$  from the boundary of the layout, for both melting and freezing

It can be seen from the gradient of the curve in the melting plot, that a prominent phase change occurred at 295.5K (22.35°C), unlike in the case of freezing. This was due to the restricted time limit of 900s. However, there was freezing in the slab prior to the 5.4mm position, as can be seen from the plot of the propagation of the freeze front in Figure 3-8.

It can also be observed in the melting curve that the concavity of the temperature profile changed before the melt point. According to the literature [114], if the expression ' $(a\lambda)^2 < 1.5$ ' is true for a PCM, a change in concavity is predicted due to micro-thermal effects, as seen in the initial 100s in this case. At the same time, it was also observed that both plots started from their respective ' $T_i$ ' to asymptotically approach ' $T_b$ ' with logarithmic decaying patterns, as expected. There was no horizontal line at the melt temperature ' $T_m$ ' as would typically be expected during phase change for the melt curve. This was due to the assumption of using a sharp, planar and zero-thickness phase change interface. This is a typical characteristic of the classical 2-phase analytical

solution, as there is no elapsed time for phase change since there is no mushy region. As soon as the phase change interface front reaches a specific point, the transition of equations takes place instantly. The propagation of the phase change fronts is depicted in Figure 3-8:

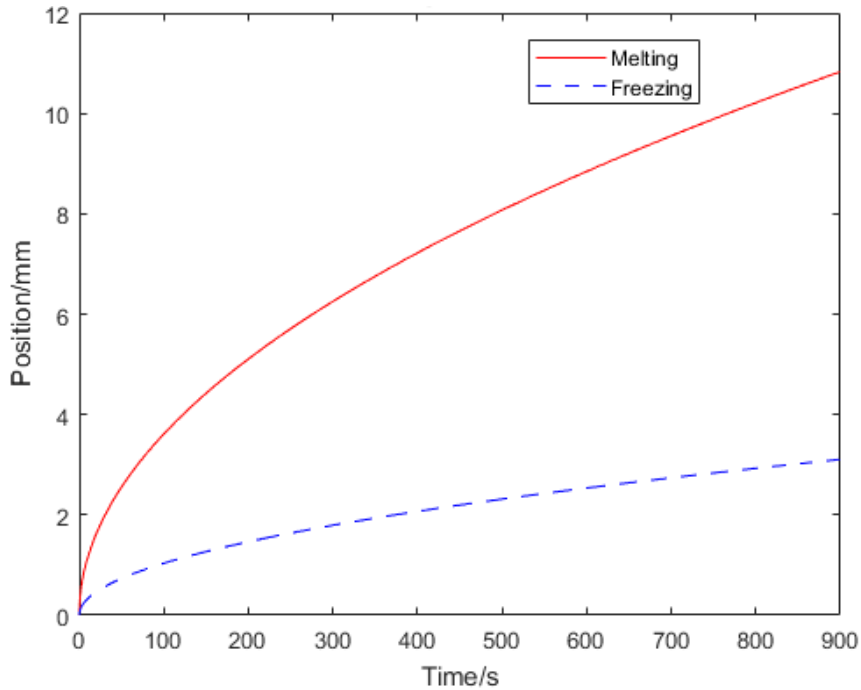


Figure 3-8: Propagation of the phase change fronts from the boundary of the layout

In 900s, about 11.5mm of PCM, adjacent to ‘ $T_b$ ’ was melted. In the same time duration, only about 3.5mm of PCM froze, which was only about one-third compared to melting. Hence, freezing is a much slower process primarily due to the fact that the thermal conductivity of the solid PCM is less than half that of the liquid phase. As most PCM adjacent to the boundary ‘ $T_b$ ’ transitions to liquid phase during melting, convection effects contribute to higher heat transfer rates. Although convection itself was not directly considered in this model, the difference in values of these thermal conductivities accounted for this aspect. Instead of an equal time of 900s, an unequal distribution between melting and freezing would have resulted in equal phase change front positions. The distribution of the heat fluxes at this optimum PCM for both processes in the 900s time duration is in Figure 3-9:



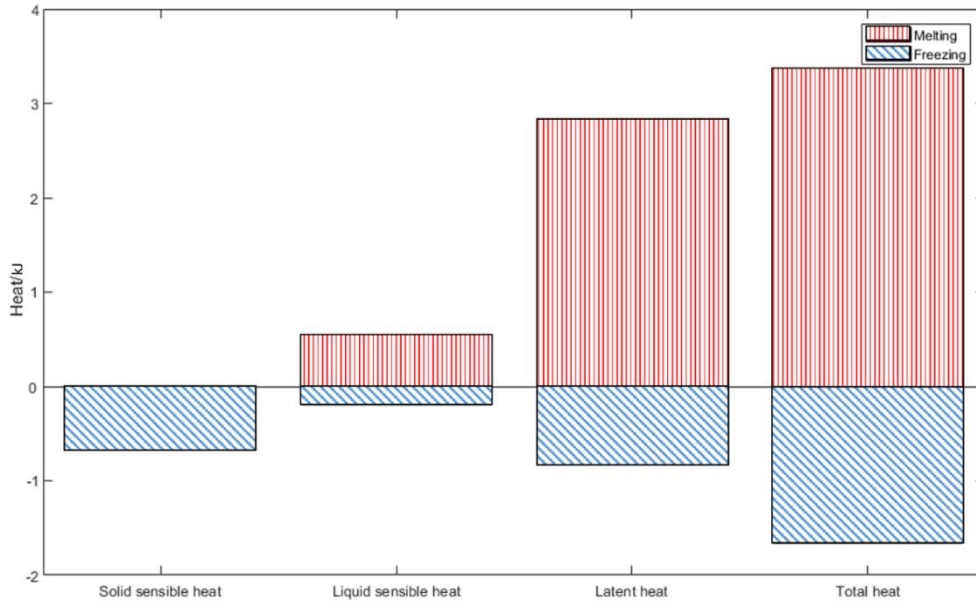


Figure 3-9: Heat flux distributions at the optimum  $T_m = 295.5K$  ( $22.35^\circ C$ ), for both melting and freezing

In this optimum combination, about 5.023kJ of total heat was transferred to and from the PCM. About 67% of this was contributed by melting while only 33% was by freezing. This was also the ratio of the phase change front positions of Figure 3-8. Latent heat was dominant in the melting process, while an equal combination of latent and sensible heat contributed to the freezing process. Due to the fact that the thermal parameters of sensible and latent heat transfer were at the maximum range limit of Table 3-3 in this optimum combination, the solution converged quite quickly, as can be seen from the plot of the fitness function ‘ $f(sBest)$ ’ in Figure 3-10:

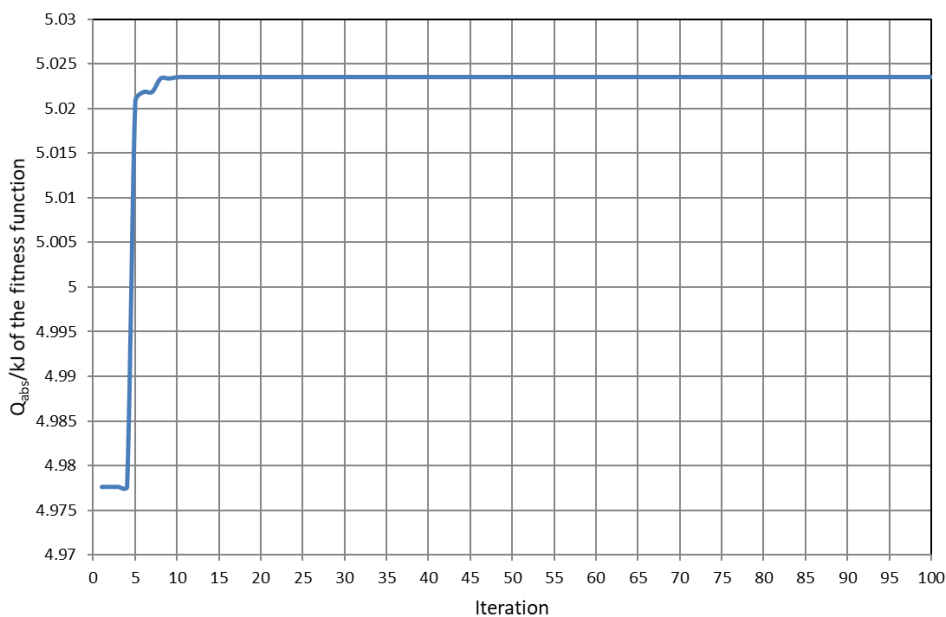


Figure 3-10: Convergence of the fitness function i.e. the total absolute heat transferred

On the contrary, ‘ $T_m$ ’ converged after about 60 iterations. To illustrate the fact that a global maxima was actually achieved, the scatter plot of Figure 3-11 displays the variation of ‘ $T_m$ ’ for each of the 8 particles after every 10 iterations:

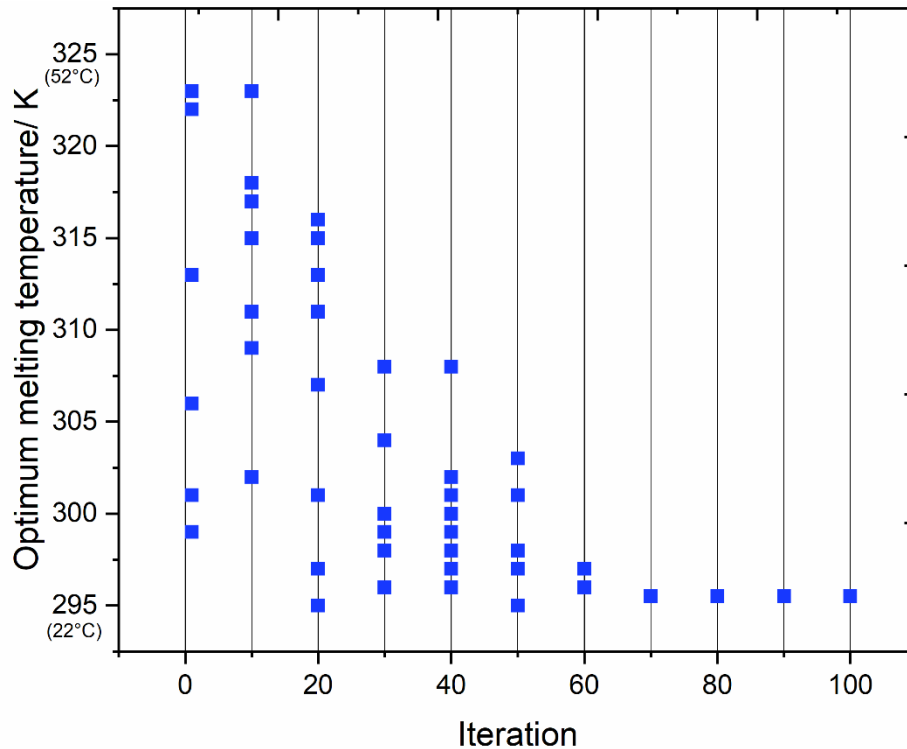


Figure 3-11: Convergence of the optimum melt temperature ' $T_m$ '

Initially in the first iteration, the particles were scattered all over the search space, while finally, all of them converged to a ' $T_m$ ' of 295.5K (22.35°C)' after the completion of the 100 iterations.

Consequently, a sensitivity analysis was also performed on both the PSO variables and the thermal parameters of the PCM with reference to this bench marked output.

### 3.4.1. Variation in PSO parameters

The three primary variables ( $w$ ,  $j_1$  and  $j_2$ ) of the PSO algorithm were systematically varied, as outlined in Table 3-6:

Table 3-6: Results of the variation in the PSO parameters

Variation variable	Constant variables	$Q_{\text{abs}}$ of the fitness function/kJ	$T_m$ /K	Maxima
w – increased to 0.90	$j_1, j_2$	5.023	295.5 (22.35°C)	Global
w – decreased to 0.10	$j_1, j_2$	4.549	311 (37.85°C)	Local
$j_1$ – increased to 2.0	$j_1, w$	5.023	295.5 (22.35°C)	Global
$j_1$ – decreased to 0.1	$j_1, w$	4.891	297 (24.35°C)	Local
$j_2$ – increased to 2.0	$j_2, w$	5.000	295 (21.85°C)	Local
$j_2$ – decreased to 0.1	$j_2, w$	4.689	303 (29.85°C)	Local

Since the search space was small in this case, most combinations more or less converged close to a global maxima, except the lower values of these variables. However, the number of particles should be increased to reach a global maxima with these lower-valued PSO variables. This would ensure that the entire search space was thoroughly assessed, resulting in faster convergence but with a larger overall computation time. With an increase to 20 particles and finally 50 particles, the same global maxima was achieved with these low-valued PSO variables. However, if the number of particles was reduced from the predefined 8, the probability of finding a local maxima would increase even with the optimum variables. Hence, the number of particles were directly proportional to the speed of convergence up to a certain limit before saturation in the swarm. At the same time, the number of particles were inversely proportional to the computation time. Therefore, a balance between the number of particles, convergence and computation time had to be achieved for every PSO application with several test trials. As mentioned, the number of particles should be a maximum of four times the dimensions for a converged global maxima.

The complexity of using decaying PSO variables or increasing their dependency on the thermal properties of the PCM would have further fine-tuned the results. This would be

suitable if more thermal parameters with larger search spaces existed. However, simple variables fulfilled the requirements in this application.

### 3.4.2. Variation in the parameters of the classical 2-phase analytical solution

As evident from Table 3-5, the algorithm preferred a maximum of both the sensible and latent heat transfer variables. At the same time, most of the heat input was in the form of latent energy from Figure 3-9, for the melting algorithm. A sensitivity analysis of these variables was expected to have a profound effect on the 'T<sub>m</sub>'. It can be argued that the upper limit of the search space of these variables in Table 3-3 was a bit out of range. For this reason, the upper limits of 'c<sub>p</sub> liquid' and 'c<sub>p</sub> solid' were decreased to 2.2 kJ/(kg.K) and 2.0 kJ/(kg.K), respectively. Similarly, the upper limit of the specific latent heat capacity was decreased in steps of 10kJ/kg, resulting in the algorithm producing a linear relationship of the optimum 'T<sub>m</sub>', as in Figure 3-12 :

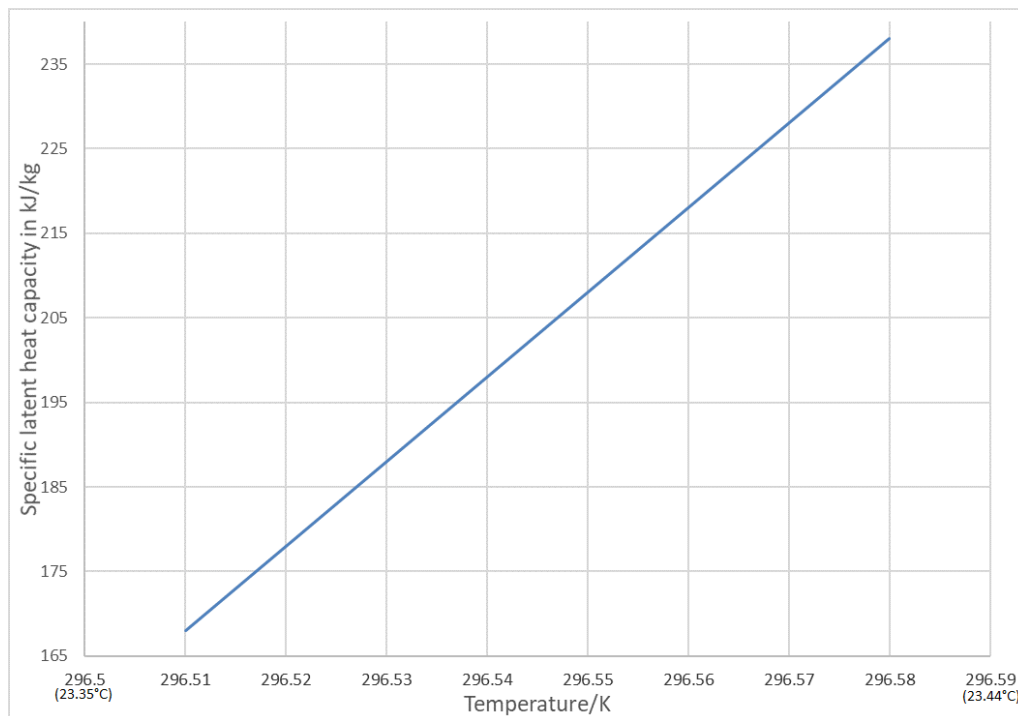


Figure 3-12: Variation of the specific latent heat capacity and optimised melt temperature as the output of the algorithm

Once again, the optimiser selected a combination of the upper limit of both the sensible and latent heat transfer variables. However, in this circumstance, the optimum 'T<sub>m</sub>' incremented by about 1K from the baseline case. In this outcome, most of the heat was

added in the melting process, with the majority being latent, as well. As the specific latent heat capacity decremented by 10kJ/kg in each step, the optimum ' $T_m$ ' dropped by 0.01K. Although this temperature decrement was not significant, it was attributed to the proportionality of heat transfer with the temperature differential. As the ' $\Delta T$ ' between the ' $T_b$ ' and ' $T_m$ ' of the PCM was greater, more heat could be added during melting. To compensate for the loss in the specific latent heat value, there was a linear decrease in the ' $T_m$ ', to increase the overall temperature differential to ensure maximum heat transfer.

Normally, the time duration of GW flow has a normal distribution from the mean 900s [3]. Hence, a variation was also investigated, but the results were independent of time. An unequal distribution with a higher time for freezing would have invoked different results.

### **3.5. Outcome**

Based on the reduced upper range of the thermal parameters in section 3.4.2, the optimum ' $T_m$ ' of the required PCM was 296.5K (23.35°C). Consequently, the most economical commercially available PCM matching these optimum thermal parameters is RT-25 developed by Rubitherm, Germany [131]. Although a PCM with the exact optimum thermal parameters based on the outcome of this algorithm could have been manufactured, it would have been a substantially expensive custom order. The difference between the optimum thermal parameters predicted by the algorithm and of RT-25 are enlisted in Table 3-7:

Table 3-7: Difference in thermal parameters of the algorithm recommended and the commercially available PCM

	<b>Classical 2-phase analytical solution-PSO algorithm</b>	<b>Commercially selected RT-25</b>
<b>Liquid specific heat capacity in kJ/(kg.K)</b>	2.2	2.0
<b>Solid specific heat capacity in kJ/(kg.K)</b>	2.0	2.0
<b>Specific latent heat capacity for the PCM in kJ/kg</b>	170	170
<b>Melt temperature of the PCM in K</b>	296.51 (23.36°C)	295-299 (21.85 – 25.85°C)
<b>Average thermal conductivity of both phases in W/(m.K)</b>	0.46	0.2
<b>Density in kg/m<sup>3</sup></b>	1,093	820

Apart from the average thermal conductivity, the differences in the thermal parameters were reasonably acceptable. The predicted thermal conductivity of 0.2 W/(m.K) does not consider convection heat transfer, eventually resulting in a higher overall heat transfer coefficient when accounted for, making the selection of RT-25 appropriate based on the optimised solution. The data sheet for this PCM is added in Appendix A.

Additionally, RT-25 is an organic paraffin-based PCM. Paraffins and salt hydrates are amongst the most commercially used and researched upon in all PCMs [132]. Paraffin is an alkane with the chemical formula of  $C_nH_{2n+2}$ , being chemically inert it is comparatively more stable and non-toxic to ecological systems [133,134]. For these reasons it was perfectly suited for this indoor application. The validation of this selected PCM was performed in the experimental study in section 5.4, in comparison to a PCM with a higher phase change temperature.

## Chapter 4 - Internal heat transfer enhancement

After selecting the PCM for this application, the next phase was to select an optimum internal heat transfer enhancement mechanism for both the GW and CW flow pipes. The next phases in the design were detailed experimental and numerical analyses followed by a parametric study using the optimum RT-25.

### 4.1. Overview

Heat transfer from working fluids within the plane pipes of HEs has an upper limit to the energy efficiency, which can easily be enhanced. The space constraints in this application coupled with the short time of flow of the GW required a compact and efficient solution. In this application, the goal was to maximise the heat extracted from the GW to be transferred to the CW via the PCM. The best passive strategy of internal heat transfer enhancement would be to boost the HTC of the flowing fluid without altering the boundary conditions of the flow. The usage of corrugated instead of plane pipes in such a HE would be the most appropriate technique for this application. The possibility of a compact design with minimal obstructions in the flow path to negatively influence the already low fluid pressures and the high risk of biofilm deposits all advocate in favour of corrugated pipes. Additionally, the external heat transfer to the PCM is also enhanced, during both melting and freezing with corrugated pipes. Hence, the best combination of dimensions for the corrugated pipe were selected to be used in this application.

As illustrated in chapter 3, the usage of PCMs in passive applications is rapidly increasing due to their high storage density [135]. In spite of PCMs being tested in a range of applications between 273-523K (0-249.85°C), organic and salt hydrated PCMs are usually recommended for low temperature applications below 373K (99.85°C); as in this application [136]. Nevertheless, most numerical research within the domain of low temperature PCM applications has focused on the use of air and refrigerants as the working fluids [3,135,136]. There are numerous numerical and experimental studies focusing on passively enhancing the HTC in internal pipe flows for a range of Reynolds (Re) numbers [137–140]. Comparatively active enhancement techniques considerably improve the HTC, but at additional costs of energy and higher pressure losses. In many

non-industrial HEs, boosts of up to six times have been recorded in the thermal performance factors (TPF) of different passive enhancement techniques compared to plane pipes [137]. Amongst the different passive enhancement techniques, corrugated pipes and internal fins increase the HTC with the least pressure drop penalty and maintenance requirements, especially in turbulent flow regimes [139]. However, these enhancement techniques have not been examined with respect to PCMs. Additionally, most research on corrugated pipes is concentrated on industrial scale HEs, specifically tube-in-tube versions, usually with water, air, oil, refrigerants, helium and even nano-fluids [140–142]. At the same time, the performance of each enhancement technique is highly dependent on the application. Depending on the ‘Re’ number of the flow, an increase in the heat transfer of between 123-232% with a raise in the friction factor ( $f$ ) of between 146-193% have been recorded for corrugated pipes compared to plane pipes [142]. The fundamental reason for the improved heat transfer in corrugated pipes is the helical oscillatory path of the fluid combined with the generation of longitudinal swirl vortices [141].

Although studies have been recorded using organic PCMs in passive waste heat storage applications, their integration with GW heat harnessing at a non-industrial scale using corrugated pipes to enhance heat transfer is a novel step. At the same time, numerically investigating the heat transfer enhancement on both sides of a corrugated pipe in conjunction to both the melting and freezing of a PCM is a research gap in the literature. Consequently, this phase of the research has the following objectives:

- A basic review of internal heat transfer enhancement techniques outlying the reasons for selecting corrugated pipes for this application.
- Conducting an experiment for a specific corrugated pipe embedded in RT-25 with the prescribed boundary conditions of GW heat harnessing.
- Development of a numerical simulation of the setup in this application, to be validated by experimental data.
- Performing a numerical parametric study to investigate the variations in heat transfer characteristics for a discrete set of corrugated pipes with varying rib height ‘e’ and pitch ‘p’ for both the melting and freezing of the PCM.
- Selecting a viable corrugated pipe to be used in this application based on the outcome of the results.



## 4.2. Internal heat transfer enhancement techniques

There are three methods to increase heat transfer in internal flow [143]:

- Changing the flow conditions, i.e. 'Re' number, boundary temperatures and/or adding additives to the flow to alter the composition.
- Increasing the surface area of contact between the pipe and the fluid.
- Enhancing the HTC using passive and/or active techniques.

The first two methods are usually constrained by the operational requirements of the specific application. Increasing the HTC is the only viable option without altering the boundary conditions of the flow. In fact, many HTC enhancement techniques concurrently increase the surface area of contact as well. The enhancement technique can either be active, passive or a hybrid combination of both [142]. The positioning of a technique can be transverse or longitudinal along the direction of flow [144]. Unlike passive techniques, active techniques require an external source of energy [137]. This external energy is required to generate swirls and vortices in the flow by creating vibrations and instabilities leading to turbulence in the fluid flow. In active techniques, the fluid absorbs energy from the pipe enclosure whilst in passive techniques, it loses energy. In active techniques, the HTC can be enhanced to a considerable level, but with an additional energy input and a comparatively higher increase in the friction factor ( $f$ ) of the internal flow. Comparatively, passive technologies are cheaper, easier to manufacture and maintain, with a relatively acceptable TPF. Consequently, passive techniques are preferred for non-industrial low temperature applications. These heat transfer enhancement techniques are presented in Figure 4-1:

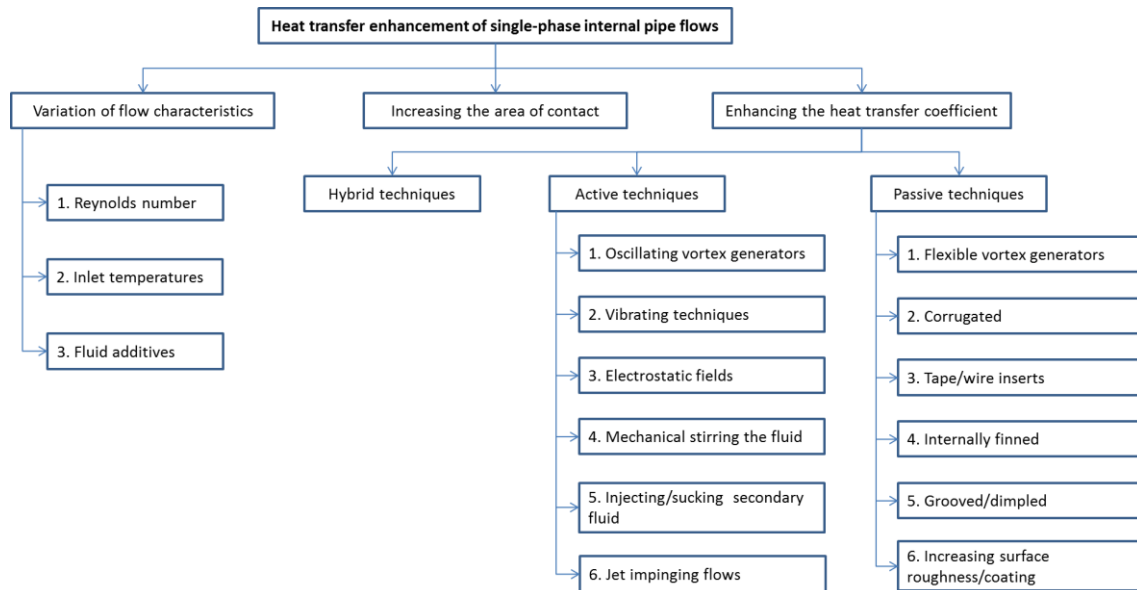


Figure 4-1: Techniques to enhance internal heat transfer in pipes

The efficiency of a passive technique depends on the geometric features of the pipe and the flow conditions in conjunction with the application of usage. According to a study [139], internally finned pipes have the best TPF amongst the passive techniques, while twisted tape inserts have the worst, as high pressure drops have been recorded. The six main passive techniques to enhance the HTC in internal flows are elaborated:

#### 4.2.1. Vortex generators

Any shape with a fixed profile is inserted in a non-uniform manner at specific points to generate vortices in the internal flow [143]. The direction of the swirl produced is either backward or forward to the direction of the main fluid flow, being an important control parameter [140]. The insertion of vortex generators can be both active or passive [145].

Manufacturing is not difficult, while fouling is also in a mid-range compared to other passive enhancement techniques [143]. Problems concerned with the development of two-phases, high pressure losses, noise and heavy vibrations of the equipment at turbulent flows are a downside to these generators [142]. Amongst the passive techniques, only vortex generators and twisted tape techniques have recorded higher pressure loss ratios with respect to their heat transfer enhancement ratios, compared to plane pipes. Experimental literature shows that the Nusselt (Nu) number enhancement

ratio is in the range of 1.5- 4, while increments in 'f' are between 3-5, compared to plane pipes [139].

#### **4.2.2. Corrugated/fluted pipes**

A pattern of uniform grooves arranged helically or axially are embedded in a pipe along the length in the direction of the main fluid flow. The control variables in the design include the 'e' and the 'p' of the corrugations [140]. Consequently, the helical angle is between 0-90° depending on these dimensions.

The major advantages of corrugated pipes compared to other passive techniques are the minimal fouling and pressure losses. Additionally, manufacturing and maintenance is the easiest, especially for internal pipe cleaning. Since the corrugations are both internal and external to the pipe, there are also enhancement effects on the other side of the pipe wall. The only drawback is a relatively lower 'Nu' number enhancement at laminar flows, although this can be eliminated with design modifications. Based on experimental literature [139], the increase in the 'Nu' number and 'f' is in the range of 1.5- 4 and 2-6, respectively, compared to plane pipes.

#### **4.2.3. Tape/wire inserts**

A metallic strip or wire is helically inserted along the circumference of a pipe in the direction of the main fluid flow. The most important design parameters are the width, thickness and twist ratio of the insertion [140]. Wire inserts that have very small diameters to variate the micro flow in pipes are preferred in laminar conditions [146].

This is the most economical passive enhancement technique. Additionally, these tapes can easily be removed for maintenance, unlike the other permanent techniques. The major drawback lies in the difficulty of consistently positioning the tapes. This unprecedented movement can cause the insert to become a hurdle to the main fluid flow with a higher vulnerability to fouling. For this reason, the pressure loss is comparatively the highest amongst passive enhancement techniques, therefore this technique is only preferred in laminar flow regimes [142]. Based on experimental literature [139], the

increase in the 'Nu' number and 'f' is in the range of 1.5-6 and 2-13, respectively compared to plane pipes.

#### **4.2.4. Internally finned/baffled**

Transverse or helically arranged ribs are machined on the internal surface of a pipe. The most important design parameters are the height, shape, arrangement and density of the fins [140]. Typically the height of the fins is much lower for liquid compared to gaseous flows [143].

This technique is relatively hard to manufacture having a mid-range pressure drop, but it is the most commonly used [139]. The biggest drawback is its vulnerability to fouling. At the same time, it is more suited for turbulent flow regimes. Based on experimental literature [139], the increase in the 'Nu' number and 'f' is in the range of 2- 4 and 1- 4, respectively, compared to plane pipes.

#### **4.2.5. Grooved/dimpled**

Non-continuous protrusions with different shapes are stamped on the internal surface of the pipe [139]. The groove depths, diameters, arrangement pattern and edge shapes dictate the design [140].

The pressure losses for such pipes are high, although smoothing out the protrusions can lower them with a lesser heat transfer enhancement. This technique usually enhances the surface tension, being suited for two phase fluid flow. Normally, the protrusions are formed on the internal pipe surface by machining the outer side as well. The depth of the protrusions is a limitation to this method of manufacturing, as they are dependent on the strength of the material. Based on experimental literature [139], the increase in the 'Nu' number and 'f' is in the range of 1.5-4 and 3-5, respectively, compared to plane pipes.

#### **4.2.6. Increased surface roughness/coating**

Grinding a surface with sand grains or knurling a pipe achieves different levels of micro and macro roughness to enhance the internal heat transfer. Surface roughness can also be developed by impregnating micro-level protrusions onto the pipe walls. This technique is known to enhance heat transfer especially for two-phase fluid flows [143].

It has been estimated that almost all surface roughening methods double the heat transfer compared to plane pipes [139]. However, in some circumstances, the pressure drop is far greater than this heat transfer enhancement [140]. This is the case when the surface roughness height is less than the thickness of the thermal boundary layer of the main fluid flow. At the same time, manufacturing is not simple and over the duration of time, the enhancement effects vanish due to fouling. Surface roughness is most commonly used in hybrid with the other passive enhancement techniques. Rough-finned pipes with tape or helical inserts are the most common hybrid combination, with recorded values of the 'Nu' number enhanced by 500% [139]. Similarly, cationic and anionic surfactants are applied to internal pipe surfaces to lower the drag and the pressure losses [142].

An overview of these passive HTC enhancement techniques is summarised in Table 4-1:

Table 4-1: Summary of the techniques of internal heat transfer enhancement

	Technique	Overview	Pros	Cons
1	Vortex generators	A fixed profile inserted non-uniformly to generate vortices in either the backward or forward direction relative to the main fluid flow [140,143,145]. 'Nu' number enhancement ratios are 1.5-4, while increments in the ' $f$ ' are 3-5 [139].	Manufacturing is not that difficult while comparatively, fouling vulnerability lies in the mid-range [143].	The likelihood of two-phases, high pressure losses, noise and heavy vibrations at turbulent flows [142]. Has higher pressure loss ratios with respect to heat transfer enhancement ratios.
2	Corrugated/fluted pipes	A pattern of uniform grooves, helically or axially arranged along the direction of the main fluid flow [140]. The increase in the 'Nu' number and ' $f$ ' is 1.5-4 and 2-6, respectively [139].	Minimal fouling and pressure losses. Maintenance is easy, especially cleaning internal deposits. Since the corrugations are both internal and external, enhancement effects outside the pipe are also witnessed.	A relatively lower 'Nu' enhancement number at laminar flows. Difficulty in non-commercial manufacturing.
3	Tape/wire inserts	A metallic strip or wire is helically inserted along the circumference in the direction of the main fluid flow to improve micro flow characteristics [140,146]. The increase in the 'Nu' number and ' $f$ ' is 1.5-6 and 2-13, respectively [139].	Economical with minimal production costs. Easily removable for maintenance purposes.	Higher pressure loss ratios with respect to heat transfer enhancement ratios. Preferred only in laminar conditions [142]. Difficulty in positioning the tapes in a consistent position, being more prone to fouling.
4	Internally finned/baffled	Transverse or helically arranged ribs are machined on the internal surface [140]. The increase in the 'Nu' number and ' $f$ ' is between 2-4 and 1-4, respectively [139].	Has a mid-range pressure drop, making it the most commonly used enhancement technique [139].	Relatively hard to manufacture. Highest vulnerability to fouling. More suited for turbulent flow regimes.
5	Grooved/dimpled	Protrusions are stamped on the internal and external surfaces of the pipe with different shapes [139]. The increase in the 'Nu'	Has a low vulnerability to fouling [139].	Pressure losses are high but smoothing the protrusions can reduce them. Enhances the

		number and ' $f$ ' is between 1.5-4 and 3-5, respectively [139].		surface tension being suited for two-phase fluid flow. Depth of the dimples is dependent on the strength of the material while manufacturing.
6	Increased surface roughness/coating	Includes micro-protrusions, surface coating, roughing the surface with sand grains or knurling a pipe, achieving different levels of micro and macro roughness. Typically doubles the heat transfer enhancement [139].	Commonly used in hybrid with other passive technologies. Cationic and anionic surfactants reduce the fluid drag and pressure losses [142].	Enhances heat transfer especially for two-phase flows [143]. Manufacturing is not simple and over the duration of time the enhancement effects vanish due to fouling. High pressure losses [140].

### 4.3. Rationale for usage of corrugated GW/CW pipes

Based on the overview of section 4.2, corrugated pipes replacing the plane pipes were deemed the most feasible for this GW heat harnessing application due to the following reasons [147]:

- The pressure loss compared is relatively low to other enhancement techniques.
- The vulnerability to fouling and biofilm deposits is the least, with no sharp edges or obstructions in the main fluid flow regime.
- Corrugated pipes are categorised as doubly enhancing since they increase heat transfer on both sides of the pipe wall, i.e. also towards the PCM side in this case [143].
- The TPF has the best ratios, as outlined in Table 4-1. Along with HTC enhancement, the helical corrugations smoothly guide the fluid flow along the length of the pipe. For this reason, the HTC is enhanced without considerable turbulence, resulting in a comparatively lesser pressure drop.
- The amount of pipe material is almost the same compared to plane pipes, with a negligible increase in costs. However, the surface area of contact between the fluid and the pipe wall along with the wet perimeter increases significantly.
- Manufacturing is difficult for small-scale custom-based designs. However, it is simple and cheap at a commercial level, as usually conventional plane pipes are simply cold rolled on their outer surfaces.

Based on a literature overview [144,148], corrugated pipes enhance the HTC in four ways:

- Enhancing swirls and secondary radial flows in the regime of the main fluid flow.
- Enhancing the turbulence in the main axial flow.
- Improving heat transfer in the area adjacent to the pipe wall by reducing the thickness of the thermal boundary layer. By disrupting this layer, the HTC is enhanced due to better thermal interaction of the core fluid with the walls of the pipe [142].



- Increasing the surface area of contact and enabling a helical path to the fluid flow.

At the same time, there are three reasons for the increase in pressure drop [147]:

- There are higher drag forces on the fluid due to higher shear stresses on the walls of the pipe. This is due to the greater surface area of contact.
- An area reduction of the main axial flow with larger radial velocity components.
- Increased turbulence, rotational flow and swirls on the walls of the pipe.

The geometric definitions of a corrugated pipe are presented in Figure 4-2:

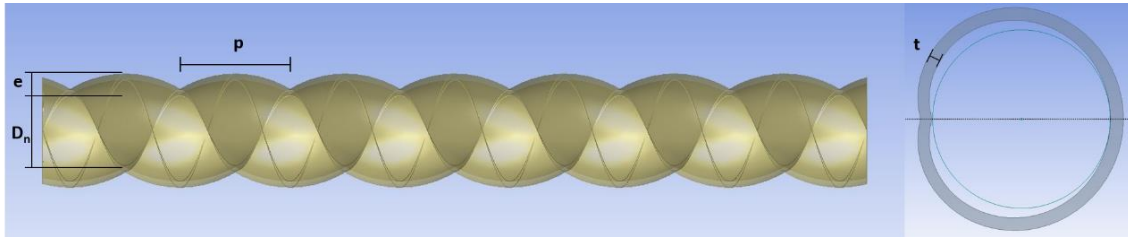


Figure 4-2: Geometric parameters of a corrugated pipe ' $D_n$ ' = nominal diameter,  $e$  = rib height,  $p$  = pitch,  $t$  = thickness

Almost every HE can be improved using passive enhancement techniques; however a theoretical technique has to be practically tested in an application [143]. The thermal performance of corrugated pipes can be independently determined using the Wilson plots [143]. Also, empirical correlations of the enhanced 'Nu' number and 'f' have been published in literature based on experimental data [143,149]. However, variations in the dimensions of corrugated pipes cause a non-linear increase in the HTC. An optimum geometry is highly dependent on the manufacturing limitations, boundary conditions and the application [148]. Hence, theoretical predictions do not suffice and the pipes must be tested either experimentally or with CFD simulations with regard to GW heat harnessing [139]. Since commercially available corrugated pipes were limited for experimental testing, a specimen available in the market was numerically tested in conjunction with this application and validated by an experimental setup. Based on this, discrete combinations with varying 'e' and 'p' of corrugated pipes were numerically assessed in section 4.5.7.

## 4.4. Experimental model

A schematic of the experimental rig is illustrated in Figure 4-3:

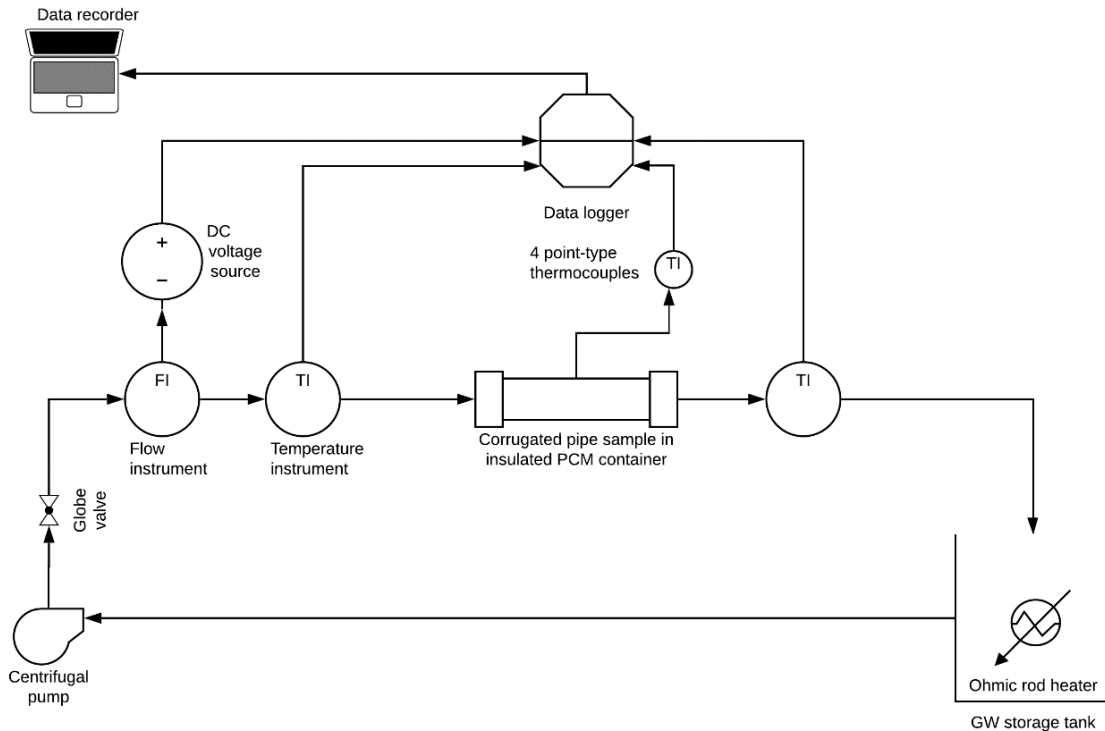


Figure 4-3: Schematic of the experimental setup to assess corrugated pipes

Actual GW with impurities, bacteria and soap residuals was used in the tank, as can be seen in the first row of Table 4-3. The ohmic rod heated the fully filled GW in the tank up to the required 325K (51.85°C), prior to the initialisation of the experiment. A thermostat was not used in the tank as the storage capacity was quite large to ensure a consistent temperature flow of GW for the 900s time duration. A centrifugal pump circulated 0.1kg/s of the GW in a closed circuit with a simple globe valve to control the mass-flow rate. A flow-meter along with six thermocouples were placed as shown in Figure 4-3. Three thermocouples embedded in the corrugated pipe were used to measure the average temperature while a fourth measured the temperature at a fixed point within the PCM, as detailed by the red dots in Figure 4-7. The tested corrugated copper pipe specimen had an ‘e’ of 0.7mm and a ‘p’ of 5mm with a ‘D<sub>n</sub>’ of 12.7mm whilst having a ‘t’ of 1mm. Although the actual diameter of the GW pipes in the building architecture was typically 25mm as outlined in section 2.2.2, a 12.7mm pipe was used to enhance the HTC with increased turbulent flow. Copper was selected as it has the highest thermal conductivity of 401W/(m.K) amongst metals and is partially used in residential

sanitary networks. As installation space is constrained for HEs to harness heat from the GW of residential appliances, a compact, low-cost and maintenance-free HE was required. For this reason, the corrugated pipe had two U-bends. As in most practical applications, bends are commonly used in HEs and it was important to incorporate their effects in the analysis. Although there are more looped pipes increasing the overall pipe length in real HEs, only two bends were considered due to computational constraints in the forthcoming numerical model. Nevertheless, a focus on the thermal performance of the corrugations was important in this phase of the research, as a holistic design of the HE was investigated in section 6.3. To ensure that the fluid flow was fully developed prior to entering the corrugated pipe, the 70mm straight pipe segment existed before the three 610mm lengths, as in Figure 4-5. In total, the length of the entire pipe was about 2,111mm, as illustrated in the layout of both the experimental and numerically simulated corrugated copper pipe in Figure 4-7. There was 30mm of PCM in the direction of each of the coordinate axes from the pipe centre. The pipe was immersed in about 0.0064m<sup>3</sup> of RT-25, as in Figure 4-5. The thermal parameters of the RT-25 based on a Differential Scanning Calorimetry (DSC) analysis [150], are in Table 4-2:

Table 4-2: Thermal parameters of RT-25

<b>Density kg/m<sup>3</sup></b>	Solid: 880, Liquid: 760
<b>Thermal conductivity in W/(m.K)</b>	0.2
<b>Specific heat capacity in kJ/(kg.K)</b>	2
<b>Dynamic viscosity in Pa.s</b>	0.0072
<b>Specific latent heat capacity in kJ/kg</b>	170
<b>Liquidus temperature in K</b>	299.15 (26°C)
<b>Solidus temperature in K</b>	295.15 (22°C)

About 10cm of Styrofoam insulation surrounded a mild steel container enclosing the pipe and PCM to make the system adiabatic, as visible in the practical setup of Figure 4-4:

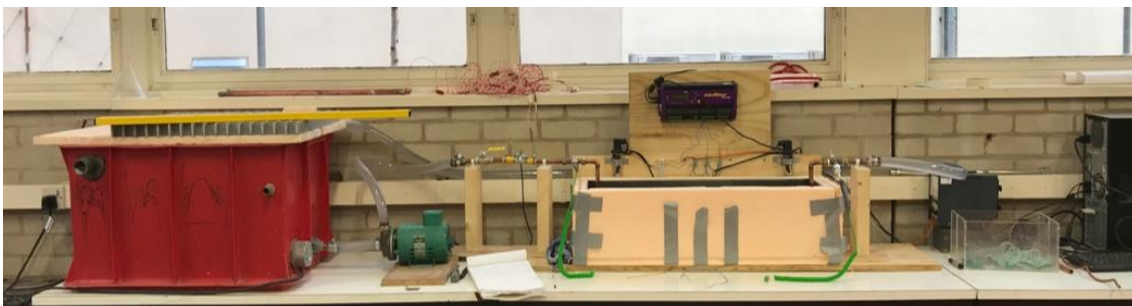








Figure 4-4: Experimental test rig to assess corrugated pipes

Heat losses in this setup were measured in section 5.4.3. The layout of this test rig was based on the schematic of Figure 4-3. Using a data logger, the readings from the instrumentation were recorded at every 5s for a time duration of 900s. An overview of the auxiliary equipment is presented in Table 4-3:

Table 4-3: Specifications of the experimental equipment

Equipment	Technical details	Images
Ohmic rod heater and tank	Tank Capacity: 0.18m <sup>3</sup> Heating elements: 2 × 5kW GW: water, soap residuals, bacteria, biological particles, impurities	
Centrifugal pump	Make & model: Stuart Turner Maximum flow rate & head: 0.92kg/s & 1.5m Minimum flow rate and head: 0.15kg/s & 6m Power supply: 230V AC	
Flow meter	Make & model: RS Pro 508-2704 Range: 0.001 – 0.17kg/s Type: Magnetic K factor: 1420 pulses per 0.0038m <sup>3</sup> Frequency: 235Hz Uncertainty: ±3% Power supply: 4.5 – 24V DC	
Probe thermocouples	Make & model: TME KM03 Type: K-type (nickel chrome–alumel) Length & thickness: 100 & 3mm Response time: 3s Temperature range: 73 – 1,373K (-200-1,100°C) Uncertainty: ±0.25%	
Point thermocouples	Make & model: RS Pro 621-2170 Type: K-type (nickel chrome–alumel) Wire thickness & coating: 0.3mm glass fibre Response time: 0.7s Temperature range: 223 – 673K (-50-400°C) Uncertainty: ±0.25%	

Data logger	Make & model: Datalogger DT85 Series 4 Memory: 128 MB internal Uncertainty: $\pm 0.15\%$ Minimum record time: 1s	
-------------	--	--

The calibration of the instruments was as per ISO 71025:2005. The cumulative uncertainty in the thermocouple readings was about 0.4%, whilst it was 3.15% for the flow meter.

#### 4.5. Numerical model

A 3D numerical simulation replicating the dimensions and boundary conditions of the experimental model was developed in Star-CCM+ v11.04. After validating this simulation based on the experimental data, a parametric analysis was conducted to select the corrugated pipe configuration with optimum internal heat transfer enhancement with respect to this GW heat harnessing application.

##### 4.5.1. Governing equations

There were seven residuals in this CFD simulation corresponding to five different physical laws. Three residuals were for the Navier-Stokes equation in each Cartesian direction: one for the energy, one for the continuity equation and two for the turbulence model, all coupled with the enthalpy method governing the behaviour of PCMs [151].

The continuity equation is also referred to as the law of conservation of mass. For a 3D transient compressible flow in a control volume, it is defined as:

$$\frac{\partial \rho}{\partial t} + \nabla \cdot (\rho v) = 0 \quad (4-1)$$

The first term represents the change of mass within the volume while the second term represents the net mass flux at the inlet and outlet. The Navier-Stokes momentum equation for a control volume is as follows:

$$\frac{\partial(\rho v)}{\partial t} + \nabla(\rho v \cdot v) = -\nabla P + \mu \nabla^2 v + \rho g \quad (4-2)$$

The first term on the LHS is the local change in velocity within the volume. The second term represents the change in velocity due to the movement at the boundaries of the control volume. The first term on the RHS is the change in pressure, while the second term represents the dissipative viscous forces and the third term is the force due to gravity. The LHS of this equation corresponds to the momentum, while the RHS corresponds to the net forces. It is a basic representation of Newton's second law of motion. The velocity field of the fluid flow was derived based on this equation. Consequently, the temperature and pressure for the fluid and metallic pipe could be calculated, using the energy equation for a control volume:

$$\frac{\partial(\rho E)}{\partial t} + \nabla \cdot (v(\rho E + P)) = \nabla \cdot (K_{eff} \nabla T + \left( \mu((\nabla v + \nabla v^T) - \frac{2}{3} \nabla \cdot vt) \cdot v \right)) \quad (4-3)$$

Similar to the Navier-Stokes equation, this is also a transport equation where the terms on the LHS account for the change in energy of the fluid. The terms on the RHS account for the causes of this change, which are the net heat fluxes due to conduction and the viscous effects of the fluid. Due to the turbulent nature of the fluid flow, the k- $\epsilon$  turbulence model is of importance as well. Two transport equations govern the parameters:

- Turbulent kinetic energy – k

$$\frac{\partial(\rho k)}{\partial t} + \frac{\partial(\rho k v_i)}{\partial x_i} = \frac{\partial}{\partial x_j} \left[ \frac{\rho C_\mu \frac{k^2}{\epsilon}}{\sigma_k} \frac{\partial k}{\partial x_j} \right] + 2\rho C_\mu \frac{k^2}{\epsilon} E_{ij} E_{ij} - \rho \epsilon \quad (4-4)$$

- Rate of dissipation of turbulent energy –  $\epsilon$

$$\frac{\partial(\rho\epsilon)}{\partial t} + \frac{\partial(\rho\epsilon v_i)}{\partial x_i} = \frac{\partial}{\partial x_j} \left[ \frac{\rho C_\mu \frac{k^2}{\epsilon}}{\sigma_\epsilon} \frac{\partial \epsilon}{\partial x_j} \right] + C_{1\epsilon} \frac{\epsilon}{k} 2\rho C_\mu \frac{k^2}{\epsilon} E_{ij} E_{ij} - C_{2\epsilon} \rho \frac{\epsilon^2}{k} \quad (4-5)$$

The terms on the LHS of both equations represent the rate of change of the parameter and its transport by convection. The terms on the RHS represent the transport of the parameter by diffusion and its rate of production and destruction, respectively [152]. However, in spite of the existence of numerous models, the flow characteristics for turbulent flow are yet to be fully understood [147].

The enthalpy method governs the melting and freezing processes of a PCM [151]. After discretisation of the PCM domain, the energy equation is applied to each control volume, based on which the non-isothermal enthalpy is updated [114]. The three possible outcomes of the enthalpy are:

$$\begin{cases} C_s T, & T < T_s, & \text{Solid phase} \\ C_{in} T + \frac{H_L (T - T_s)}{(T_L - T_s)}, & T_s \leq T \leq T_L, & \text{Mushy region} \\ C_L T + H_L + C_{in} (T_L - T_s), & T \geq T_L, & \text{Liquid phase} \end{cases} \quad (4-6)$$

The PCM at the phase change interface was in a mushy state, being partially liquid and solid, corresponding to the Stefan condition. This is unlike the assumption of the model developed in section 3.2.1. The enthalpy method is not a direct interface tracking approach. Based on an analysis of a unit volume, the interface was consequently tracked. After this step, the temperatures and pressure fields within the PCM were numerically calculated [117].

#### 4.5.2. Geometry

The geometry of the 3D model was constructed in ANSYS Design Modeler v18.2. The generated parasolid files were imported into Star-CCM with custom tessellation settings to account for the corrugations. There were three distinct regions merged into a single part: the fluid domain, the corrugated copper pipe and the PCM. Each region was imprinted at the interface to ensure non-intersecting surfaces and non-manifold edges. An overview of the developed model is in Figure 4-5:

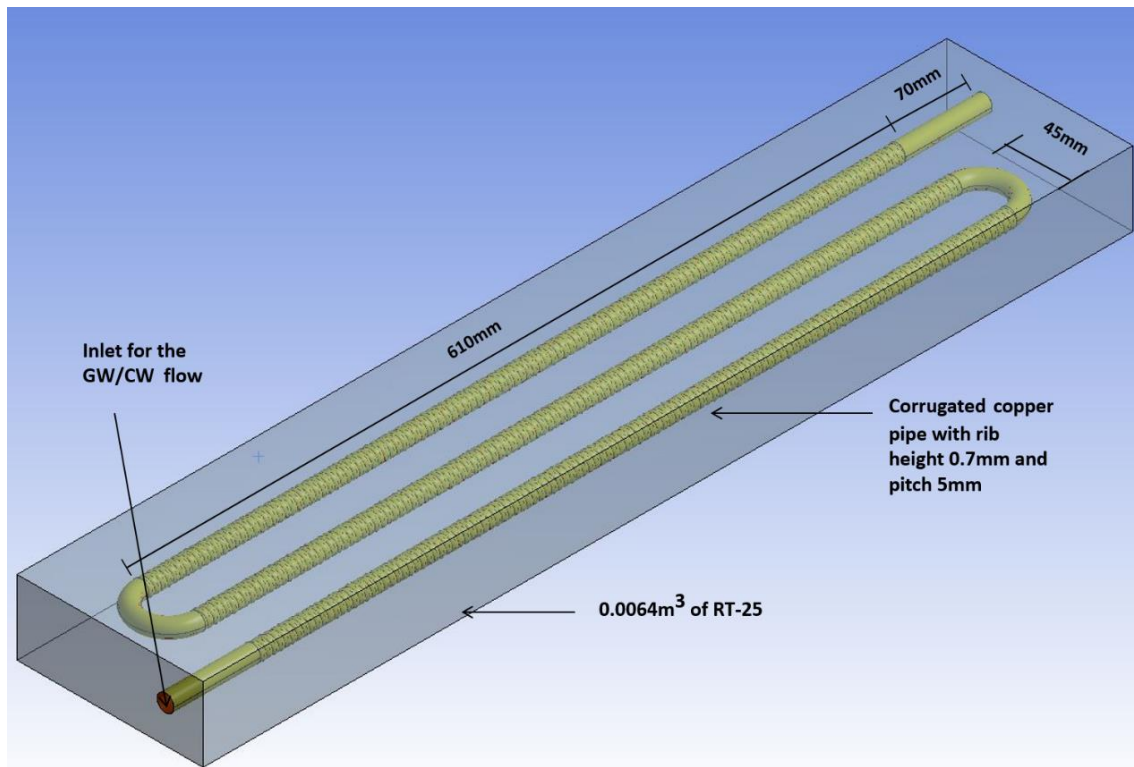


Figure 4-5: Layout of the geometric model with three domains: fluid flow, corrugated copper pipe and the PCM

As highlighted in Figure 2-11, vertical pipe orientations for GW heat harnessing in conventional HEs generally have a better performance compared to horizontal orientations. Nevertheless, horizontal pipes were used in this configuration due to the following reasons:

- At relatively high flow rates of 0.1kg/s, most of the fluid would escape through the centre without transferring heat at the interface as the pipe diameter was only 12.7mm, making the vertical orientation ineffective.
- Using a vertical orientation in conjunction with corrugated pipes is not recommended [139]. A vertical orientation would considerably enhance a haphazard turbulent movement to increase pressure losses, making the enhancement via the corrugations ineffective.

Although the flow of GW and CW would be in different pipes in a practical HE due to contamination issues, in this primary design a single pipe was used for both flows as the focus of this stage of the research, but this was only to analyse the internal enhancement effect.



### 4.5.3. Mesh

Using the automated mesh generation option in Star-CCM, the three domains were discretised using an unstructured conformal polyhedral mesh. To capture the details of the corrugations, a surface mesh was generated before a volume mesh. A set of nine prism layers were also used to account for the fluid boundary layers adjacent to the pipe walls. An all ‘y+’ wall treatment model was used to calculate both the viscous and turbulent effects adjacent to the pipe corrugations. This model was automatically selected by the ‘k-ε’ turbulence scheme as it is suited for difficult cases in which it is not possible to achieve a purely high or low ‘y+’ mesh [151]. Such a fluid flow was due to the corrugations of the copper pipe. In this simulation, a targeted ‘y+’ between 80-100 was used with the ‘Re’ number varying to a maximum of about 15,000, due to the 0.1kg/s mass-flow rate of the fluid. Correspondingly, the maximum ‘y’ value of 1.1mm was calculated as the height of the first element of the prism layer adjacent to the pipe wall, based on expressions of frictional velocity and the skin friction coefficient, using the following equation:

$$y = \frac{y^+ \cdot \mu}{\rho \cdot \sqrt{0.395 \cdot Re^{-0.25} \cdot v^2}} \quad (4-7)$$

Based upon this, the height of the entire prism layer was about 4.5mm, adjacent to the walls of the corrugated pipe. An overview of the cross-section of the mesh is displayed in Figure 4-6:

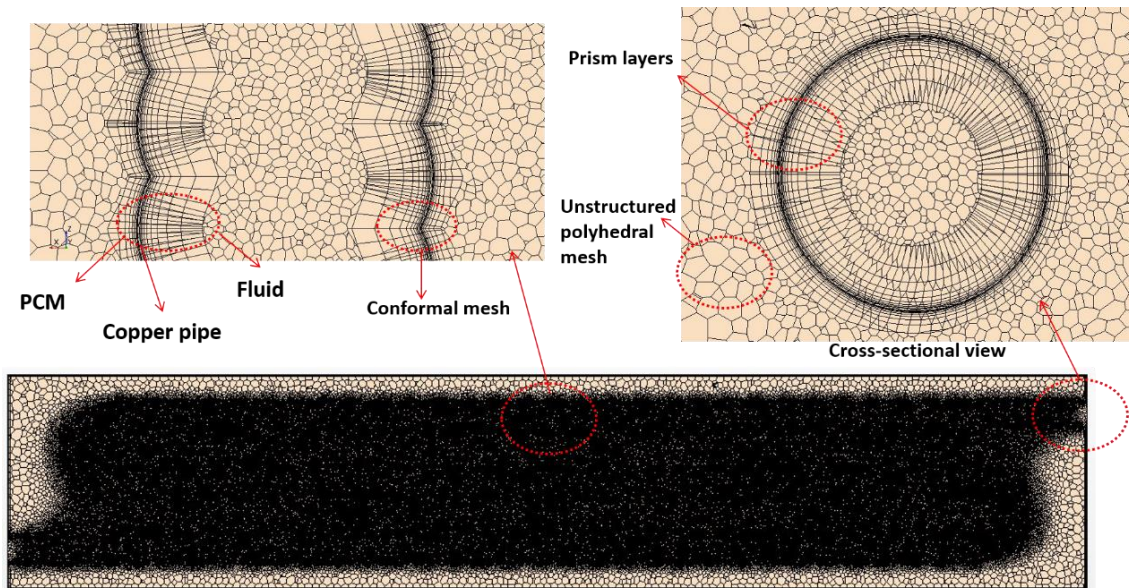


Figure 4-6: Structure of the mesh for the geometry

To conduct a mesh convergence study, four different grid sizes of about 10, 15, 20 and 25 million elements were set up for melting the PCM with GW flow. For both the 20 and 25 million element structure, the difference in the outlet temperature of the GW flow was less than 4%, after 900s of the simulation with the end temperatures being less than 1% apart. However, the computation time of the 25 million grid size increased by about 250% in spite of using a 12-core per node High Performance Computer (HPC). Thus, the results were considered as independent with a mesh size of 20 million elements.

#### 4.5.4. Boundary conditions and solvers

A summary of the boundary conditions and solvers used for the three distinct regions of the simulation is in Table 4-4:

Table 4-4: Boundary conditions and solvers for the three regions of the numerical simulation, M = melting, F = freezing

Region	Boundary conditions	Solvers
Fluid (GW and CW)	Inlet type: mass-flow inlet Outlet type: pressure outlet Inlet temperatures/K: 325 (51.85°C) (M) & 285 (11.85°C) (F)	Three dimensional Implicit unsteady Domain type: liquid water Segregated flow Constant density K-epsilon turbulence – realisable two layer Two layer all ‘y+’ wall treatment

	Mass-flow rate/kgs <sup>-1</sup> : 0.10 Initial temperatures/K: 325 (51.85°C) (M) & 285 (11.85°C) (F) Interfaces: conformal contact	Segregated fluid temperature
Pipe	Initial temperatures/K: 295 (21.85°C) (M) & 315 (41.85°C) (F) Interfaces: conformal contact	Three dimensional Implicit unsteady Domain type: solid copper Segregated solid energy Constant density
PCM	Outer walls: adiabatic no-slip Initial temperature/K: 295 (21.85°C) (M) & 315 (41.85°C) (F)	Three dimensional Implicit unsteady Domain type: fluid (multiphase) Eulerian multiphase Multiphase interaction Volume of fluid Multiphase equation of state Segregated flow K-epsilon turbulence – realisable two layer Two layer all y+ wall treatment Segregated multiphase temperature Melting solidification Polynomial density Gravity

The inlet temperature for the GW (PCM melting) and CW (PCM freezing) flows were based on the values outlined in section 2.5. Due to impurities in the GW compared to the CW, it was modelled as water but with a relatively higher constant density of 1,005 kg/m<sup>3</sup>. For melting the PCM, the copper pipe and the PCM were initially at the ambient temperature of 295K (21.85°C), as in section 3.3. For freezing, it was assumed that the copper pipe and the PCM had retained heat from the melting process, being at 315K (41.85°C). The thermal properties of RT-25 in Table 4-2 were used to model the PCM.

Generally, a liquid PCM is Boussinesq and Newtonian along with being incompressible, having a laminar buoyancy motion and a negligible viscous dissipation [153].

Convection is also a dominant mode of heat transfer along with conduction, especially during the melting of a PCM, as outlined in section 3.2.1. There are three approaches in Star-CCM to account for this natural convection [151]:

- Using only a conduction-based model with different constant thermal conductivities for the liquid and solid PCM, as in section 3.2.1. The thermal conductivity of the liquid phase is higher than the solid, as melting is convection-dominated.
- Using a constant density PCM with the Boussinesq model. However, this is only valid for small temperature and density variations.
- Using a temperature dependent variable density PCM with the effects of gravity enabled.

Unlike the model developed in section 3.2.1, the third approach was used at this stage to assess the influence in this 3D simulation with greater accuracy. With this approach, the PCM had a polynomial density of first-order. Typically, the density of the solid phase was higher than the liquid phase, resulting in ullage as will be discussed in chapter 5. The density was  $880 \text{ kg/m}^3$  at the solidus temperature of  $295.15\text{K}$  ( $22^\circ\text{C}$ ) and  $760 \text{ kg/m}^3$  at the liquidus temperature of  $299.15\text{K}$  ( $26^\circ\text{C}$ ) [131]. The equation used to compute the linearly varying density of the PCM is:

$$\text{Density} = 9734.5 - 30 \times \text{Temperature} \quad (4-8)$$

The segregated energy solver was enabled for all three domains of the geometry, as it sequentially solves the governing equations of section 4.5.1. Typically, it is accurately used for incompressible or mildly compressible flows and is also suited to model convection in PCMs having a low Rayleigh number, as in this application. Although the coupled solver is more appropriate to model natural convection, it was inapplicable for a multi-domain integrated geometry, as in this case. At the same time, the coupled solver is more computationally intensive with reported convergence issues [151]. An implicit transient simulation with time steps of 0.1s for the 900s time duration was performed for both the GW and CW flows. The first-order temporal discretisation scheme was selected for the mesh; the second-order discretisation scheme for the convection terms while the Hybrid-Gauss LSQ scheme was used for the gradient discretisation.

#### **4.5.5. Verification and calibration**

A five step verification scheme was implemented to ensure that the CFD simulation accurately implemented the conceptual framework [154].

As a first step, a mesh convergence study was performed to ensure spatial discretisation convergence, as explained in section 4.5.3. Secondly, temporal discretisation convergence was ensured by varying the initial time-step of the transient solution. With a 0.1s initial time-step, the solution converged with an acceptable real-time computational duration with no loss of accuracy in comparison to lower values. Thirdly, to ensure iterative convergence, all seven residuals corresponding to the governing equations of section 4.5.1 converged by values of  $10^{-2}$  or lower after the initial transient zone. Due to the nature of the 3D turbulent flow in the corrugated pipes and phase change phenomenon of the PCM, this value was considerably acceptable after the 900s time duration. Fourthly, to verify consistency in the results, the simulation for both melting and freezing was repeated twelve times with the same boundary conditions. The confidence level in the results was 99% after assessing three different thermal parameters in the configuration. Finally, a sensitivity analysis was performed to consider any abnormalities in the thermal parameters and to theoretically verify the results. Variations in the inlet mass-flow rate and temperature of the GW and CW were proportional to the amount of phase changed PCM, as predicted in the literature [132,155,156]. Similarly, the phase change behaviour of the PCM and the magnitudes of the natural convective currents were within the expected limits, as per the literature [133,157]. Additionally, a closed system energy and mass balance of the configuration ensured that the governing equations were verified in the simulation.

#### **4.5.6. Validation**

With an overview of the layout of the corrugated pipes in Figure 4-7, the numerical model was validated based on experimental data for the melting of the PCM with a GW mass-flow rate of 0.1kg/s:

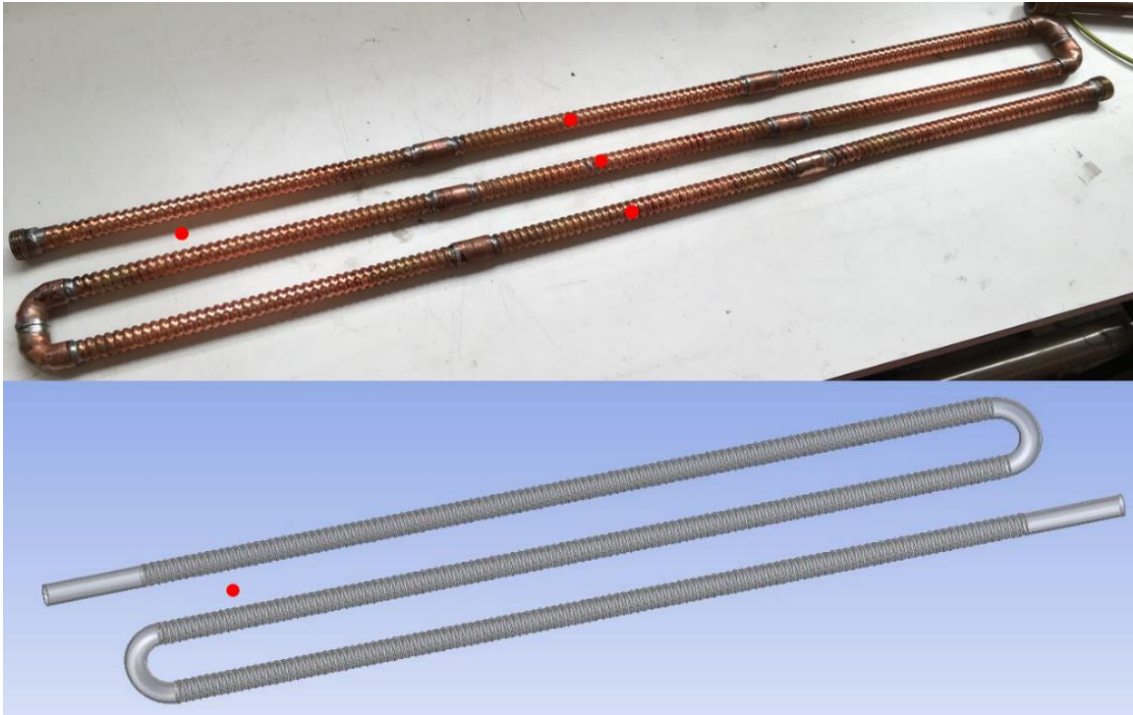


Figure 4-7: Layout of the corrugated pipe with an 'e' = 0.7mm, 'p' = 5mm for the experimental and numerical models with thermocouples positioned at the red dots

The average percentage error was calculated as follows:

$$\text{Average percentage error} = \left[ \frac{\sum \left( \frac{T_{exp} - T_{sim}}{T_{exp}} \right)_t}{N_t} \right] \times 100 \quad (4-9)$$

As depicted in Figure 4-3, three different temperatures readings from the experimental setup were compared to similar readings from the numerical model for the 900s time duration. A plot of the difference between the inlet and outlet temperature of the GW flow is in Figure 4-8:

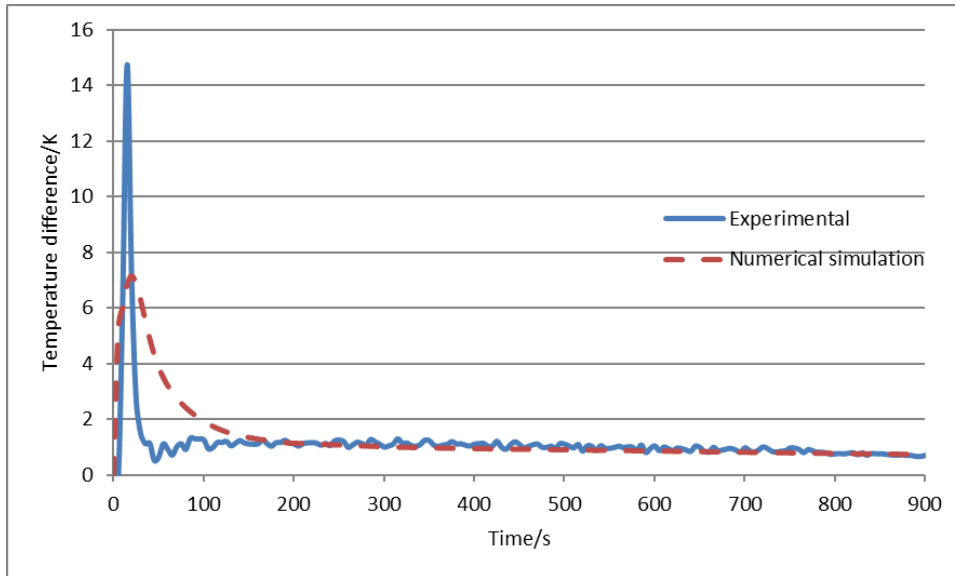


Figure 4-8: Inlet and outlet temperature differential of the GW flow of both datasets

It was observed that a steady-state condition was achieved after the initial 150s. The average error for the entire time duration was 8.5%, while the mean difference between the readings was 0.40K. A plot of the average temperature of the corrugated copper pipe is in Figure 4-9:

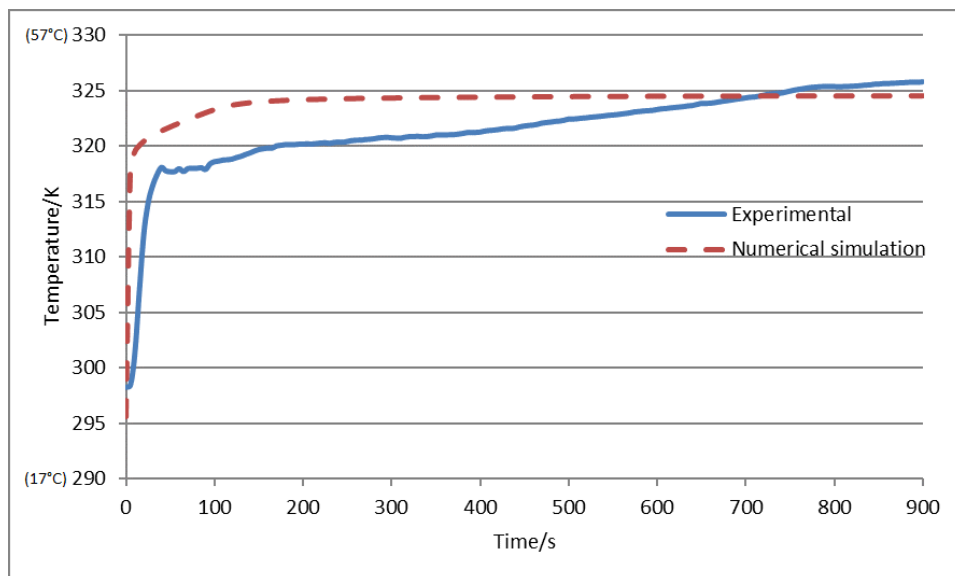


Figure 4-9: Average pipe temperature of both datasets

The average error for the time duration was 0.85%, while the mean difference between the readings was 2.7K. A plot of the temperature of a point in the PCM region is in Figure 4-10:

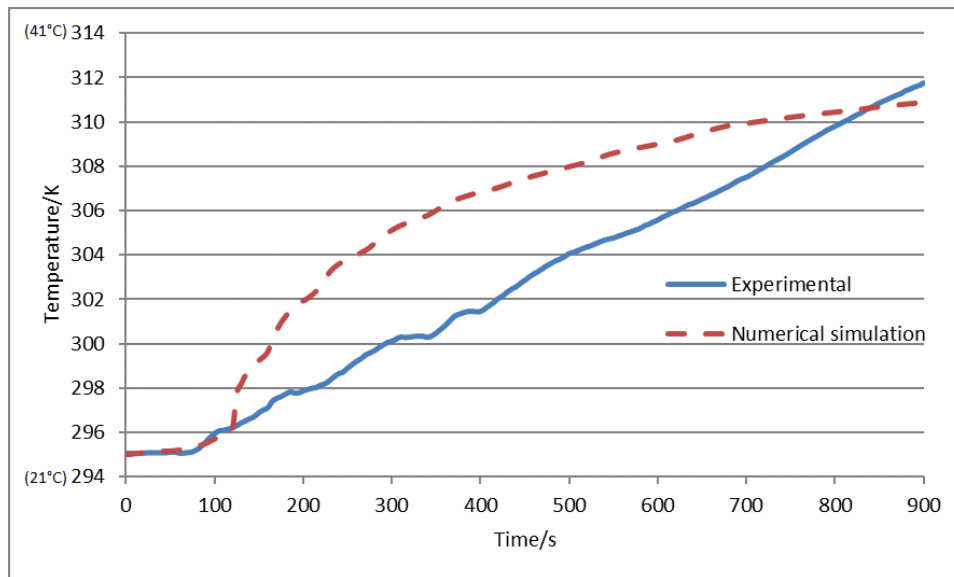


Figure 4-10: PCM temperature at 100mm from the GW inlet and 2mm from the edge of the pipe, for both datasets

The average error was 0.93%, while the mean difference between the readings was 2.8K. A summary of these validation results is in Table 4-5:

Table 4-5: Difference between the numerical and experimental results to assess corrugated pipes

	Description	Average percentage error	Mean difference between values
1	Difference between the inlet & outlet temperature of the GW flow	8.5%	0.40K
2	Average pipe temperature	0.85%	2.70K
3	Temperature of a point in the PCM: 100 mm from the GW inlet & 2 mm from the edge of the pipe	0.93%	2.80K

The reasons of the deviations in these validation results are:

- Several assumptions model the practical experiment in the numerical simulation. This includes the assumption of the valued initial temperatures of all three domains. The effect of these assumptions was amplified in the transient zone, as can be seen specifically in Figure 4-8.
- In Figure 4-9, the readings for the average pipe temperature in the experiment were taken at only three discrete points on the pipe. However, this was compared to the mass averaged temperature of the entire copper pipe in the simulation. A larger set of discrete experimental thermocouple readings could



minimise this error. At the same time, it was quite difficult to attach the thermocouples inside the PCM on the uneven surface of the corrugated copper pipe. The contact between the thermocouples and the pipe was not firm through the time duration of the experiment. Adhesives get corroded by the PCM over the duration of time, requiring a more durable solution.

- The inlet temperature of the GW flow in the experiment varied by  $\pm 3\text{K}$ , as it was not always at  $325\text{K}$  ( $51.85^\circ\text{C}$ ). However, this temperature was consistent in the numerical simulation, which was the reason for the variation in endpoint temperatures in Figure 4-9 and Figure 4-10. The inclusion of a thermostat instead of relying on the initially uniform temperature GW tank would have brought in more accuracy.
- While measuring the experimental temperature of a point in the PCM in Figure 4-10, the K-type point thermocouples developed a covering of a non-conductive solid coat, which decreased their response time and accuracy, corresponding to the deviation in behaviour. More accurate E-type thermocouples or Resistance Temperature Detectors (RTD) would have minimised this error.
- The experimental data was recorded for every 5s to be interpolated for lesser time values, while the simulation data was accurate up to 0.1s.

Nevertheless, the end values and trends of all the plots were in satisfactory limits for the purpose of validating the numerical model.

#### **4.5.7. Results**

After the validation of the numerical model, the corrugated pipe in Figure 4-7 with an 'e' of 0.7mm and a 'p' of 5mm was compared to a similar numerical simulation of a plane copper pipe having the same overall dimensions and boundary conditions.

However, contrary to the desired outcome, the results of the corrugated pipe showed minor improvements in comparison. The HTC increased by only 2%, the phase changed PCM by about 4% and the pressure drop by 45%, as observed in comparison to the plane pipe. It was clear that a parametric study based on varying 'e' and 'p' lengths of a corrugated pipe must be numerically simulated to optimally select the best configuration

for this application. Hence, an additional nine geometries were developed to be compared with the benchmark plane pipe, as displayed in Figure 4-11:

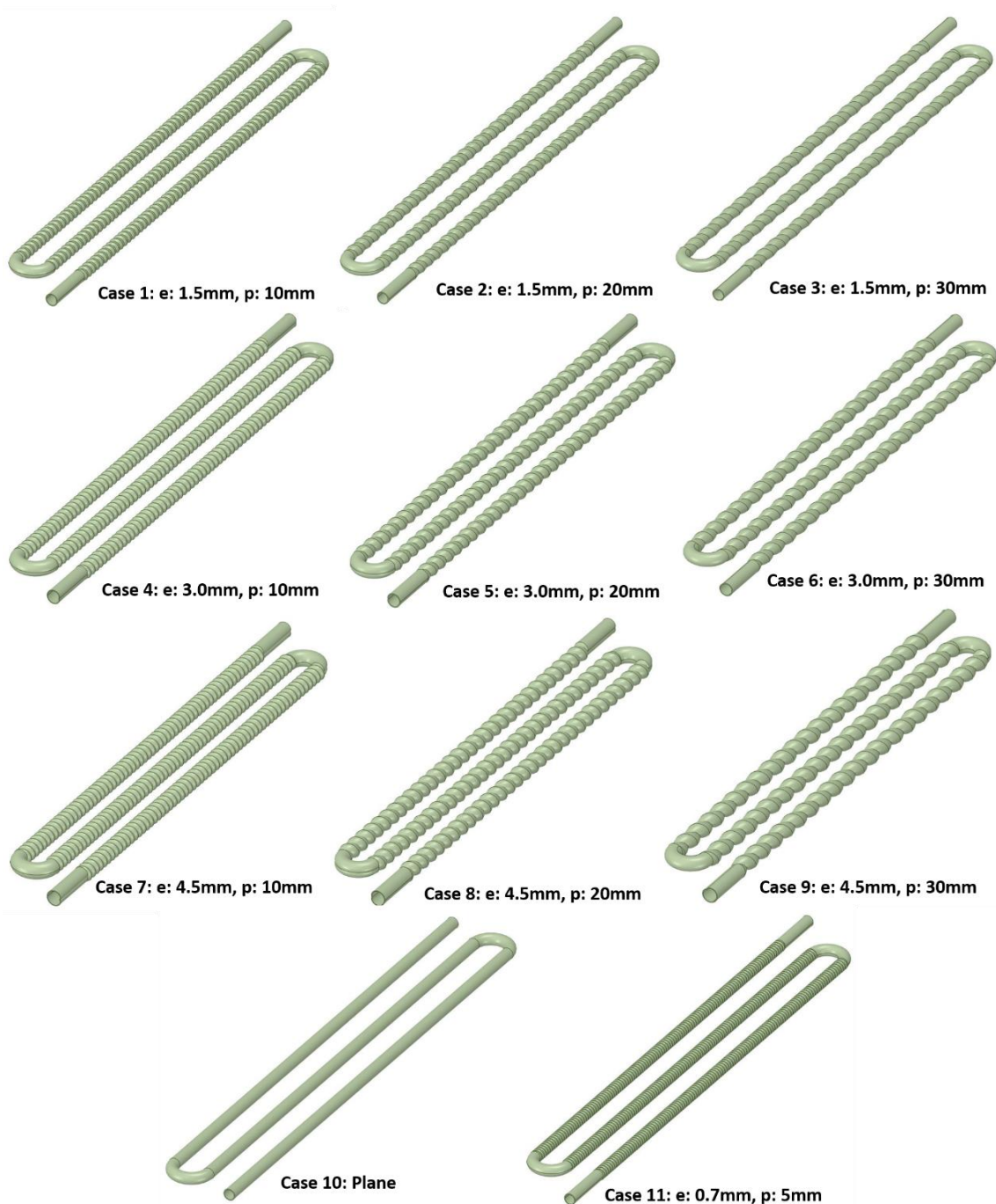


Figure 4-11: Parametric study of the corrugated pipes with varying 'e' and 'p' values

Case 10 corresponded to the benchmark plane pipe, while case 11 (e0.7p5 mm) represented the validated corrugated pipe in section 4.5.6. Apart from the systematic variations in 'e' and 'p', the dimensions of the geometries in this parametric study were exactly the same. Additionally, with the same mesh (section 4.5.3) and boundary

settings (Table 4-4), the resulting grid sizes were also about 20 million elements, for all cases. Results for both the GW and CW flows at different mass-flow rates for each corrugated pipe were differentiated based on the overall, flow and thermal performance. Although the typical mass-flow rate of GW and CW was 0.1kg/s based on section 2.5, three discrete mass-flow rates (0.02, 0.06, 0.10 kg/s) were assessed to gain a complete insight of flows with different ‘Re’ numbers.

### I. Overall performance

The overall performance of each corrugated pipe was assessed based on two different criteria. Firstly, the ratio of the comparatively famous TPF1 was defined as [137]:

$$TPF1 = \frac{Nu_{corrugated}/Nu_{plane}}{(f_{corrugated}/f_{plane})^{1/3}} \quad (4-10)$$

The volumetric diameter ‘ $D_v$ ’ of a corrugated pipe was defined as [149]:

$$D_v = \sqrt{\frac{4 \times \text{Volume enclosed inside the corrugated pipe}}{\pi \times \text{Length of the corrugated pipe}}} \quad (4-11)$$

Both the volume and length could be estimated while constructing the geometry in the numerical simulation. Based on the ‘ $D_v$ ’, the ‘Nu’ number was calculated as:

$$Nu = \frac{h \cdot D_v}{k} \quad (4-12)$$

The average HTC ‘h’ was computed in the numerical simulation while the thermal conductivity ‘k’ of water was 0.628 W/(m.K).

The friction factor (f) was defined as:

$$f = \frac{\Delta P}{\left(\frac{\rho v^2}{2}\right)\left(\frac{l}{D_v}\right)} \quad (4-13)$$

The pressure drop of the fluid between the inlet and outlet was computed in the numerical simulation. The density of the CW was 997kg/m<sup>3</sup> and 1,005kg/m<sup>3</sup> of the GW. The average velocity of the flow through the pipe was calculated based on the continuity equation:

$$v = \frac{4\dot{m}}{\rho \cdot \pi \cdot D_v^2} \quad (4-14)$$

The ratios were computed based on the values of the corrugated specimen to that of a plane pipe. Comparing TPF1 for the different mass-flow rates, case 3 (e1.5p30 mm) stood out to be the best followed by case 6 (e3.0p30 mm) and case 9 (e4.5p30 mm), as in the results presented in Figure 4-12:

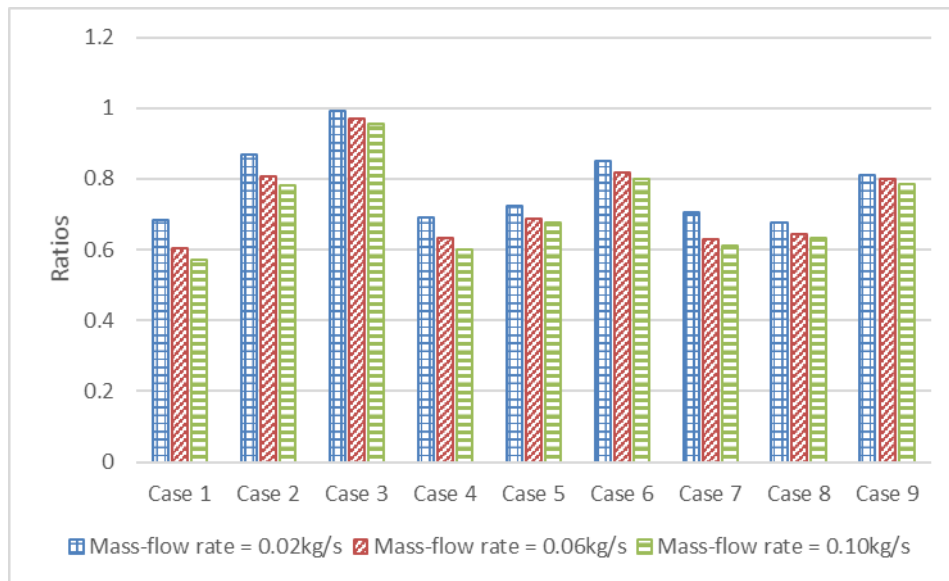


Figure 4-12: TPF1 for both melting (GW flow) and freezing (CW flow)

The results were the same for both melting and freezing, since TPF1 is a measure of the surface enhancement with the same flow profiles for both the CW and GW flow. Additionally, the temperature differentials of 30K were the same between both the fluids and the initial pipe temperature as outlined in Table 4-4.

From the pattern of the bars in Figure 4-12, corrugated pipes with lower ‘p’ values were not preferable. Another observable pattern was that the corrugated pipes performed much better at lower mass-flow rates. An important outcome was that all the TPF1 ratios were less than one in comparison to plane pipes. This was due to the simplification of using the average ‘Nu’ number, ‘f’ and ‘v’ derived from the expression of ‘D<sub>v</sub>’. The ratios of the computed ‘D<sub>v</sub>’ of equation (4-11) and ‘v’ of equation (4-14) with plane pipes are shown in Figure 4-13:

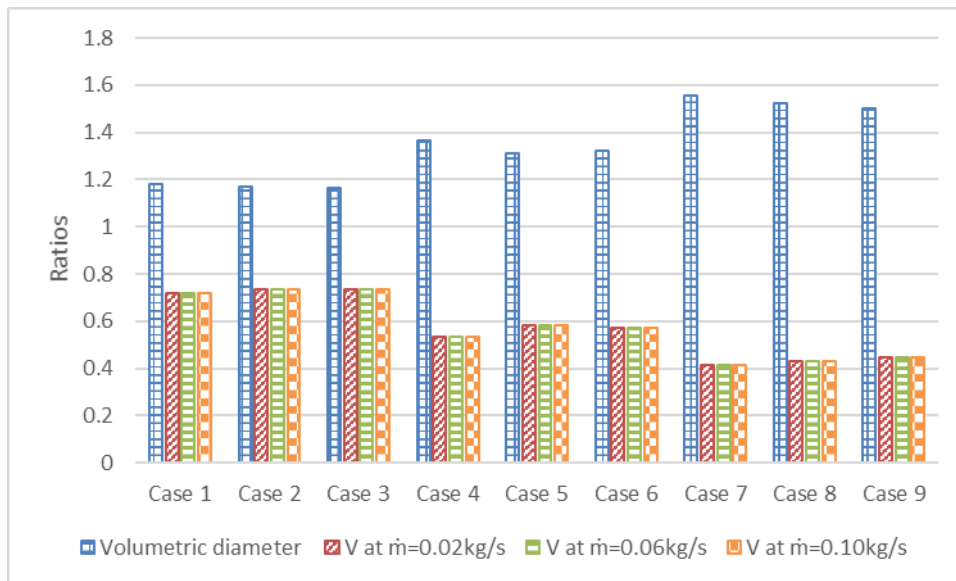


Figure 4-13: Variations in the ratios of ‘D<sub>v</sub>’ and ‘v’, compared to a plane pipe (Case 10)

From Figure 4-13, the ‘D<sub>v</sub>’ of a corrugated pipe increases simultaneously as ‘e’ increases. However it was not greatly affected by increments in the ‘p’. However ‘v’ was inversely proportional to ‘e’, as the mass-flow rate was the same with a larger flow cross-sectional area. The ‘v’ ratios of both pipes were independent of the mass-flow rates as they were a surface and not a flow property. An increment in ‘D<sub>v</sub>’, affects ‘v’ by an inverse square law which eventually inversely effects ‘f’ to the power of five. However, the ‘Nu’ number was only affected proportionally, as observed from equations (4-11) to (4-14). For this reason, the ratios of TPF1 were altered to be below one.

It can be argued that TPF1 does not accurately depict the thermal performance of the corrugated pipes. Using ‘D<sub>v</sub>’, the varying ‘v’ and HTC of the flow were taken as an average over the entire fluid domain, without fully incorporating the conditions adjacent to the pipe walls. In corrugated pipes, the use of this diameter does not accurately

estimate the effects of turbulence and the helical flow regime [158]. TPF1 is a measure of the surface and not the performance enhancement [158]. For this application, the prime variables of concern were the heat transfer and the pumping power. For this reason, another performance criteria TPF2 was defined, independent of the fluid and pipe characteristics as [158]:

$$TPF2 = \frac{\text{Heat transfer at the interface}}{\text{Pumping power}} = \frac{(\dot{Q}_{corrugated}/\dot{Q}_{plane})}{\left(\frac{\dot{V}\Delta P_{corrugated}}{\dot{V}\Delta P_{plane}}\right)} \quad (4-15)$$

Considering TPF2, the results for both the melting and freezing of the PCM are presented in Figure 4-14:

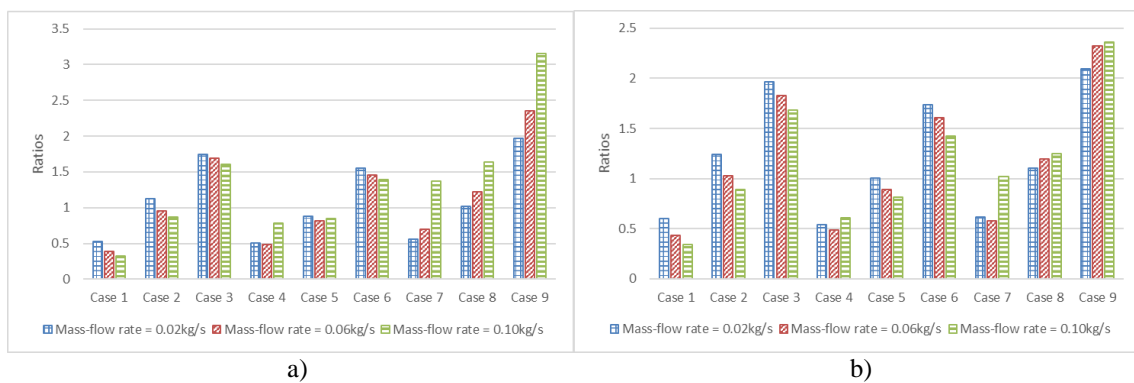


Figure 4-14: TPF2 for a) melting (GW flow) b) freezing (CW flow)

Similar to TPF1, this application preferred higher values of ‘p’ for the corrugated pipes. However on the contrary, greater mass-flow rates were favoured by higher ‘e’ values at these higher ‘p’ values. Performance was better at these conditions, as more fluid mass passed through the pipe with a better helical path and less turbulence. For freezing, the difference in performance with varying mass-flow rates was linear instead of parabolic, as in the melting process. In this performance criteria, the best results were obtained with case 9 (e4.5p30 mm) followed by case 3 (e1.5p30 mm) and case 6 (e3.0p30 mm). In the melting process, enhancement ratios greater than two were observed for all mass-flow rates of case 9 (e4.5p30 mm). The most prominent difference between the melting and freezing plots were the values on the y-axis. The highest ratio was hardly greater than two for freezing, compared to three for melting.

As mentioned in section 4.3, corrugated pipes doubly boost performance on both sides of the pipe. For this reason, the increase in the phase changed mass of the PCM was another criterion of importance. The total phase changed mass of the PCM, external to the pipe for all cases of Figure 4-11 for both melting and freezing, are presented in Figure 4-15:

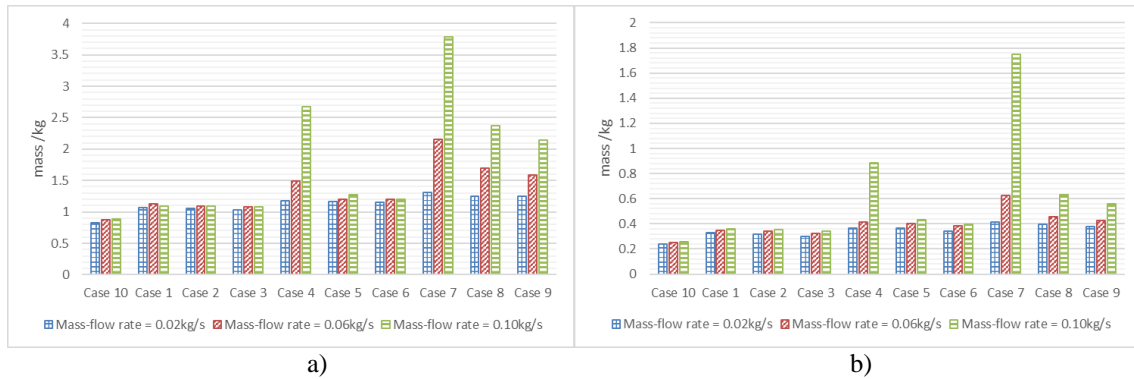


Figure 4-15: Amount of a) melted PCM b) frozen PCM, for all cases

In this outcome, lower ‘p’ values with higher ‘e’ values performed the best, especially at higher mass-flow rates, due to increased turbulent effects. In all cases, the phase changed mass of the PCM was greater than the benchmark case 10, proving that corrugated pipes have doubly enhancing effects. The trends and patterns of this enhancement criteria were similar for both melting and freezing. However, about 65% less PCM froze in the 900s time duration for all cases compared to melting.

## II. Flow performance

The initial temperature differential between the fluid flows and the pipe/PCM was 30K for both melting (325K & 295K) (51.85°C & 21.85°C) and freezing (285K & 315K) (11.85°C & 41.85°C), as outlined in Table 4-4. For this reason, the TPF1 ratios in the last section, along with the resulting fluid flow profiles, were exactly the same, for both melting and freezing.

As outlined in section 4.3, the pressure drop increased due to three primary reasons, as in the ratios in comparison with plane pipes in Figure 4-16:

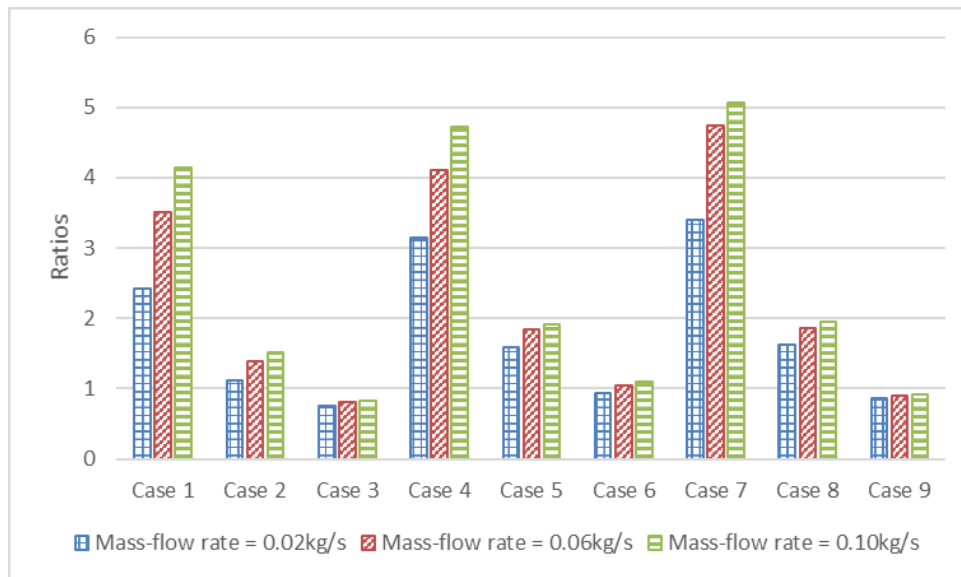


Figure 4-16: Pressure drop ratios for both melting (GW flow) and freezing (CW flow), compared to a plane pipe (Case 10)

Surprisingly, the pressure drop decreased at higher ‘p’ values in comparison to flow in a plane pipe. At lower mass-flow rates, the pressure drop was lower which was one of the reasons for a better TPF1 in these conditions. The best combinations of case 9 (e4.5p30 mm) and case 3 (e1.5p30 mm) had pressure drop ratios below one at all mass-flow rates. This was because a high-pitched corrugated pipe provides a smooth helical path to guide the fluid flow. Due to this movement of the fluid along the corrugations, the resulting shear forces and turbulence decreases, eventually minimising the pressure drops even compared to a plane pipe. However, this helical path was not provided at lower ‘p’ values, resulting in a more turbulent and less smooth flow. Evidently, turbulence was a major contributor to increments in the pressure drop. Additionally, at lower mass-flow rates, the possibility was higher of all the fluid flow pursuing a helical path with lesser drag. As discussed in the last section, the ‘f’ used for the TPF1 calculation was influenced manifold by ‘D<sub>v</sub>’, as presented in Figure 4-17:



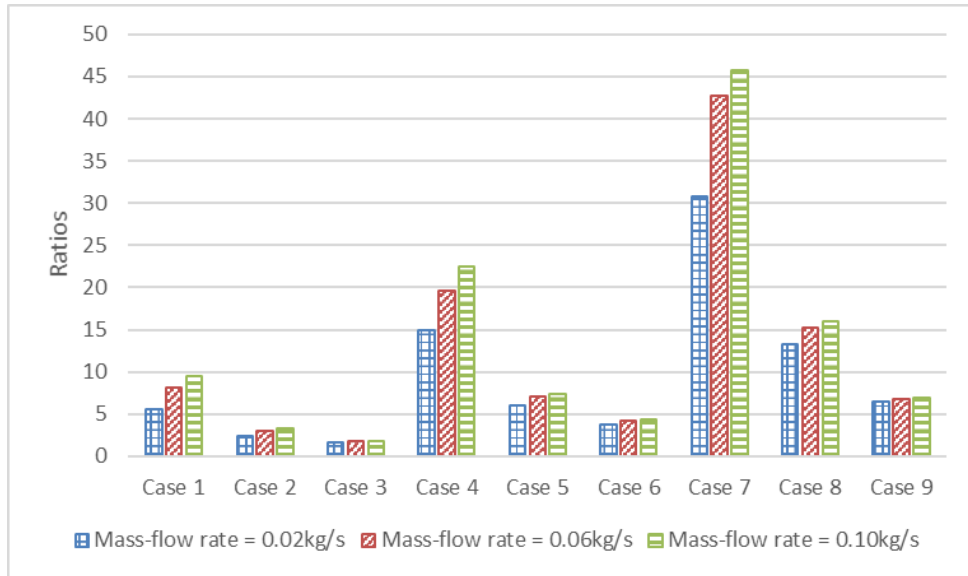


Figure 4-17: Friction factor ' $f$ ' ratios for both melting (GW flow) and freezing (CW flow), compared to a plane pipe (Case 10)

From Figure 4-16, the maximum pressure drop ratio was about 5, while from Figure 4-17, the maximum ' $f$ ' ratio reached about 45. Consequently, as discussed in the last section, the TPF1 ratios were below one, but were nevertheless still useful for a comparative analysis.

To illustrate the fact that the higher ' $p$ ' values of the corrugated pipes provided a smoother helical flow path in comparison to the plane pipes, the fluid vorticity and helicity were compared. Vorticity measures the number of vortices or swirls, while the helicity measures the helical path from the central axis of the fluid flow. The ratios of the volume averaged vorticity of the entire fluid domain are in Figure 4-18:

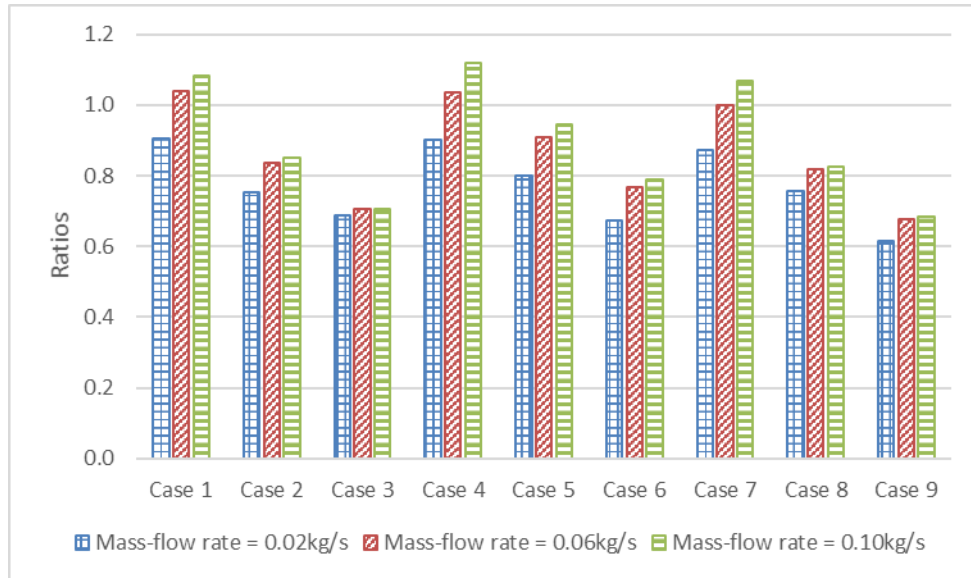
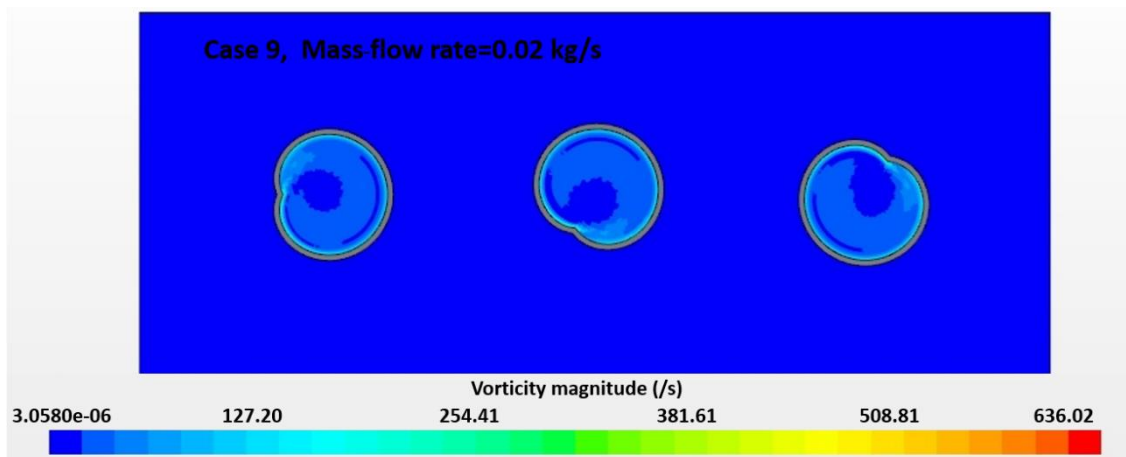
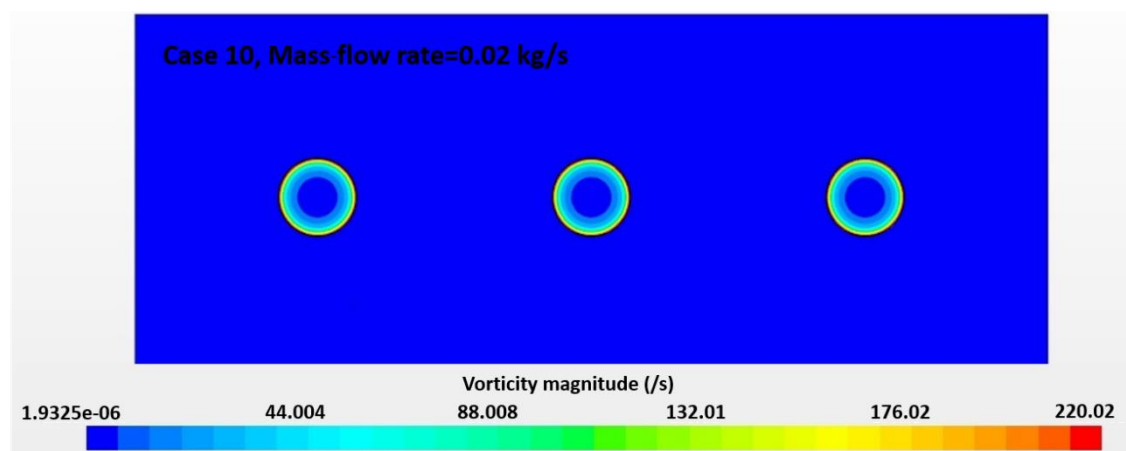


Figure 4-18: Volume averaged vorticity ratios for both melting (GW flow) and freezing (CW flow), compared to a plane pipe (Case 10)

It can be observed that the vorticity fell below one for all the pipes at a higher ‘p’ value, while it usually increased at a higher mass-flow rate. This supports the claim that high ‘p’ corrugations enable lesser turbulence, especially along the outer circumference of the pipe. Turbulence was even lower as the fluid mass decreased, eventually effecting the pressure ratios of Figure 4-16. For the best case 9 (e4.5p30 mm) at a mass-flow rate of 0.02kg/s, the vorticity was compared to a plane pipe and displayed at a cross-sectional plane midway between the inlet and outlet as in Figure 4-19:



a)



b)

Figure 4-19: Vorticity contours for a) (e4.5p30 mm) Case 9 b) (plane pipe) Case 10, at a mass-flow rate of 0.02 kg/s

It was clear that the plane pipe (case 10) had more turbulence, especially closer to the pipe walls. Similarly, the helicity for corrugated pipes was substantially incremented in comparison to plane pipes, as in Figure 4-20:

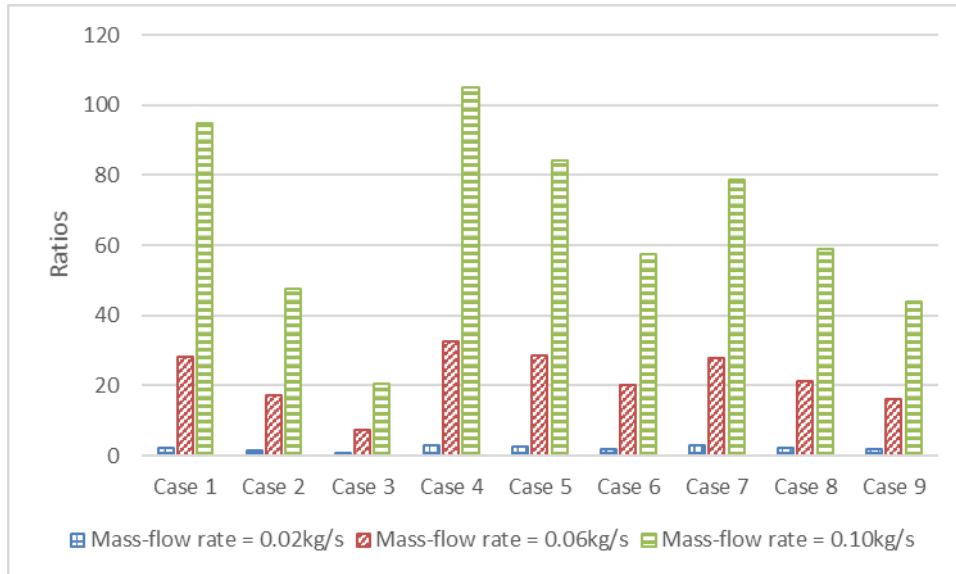


Figure 4-20: Volume averaged helicity ratios for both melting (GW flow) and freezing (CW flow), compared to a plane pipe (Case 10)

The fluid flow in a plane pipe has negligible helicity, since there is no helical movement around the central axis of the flow, therefore an increment as high as a 100 times was recorded in some cases. The helicities were relatively higher at lower ‘p’ values of the corrugated pipe and at higher mass-flow rates. This was due to the method of calculation by the numerical simulation, since more fluid mass per unit length, revolves around the central flow axis for the aforementioned conditions. For this reason, the volume averaged helicity was incremented by only two times for the best case 9 (e4.5p30 mm), at a mass-flow rate of 0.02kg/s. Nevertheless, the helical pathway was clearly visible compared to the plane pipe, as shown in the streamlines of fluid flow in Figure 4-21:

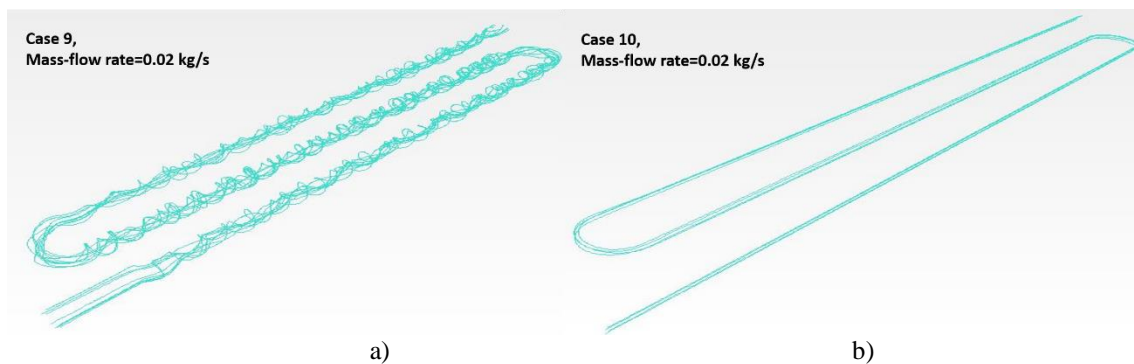
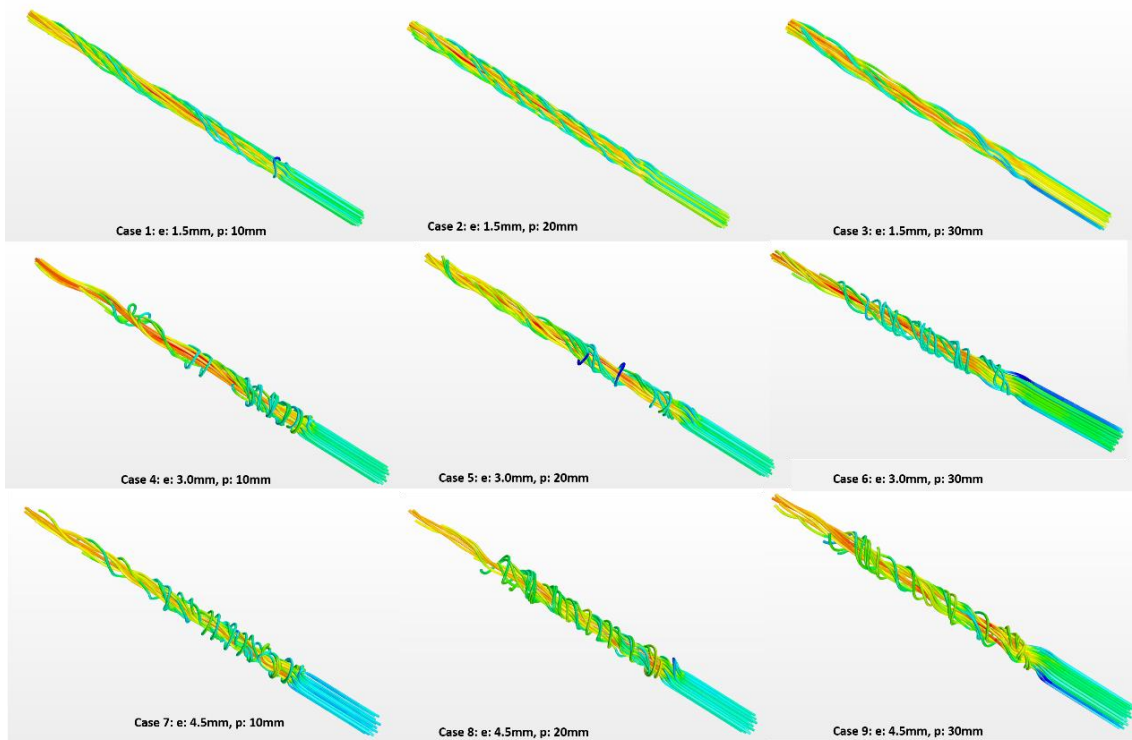


Figure 4-21: Streamlines of the fluid pathway of a) (e4.5p30 mm) Case 9 b) (plane pipe) Case 10, at a mass-flow rate of 0.02 kg/s

These fluid flow streamlines were relatively more helical and smoother at higher mass-flow rates, but could not be completely generated due to computational limitations. However, Figure 4-22 displays the high resolution streamlines of the initial 0.5m of fluid flow for all combinations of the corrugated pipes at a mass-flow rate of 0.1kg/s:



*Figure 4-22: High definition streamlines of the fluid pathway for the first 0.5m of all cases*

It was clear that for a same ‘e’ value, the fluid flow developed helically with an increasing ‘p’ value. Similarly, for a same ‘p’ value, a higher ‘e’ value induced more turbulence in the smooth fluid flow. The effects on fluid flow due to corrugations were least visible at an ‘e’ value of 1.5mm, compared to a value of 4.5mm.

Amongst all the configurations for the best case 9 (e4.5p30 mm), the pressure drop was 120Pa, the ‘f’ was 0.44, the volume averaged vorticity was 35 rotations/s, while the volume averaged helicity was  $1.73\text{m}^2/\text{s}^2$  at a mass-flow rate of 0.02kg/s.

### III. Thermal performance

The fluid flow characteristics directly influence the heat transfer across the pipe walls and eventually the phase change of the PCM.

The ratios of the ‘Nu’ number of the corrugated compared to plane pipes, for both melting and freezing, are in Figure 4-23:

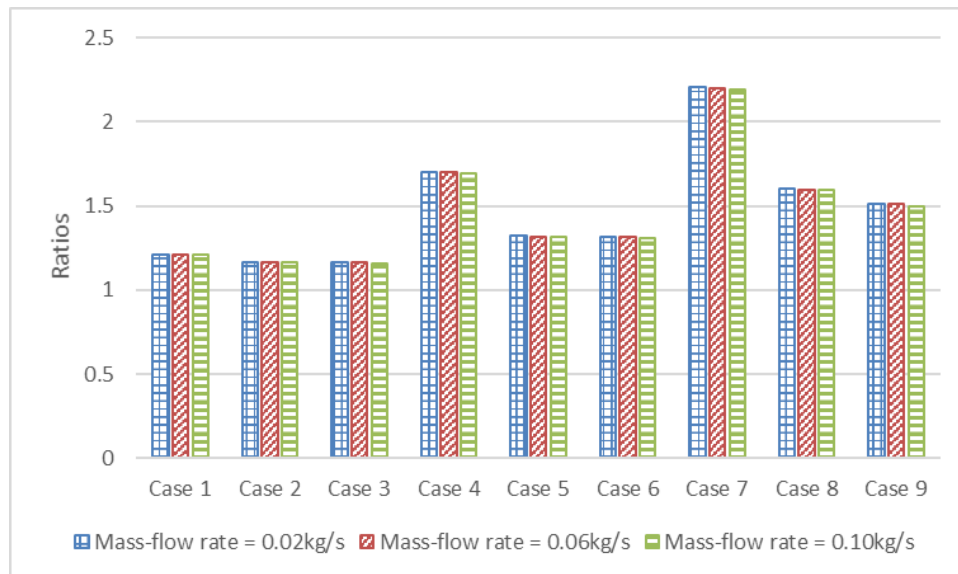


Figure 4-23: Nusselt ‘Nu’ number ratios for both melting (GW flow) and freezing (CW flow), compared to a plane pipe (Case 10)

The ‘Nu’ number ratios were similar for both the melting and freezing processes, due to the fluid flows having the same characteristics, as explained in the last two sections. It was clear that the ratio was independent of the mass-flow rate, as it is a surface and not a flow property. Generally a high ‘e’ value and a low ‘p’ value were preferred in this criteria. The HTC was directly influenced by the ‘Nu’ number, which incorporates both the effects of the helical fluid flow path with the increased surface area of contact to the pipe and the turbulence. Consequently, the HTC, dictates the heat transfer through the pipe walls as in Figure 4-24:

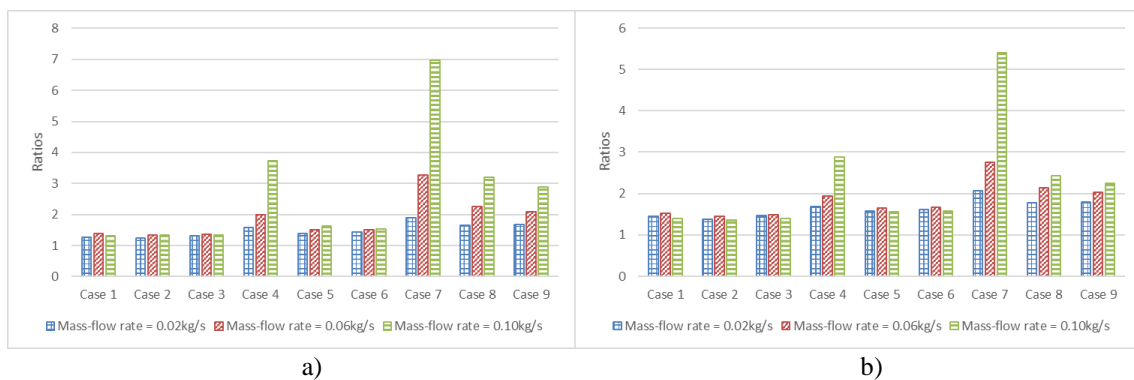


Figure 4-24: Heat transfer ratios at the pipe-fluid interface for a) melting (GW flow) b) freezing (CW flow), compared to a plane pipe (Case 10)

A prominent difference between the melting and freezing processes of Figure 4-24 were the values on the y-axis. On an average, the heat transfer during the freezing process was about 30% less compared to melting. It was observable that the heat transfer relatively increases for lower ‘p’ values. This was because there was more turbulence in these conditions, which also undesirably increments the pressure drops. For this reason, the best TPF-based results were at higher ‘p’ values. Additionally, there was less turbulence at a lower mass-flow rate, resulting in a slightly reduced heat transfer but at a relatively lesser pressure drop penalty compared to higher mass-flow rates, also resulting in better TPF ratings. In terms of heat transfer, case 4 (e3.0p10 mm) and case 7 (e4.5p10 mm) had the best outcomes. However as per the TPF criteria’s, case 9 (e4.5p30 mm) was considered to have the best performance. For case 9 (e4.5p30 mm), the helical path of the fluid flow provided a considerable heat transfer at an acceptable pressure loss. At the same time, more fluid was always in contact with the external circumference of the pipe also increasing heat transfer without a high pressure drop, desirable towards the TPF ratings. The ratios of increment in this surface area of contact compared to plane pipes along with the other geometrical features are presented in Figure 4-25:

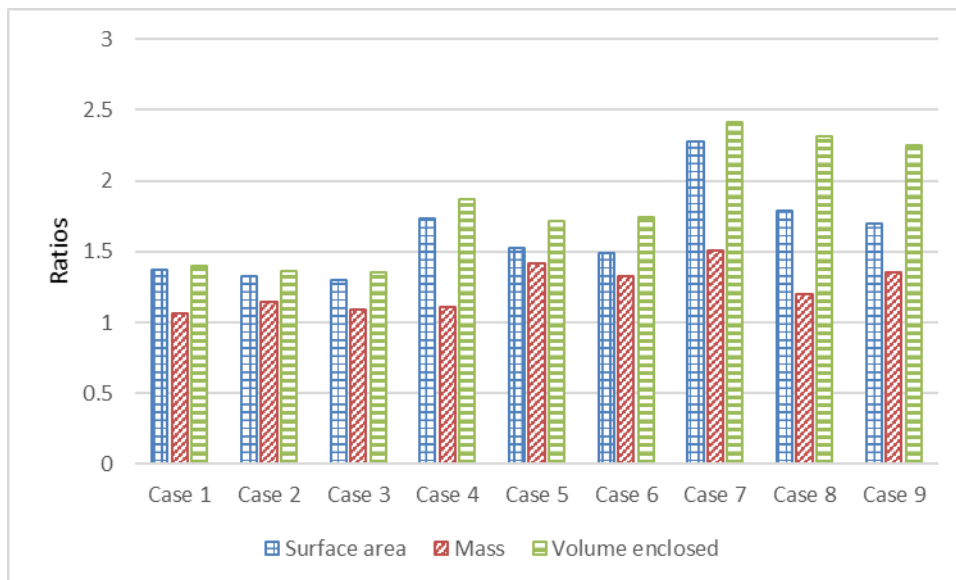


Figure 4-25: Geometrical parameter ratios compared to a plane pipe (Case 10)

Corrugated pipes increase the surface area of contact between the fluid and the pipe by approximately 1-2.3 times, while barely increasing the used mass of the material. This gives a reasonable cost-to-benefit ratio, justifying the usage of corrugated pipes in this

GW heat harnessing application. In general, a fluid flow with a bit of vorticity, a higher amount of helicity along with a greater surface area of contact are the key ingredients for enhanced heat transfer with a minimum pressure drop penalty. The mean outlet temperatures of the fluids for the different combinations are in Figure 4-26:

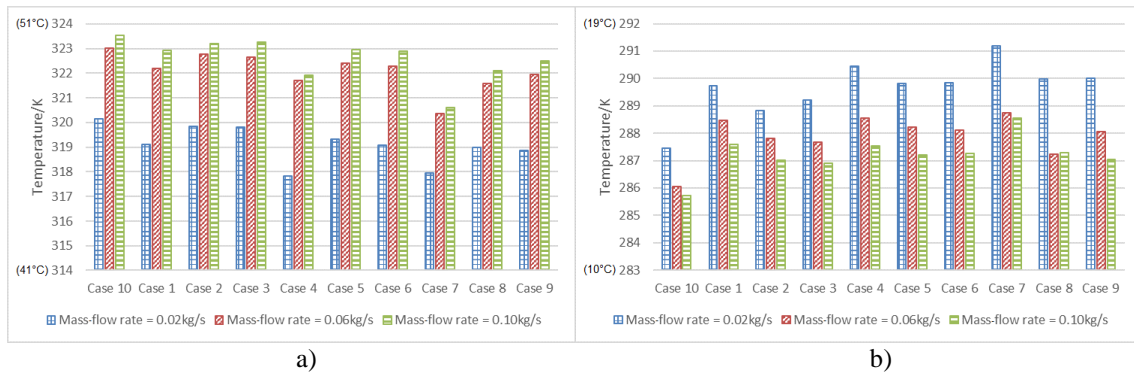


Figure 4-26: Area averaged outlet temperatures for a) GW in melting b) CW in freezing

Compared to the plane pipe, a lower outlet temperature for the GW flow was desirable for melting, as observed in all cases of the corrugated pipes, while the opposite was true in the CW flow for freezing. Amongst the three mass-flow rates, the CW gained the most heat rate for PCM freezing at a lower mass-flow, while the GW lost the most heat for PCM melting. This was because most of the fluid was in contact with the pipe walls at lower mass-flow rates. Consequently, a higher amount of heat was transferred, resulting in larger temperature differentials between the inlet and outlet of the fluid flow. For the best case 9 (e4.5p30 mm), the variation of the mean outlet temperature of the fluids for the 900s time duration compared to a plane pipe are in Figure 4-27:

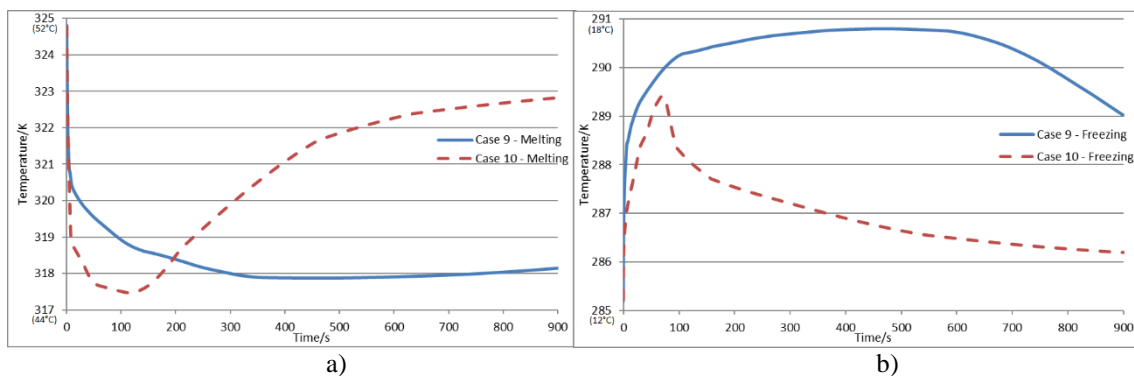


Figure 4-27: Fluid outlet temperature for (e4.5p30 mm) Case 9 and (plane pipe) Case 10, for a) melting (GW flow) b) freezing (CW flow)

The bell-shaped temperature curves of the fluid flows are typical of PCM-based applications. It is primarily due to the variation in values of thermal diffusivity between



the copper pipe and the PCM. In the initial time duration, the temperature differential between the fluid flow and the copper pipe was the highest, resulting in significant heat transfer from the fluid. However, with the passage of time, the temperature of the copper pipe changes rapidly compared to the PCM. The copper transmits heat quickly due to its higher thermal diffusivity which the PCM was unable to propagate due to its lower value. Hence, the copper pipe reaches thermal equilibrium with the fluid flow resulting in the fluid transmitting much less heat with the passage of time. Had the PCM a higher thermal diffusivity, the copper pipe would effectively transmit the heat forward without accumulating it. To illustrate this difference in thermal diffusivity, the temperature contours of the best case 9 (e4.5p30 mm) are compared with the plane pipe (case 10) for both the melting and freezing processes in Figure 4-28:

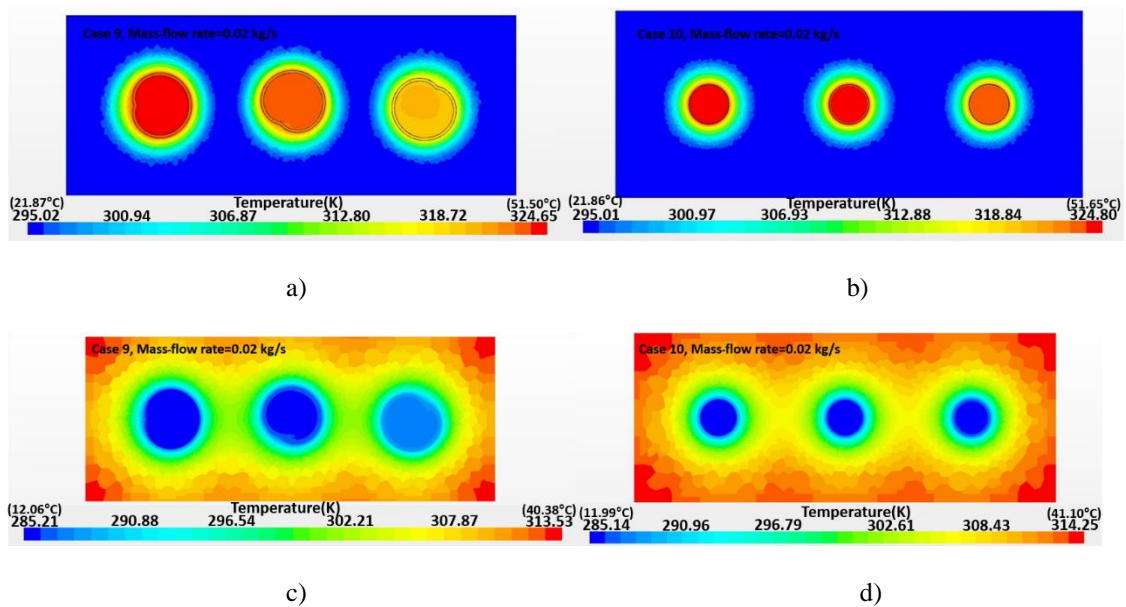


Figure 4-28: Temperature contours for a) melting of (e4.5p30 mm) Case 9 b) melting of (plane pipe) Case 10 c) freezing of Case 9 d) freezing of Case 10, at a mass-flow rate of 0.02 kg/s

After the 900s time duration, it was clear that the temperature of the pipes was almost similar to that of the fluid domain, while the PCM had a much lower temperature. In comparison to melting, corrugated pipes transfer heat much further into the PCM domain compared to plane pipes, resulting in higher melting rates. At the same time, the temperature change of the fluid domain along the three lengths of the pipe was greater for case 9 (e4.5p30 mm) compared to the plane pipe.

Compared to melting the PCM, the propagation of the temperature from the fluid flow was higher for PCM freezing. However, the actual phase changed PCM around the pipes was much less, as freezing is a much slower process with only conduction as the primary mode of heat transfer. To illustrate this fact, the phase change contours for melting and freezing the PCM for case 9 (e4.5p30 mm) compared to plane pipes (case 10) are in Figure 4-29:

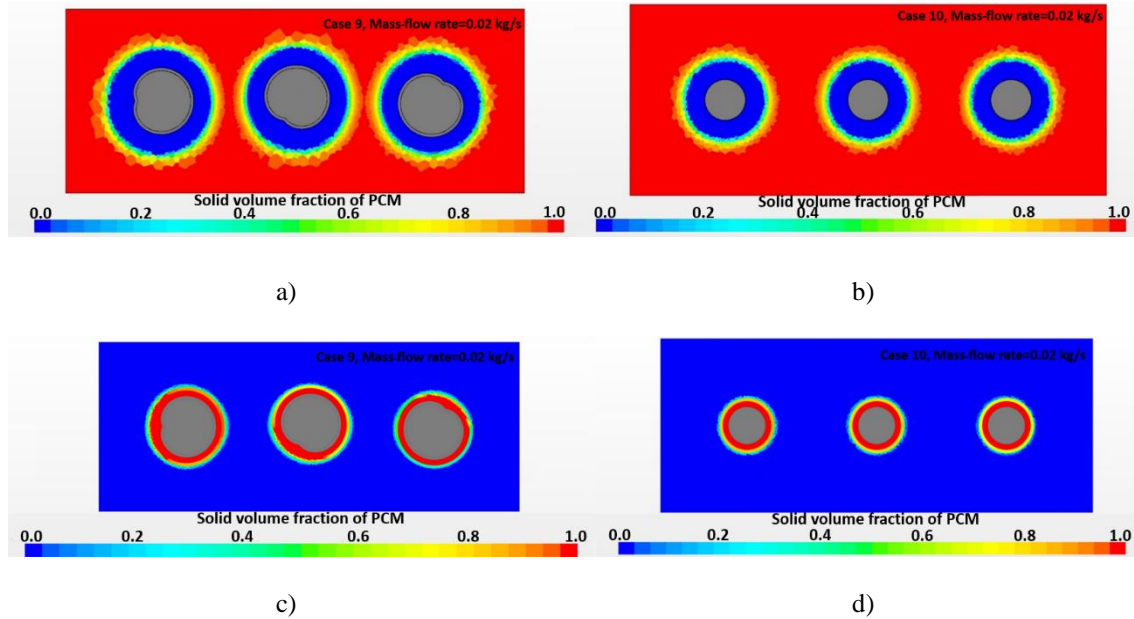


Figure 4-29: Solid volume fractions of a PCM for a) melting of (e4.5p30 mm) Case 9 b) melting of (plane pipe) Case 10 c) freezing of Case 9 d) freezing of Case 10, at a mass-flow rate of 0.02 kg/s

It was clear from the comparison of both melting and freezing, that corrugated pipes have a doubly enhancing effect as there was more phase change compared to plane pipes. For the plane pipe, about 6mm of PCM around the pipe melted with about 10mm for the corrugated pipe. Similarly, for the plane pipe, about 2.4mm of PCM around the pipe froze with about 4mm for the corrugated pipe. Phase change in freezing was about 60-70% less compared to melting in the 900s time duration.

Amongst all the configurations for the best case 9 (e4.5p30 mm), the heat transfer across the pipe wall with the GW flow was about 460kJ, causing 2.1kg of PCM to melt. Similarly, heat transfer with the CW flow was 270kJ causing 0.56kg of PCM to freeze, both at a mass-flow rate of 0.02kg/s.

## 4.6. Outcome

Based on the outcome of the results, the corrugated pipe of case 9 (e4.5p30 mm) was considered the best at a mass-flow rate of 0.1kg/s, as required in this application. A summary of the results of this configuration are in Table 4-6:

Table 4-6: Performance results of the optimal corrugated pipe at a mass-flow rate of 0.1kg/s

	<b>Case 9 (e4.5p30 mm)</b>
<b>TPF1</b>	0.79
<b>TPF2 for melting</b>	3.15
<b>TPF2 for freezing</b>	2.36
<b>Increment in PCM mass melted compared to plane pipes</b>	2.40
<b>Increment in PCM mass frozen compared to plane pipes</b>	2.15

A layout of the optimum corrugated pipe is Figure 4-30:

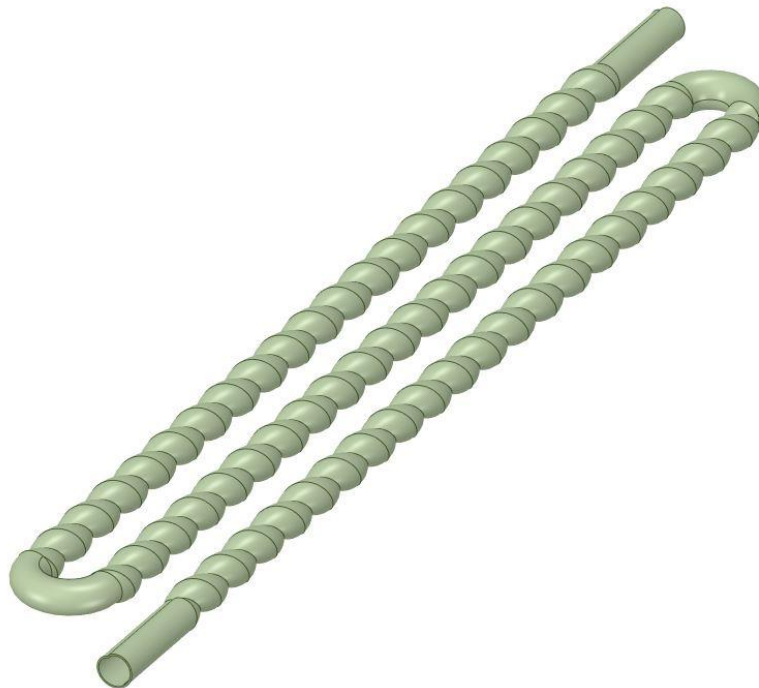


Figure 4-30: Layout of the optimum corrugated pipe with 'e' of 4.5mm and 'p' of 30mm

## Chapter 5 - External heat transfer enhancement

After the selection of RT-25 as the PCM and a corrugated pipe ( $\phi 4.5 \times 30$  mm) as a mode of internal heat transfer enhancement, the next phase was to select an external heat transfer enhancement technique for the PCM, with regard to this application [159]. An obvious result from chapter 4, pointing towards the enhancement of the heat transfer of the PCM, were the low phase change masses (10-30% of the total mass) for both melting and freezing. The next phases in the design were detailed experimental and numerical analysis followed by a sensitivity analysis.

### 5.1. Overview

PCMs have a long history of passively reducing the energy demand in buildings [160]. Although the concept has gained considerable momentum over the last decades, the principal obstacle is the slow rate of heat transfer [161,162]. A high rate within the PCM was important in this application due to the large flow impulse of GW. The GW has a relatively high mass-flow rate over a short duration of time. There are three main techniques of enhancement in the heat transfer rate of a PCM, amongst which the usage of macro-structured fins is the most common, especially in applications of passive heat transfer from fluids [163,164].

Al-Abidi et al. [165], experimentally investigated the usage of longitudinal fins in a concentric pipe HE filled with PCM in the centre, for a liquid desiccant air-conditioning unit. Based on a comparison with a similar configuration without the four longitudinal fins, the melting time was reduced by 40%. Solomon et al. [134], experimentally investigated the effects of adding eight longitudinal fins during the freezing of a PCM in a cylindrical HE in order to select the optimum fin height. A reduction in the freezing time of up to 17.6% was achieved with longer fin heights having an outreach to the extreme ends of the container of the HE. Similarly, enhancement with fins was more effective in turbulent flows of the heat transfer fluid (HTF) compared to laminar flow regimes. In a case study [155], the PCM melting was ten times faster with turbulent flow and the disparity in the temperature of the PCM was reduced from 15K to 6K in comparison to laminar flow. Acir et al. [133], performed an analysis of the melting of a

PCM using different numbers of fins in a laboratory experiment with artificial solar radiation. It was found that enhancement in melting time was proportional to the number and inversely proportional to the thickness of the fins. Gil et al. [166], conducted an experimental study on a large-scale tank filled with the PCM 'hydroquinone' with 196 square shaped fins. It was concluded that compared to an arrangement without fins, the effective thermal conductivity increased by 4.11- 25.83% depending on the input energy of the HTF. Laing et al. [167], successfully designed radial fins for usage in a large 700kWh PCM storage unit. The operation of this unit was assessed with various flow rates, pressure and operation conditions of the HTF. It was put forward that the fin design process is subject to continuous optimisation in an iterative manner, both in terms of performance and cost. Hosseini et al. [157], numerically studied the variation in angles of installation between longitudinal fins for the melting of RT-35, with a HTF in laminar flow at 333K (59.85°C). In this triple fin arrangement, angles of 120° with two fins on the lower side of the pipe reduced the melting time by 22.5%. Since natural convection originated from the bottom of the container to move upwards, the upper fin had the least impact on enhancing the melting time. Rudonja et al. [168], numerically investigated enhancement in the heat transfer rate of a cylinder shaped HE filled with paraffin and with longitudinal copper fins. A unique geometric parameter termed the surface ratio was introduced for the fins being inversely proportional to the melting time. In a unique study [169], a Layered Thermal Resistance model was developed to simulate multi-dimensional fins in a PCM. This model can help design an optimal fin arrangement based on the tuning curve/surface, geometry and shape of the layout with the possibility of being integrated in various optimisation algorithms, unlike typical CFD softwares. Sharifi et al. [153], developed a transient numerical model along with analytical correlations to analyse the influence of the number, dimensions and thickness of horizontal plate fins, on the melting of a 2D rectangular PCM HE. The incorporation of fins accelerated melting with the rate being proportional to the number and length of the fins, whilst the thickness had the least influence. Since it is an established fact that fin inclusions enhance the heat transfer rate in a PCM, analysing the effects of a variable sized fin arrangement would be interesting. Based on this research gap, Ji et al. [170], numerically investigated the improvement of a double fin variable length arrangement in internal fluid flow, with a transient simulation. Two unequal parallel horizontal fins were analysed in the melting of RT-42 stored in a rectangular container with a plate heater. A shorter upper with a longer lower

fin was the optimum solution in terms of buoyancy driven natural convection, reducing the melting time by 25%. Abujas et al. [171], numerically simulated melting in a PCM in a 2D model of a tree-shaped branched fin having different materials. It was designed to ensure phase change towards the furthest parts of the HE container, along with a uniform temperature distribution. It was concluded that aluminium fins gave a 20% reduction in melt times to outperform carbon steel fins. The performance was proportional to the amount of fin material used until an optimum saturation point, after which an increment of fin branches produced no additional improvement. At the same time, opening a new branch on this fin tree was better than thickening an existing one. Tiari et al. [172], investigated the thermal response and natural convection movement within a PCM that had different geometric configurations of a finned heat pipe in a 2D transient melting simulation. Results showed a direct correlation between the number of heat pipes and the melting rate, whilst the fins ensured a uniform temperature distribution within the PCM. Additionally, numerical simulations of heat pipes are comparatively complex due to the multiple combinations of physical phenomena.

Most finned-PCM based research has conflicting outcomes in terms of the effects of fin dimensions, thickness and pitch [153,173]. The diversity of this research reveals that it was hard to draw a direct hypothesis, as every application of fins in a PCM requires a custom designed solution [174]. Most studies in the domain of finned-PCMs can either be classified as experimental or numerical [174]. However, numerical simulations do not give realistic results unless a practical experimental model is used for validation [166]. Most research reporting the usage of fins with PCMs is primarily limited to solar energy storage, passive heat transfer in buildings, air-conditioning, refrigeration, electronic cooling, industrial waste heat recovery and smart textile manufacturing applications [157,170,172]. Studies have been conducted for passively using PCMs in common building applications for various climatic zones in the world [175]. However, most work is limited to only space heating, cooling and air-conditioning applications [176]. Additionally, most of the work, emphasises either the melting or freezing of the PCM with either a laminar or turbulent HTF flow [177].

Assessing both aspects of melting and freezing in an organic PCM with fins in a thermal recovery application of non-industrial GW was a research gap and a novel idea, which was to be investigated. A detailed experimental study was performed of a complete HE,

using a dual-purpose single fin arranged on two different pipes to harness waste heat from GW as the HTF to be transferred to CW as the heat absorbing fluid (HAF), linked with a PCM. The fins had to be designed as per the application, in a study [155], as an improper configuration led to an enhancement of only two times compared to a non-finned design, with a low cost-to-benefit ratio. Upon validation of a numerical simulation based on the experimental model, the optimum fin configuration for this application was selected based on a sensitivity analysis. The parameter for optimisation in most numerical studies is the phase change time. However, for this application, optimisation with respect to a complete PCM phase change for both melting and freezing in the 900s time duration was to be achieved [3]. General correlations of the performance of fins in PCM applications have not been established until now, partly because natural convection in finned-PCM designs is highly dependent on the geometrical layout being difficult to mathematically predict [153]. This stresses the need for a numerical study for this application, to gain a detailed insight into the performance in order to formulate empirical correlations.

This phase of the research has the following objectives:

- A basic review of external heat transfer enhancement techniques in PCMs outlining the reasons for selecting fins for this application.
- Conducting an experiment for a specific finned-PCM HE with the prescribed boundary conditions of GW heat harnessing and performing a sensitivity analysis of the parameters.
- Development of a numerical simulation of the model, to be validated by experimental data.
- Performing a sensitivity analysis to investigate the effects of fin dimensions on the phase change behaviour of the PCM, for both melting and freezing.
- Selecting an optimum finned configuration to be used in this application based on the outcome of the results.

## 5.2. Heat transfer enhancement techniques for PCMs

The heat transfer rate of a PCM can be increased by enhancing its thermal conductivity, the surface area of contact or the temperature difference between the PCM and the HTF/HAF as per the following equation [161]:

$$Q = UA\Delta T \quad (5-1)$$

The various techniques based on these three methods are presented in Figure 5-1:

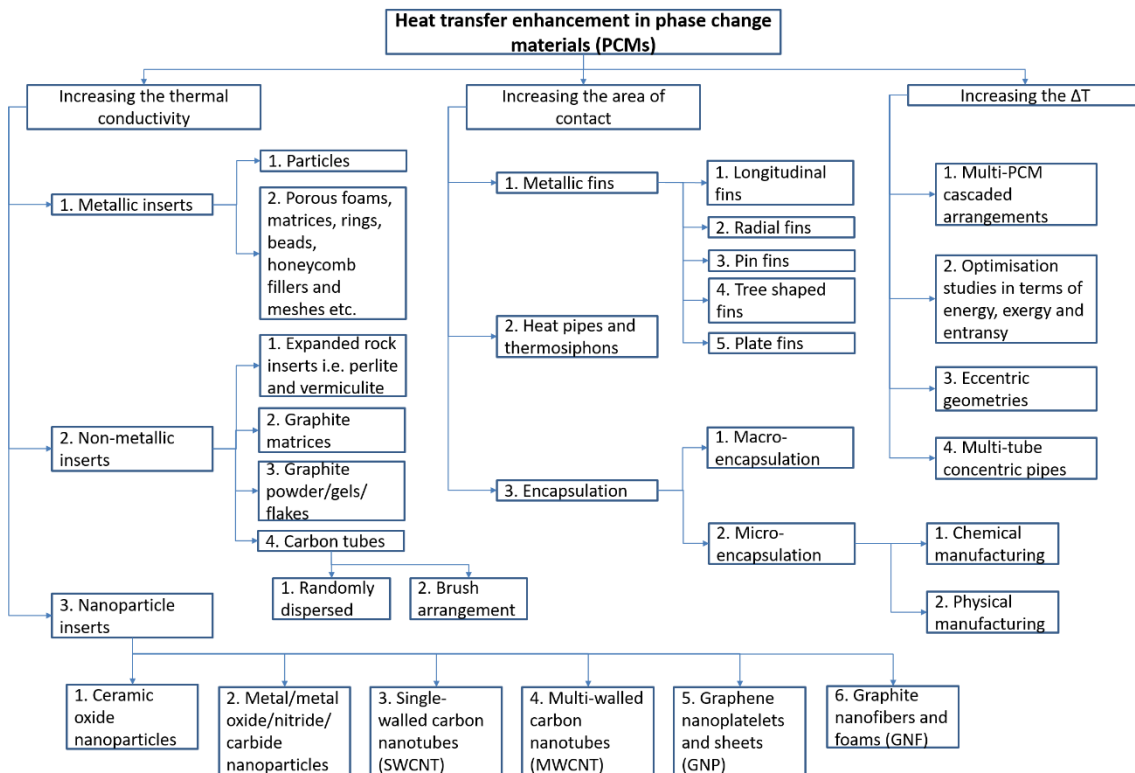


Figure 5-1: Techniques to enhance heat transfer in PCMs

An overview of each of these techniques is presented:

### 5.2.1. Thermal conductivity

In this technique, inserts with a higher thermal conductivity compared to the PCM are embedded into it. This offers a low resistance conductive heat flow path penetrating



deep into the PCM, to minimise excessive heating/cooling of the PCM layer only adjacent to the HTF/HAF [121].

The most commonly used metallic inserts include aluminium, copper, steel and nickel [161]. However, copper is the most effective and is known to have enhanced the thermal conductivity of organic PCMs by 80% compared to the other metal inserts [132]. At the same time, metallic structural inserts are more common than particle inserts. Metallic foams can be in the form of a wired matrix structure, rings, composite discs or meshes [155]. The PCM is contained in the open cells or the pores of the metallic structure. Initially, the heat conducts rapidly through the structure and then diffuses slowly through each pore in the PCM [121]. The structures can be closed cell in the form of pockets or open cell with an interconnected network [178]. Copper foams with 1mm spacing between the pores, having an 88% porosity, have recorded effective thermal conductivities increments in a PCM of up to 16W/(m.K) [121]. Wang et al. [179], numerically demonstrated that using a paraffin-based PCM in a copper metal foam reduced the melting time by 40%. However, metallic structural inserts occupy considerable space, reducing the latent heat capacity and volume of the PCM by as much as 80% [171]. Most present research within this domain is focused on increasing porosity ratios and the chemical stability of the structure [171].

Non-metallic inserts are comparatively more common, having versatile configurations. Expanded rock inserts are rarely used due to their lower conductivity but are an option to increase mechanical strength. On the other hand, graphite and carbon inserts are famous due to their lightness and higher thermal conductivity, along with having a high porosity [171]. These inserts are usually in the form of powders, flakes, tubes, fibres or foams. Expanded natural graphite (ENG) powder is commonly dissolved into liquid PCM below the saturation limit, to avoid separation during the melting and freezing [171]. Graphite aerogels and tubes of single layer known as graphene have a thermal conductivity as high as 400-5,300W/(m.K). Typically, the volume fraction of inserts is between 2-5%, beyond which the loss in heat capacity outweighs the benefit of increased thermal conductivity. On the other hand, carbon-based graphite tubes and fibres are also known as a good solution. A 10% inclusion of graphite can increase the thermal conductivity of a PCM by four times and reduce the melting time by 32% whilst only reducing the thermal storage capacity by 9% [121]. The orientation of the

tubes significantly effects performance as the brush type configuration increases effective thermal conductivity by three times that of randomly dispersed tubes [121]. Contrary to metallic foams, the use of non-metallic foams is far less common. Carefully designing and controlling the impregnation process of a non-metallic foam during manufacturing is essential. Compared to metallic foams, infiltration into the pores of graphite foams is 53-81% less [121]. Typically, a vacuum oven is needed to remove the air within the foam before filling the PCM. However, graphene matrixes improve conductivity by thirteen times with only a 2-5% loss in the volume and thermal storage capacity. Most research in this domain is focused on improvements in terms of manufacturing, PCM embedding, mechanical stability and economics [132].

With improvements in technology, nanomaterial additives are the fastest growing research domain in terms of enhancement, especially macro structured matrixes with nano-sized walls providing a better surface area to volume ratio with mechanical stability compared to nanofibers and particles [180]. Nanoparticle inserts are common both in terms of metals and non-metals. To avoid complex manufacturing processes, metal nanoparticle additives are an alternative to non-metallic particles. The biggest concern is the increase in mass fraction since metallic particles have a higher density. Addition beyond a mass fraction of 0.5 is not recommended, whilst lower mass fractions have resulted in 60% less melting times of PCMs [132]. Silver and copper nanoparticles are abundantly used, being cheaply available, lighter and less prone to oxidation [180]. Although metal oxide nanoparticles have lower thermal conductivities, they are chemically less prone to corrosion, more stable and comparatively cheap to produce [180]. In terms of non-metals, Multi Walled Carbon Nano Tubes (MWCNT) are the most widely used with enhancements in thermal conductivity of up to 65% [161]. The increase in thermal conductivity of the PCM is linear with the loading level of these inserts. More than 35% enhancement has been recorded with only a 2% loading level [121]. Atomic lattice vibrations enable conduction through the material to effectively transfer heat, proportional to the density of particles. As the PCM composition is altered in case of particle insertions, a composite structure is formed [161]. Most research within this domain is focused on manufacturing and effectively embedding the particles into the PCM.

### 5.2.2. Area of contact

Insertion of metallic fins, heat pipes and the encapsulation of the PCM are long-known methods to increase the heat transfer area of the PCM, resulting in better thermal performance [121].

Fins are the most common enhancement technique for industrial HEs [171]. In PCM applications, the shape, position and spacing between the fins are the most critical parameters. Fins separate the PCM mass into thinner volumes, making the diffusion of heat easier and are recommended for liquid HTF/HAFs [121]. Thin fins considerably increase the PCM's surface area of contact, while negligibly incrementing the volume occupied. For shell and tube HEs, longitudinal and radial fins are preferred. Pin and plate type fins are more suited for electronic components with flat plate bases acting as heat sinks [173]. Tree shaped fins are difficult to manufacture and are rarely used. For better performance and compatibility, the HTF/HAF pipe and fin material should be similar, although different materials have been used [167].

Heat pipes can transfer larger amounts of heat over longer distances compared to fins with a small temperature drop through their length [172]. In a heat pipe, a working fluid undergoes a cycle of a phase transition to transfer latent heat [181]. The most common heat pipes in PCM applications have copper casings, with water as the working fluid [182]. The evaporator to condenser length ratio, along with the manufacturing of the working fluid, influence the operation and must be optimally designed for each application [183]. Compared to a simple copper rod, a heat pipe with similar dimensions has a ninety times greater thermal conductivity [172]. Robak et al. [182], reduced the melting rate of a PCM by 70% whilst doubling the freezing rates with the inclusion of thermosiphons. Sharifi et al. [183], investigated the effects of a novel heat pipe metal foil hybrid on both the melting and freezing of a PCM. With a 1% by volume ratio of the foil and heat pipe, the phase change rate of a PCM, increased by approximately 200-300%.

PCM encapsulation with a high thermal conductivity coating material in the order of millimetres is termed macro, whilst micro/nano scaled coating is termed micro-

encapsulation. The most common macro-encapsulation in building applications is in rectangular metallic boxes [121]. Although spherical encapsulation has the advantage of a larger surface area to volume ratio, it is harder to manufacture with PCM leakage issues. Whilst manufacturing, it is important to partially fill the encapsulation shell to allow for variations in volume of the solid and liquid phases of the PCM [171]. For organic PCMs, stainless steel is the most corrosion-resistant coating material. Thin plastic film packaging can also be used for encapsulation when structural strength is not an issue. Thin film plastics eliminate ullage concerns since the material is flexible, but the risk of rupture, abrasion and ageing reduce their long-term usage. Based on the literature [132], it is found that spherical capsules of 2mm with a coating thickness of 0.2mm have the best thermal performance. Typically, micro-encapsulation has small spherical polymeric shells with PCM cores [161]. The shell can be made with both synthetic and natural polymers [164], being physically or chemically manufactured [132]. Physical methods include air-suspension coating, vibration nozzles and spray drying. Chemical methods are based on different forms of polymerisation including interfacial, suspension and emulsion polymerisation. Chemical methods provide uniform coating; however they are more expensive. The prime variable in designing is the core to coating ratio, as with too high a value, the coating strength deteriorates with PCM leakage [132]. Micro-encapsulated PCMs are used in the fabrication of wallboards, concrete, roofing materials and even fabrics [121]. Encapsulation makes PCM usage possible in environments with close human contact including buildings, food storage and medical applications, since raw organic PCMs can be inflammable [132]. Recently, research into ceramic encapsulation has been demonstrated with promising results [161].

### **5.2.3. Flow conditions**

Optimisation in flow conditions is usually used in conjunction with the two aforementioned enhancement techniques.

The most common technique is using PCMs in multiple cascaded arrangements. In this technique, multiple PCMs with sequentially decreasing melt temperatures are arranged along the flow length of the HTF pipe. This maintains a consistent  $\Delta T$  between the flowing fluid and the PCM melt temperature. Consequently, it provides a consistent

heat flux eventually incrementing the overall heat transfer, as most energy transfer to the PCMs is latent instead of sensible. Normally, cascaded combinations of PCMs are macro-encapsulated to avoid mixing and leakages [171], with the HTF/HAF pipes in a counter-flow arrangement. The most commonly used number of PCMs in such an arrangement is three, as enhancement beyond this number has a low cost-to-benefit ratio [161]. In an experimental setup of such an arrangement [132], three commercial PCMs were used with a descending melt temperature between 337-317K (63.85-43.85°C). The heat transfer rate was enhanced by 10-15% of a single PCM. The selection of the PCM melt temperatures along, with their mass ratios, is a common research domain [161].

At the same time, optimisation studies in terms of energy, exergy and entransy are common with the aim of providing a uniform  $\Delta T$  between the fluid flow and the PCM melt temperature [161]. An entransy dissipation is useful to characterise the ability to transfer heat irreversibly, whilst an exergy analysis is useful to characterise the total potential of the transfer.

Eccentric geometries aim to provide an optimum positioning of the HTF/HAF pipes relative to each other and the PCM container to maximise heat transfer [178]. These configurations are especially useful during melting as they intensify natural convection [173]. In a study [178], an eccentric arrangement of a HTF pipe embedded in a concentric PCM container reduced the melt time by 67% compared to a simple arrangement. Similarly, the orientation of flow and the use of multi-tube arrangements can enhance heat transfer in a HE with simple designs. An inclined HTF flow arrangement in a multi-tube concentric pipe within a PCM improved the PCM melting time by 35-53% [178].

An overview of the advantages and disadvantages of each enhancement technique are presented in Table 5-1:

Table 5-1: Summary of the techniques of heat transfer enhancement of PCMs

	<b>Technique</b>	<b>Pros</b>	<b>Cons</b>
<b>1</b>	Metallic inserts	Enhances the thermal response and diffusivity of the PCM along with providing mechanical rigidity. Conduction heat transfer is enhanced improving both PCM freezing and melting [121]. During freezing, these inserts minimise temperature variations in the PCM making it more uniform.	Metallic inserts are prone to oxidation and corrosion with limited chemical and thermal stability in the long term. Not all inserts are compatible with every PCM [132]. The PCM volume change from solid to liquid can destroy foams and matrices or separate the inserts, making a heterogeneous mixture with a loss in contact [155]. Voids in the pores of structures is an operational concern [171]. Metal foam PCMs are prone to sub-cooling due to increased air bubbles in the pores causing flow resistance [178]. Metallic inserts are not suitable with piped HEs as they cause misalignment, holes and dilatation due to the circular geometry of the pipe [171]. Has maintenance issues over the long term with high costs. Dense foams have a haphazard structure, giving the PCM a non-uniform melt temperature and thermal properties whilst hampering natural convection [179]. Has the least enhancement in surface area to volume ratios.
<b>2</b>	Non-metallic inserts	Typically are corrosion resistant and robust. Have extremely high effective thermal conductivities even along the length of the fibre with values of about 220 W/(m.K). Lightness due to their low density and a high porosity [171]. Also, conduction dominating resulting in improvements in freezing as well. The increment in surface area to volume ratio is high.	It lacks mechanical and thermal stability over the long-term. Complete PCM infiltration is not possible with unoccupied pores and air traps making it a heterogeneous mixture with non-uniform temperature distributions. Comparatively higher manufacturing, operational and maintenance costs [132]. Carefully designing and controlling the impregnation process in manufacturing is essential [121]. Also hampers natural convection in the PCM.
<b>3</b>	Nanoparticle inserts	The increase in conduction offsets the reduction in convection heat transfer, which is desirable for short time durations. Minimal reduction in the latent heat capacity with the	Greatly enhances melting with little improvements in freezing [180]. Nanoparticles separate from the core PCM when melting into big agglomerated clusters

		maximum increment in thermal conductivity. High thermal conductivities in the range of 300-3,000 W/(m.K) with the best surface area to volume ratios [180].	resulting in low freezing enhancement [132]. In the long-term, nanoparticles deposit to the bottom of the container due to gravity and density differences of the PCM [168]. Lack of thermal, mechanical and chemical stability over the long-term [132]. Manufacturing and maintenance is complex as well as expensive.
4	Metallic fins	Conduction dominated, hence improves PCM freezing along with melting [121]. Fins promote rapid conduction bringing much quicker natural convection in melting. Has the best increment in effective thermal conductivity with the least loss in latent heat capacity. Provides a homogenous and consistent temperature distribution without altering the bulk PCM structure [171]. No mechanical or thermal stability concerns over the long term. Simplest and most economical technique, being the easiest to design, fabricate, install and maintain along with providing a compact solution [171,173]. Can easily be coupled in hybrid with insertion techniques.	Corrosion issues of the fin material if not compatible with the PCM [167]. The surface area to volume ratio increment in heat transfer is comparatively lesser than other techniques.
5	Heat pipes and thermosiphons	Potential to transfer large amounts of heat over longer distances with a small temperature drop through its length [172]. Transfer of latent heat of the working fluid instead of low density sensible heat [181]. Is mechanically and thermally stable over the long term. Minimal interference in the core PCM structure providing a homogenous structure, without impeding natural convection. Enhances heat transfer in both freezing and melting. Can easily be coupled in hybrid with insertion techniques [183].	Chemical stability of the heat pipe casing with the PCM is an issue. Not suitable for piped HEs as the versatility in application usage is limited [182]. Expensive manufacturing and maintenance. Operationally it is not reliable with PCMs, as the heat fluxes in the condenser and evaporator of the heat pipe vary with time. Start-up from ambient conditions takes at least a few minutes [172]. Occupies considerable volume thereby decreasing the latent heat capacity of the PCM. Has the least surface area to volume enhancement ratio.
6	Encapsulation	Encapsulation makes PCM usage possible in environments with close human contact including buildings, food storage and medical applications, since raw organic PCMs can be inflammable [132]. Direct contact of the HTF/HAF with the PCM is also possible without contamination and leakage	Volume expansion management in the encapsulated core due to ullage compensation limits the operating conditions [164]. The shell chemically degrades, is vulnerable to mechanical stress and extreme conditions [171]. It also absorbs moisture and gets contaminated

		<p>issues [171]. Lightweight and cheap at a macro-level [132]. Microencapsulation has the highest surface area to volume ratio amongst all techniques. Has a homogenous bulk structure with uniform thermo-physical properties.</p>	<p>over the long-term [132]. Typically, the thermal stability is limited to 200-5,000 cycles only. A uniform non-porous polymeric shell makes manufacturing expensive, especially at micro-level chemical encapsulation [161]. Has the greatest reduction in latent heat capacity of the PCM. Enhances only conduction heat transfer with natural bulk convection almost eliminated, being more beneficial in freezing.</p>
--	--	---	---



### 5.3. Rationale for fin usage

Numerous hybrid combinations of enhancement techniques have been reported with the most common being metallic inserts combined with nanomaterial composite-PCMs [132,161]. At the same time, finned-heat pipes have proven to be more effective as well [161]. Additionally, strategies to enhance flow conditions are typically combined with the other enhancement techniques.

A comparative analysis between the different enhancement techniques is difficult since the mass and thermal properties of the PCM vary with each technique, while the performance is also application-specific [155]. Nevertheless, fins were used to enhance the PCM heat transfer rate in this application because:

- Particle inserts, especially graphite and nanoparticles, are known to be the best area enhancement techniques [171]. In a comparative study [155], a graphite matrix was the best with a heat transfer enhancement of eight times at a cost increment of only about 30%, followed by graphite powder with three times and fins with two times, compared to a simple PCM configuration. However, particle inserts lack long term mechanical and thermal stability, especially in geometries involving a pipe, having misalignment issues. They result in the PCM having a heterogeneous structure with uneven thermal characteristics. At the same time, their manufacturing and operational costs are high with regular maintenance requirements in indoor building environments, not suitable for this passive application.
- Although heat pipes are known to have a superior enhancement compared to fins, they are unsuitable for this application. Usually, vertical heat pipes are connected to plate sinks in electronic applications providing a constant heat flux with operational stability [184–186]. In this application with a pipe flow, the circular cross-section made thermal contact of the copper pipe with the heat pipe difficult. Even circular looped heat pipes were unable to perform consistently due to the transient input heat fluxes. Since this application has a high heat impulse with a short time duration, heat pipes would also be unsuitable as they require a start-up time to operate. Additionally, heat pipes increment both the

manufacturing and operational costs by manifolds, making them unsuitable for this application.

- Although encapsulated PCM would advocate in favour of this application due to compatibility in indoor applications, they considerably reduce the latent heat storage capacity of the PCM. At the same time, they lack long term thermal, mechanical and chemical stability. Their operational limitations and void management concerns were unsuitable in this application whilst making them expensive and not so compact.

Fins are superior to all the other methods in terms of the long-term mechanical, thermal and chemical stability, especially in this application's piped shell-tube type HEs [169]. At the same time, fins enhance both the melting and freezing of the PCM since they are conduction dominated, as required by this high impulse application. Long fins are the best approach to minimise non-phase changed patches along the outer edges of a HE [171]. They are the least expensive with the greatest cost-to-benefit ratio, along with being reliable, compact and easiest to install [171]. Copper fins are known to perform the best in paraffin PCM applications with the least corrosion [153].

## 5.4. Experimental model

### 5.4.1. Equipment

Expanding on the experimental setup of section 4.4, an open circuit for incoming CW and a complete HE were installed [156]. The closed circuit GW and the open circuit CW flow arrangements are observable in Figure 5-2:

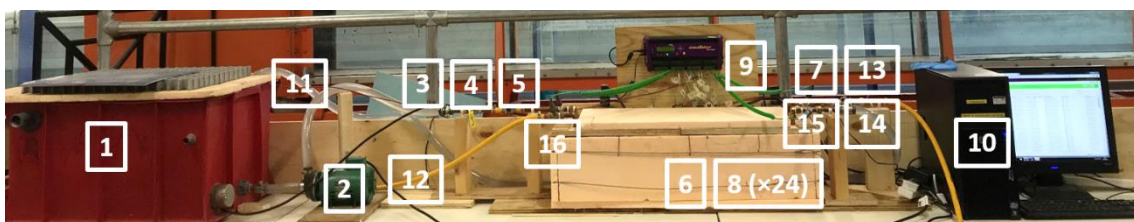


Figure 5-2: Experimental test rig to assess the HE with fins

The storage tank (1) had a supply of conventional GW, with an ohmic rod heater embedded in it. It was connected to a centrifugal pump (2) which in turn was linked to a globe valve (3) to control the flow rate of the fluid. The circuit then consisted of a flow meter (4) followed by a probe-type thermocouple (5) to record the inlet conditions of the GW. This circuit was connected to the HE (6) followed by another probe-type thermocouple to measure the GW outlet temperature (7). Within the HE, twenty-four point-type thermocouples (8) were arranged on the fins and within the PCM to measure the conditions. The GW then flowed back to the tank through the plastic pipe in a closed circuit (11). Similarly, the CW came from a conventional building tap into a globe valve (13) followed by a flow meter (14) and a probe-type thermocouple (15) to record the inlet conditions. It was then routed through the HE (6) in a counter-flow arrangement with the GW, following an outlet probe-type thermocouple (16) before going down a drain through the yellow plastic pipe in this open circuit (12). The lid of the HE was removable for better internal visualisation. All twenty-eight thermocouples were connected to a data logger (9) which in turn stored the instrument readings every 10s in a desktop computer (10). Compared to the 5s readings in section 4.4, the amount of data was much larger, resulting in the 10s interval readings. A labelled schematic with the same numbering arrangement is presented in Figure 5-3:

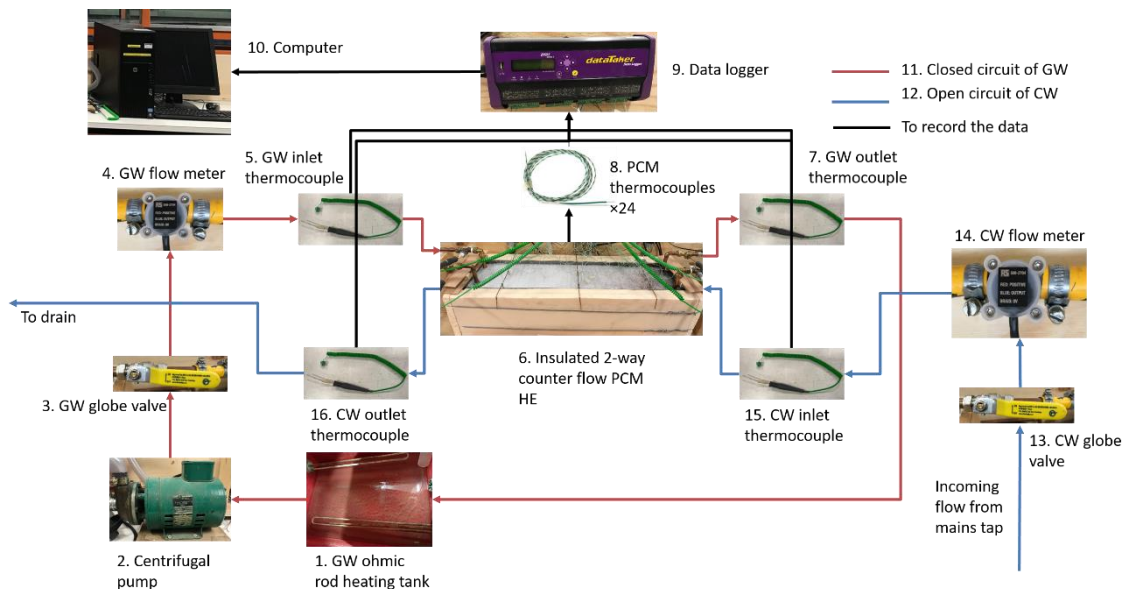


Figure 5-3: Schematic of the experimental setup to assess the HE with fins

The specifications of the auxiliary equipment remained the same as in Table 4-3. The boundary temperatures of the GW (325K or 51.85°C) and CW (285K or 11.85°C) were as specified in section 2.5. Counter-flow copper pipes were embedded in a PCM filled HE with a mild steel container enclosed with insulating Styrofoam.

It is an established fact that the thermal performance of counter-flow fluid pipes is superior in comparison to parallel-flow arrangements [143]. In the past, plumbing systems in buildings were made with metals including copper, cast iron or even lead. Nowadays, PVC plastic piping is sufficiently cheap for usage within conventional buildings. However, their thermal conductivity is quite low. Hence, as in section 4.4, copper with a high thermal conductivity was used as the material for both the GW and CW pipes. In section 4.6, an optimum corrugated pipe was selected with regard to this application. However, due to manufacturing limitations, the design could not be integrated with fins in a laboratory [156]. For this reason, a plane pipe was used in this experimental setup, whilst the corrugated pipe design was used for the analysis in the numerical simulation. Thin pipes (1mm) of 12.7mm diameter were used, although as mentioned in section 4.4, typical sanitary pipes are 25mm. A reducer could easily be used for adjustment when practically connecting the HE to an appliance.

The main piping sections of both the GW and CW were identical with two welded U-bends and reducers, as depicted in Figure 5-4:



Figure 5-4: Layout of the copper pipe of the GW and CW flows with a 12.7mm diameter

Both the pipes were vertically cascaded upon each other in a counter-flow arrangement as in Figure 5-5:

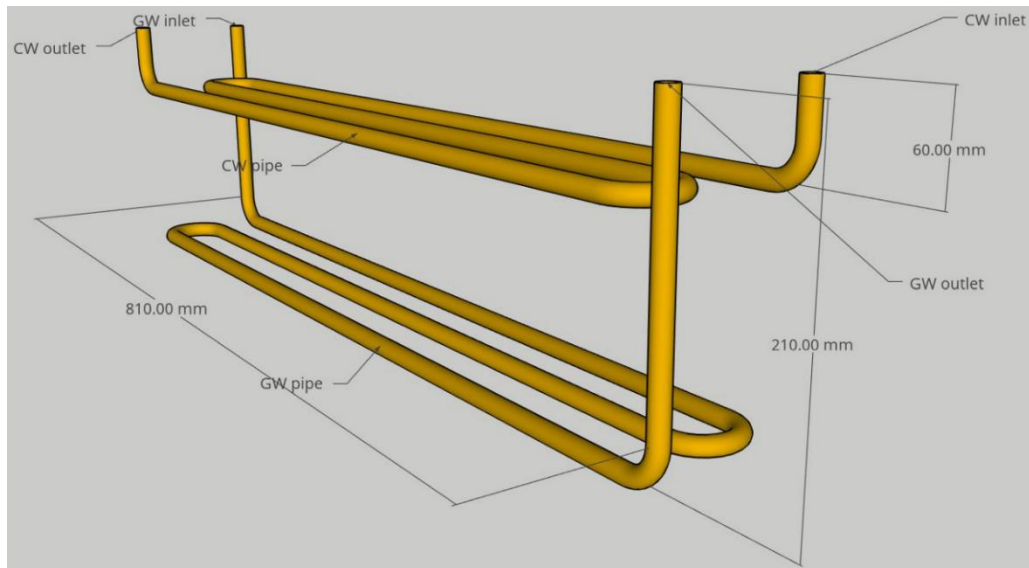
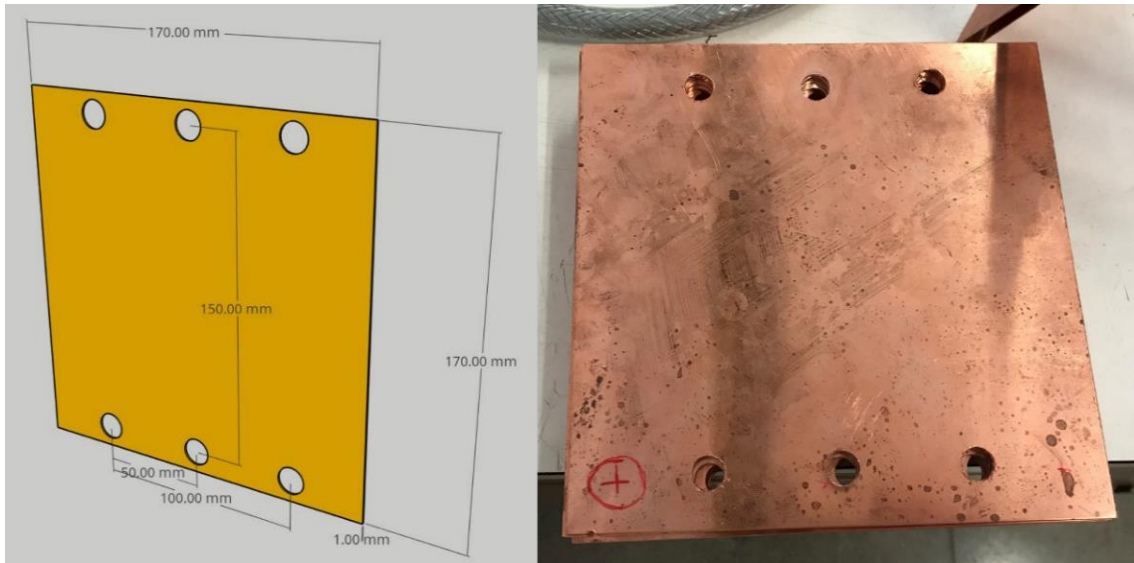


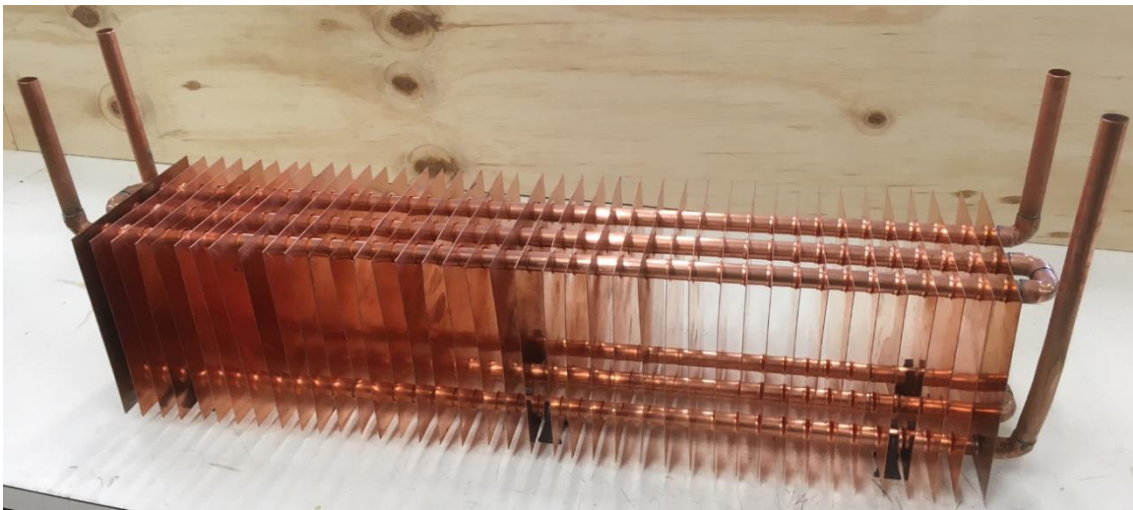
Figure 5-5: Counter-flow arrangement of the vertically cascaded GW and CW pipes

Due to differences in density between both phases of the PCM, gravity-assisted natural convection induced by buoyancy had a primary role in the PCM's phase change, especially during melting. Unlike in section 4.4, convection was prominent at this stage since the height of the HE was higher. For this reason, the GW pipe was best suited to being vertically below the CW pipe on contrary to Figure 3-1 [157]. If both were horizontally parallel, the advantages of natural convection could not quite have been fully exploited. In this configuration with the GW pipe in the lower half of the HE, a larger portion of the PCM was exposed to natural convection, which in turn enabled the CW to maximise the heat absorbed [132]. To enhance the thermal conductivity of the PCM [164], rectangular copper fins were attached to the circumference of both pipes external to the pipe flows. The dimensions of the attached fins are displayed in Figure 5-6:



*Figure 5-6: Layout of the fins installed on the counter-flow pipes*

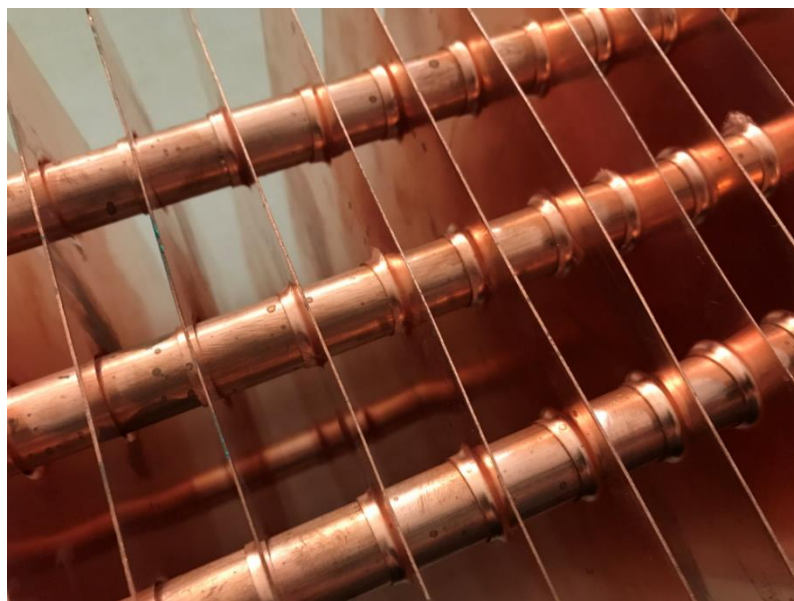
If the length of the fins is not long enough, heat by conduction is not propagated to the far ends of the container. The aspect ratio can be defined as the height of the fins to the gap between them [121]. A high aspect ratio corresponds to tall, tightly packed fins while a low ratio to short, widely spaced fins. Low aspect ratios are effective only near the vicinity of the HTF/HAF, while large ratios propagate heat further into the PCM, as required in this application. A total of forty radial fins were attached along the circumference of the pipes, with a gap of about 18mm, as displayed in Figure 5-7:



*Figure 5-7: Layout of the assembled HE with the copper pipes and fins*

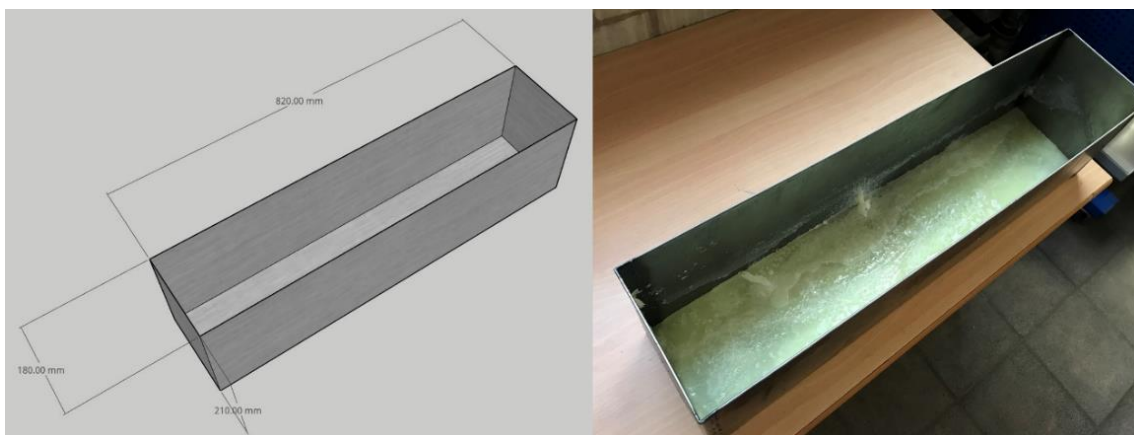


As visible, the lower GW pipe was supported by six plastic stands at a height of 25mm from the lower surface of the steel container to keep the layout erect. It was predicted that increasing the number of fins with higher dimensions would result in better thermal performance. However, the fin thickness had the least effect on this performance [170]. The fin thickness of 1mm was selected based on the cost, ease to manufacture and commercial availability. Additionally, thinner fins would be difficult to manufacture and combine with the pipes, as the contact area at the interface would decrease [171]. Generally, with the inclusion of fins in the HE, a lesser volume remains for the PCM [153]. However, since the thickness was only 1mm, the volume occupied in this case was negligible. Nevertheless, in all PCM heat transfer enhancement techniques, a trade-off has to be achieved in the increment in the speed of the phase change to that of the decrease in storage capacity due to the reduction in PCM mass. The dimensions and pitch of the fins were selected to maximise phase change to the entire HE [3,159]. Most experimental studies use welded or clipped fins attached to the fluid flow pipes [165,167]. Welding the fins causes a comparatively higher thermal contact resistance especially with dissimilar filler metals, while clipping has losses in the mechanical bond after several thermal cycles. In this model, the fins were not welded or clipped onto the pipe, but had a unique mechanical attachment made using a jig. This would ensure better thermal contact of the fin with the pipe, uniformity in manufacturing unlike welding and would be more economical. A close up of the attachment of the fins to the pipes is shown in Figure 5-8:



*Figure 5-8: Surface contact between the fins and pipes, fabricated using a mechanical jig*

Typically, the geometrical configurations of PCM containers are cylindrical, spherical, rectangular and square slab types [173]. Rectangular shell and tube enclosures of finned-PCM applications are the most common and are used as a benchmark for comparison to other geometries [132,170]. For this reason, a rectangular layout was used, with the PCM filling the shell side having the GW and CW tubes inside. Since concentric double pipe and plate HEs have the worst performance with PCMs over the long-term, they were not opted for in this application [132]. The relatively low viscosity of liquid phased PCM make sealing the HEs quite challenging, hence the pipes came out of the top in this application's layout [121]. This minimised manufacturing costs, without the need to drill and seal holes. Gaskets and sealants are effective along with welding, brazing and soldering in case holes are drilled in the container body. For this reason, sealing cylindrical and spherical containers can be even more difficult whilst retaining the shape, another reason for selecting the rectangular design. The container was made out of mild steel sheets 2mm in thickness, to ensure the PCM did not corrode it over the long term [162]. Plastic is lightweight and insulating and considered as a good option for PCM containers. However, over a ten month investigation, a high moisture sorption with plastic contaminating the PCM has been observed over several melting and freezing cycles [132]. Apart from stainless steel, even brass, aluminium and copper containers are corroded when in long-term contact with PCMs [132]. Mild steel does corrode, but at a fairly low rate, whilst being more economical compared to stainless steel. A dimensioned image with the real version partially filled with a PCM is shown in Figure 5-9:



*Figure 5-9: Layout of the mild-steel container of the HE*



The thickness of the Styrofoam used around the container was 10cm, having a thermal conductivity of 0.033 W/(m.K) [133]. The lid was made up of removable wood coupled with Styrofoam, to facilitate installation of the thermocouples and the visualisation of the melting and freezing of the PCM without considerable heat losses. A final internal layout of the cross-section of the assembled HE is presented in Figure 5-10:

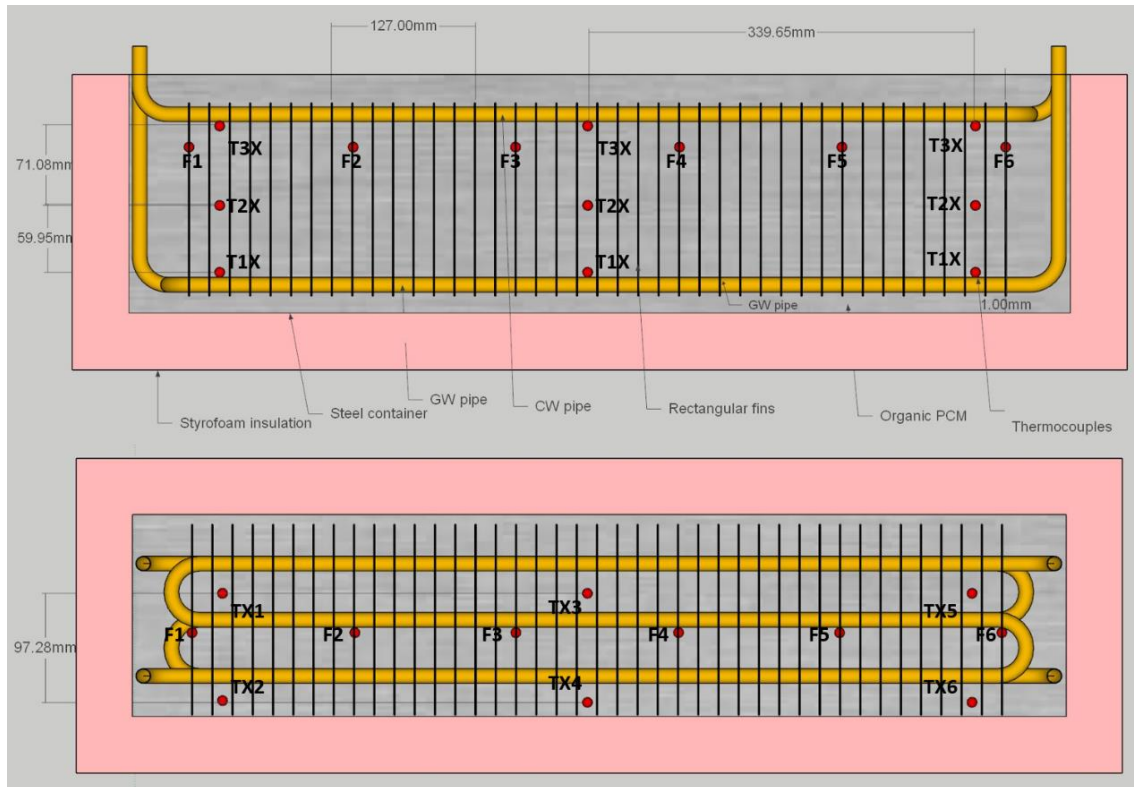


Figure 5-10: Layout of the assembled HE labelled with the thermocouple positions

As stated previously, a set of twenty-four thermocouples was arranged within to measure the temperature profiles of the fins and the PCM over the time duration, with the rod dots representing their positioning as in Figure 5-10. The lower layer of the thermocouples placed inside the PCM were numbered T1X with X from 1-6. Similarly, the middle layer had a prefix of 2 while the top layer of thermocouples had a prefix of 3. The thermocouples on the fin were labelled FX from 1-6. Although there would be natural convection currents due to the density difference in both phases of the PCMs, it would not affect the position of the thermocouples as they were rigidly fixed.

### 5.4.2. Procedure

To perform a sensitivity analysis in order to investigate the effects of the various parameters, the experiment was conducted by varying different operating conditions [156]. An overview of the strategy is illustrated in Figure 5-11:

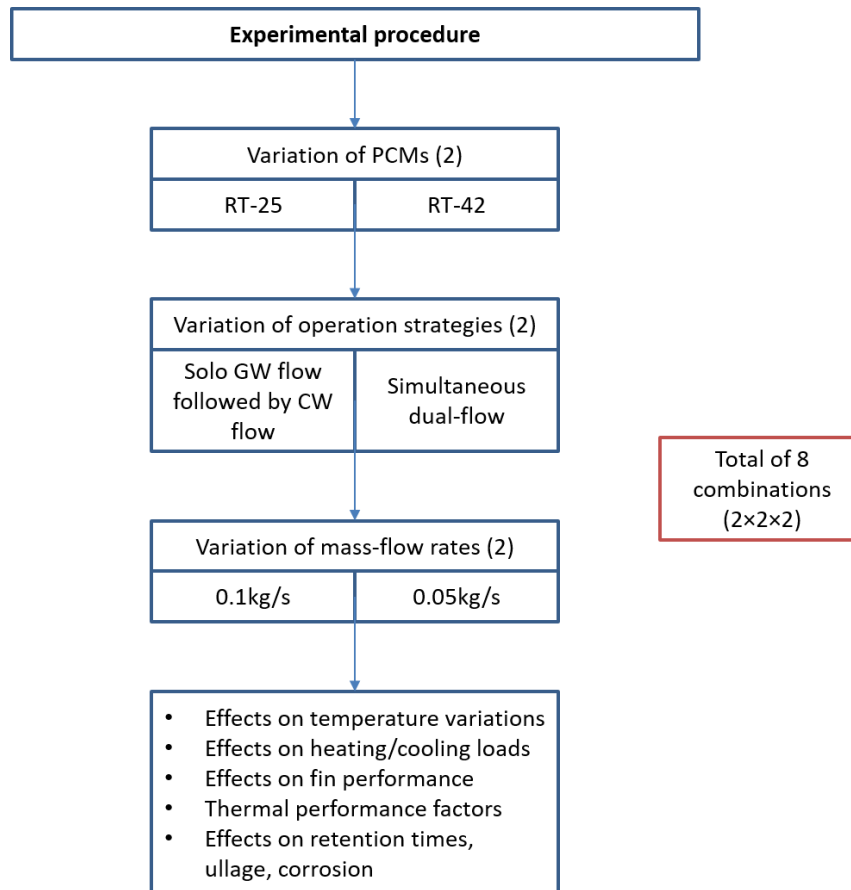


Figure 5-11: Procedure for the experimental sensitivity analysis to assess the HE with fins

Based on the classical 2-phase analytical solution and PSO algorithm, the optimum PCM for this application was RT-25, as outlined in section 3.5. Nevertheless it was important to practically confirm this and it was also interesting to observe the thermal effects in the HE using another PCM with a higher phase change temperature. As detailed in section 2.5, the inlet temperature of the GW was 325K (51.85°C) while that of the CW was 285K (11.85°C). Using RT-25 provided a higher  $\Delta T$  between GW and the PCM melt temperature, while using RT-42 provided a higher  $\Delta T$  with the CW, both

of about 30K. In this way, the strength of both the melting and freezing processes could also be assessed. The thermal characteristics of RT-42 [184], are presented in Table 5-2:

Table 5-2: Thermal parameters of RT-42

<b>Density kg/m<sup>3</sup></b>	Solid: 880, Liquid: 760
<b>Thermal conductivity in W/(m.K)</b>	0.2
<b>Specific heat capacity in kJ/(kg.K)</b>	2
<b>Dynamic viscosity in Pa.s</b>	0.0072
<b>Specific latent heat capacity in kJ/kg</b>	165
<b>Liquidus temperature in K</b>	316.15 (43°C)
<b>Solidus temperature in K</b>	311.15 (38°C)

The data sheet for this PCM is added in Appendix A. The mass of the PCM used to fill the HE was about 20 kg. Both PCMs were paraffin-based thus transparent in their liquid phase, permitting the visual observance of both melting and freezing through the HE's removable lid.

As outlined in section 1.3, a fundamental reason for using PCMs in GW heat harnessing was to decouple the supply of GW and the demand of CW. It would be valuable to assess the effectivity of this decoupling in the HE. Hence, two different operation strategies were used in this experiment. In the solo-flow operation strategy only, the GW followed by the CW flowed for 2700s each, while in the simultaneous operation, both flowed together for 2700s. The mass-flow rates of both fluids were similar when assessing an operation strategy. Although the average flow time of GW in appliances was 900s based on section 2.5, a higher time duration of 2700s was used in this experiment. This was to investigate the complete effects based on the different phase change behaviour of both PCMs, especially RT-42. Nevertheless the performance after 900s could also be assessed in this condition.

Although the typical mass-flow rate of GW in appliances based on section 2.5 was 0.1kg/s, two different values of 0.05kg/s and 0.1kg/s were investigated for a sensitivity analysis. At the same time, the probability of this lower mass-flow rate also exists in appliances. This condition would also assess the effect of increased turbulence on the thermal performance of the HE. A total of eight experimental tests were carried out in this sensitivity analysis, with the different combinations in Figure 5-11.

Most experimental studies have established that the inclusion of fins increases the thermal performance in comparison to a non-finned arrangement, whilst most have also effectively analysed the appropriate application-specific fin dimensions as well. [170]. It is also an established fact that the rate of PCM phase change is directly proportional to the inlet temperature of the HTF [157,166,173]. For this reason, a comparison without a fin arrangement was not executed at this stage, but a sensitivity analysis was performed based on the PCM used, the HTF/HAF flow rates and the operation strategy. Finally, unlike in recent research, the aspect of ullage was analysed along with the corrosion affects and PCM retention times.

### 5.4.3. Results

Results for all the thermocouple readings were analysed for both melting and freezing, based on measures of thermal performance. The entire PCM domain can be assumed to be divided into eighteen equal volume rectangular blocks around each thermocouple, giving the average temperature of a block. The approximate liquid fraction was calculated based on the commonly used lever rule [166]:

$$\text{Liquid volume fraction} = \frac{T - T_{Solidus}}{T_{Liquidus} - T_{Solidus}} \quad (5-2)$$

The Stefan number is the ratio of the sensible to latent heat transferred by the PCM, defined as:

$$St = \frac{\text{Sensible heat transfer}}{\text{Latent heat transfer}} = \frac{mc(T_{final} - T_{initial})}{mL} \quad (5-3)$$

The average temperature of the eighteen thermocouples was used to calculate the sensible energy. The latent heat transfer was calculated based on the change in the mass fraction of a phase, as per equation (5-2). The overall objective of this HE was to maximise the heat transfer from the GW to the CW. This transfer efficiency was defined as:

$$\begin{aligned}
 \text{Heat transfer efficiency} &= \frac{\text{Heat absorbed by CW}}{\text{Heat transferred from GW}} \\
 &= \frac{\dot{m}_{CW} \times C \times (T_{out} - T_{in})}{\dot{m}_{GW} \times C \times (T_{in} - T_{out})}
 \end{aligned} \tag{5-4}$$

In a similar experiment, this efficiency was at 71.8% which meant that 28.2% of the heat was lost within the PCM during the heat exchange process [165]. To minimise uncertainties in the results, several trials were conducted for both melting and freezing based on which 90% confidence levels were achieved. This was performed due to the fact that PCM properties are non-homogenous along with a high rate of the accumulation of impurities over time. The experiment readings were recorded in an indoor laboratory with an ambient temperature of 295-297K (21.85-23.85°C).

I. Solo-flow (one at a time GW/CW flow) operation strategy

The readings for all thermocouples in the solo-flow strategy are presented in Appendix B. For simplification, an overview of the temperature variations in the odd-numbered thermocouples of all tiers on the upper side of the HE are presented in Figure 5-12:

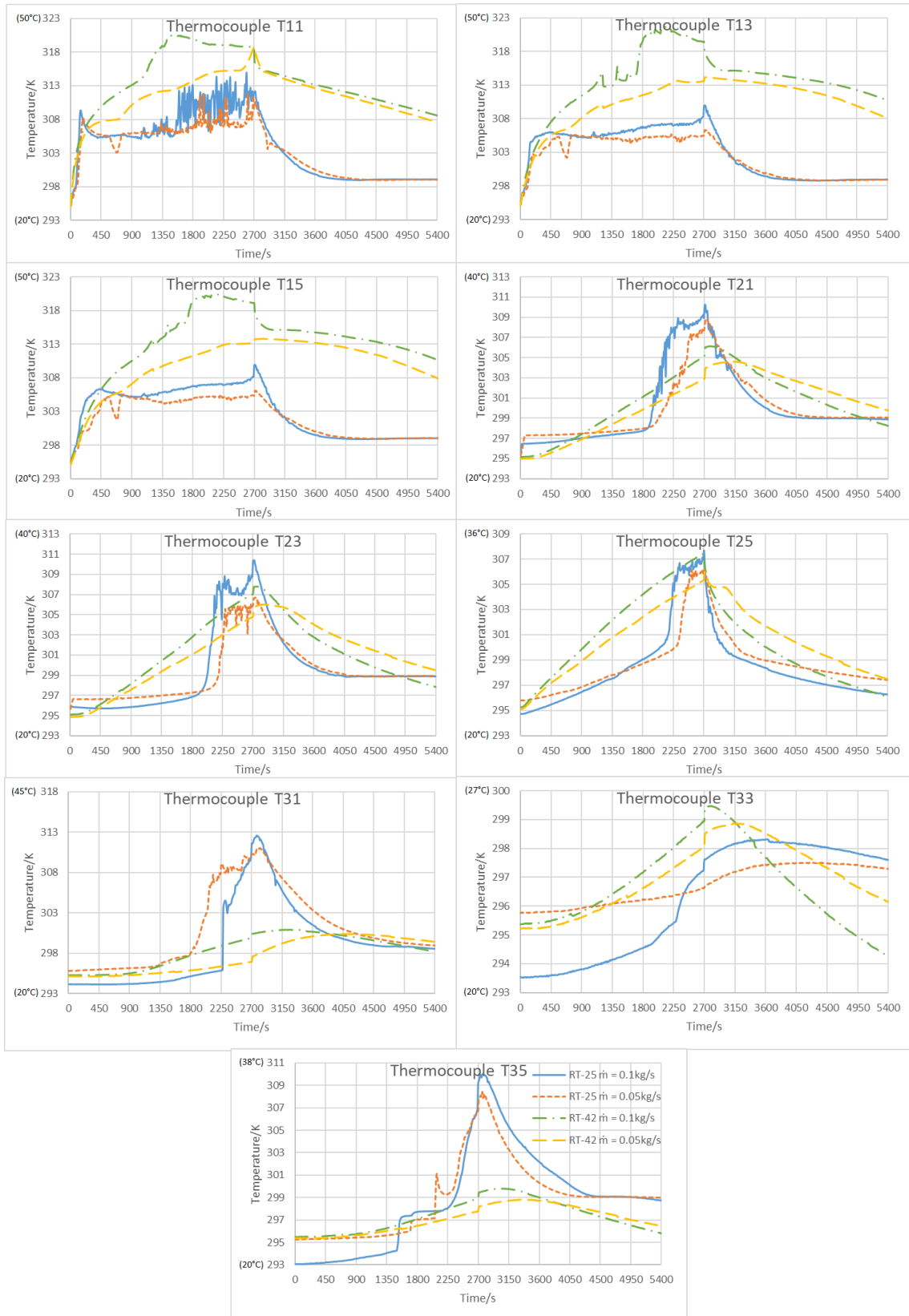


Figure 5-12: Temperature variation for the odd-numbered thermocouples in the solo-flow strategy

The general trend in the even numbered lower side thermocouples of Figure 5-10 were more or less similar to these thermocouples in Figure 5-12, as illustrated in Appendix B. Several important trends can be observed from these plots. Firstly, due to buoyancy induced natural convection, the curves exhibit waviness and spikes, especially during the melting phase (initial 2,700s) and especially for RT-25, at a mass-flow rate of 0.1 kg/s in thermocouple T11. A reason for this was the close proximity of the thermocouple to the higher heat influx from the GW pipe. In a similar study [155], the PCM in close proximity to a fin melted four times faster compared to the PCM a few millimetres away. This was because the speed of conduction in the initial phases of melting was much higher compared to the slower laminar natural convection in the later phases. Hence, conduction was initially the main source of heat transfer followed by natural convection in melting. This waviness was prominent for RT-25 but not RT-42, since complete phase change occurred only in RT-25 during melting. In the lower tier of thermocouples, RT-42 had a comparatively higher temperature gain in the initial 2,700s of melting. This was attributed to the fact that most of the heat gained during this phase was sensible without phase change. Another observation was that the waviness in the plots was present only during melting but not freezing, proving that the melting of a PCM is convection dominated, while freezing is conduction dominated. At these lower tiers of thermocouples, the mass-flow rate did not have any significant impact for RT-25 but the adverse was for RT-42. This highlights the fact that RT-25 was more responsive and less dependent on external conditions, with a higher performance irrespective of the flow conditions.

Similarly, in freezing (2,700-5,400s), sensible cooling was much faster compared to latent cooling as observable between the RT-25 and RT-42 trend lines. There was a gradual decrease in the temperature of RT-42 compared to an abrupt decrease of RT-25. Initially, the slopes of the curves for RT-25 were much greater during the sensible cooling regime followed by a less steep curve during latent cooling. Latent cooling was much faster in the initial phases, followed by almost horizontal cooling trends. This was attributed to the fact that in freezing, the role of natural convection is initially prominent but vanishes as it is replaced by conduction heat transfer.

Compared to the first tier of thermocouples, in the second tier the peak temperature for both PCMs in the initial 2,700s of melting shifted to the right by about 1,500s. At the

same time, the temperature of RT-25 overtook RT-42 in this layer, showing that melting propagated faster due to natural convection-induced heat transfer compared to only conduction in RT-42, as there was no phase change in RT-42 and it remained in the solid phase. In the RT-25 curves, waviness was somewhat present in melting. However this waviness, was only initially present in freezing and completely disappeared after the phase change. Then, conduction dominated and due to the low thermal conductivity of the solid PCM, it behaved like an insulating medium around the pipes [172]. The thermal conductivity of a PCM in the liquid phase is lesser than that in the solid and for this reason, convection is extremely important during melting [164]. It is estimated that without natural convection, the melting time would increase by 30% [172]. At the same time, natural convection yields a more unified temperature distribution in the melting of the PCM, unlike that witnessed in freezing based on these thermocouple readings. Heat propagation lowered along the length of the pipe, resulting in a later peak for thermocouples TX5 compared to the initial thermocouples. This was because the larger the  $\Delta T$  between the HTF and the PCM, the faster the phase change [121]. As the GW moves through the pipe, it lost heat evolving to a lower temperature.

In the upper tier of thermocouples, RT-42 had a negligible temperature increment and eventually a similar trend in freezing, since the phase had not changed at all. In this tier the RT-25 melted only at the end of the 2,700s time period. Based on the trend lines, almost all of the RT-25 melted in the 2,700s, whilst only the first tier of thermocouples of the RT-42 case melted. Almost all the RT-25 around the edges of the container melted in the 2,700s time duration. It can also be concluded that phase change propagates from the outside to the inside of the container. With the passage of time, the amount of melted PCM increases, which eventually intensifies buoyancy-driven natural convection. The liquid phase was pushed upwards and sideways, whilst the solid phase was sandwiched in the middle [157]. For all the thermocouples, the trend lines were similar for both mass-flow rates with 0.05 kg/s being below by an average of 2K compared to 0.1kg/s. This was quite interesting since the amount of heat flux from both 0.05kg/s and 0.1kg/s did not vary significantly. Although there was more turbulence in the 0.1kg/s flow condition, most of the fluid passed through the pipe section without contact with the pipe surface. This inhibited heat transfer and compared to the 0.05kg/s flow regime, most of the fluid remained in contact with the pipe surface providing a comparatively similar heat transfer. As per the literature [132,134,169], it can be



verified from the temperature plots that melting and freezing have four distinct heat transfer regimes as per Table 5-3:

Table 5-3: Heat transfer regimes of melting and freezing in PCMs

Order	Melting	Freezing
1	Conduction	Natural convection
2	Conduction and natural convection	Conduction and natural convection
3	Natural convection	Conduction
4	Expansion of volume	Shrinkage of volume

An overview of the heat transferred by the GW and the CW flow is presented in Figure 5-13:

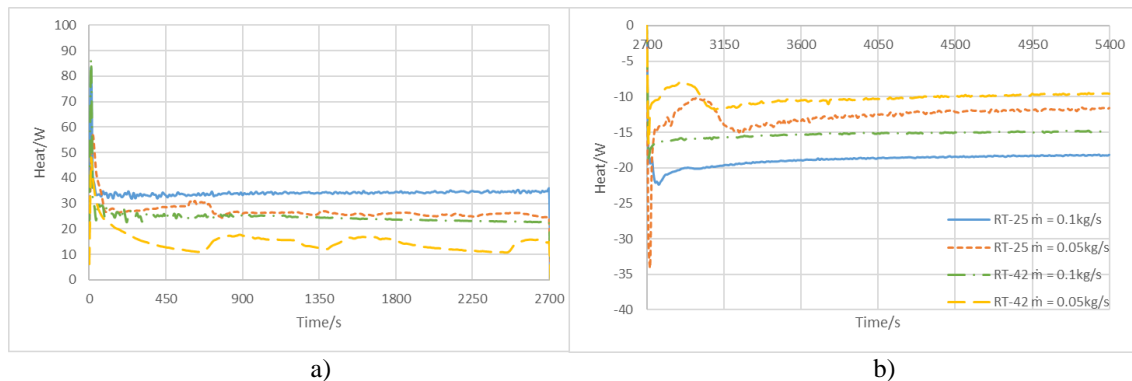


Figure 5-13: Heat transferred a) from the GW b) to the CW flows, in the solo-flow strategy

Initially, the amount of heat transferred was high for both GW and CW as it eventually asymptotically reduced with the passage of time. As the PCM temperature rose the  $\Delta T$  between the HTF and the PCM diminished, resulting in a decreased heat transfer with similar trends as in the literature [155]. Eventually, the heat transfer would approach zero as the temperature of the PCM tended to that of the HTF/HAF. Similarly, the magnitude of heat transferred by the GW was much larger compared to the heat absorbed by the CW, which proved that melting is comparatively faster due to natural convection domination. The average temperature profiles of the six thermocouples attached to the fins are presented in Figure 5-14:

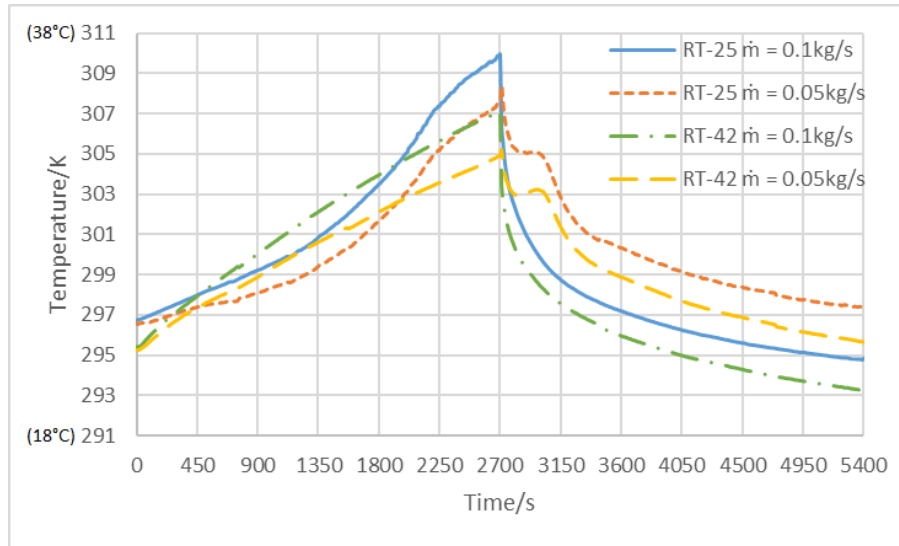


Figure 5-14: Average temperature of the fins in the solo-flow strategy

Clearly, the inclusion of fins results in uniformity in the PCM temperature distribution and enhancement in the heat transfer rate along with a decrement in the melting time [170]. This was primarily because the average temperature of the fins approaches that of the fluid flows in the pipes. This temperature was comparatively higher for RT-25 as the PCM melt temperature had a greater  $\Delta T$  with the GW flow being independent of the mass-flow rate. In this case, the fins propagated the heat effectively into the PCM resulting in a minutely higher average temperature. The initial conduction in the PCM was larger with the fins, enabling natural convection to initiate earlier compared to a case without fins [172]. An overview of the calculated thermal parameters to establish the performance of the HE are in Table 5-4:

Table 5-4: Thermal performance for the solo-flow operation strategy

Solo-flow operation					
Criteria		RT-25 $\dot{m} = 0.1\text{kg/s}$	RT-25 $\dot{m} = 0.05\text{kg/s}$	RT-42 $\dot{m} = 0.1\text{kg/s}$	RT-42 $\dot{m} = 0.05\text{kg/s}$
1	Order of propagation of heat in lower thermocouple layer T1X	1-3-5-4-2-6	1-3-5-4-2-6	1-3-5-4-2-6	1-3-5-4-2-6
2	Order of propagation of heat in middle thermocouple layer T2X	4-1-3-5-6-2	4-1-3-5-6-2	5-3-4-6-1-2	5-3-4-6-1-2

<b>3</b>	<b>Order of propagation of heat in upper thermocouple layer T3X</b>	6-1-5-2-4-3	1-6-5-2-3-4	1-6-3-5-2-4	6-3-2-5-4-1
<b>4</b>	<b>Liquid fraction after GW flow</b>	0.94	0.92	0.28	0.12
<b>5</b>	<b>Liquid fraction after CW flow</b>	0.84	0.87	0.00	0.00
<b>6</b>	<b>Stefan number after GW flow</b>	0.16	0.12	0.53	0.95
<b>7</b>	<b>Stefan number after CW flow</b>	1.11	1.54	0.25	0.30
<b>8</b>	<b>GW to CW heat transfer efficiency</b>	54.76	46.82	61.61	66.95
<b>9</b>	<b>Average temperature lost by GW/K</b>	-8.19	-12.89	-5.89	-7.22
<b>10</b>	<b>Average temperature gain by CW/K</b>	4.52	6.09	3.68	4.88

The first three rows represent the order of temperature change of the thermocouples based on the numbering topology of Figure 5-10. From these first three rows, it was clear that irrespective of the mass-flow rate or type of PCM, heat propagated from the outer edges of the container towards the centre. Due to the vertical lengths of the GW pipe as depicted in Figure 5-5, the thermocouples T36 and T16 were the fastest to melt amongst the third tier of thermocouples. Melting propagates upwards due to buoyancy, while freezing propagates downwards due to the higher density of the solid phase, which proves that this orientation was suited for this application [132].

A lower Stefan number was desired to maximise latent and minimise sensible heat transfer. This ensured a higher net heat transfer, as this value should be zero in the ideal case. The Stefan number was inversely proportional to the mass-flow rate of the CW for freezing in both PCMs. However for melting, it was dependent on both the type of PCM and the GW mass-flow rate. A 0.05kg/s mass-flow rate with RT-25 as the PCM gave the best result, since most heat transfer in this condition was latent-dominated. Since most heat transfer in the freezing of RT-25 was sensible, the Stefan numbers were comparatively much higher. An interesting observation was that the heat transfer

efficiency for RT-42 was higher compared to that of RT-25 because the average temperature differentials of the GW and CW were comparatively less for this PCM. For the GW heat harnessing application, the desire was to have a higher  $\Delta T$  for the fluid flows. The heat transfer efficiency in all cases was considerably lower, probably due to the fact that the distance between the pipes was large.

Almost the entire 20kg of RT-25 melted in the 2700s compared to only 25% of RT-42. Similarly, the temperature differentials for both the GW and CW flows were higher for RT-25. This proves the prediction of the classical 2-phase analytical solution-PSO algorithm in section 3.5 as the net heat transfer was greater, making RT-25 more suitable to this application. However freezing was almost negligible in RT-25 while being quite dominant in RT-42, hence proving that  $\Delta T$  has a major role in thermal performance as well. This also resonated in the fact that the Stefan numbers for RT-25 were lesser in melting compared to freezing. Most heat transfer in melting was latent, while it was sensible in freezing as predicted by Figure 3-9. The requirement of a numerical simulation for this application to optimise the fin configuration with respect to freezing was a consequence of these Stefan numbers and the low phase change of RT-25 in freezing, as in the forthcoming section.

## II. Simultaneous dual-flow operation strategy

The readings for all thermocouples in the dual-flow strategy are also presented in Appendix B. To draw a comparative analysis with the solo-flow strategy, similar plots are presented for the dual-flow operation strategy. An overview of the temperature variations in the similar set of thermocouples is in Figure 5-15:

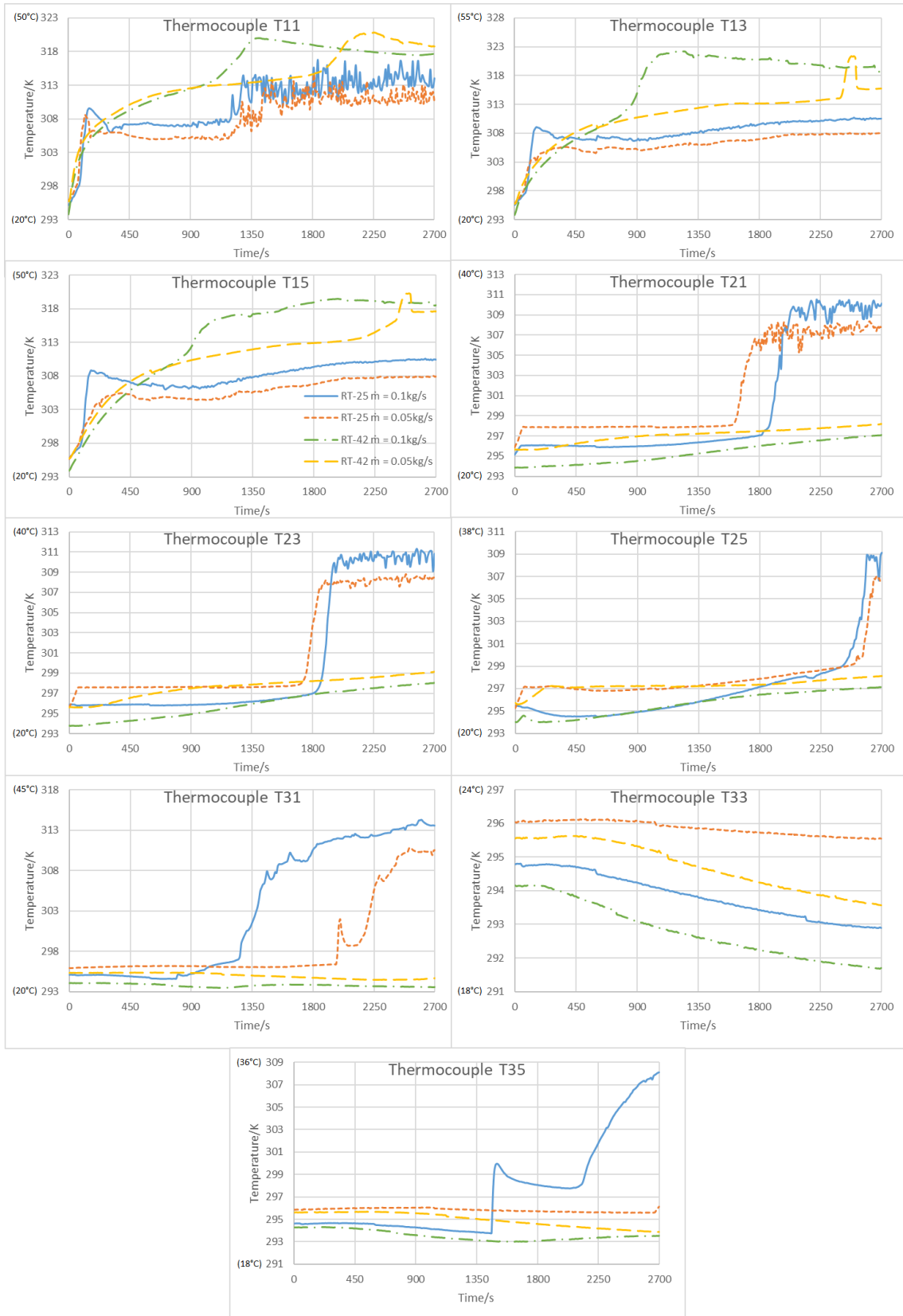


Figure 5-15: Temperature variation for the odd-numbered thermocouples in the dual-flow strategy

The general trends for the lower tier of thermocouples were mostly similar to the solo-flow strategy, since this tier of thermocouples was in close proximity to the GW pipe.

For both the PCMs and flow rates in this layer, the thermocouples were melting-dominated, with gradual increments in temperature after an initial spike. The main difference in the outcome lay in the middle tier of the thermocouples. For RT-42, there was almost no change in phase with minimal temperature differentials. The CW flow pressed the freezing front from the top, while the GW pushed the melting front from the bottom. However, since the  $\Delta T$  of RT-25 favoured the GW flow for melting, it dominated after the initial 1,800s. Eventually, the RT-25 in this layer melted with convection trends visible towards the end of the plot.

The most interesting trends were observed in the top tier of thermocouples. As mentioned, phase change occurred from the outside towards the inside of the HE. For this reason, thermocouples T31 and T35 exhibited phase change only for RT-25. However all PCMs in the T33 thermocouple decreased in temperature and remained in solid state. The melting front in RT-25 was able to propagate only upwards and on the outskirts of the container. Also, during this dual-flow operation strategy, the solid PCM sank to the middle of the container close to the centre of gravity, as reported in the literature [155], due to the liquid having a lower density compared to the solid phase. There was a combination of both conduction and convection at the phase change interface. Convection in the liquid phase dominated the conduction in the solid phase as evident from the propagation of the melt front for RT-25. On the other hand, in this top layer, the RT-42 was at a temperature below the ambient (295K or 21.85°C) since the incoming CW was at 285-288K (11.85-14.85°C). During this dual mode operation, the solid PCM was sandwiched in the centre of the container close to its centre of gravity, for all cases. Similarly, the variation in heat transferred by the GW and the CW flow is presented in Figure 5-16:

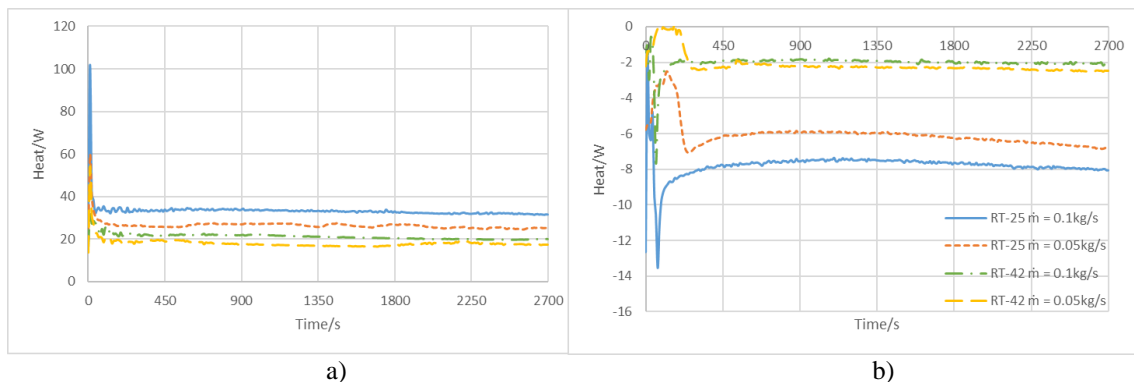


Figure 5-16: Heat transferred a) from the GW b) to the CW flows in the dual-flow strategy

The trends were exactly the same for the solo-flow strategy, with a notable difference in the values of the y-axis being lesser, especially for the CW flow. This was due to the fact that the melt front never reached the CW pipe. Typically, uneven melting and freezing prolongs the total phase change time [170]. An overview of the average fin temperatures is presented in Figure 5-17:

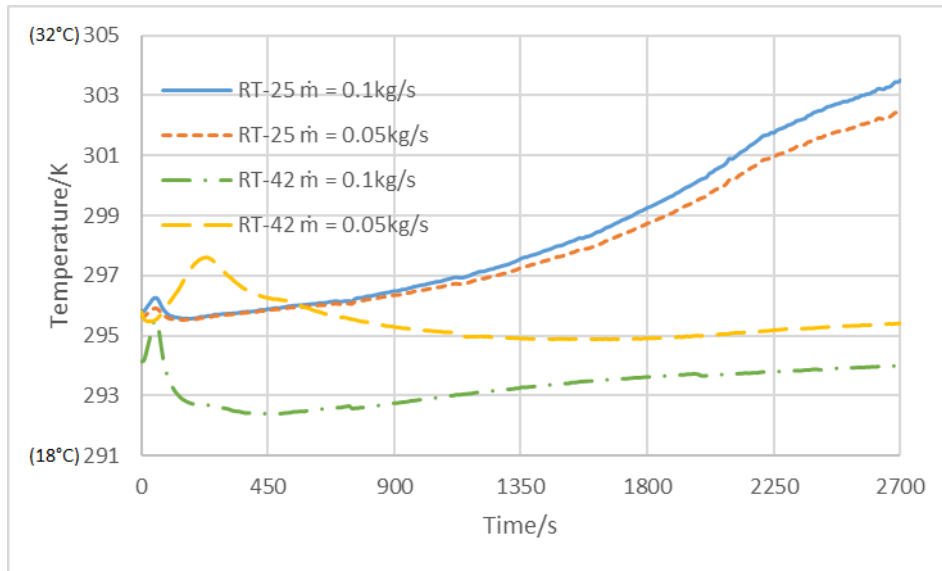


Figure 5-17: Average temperature of the fins in the dual-flow strategy

Compared to the solo-flow operation strategy, the temperature of the fins was lower for RT-25 at both mass-flow rates. However for RT-42, the temperature was closer to that of the CW flow. This was due to the fact that the thermocouples were attached much closer to the CW flow, due to manufacturing constraints. Nevertheless, RT-25 managed to considerably increase the temperature of the fins, towards the GW flow regime, proving the strength of the melting process in this strategy. The thermal parameters calculated for this dual-flow strategy after 2,700s are presented in Table 5-5:

Table 5-5: Thermal performance for the dual-flow operation strategy

Dual-flow operation					
Criteria		RT-25 $\dot{m} = 0.1$ kg/s	RT-25 $\dot{m} = 0.05$ kg/s	RT-42 $\dot{m} = 0.1$ kg/s	RT-42 $\dot{m} = 0.05$ kg/s
1	Order of propagation of heat in lower thermocouple layer T1X	1-3-5-4-2-6	1-3-5-4-2-6	1-3-5-4-2-6	1-3-5-4-2-6

<b>2</b>	<b>Order of propagation of heat in middle thermocouple layer T2X</b>	3-1-4-2-6-5	1-3-4-2-6-5	6-4-3-5-2-1	5-4-6-3-1-2
<b>3</b>	<b>Order of propagation of heat in upper thermocouple layer T3X</b>	1-2-5-6-4-3	6-1-2-4-5-3	6-2-1-5-4-3	2-6-4-1-5-3
<b>4</b>	<b>Liquid fraction</b>	0.93	0.86	0.25	0.23
<b>5</b>	<b>Stefan number</b>	0.17	0.09	0.42	0.39
<b>6</b>	<b>GW to CW heat transfer efficiency</b>	23.46	22.84	9.44	11.70
<b>7</b>	<b>Average temperature lost by GW/K</b>	-7.92	-12.60	-5.09	-8.69
<b>8</b>	<b>Average temperature gain by CW/K</b>	1.86	2.88	0.48	1.02

As a comparison to the solo-flow strategy, the lower tier of thermocouples propagated the heat in the exact same order, since they were in the vicinity of the GW. However, the middle tier of thermocouples had a reverse order. Also evident from the third tier of thermocouples, the phase change front propagated along the length of the GW pipe for RT-25. For RT-42, the CW flow suppressed the phase change in most parts of the container. An interesting result was that in spite of the freezing front pressing downwards, both PCMs managed similar or even higher phase change fractions. Most of the heat from the GW did not propagate deep into the container and was focused around the pipe, resulting in a higher phase change in this region. For RT-42, either a purely solid or liquid phase existed instead of a mushier PCM, as the average temperature of the entire domain was about 4K lower compared to the solo-flow strategy. This was also observable with the HE's removable wooden lid. The thermal resistance beyond this volume in the pipe vicinity was high and the heat flux was unable to diffuse deep into the PCM. The remaining PCM acted as a thermal insulator instead of a heat sink, especially in such applications involving a high impulse flow of GW [121]. This was also evident from the lower Stefan numbers indicating that most of the heat transfer was latent with higher phase change. In this dual-flow strategy, most heat



was confined close to the GW pipe, making it of little use for extraction by the CW, resulting in lesser temperature differentials overall for both flows. Consequently, the heat transfer efficiencies were even lower than the solo-flow operation strategy. As per the outlined investigation in section 5.4.2 of the sensitivity analysis, the incorporation of PCMs enabled the decoupling of demand and supply for this GW heat harnessing application, making them unsuitable for dual-flow operations.

### III. Retention time, ullage and corrosion

Additionally, three observations were important especially for the long-term usage of the PCM over numerous melting and freezing cycles. The retention of heat in both PCMs for a duration of 40 hours is presented in Figure 5-18:

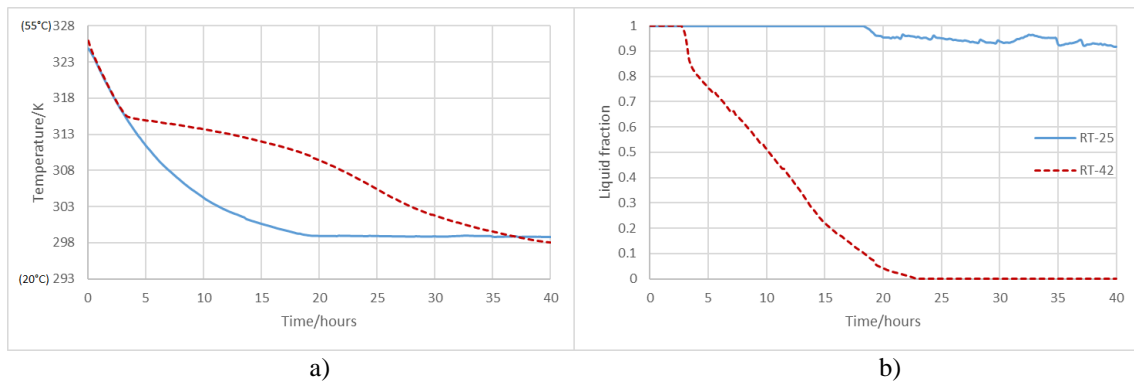


Figure 5-18: Retention of a) temperature b) phase, for both the PCMs

Eventually, both the PCMs reached the ambient temperature of at the end of the 40 hour time duration. However since the melt temperature of RT-25 was closer to the ambient, it remained in liquid phase, retaining most of its thermal energy. This was extremely beneficial for this application, since the original objective to decouple demand and supply was possible to a maximum extent. However, a negative aspect was that as the melt temperature of RT-25 was close to the ambient, a uniform temperature distribution within this PCM was not possible, even after several cooling cycles. This was an added systematic uncertainty in the results, as sometimes portions of RT-25 were already in the mushy state and could not be further cooled.

At the same time, an important observation from all the thermocouple plots of both strategies showed that PCMs have no specific phase change temperature and this is so over a range [179]. This is because PCMs are non-crystalline with an amorphous

structure. At the same time it is due to impurities and the non-homogenous thermo-physical characteristics of the PCM over many cycles. Transition temperatures are greatly dependent on the heat input [132]. Uneven ullage formation is also a direct consequence of this non-homogenous lattice. The solid is typically less in volume compared to the liquid and as a consequence the development of voids are referred to as the ullage [121]. In this setup, there was a reduction of about 2-3mm in the height of PCM when transforming from liquid to solid. This was in agreement with the numbers in the literature [121,134], where the change in volume is between 15-20%. At the same time, ullage creates air bubbles which act as an insulator. An overview of this phenomenon, as witnessed during the experiment, is presented in Figure 5-19:



*Figure 5-19: Shrinkage of volume and air bubble formation, due to ullage after the freezing of the PCM*

Ullage is inevitable and is highly dependent on the container design. The primary goal of the design of a PCM-based HE is to spread the PCM further away from the HTF to achieve a uniform phase change by minimising the creation of an insulating air layer within the ullage space [121]. PCM shape stability is also a widely researched area to eliminate ullage, typically by inserting polyethylene into the structure of the liquid PCM to retain its volume [132]. However, it is believed that fins and surface area enhancement techniques reduce the possibility of void formation to make the PCM more uniform and consistent [178].

Paraffin is known to be the most stable amongst all PCMs, as in this case phase segregation and super-cooling effects were not observed [132]. However, minor pitting

was observed as expected in the mild steel container and copper fins that were in contact with the paraffin, as presented in Figure 5-20:



*Figure 5-20: Pitting on the surface of the mild steel container and copper fins*

This was a result of the direct contact of the metals with the PCM for a duration of about eight months. Paraffin PCMs themselves only have issues with thermal conductivity and in general do not have limitations of internal corrosiveness, thermal and mechanical instability [180].

## **5.5. Numerical model**

A 3D numerical simulation replicating the dimensions and boundary conditions of the experimental model was developed in Star-CCM+ v12.04. After validating this simulation based on the experimental data, a sensitivity analysis was conducted to select the fin configuration with optimum external heat transfer enhancement to the PCM, with respect to this GW heat harnessing application.

### **5.5.1. Geometry, mesh and solvers**

The governing equations of this numerical simulation remain the same as in section 4.5.1. A 3D geometrical model was simulated in Star-CCM v12.04, having the same

dimensions of the HE in section 5.4.1. There were four distinct regions merged as a single part: a) the GW fluid domain, b) CW fluid domain, c) the copper pipe with the rectangular fins and d) the PCM. An overview of the geometrical layout is presented in Figure 5-21:

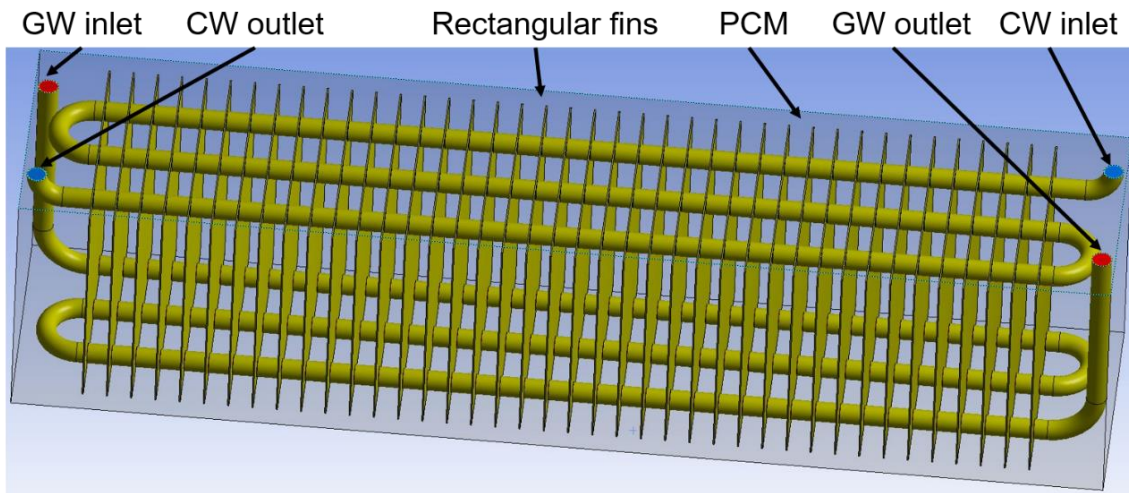


Figure 5-21: Layout of the geometric model with four domains: GW fluid flow, CW fluid flow, corrugated copper pipe and the PCM

Both the pipes and the fins were considered as one part, with no thermal contact losses between them. The four domains were discretised using an unstructured polyhedral mesh, similar to the settings in section 4.5.3. A mesh convergence study was performed as the first step in all the numerical simulations. Using four different grid sizes, the melt fraction of the PCM was analysed for the GW flow. The third largest grid size was considered the most suitable with a difference of less than 3% from the largest configuration. It also had about 20 million elements with a reasonable computation time. The solvers and boundary conditions of the simulation were similar to the model developed in section 4.5.4. The same procedure was repeated for this numerical simulation as in section 5.4.2. An implicit transient simulation for 2700s each was performed for both the melting (GW flow) and freezing (CW flow) of the PCM. After the completion of an initial melting process, the temperature profiles of the PCM and copper domains were imported as initial conditions into the follow-up simulation of the freezing process. The time step was varied to be initially at 0.01s and gradually incremented to 1s, as the solution stabilised and converged to a steady-state. The real-

time completion of this simulation was about 48 hours using a HPC, owing to the large mesh size and the complexity of the solvers.

### 5.5.2. Validation

The numerical model was validated based on the experimental data for the melting and freezing of both PCMs at the two mass-flow rates, for the solo-flow operation strategy as per section 5.4.2. Three different variables were compared, with the average deviations between the numerical and experimental results listed in Table 5-6:

Table 5-6: Difference between the numerical and experimental results to assess the HE with fins

Operation		Parameter	Linear R-square value	Maximum difference	Mean difference	End value difference
<b>Melting (GW flow)</b>	<b>1</b>	GW (Outlet - Inlet) temperature/K	0.865	0.930	0.599	0.693
	<b>2</b>	Melt fraction of the PCM	0.947	0.186	0.087	0.042
	<b>3</b>	Average temperature of fins/K	0.987	2.380	1.175	2.105
<b>Freezing (CW flow)</b>	<b>1</b>	CW (Outlet- Inlet) temperature/K	0.897	0.783	0.492	0.447
	<b>2</b>	Freeze fraction of the PCM	0.878	0.083	0.055	0.028
	<b>3</b>	Average temperature of fins/K	0.930	4.377	1.871	1.546

An R-squared value was between 0-1 to consider the closeness of the trends in values, with one showing good agreement between both the datasets. Based on Table 5-6, the R-squared values for both datasets were in the range of 0.85-0.98. At the same time, the remaining criteria were also in close agreement to sufficiently validate the numerical model. The slight discrepancies in the validation were due to the following reasons:

- The systematic uncertainties in the equipment of the experiment were inevitable. Most of these errors and limitations in the equipment have already been highlighted in section 4.5.6. There were uncertainties in the K-type thermocouples coupled with the data logger, along with their slow response time. There are always limitations to experimental setups due to resource constraints, which always have room for improvement. During this phase of the experiment, it was observed that the radially inserted probe type thermocouples measured the temperature of the flowing CW and GW in the central portion of the cross-sectional area of the pipe, with less sensitivity to the circumferential flow.
- The change in environmental conditions in the experiment also contributed to systematic errors not present in the simulation. At the same time, the boundary conditions of the experiment fluctuated within tolerable limits while they were modelled as being consistent in the simulation. Usually, these differences are amplified in the initial transient zone of the results as highlighted in section 4.5.6. In general, the differences were much smaller as the solution converged to a steady-state, as witnessed in the literature as well [179].
- Several assumptions were taken into the simulation that did not completely mimic the experimental test rig. A thermal contact resistance existed between the mechanically fitted fins and pipes in the experiment whilst they were treated as a single domain in the simulation, due to computational constraints. At the same time, the walls of the container in the simulation were adiabatic whilst in reality there was always some heat loss.
- Since a PCM is an amorphous structure, its thermo-physical properties change slightly after every cycle [179]. The amount of disorder in the micro structure of a PCM is unpredictable at a macro-scale simulation and is highly dependent on the environmental and loading conditions. At the same time, there is no single consistent phase change temperature as it is dependent on the transient heat flux [150]. For this reason, the PCM close to the pipes and fins exhibited different phase change properties compared to the bulk PCM within the HE. However, these properties were taken as constant values in the simulation. At the same time, the errors accumulated in melting were carried forward to the freezing process.



### 5.5.3. Results

With this geometric configuration of the HE, only 0.4 of the RT-25 volume fraction melted while only 0.1 of it froze in a 900s time duration. Based on this result, it was clear that an optimum fin configuration must be selected to suit this high-impulse application. For this GW heat harnessing application involving a low time duration of GW flow, a larger aspect ratio of the fins was desired for rapid phase change [172]. However, a fin configuration with a high aspect ratio is also known to inhibit natural convection flow within the PCM. The fin pitch is inversely proportional to the Rayleigh number which dictates the amount of convection in the PCM domain [153]. Similarly, in a lower number of fins, the thermal resistance is higher but this arrangement does not restrict natural convection [134]. As fin design is application-specific, the geometrical aspects with respect to the HE determined the overall performance, which had to be investigated. The five important parameters optimised in this application are numbered in Figure 5-22:

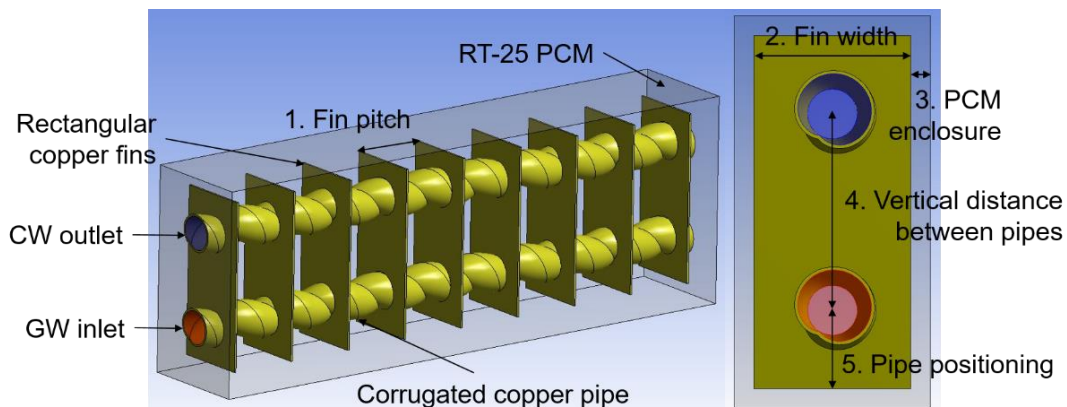


Figure 5-22: Configuration of the fins to be optimised

As the focus was on the optimal development of the fins with the associated pipe configuration, a straight 600mm length section was assessed [159]. A randomly selected model was assessed with a fin pitch of 35mm, a width of 60mm, a PCM enclosure length of 10mm, a fin height of 150mm and a pipe positioning of 15mm. Evidently, freezing was slower as it is conduction dominated compared to melting [171]. Hence, the design had to be based on this bottleneck, since the objective was complete phase change for both melting and freezing in 900s to maximise latent heat transfer from the PCM to be transferred from the GW to the CW. The configuration, mesh settings and

boundary conditions were similar to the model developed in the last section. Based on this analysis of a smaller length configuration, the HE could be elongated with both longitudinal and lateral bends as required by installation constraints in the final building environment. Compared to the plane pipe, the optimum corrugated pipe of section 4.6 was used to enhance the internal heat transfer of both the GW and CW flow. Corrugated pipes were another reason for this smaller 600mm geometry, as a longer configuration would be impossible to generate and solve with limited computational resources. This design was optimised based on the average boundary conditions for the flow highlighted in section 2.5. This would ensure that the HE was not out of proportion due to an over-design or completely ineffective due to an under-design.

### I. Optimised geometry

To determine the five optimum geometric variables of Figure 5-22, line probes were set adjacent to all three Cartesian directions of the fins, as presented in Figure 5-23:

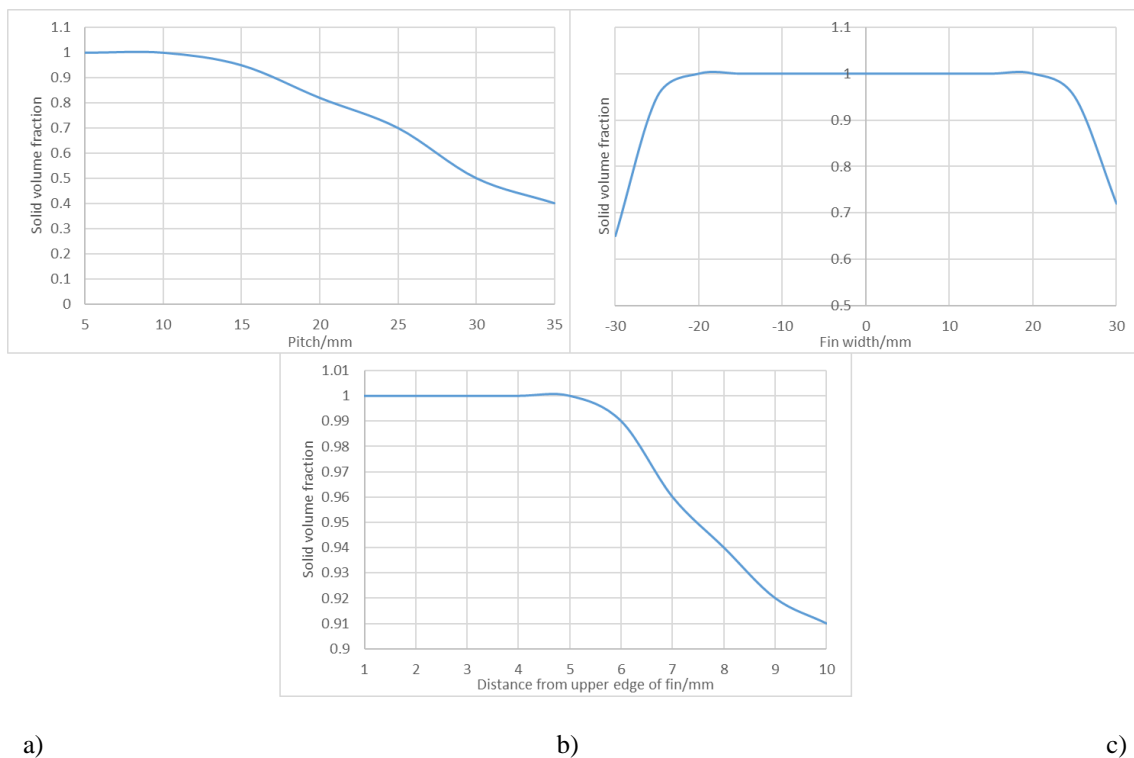


Figure 5-23: Solid volume fractions at line probes a) perpendicular to the fin (z-axis) b) adjacent to the horizontal edge of the fin (y-axis) c) parallel to the fin width offset by 15mm (x-axis), for freezing



The results were based on the solid volume fraction of the bottleneck freezing case after the complete melting of the domain in the 900s time duration. Based on the line probe perpendicular to the centre of the fin, complete freezing of the PCM was observed only until a distance of 10mm. The second line probe parallel by 15mm to the width of the fin depicted that the amount of frozen PCM decreased in a quadratic behaviour beyond a width of 40mm from the origin. This was due to the fact that natural convection effects were prominent only in the initial phases of freezing in the vertical orientation and were not effective beyond a certain horizontal distance. This was proven by the fact that phase change initiated after about 200s within the 40mm fin width, whilst increasing in time at widths beyond this. Finally, a line probe measured the solid volume fraction in a vertical direction adjacent to the upper edge of the fin. It was observed that the PCM was not completely solidified beyond 5mm. The required dimensions were selected based on these amounts of completely frozen PCM in the directions of the line probes. However, to assess the height of the fin and pipe positioning, the fin temperature contours for both melting and freezing are depicted in Figure 5-24:

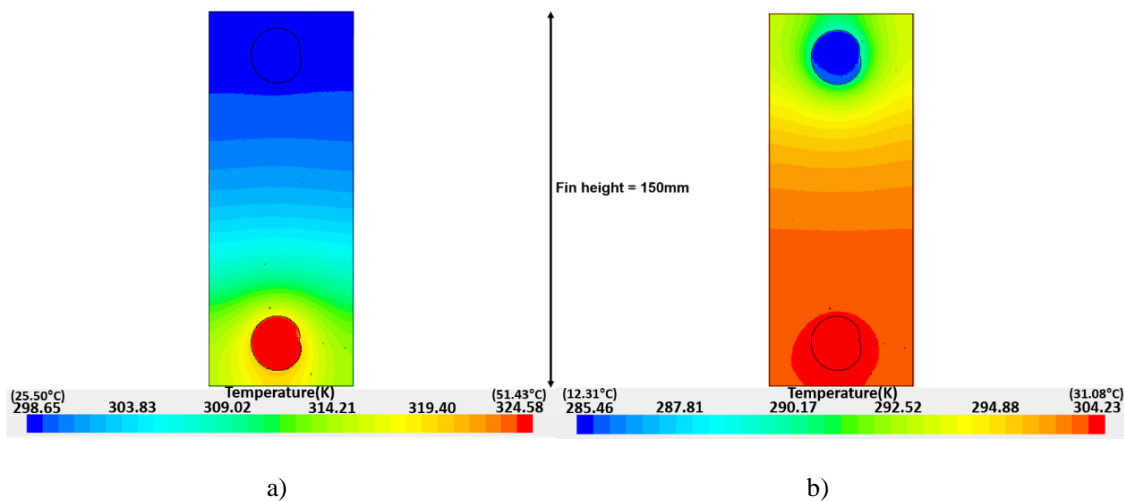


Figure 5-24: Assessment of the fin height based on the temperature gradient for a) melting b) freezing of the PCM

There exists a steep temperature gradient along the height of the fin of about 25K for melting and 20K for freezing. Freezing had a lesser temperature gradient primarily because less PCM was frozen, minimising the capacity of the fin to conduct and propagate heat. It was observable in both processes that beyond about two-thirds the

height, the fin was unable to effectively conduct heat as the temperature gradient dropped rapidly. However, the magnitude of the temperature gradient increased rapidly in the initial distance from the pipes, for both cases. The temperature at the extreme end for freezing was even more out of proportion than the liquidus temperature, resulting in no phase change at all in this position. The variation of the temperature after 900s at these extreme ends of the fin for both melting and freezing was almost negligible in comparison to the initial temperature. Therefore, it can be deduced that if the height was reduced by at least two-thirds, the fin would be more effective in providing complete phase change with a more uniform temperature gradient. Additionally, it was observed that the fin temperature profile was consistent for both melting and freezing at a radius of about 5-10mm from the pipe. For this reason, it was viable to minutely increase the pipe positioning from the fin edge to 20mm instead of 15mm. This would also promote a more uniform temperature distribution within the fin.

For thin fins, it can be reasonably assumed that the temperature would be uniform across this 1mm thickness [173]. Normally, thicker fins have more uniform temperature profiles along their height while thinner fins exhibit a temperature gradient, as was evident in this application [121]. However, thicker fins take longer for temperature increments. Based on this analysis, the five optimised parameters are presented in Table 5-7:

*Table 5-7: Optimised geometric parameters of the fins with respect to the HE*

	<b>Parameter</b>	<b>Value/mm</b>
<b>1</b>	Fin pitch	10
<b>2</b>	Fin width and height	40 × 90
<b>3</b>	PCM enclosed on sides of fin	5
<b>4</b>	Vertical height between pipes	50
<b>5</b>	Pipe position with respect to fin edge	20

This is only a single discrete set of parameters amongst numerous combinations resulting in complete melting and freezing. Further combinations are certainly possible, but since each parameter is interdependent on each other, a direct optimisation study was not possible. Similar to this sensitivity analysis, a combination would have to be constructed and systematically analysed.

## II. Fin vs. non-finned comparison

Based on the geometrical configuration of Table 5-7, a finned model was compared to a non-finned version as depicted in Figure 5-25, with the same dimensions and boundary conditions.

With the 60 fins of 10mm pitch on the 600mm length corrugated pipe, the increment in surface area of the copper domain was by a factor of 13.75, compared to the non-finned version. Similarly, the amount of volume occupied by the fins was  $1.78 \times 10^{-4} \text{ m}^3$ . This corresponds to a surface area to volume increment ratio of 5,607. The increment in the mass of the arrangement was only 1.45kg, proving that the cost-to-benefit ratio with fins was enormous. Aluminium fins would have been even lighter but with less thermal conductivity and an increase in contact losses, as both the pipe and the fins would be of different materials with dissimilar thermal expansion coefficients. The percentage reduction in the PCM mass with this fin configuration was only 6.7% and the latent storage capacity loss was about 25kJ.

As the initial objective was of maximising heat transfer, the amount transferred to the PCM in the finned arrangement was about 360kJ, with an average heat flux rate of 0.40kW for melting and 340kJ from the PCM at 0.38kW for freezing. These values correspond to 260kJ with 0.29kW for melting and 71kJ with 0.08kW for freezing compared to the non-finned arrangement.

The ratio of the actual to the maximum theoretical capacity in lieu of both sensible and latent heat is a widely used norm to categorise the exergetic efficiency of PCM HEs [167]. The maximum theoretical limit of heat transfer was when the PCM reaches the GW temperature while melting and the CW temperature while freezing, defined as:

$$\begin{aligned} \eta_{exergy} &= \frac{\text{Actual heat transferred to PCM}}{\text{Maximum theoretical heat transferred to PCM}} \\ &= \frac{mC_p(T_{final} - T_{initial}) + mL}{mC_p(T_{GW/CW} - T_{initial}) + mL} \end{aligned} \quad (5-5)$$

The exergetic efficiency for the finned case was 91.3% for melting, while that of freezing was 85.6%. These values were considerably high, yet below the maximum

since there was an upper limit to the amount of sensible heating, as per the law of thermodynamics. The same values for the non-finned case were 57.1% and 16.8%, clearly emphasising the effectiveness of the optimum fin geometry. Similarly, the Stefan number for this comparison was as defined in equation (5-3). For the finned case, the Stefan number for both melting and freezing was about 0.24. However, for the non-finned version it was 0.1 for melting and 0.24 for freezing. There was considerable sensible heating for melting in the finned geometry, since the optimisation was done based on freezing. Comparatively, most heat was added as latent energy in the non-finned version, without complete phase change. As in the finned case, both values in optimum configurations should be equal for complete phase change [121].

Although the enhancement in melting was noticeable, the improvement in the freezing process was substantial with the optimised fin arrangement. A widely used parameter in PCM HEs with enhanced heat transfer mechanisms is the effective thermal conductivity [166], defined as the ratio of the heat transferred with and without fins [121]. It was about 1.38 for melting and 4.75 for freezing in this application. The reason for this enhancement is depicted in the resistance diagram in Figure 5-25:

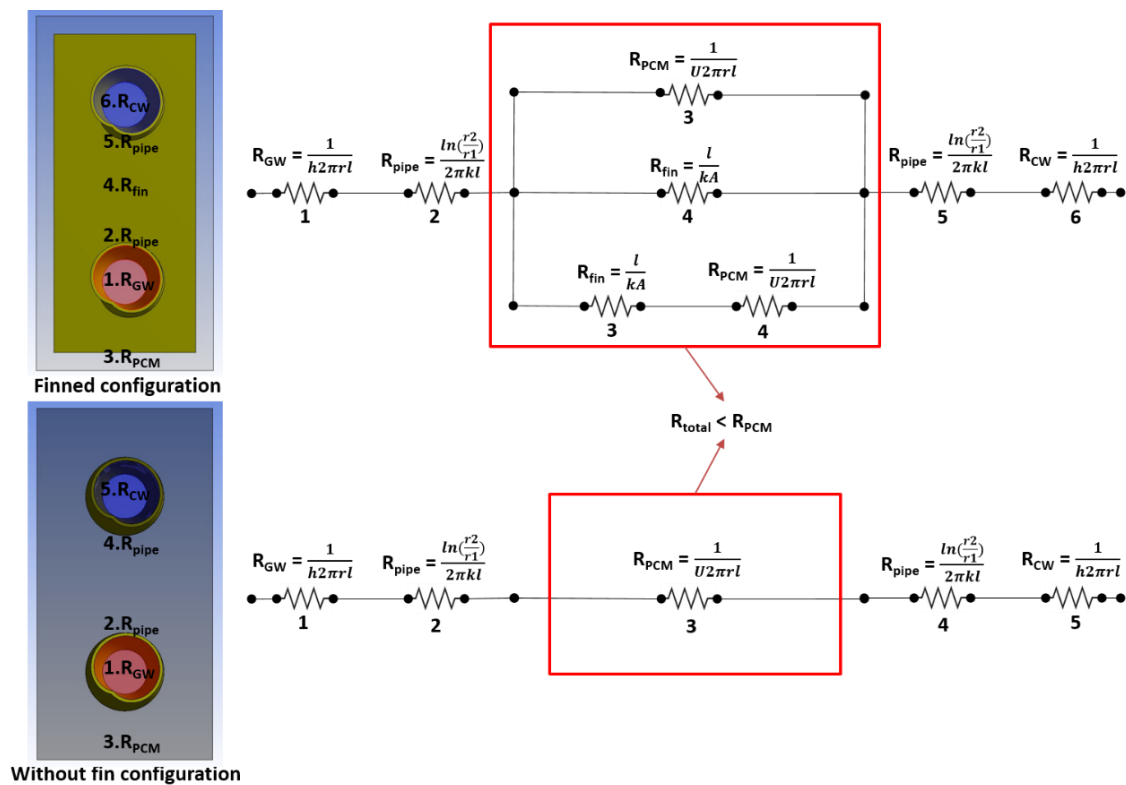


Figure 5-25: Thermal resistance diagram of the finned and non-finned configurations

Fins decrease the overall thermal resistance compared to a non-finned version, as two additional flow paths for the heat to propagate are provided [121]. The total thermal resistance of a parallel arrangement is much less compared to a series arrangement, resulting in an overall lower thermal resistance to heat flow. It is clear that the response time of PCMs is extremely slow. This becomes a hurdle in electronics and space applications unlike in solar thermal and building applications, where a response time of a few hours is acceptable [167], due to which fins are extremely effective. As a follow on from Figure 5-24, the temperature profiles of the fin in the optimised geometry are depicted in Figure 5-26:

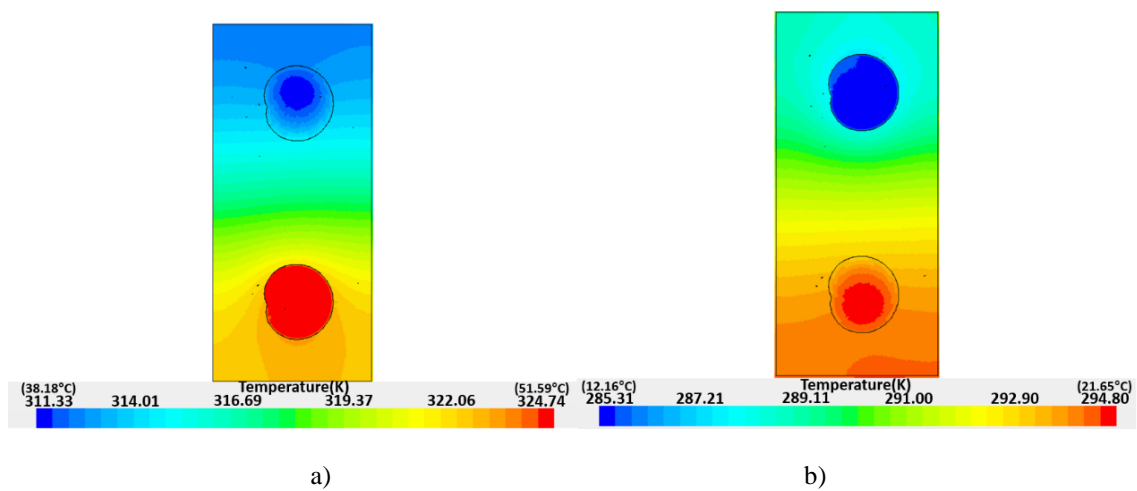
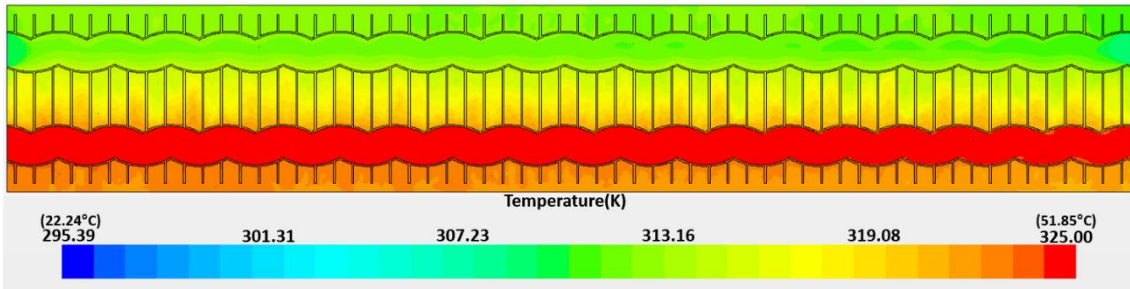
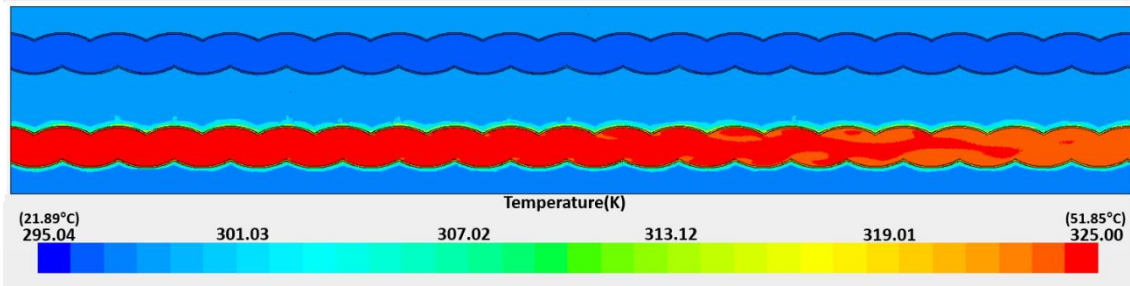


Figure 5-26: Temperature profile of the fin for the optimised geometry for a) melting b) freezing of the PCM

Comparative to Figure 5-24, heat propagation across the height of the fin was more uniform with a lower temperature gradient of only 13K for melting and 9K for freezing. At the same time, the temperature of the entire fin in freezing was well below the solidus temperature, resulting in complete freezing. On the other hand, in the case of melting, the fin propagated heat even more efficiently, being considerably above the liquidus temperature. Complete PCM phase change with uniform temperature profiles was clearly resonated in the temperature contour for melting of the finned compared to the non-finned arrangement of Figure 5-27:



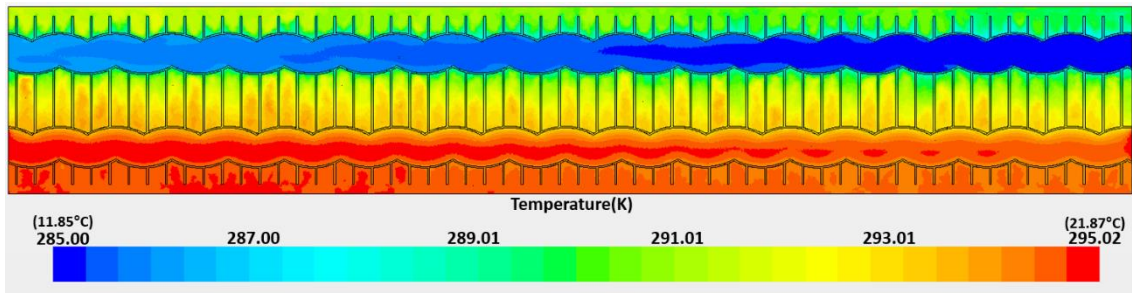
a)



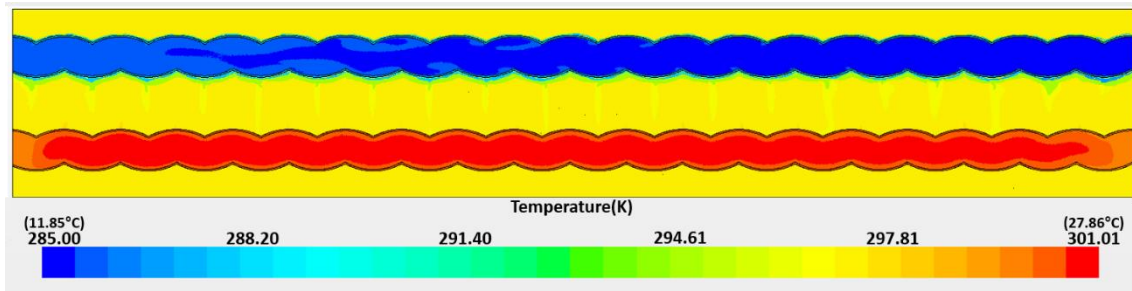
b)

Figure 5-27: Cross-sectional view of the temperature profile of the a) finned b) non-finned configurations for melting

For the finned configuration, the PCM in the vicinity of the GW pipe had an average temperature close to the fluid while the PCM close to the CW pipe was at a relatively lower temperature, but still in liquid phase. Compared to the non-finned version, PCM melting occurred only on the edges of the GW pipe with the remaining PCM having a uniform temperature profile below the liquidus temperature. After the melting process, the temperature profiles of the PCM and copper domain were imported into the freezing simulation. Consequently, the resulting temperature profiles for freezing had a similar trend as depicted in Figure 5-28:



a)



b)

Figure 5-28: Cross-sectional view of the temperature profile of the a) finned b) non-finned configurations for freezing

Similar to the melting phenomena, the fins ensured complete freezing of the PCM with the temperature differential only at about 5K from top to bottom of the HE. Since the PCM close to the GW pipe was already at a much higher temperature after the melting process, it remained so but in a solid phase. On the other hand, the non-finned version had freezing only near the lower edges of the pipe. The thickness of the frozen layer was even less compared to the phase changed layer in melting. This was because freezing is conduction dominated and the solid frozen PCM around the edges acts as an insulation layer making the entire process much slower compared to melting. Phase change for the non-finned version was almost negligible. Since the optimisation of the fins was done based on the bottleneck case of freezing, there was a considerable amount of sensible heat transfer in melting compared to freezing, as depicted by the time variant phase change plots in Figure 5-29:

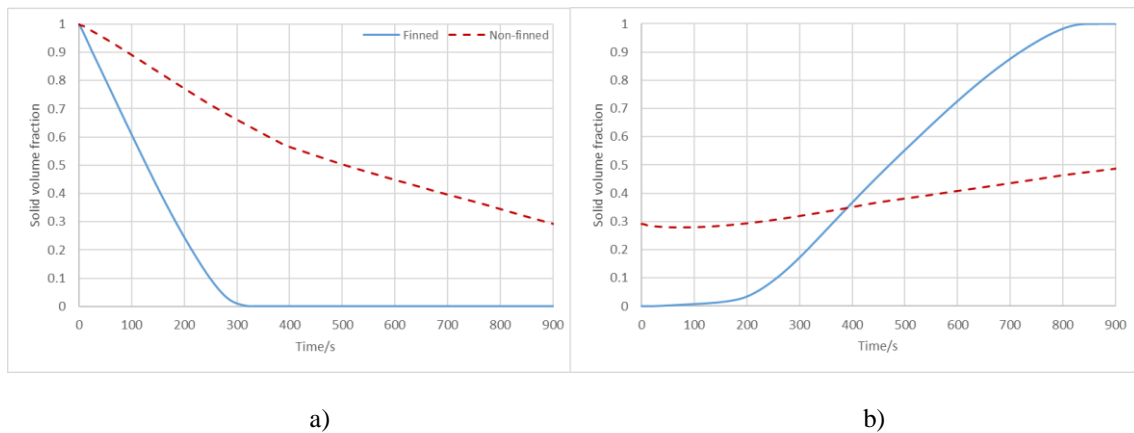
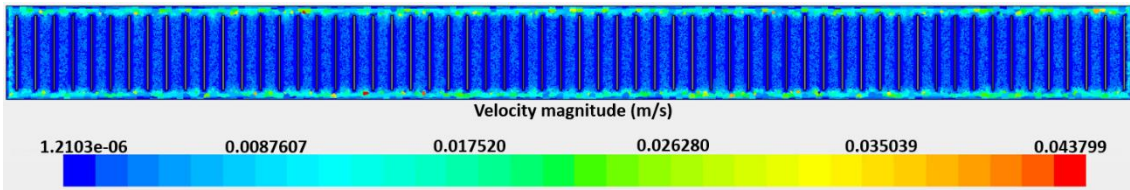


Figure 5-29: Phase change profile for a) melting b) freezing, of the PCM

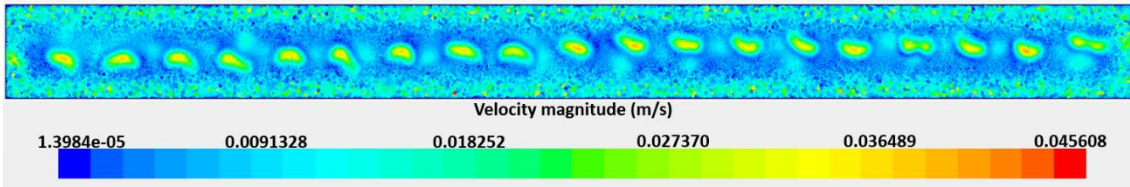
At about 320s, complete phase change of the PCM in melting occurred, after which the heat transferred was sensible. As expected [133], the heat transfer could be divided into three areas: pre-phase change sensible, phase change latent and post-phase change sensible heat, clearly visible in the freezing plot. Similarly, three distinctive freezing regimes were present with the fins involving slow initial convection followed by a sharp change to a faster conduction dominated regime for the remaining duration, completed by a slow conduction finish [153]. Initially, convection in the liquid PCM was followed by conduction as soon as the temperature falls below the liquidus temperature. The fins enhanced this conduction in the PCM, resulting in a much steeper gradient during this regime. In the non-finned version this regime was lacking, which eventually made the entire difference towards complete phase change.

The reason for a decrease in the melting time was that fins enhance conduction to initiate convection much earlier in the entire PCM volume. Although it is a known fact that fins are a hurdle to the flow of natural convection currents, the offset in convection hindrance is much smaller than the increment in conduction propagation, resulting in an overall improvement. Natural convection is initiated in the PCM as the Rayleigh number exceeds  $10^5$  [151] and is known to at least double the melting rate compared to heat transfer only via conduction in PCMs [121]. It was clearly an important heat transfer mechanism in both the arrangements, as can be seen in a cross-sectional velocity contour along the length of the geometries for melting in Figure 5-30:





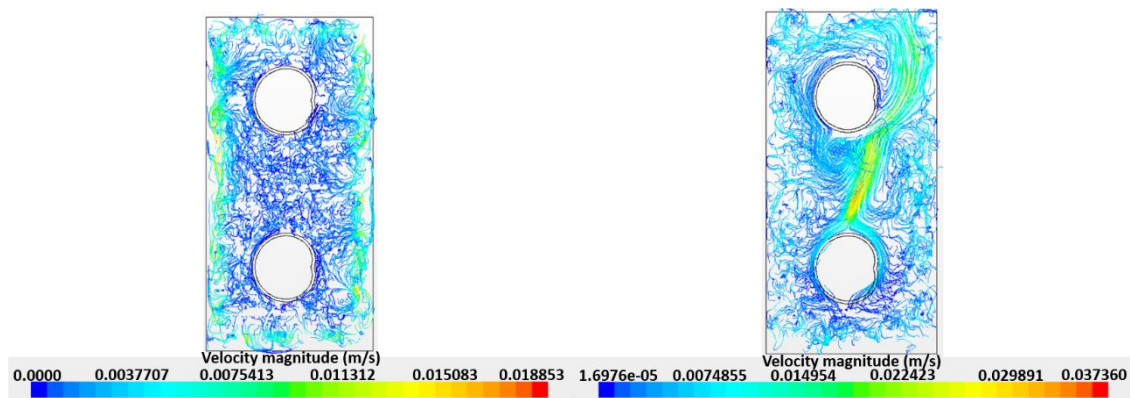
a)



b)

Figure 5-30: Cross-sectional view of the velocity profile of the a) finned b) non-finned configurations

The volume average velocity for the finned version was 0.004m/s and about 0.008m/s for the non-finned arrangement. The finned version inhibited convectional currents in the central portion of the contour while only allowing them to develop freely on the outskirts. In the non-finned version, the convection vortices were originating across the entire length, as in this case there were no restrictions to the movement. In a similar study [157], it was also observed that small vortices form only around the fins and the HTF pipe even in the early stages of melting. With the passage of time, these vortices increase in size along with moving vertically upwards due to buoyancy. They are clearly visible in the streamlines of the liquid PCM regime for both configurations in Figure 5-31:



a)

b)

Figure 5-31: Propagation of natural convection vortices in the a) finned b) non-finned configuration

In the non-finned version the vortices can be seen originating from the GW pipe towards the top of the HE. For the finned version there was no organised bulk movement of the vortices, but only towards the edges of the container. Most of the movement in the remaining portion was haphazard with limited velocities. Another parameter of interest was the change in temperature of the incoming fluids, as the CW would eventually be used for heating purposes in residential appliances. An overview of the outlet temperature profile for 900s is in Figure 5-32:

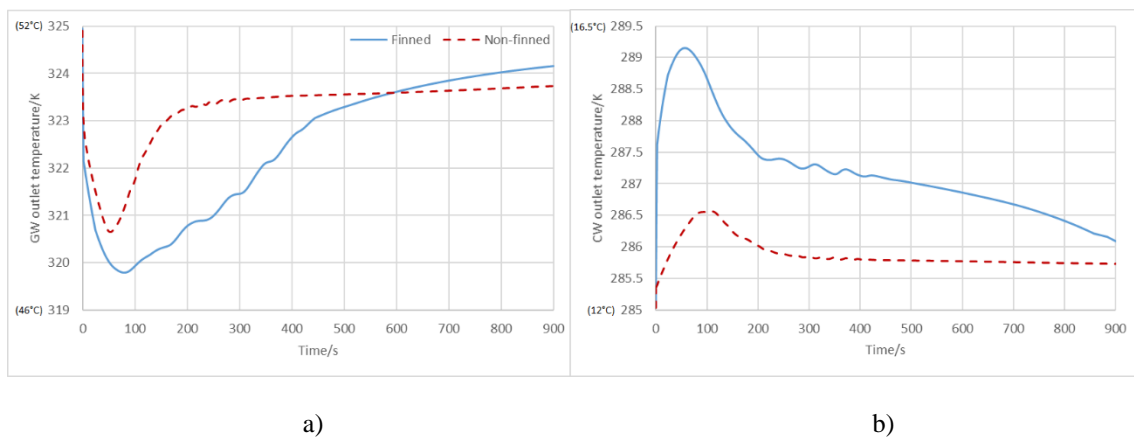


Figure 5-32: Outlet temperature profile for the a) GW b) CW flows

Initially, the temperature differentials were high for both processes, but eventually reached a steady-state to asymptotically decrease to the flow inlet temperatures. The average GW outlet temperature for melting in the finned case was 322.1K (48.95°C) while for the non-finned case, it was 323.1K (49.95°C). Similarly, the average CW outlet temperature for the finned case was 287.1K (13.95°C) while for the non-finned case, it was 285.9K (12.75°C). Although the change was not significant, the short length of this layout must be considered. In real practical HEs with longer pipe lengths this value would amplify to act as a decentralised heat source, as envisioned [10]. A measure of the effectiveness of this HE was based on the average heat transfer between both fluids defined as in equation (5-4) [165]. For the finned case, the effectiveness was 72.4% while for the non-finned geometry, it was 47.3%. At the same time, the temperature differentials in the fluid flows were much lower for the non-finned geometry.

## 5.6. Outcome

The values in this section signify that the developed prototype has a higher energy and exergetic efficiency, along with successfully decoupling CW and GW supply with demand. Based on the outcome of the results, a rectangular copper fin with 1mm thickness and configuration dimensions as presented in Table 5-7, was considered the best at a mass-flow rate of 0.1kg/s, as required in this application. A summary of the results of this configuration are presented in Table 5-8:

*Table 5-8: Performance results of the optimal fin configuration at a mass-flow rate of 0.1kg/s*

	<b>Finned configuration</b>
<b>Surface area to volume increment ratio</b>	5,607
<b>Exergetic efficiency for melting</b>	91.3%
<b>Exergetic efficiency for freezing</b>	85.6%
<b>Stefan number for melting and freezing</b>	0.24
<b>Effective thermal conductivity for melting</b>	1.38
<b>Effective thermal conductivity for freezing</b>	4.75
<b>Heat transfer effectiveness of GW to CW</b>	72.4%

## Chapter 6 - Design of the holistic heat exchanger (HE)

After selecting RT-25 as the PCM, a corrugated pipe (e4.5p30 mm) as a mode of internal heat transfer enhancement and 1mm thick rectangular copper fins as a mode of external heat transfer enhancement, the next phase was to holistically assess the performance of a full-scale HE with regard to GW heat harnessing for appliances. At the same time, assessing the techno-economic feasibility of installing such HE would also be beneficial. The next phases in the design were detailed numerical analyses to establish the thermal performance of the holistic HE as the basis of empirical correlations.

### 6.1. Overview

A holistic analysis of PCM-based HEs in many different applications have been conducted both numerically and experimentally. The most common application is in the passive heating and cooling of indoor air in buildings. Garg et al. [188], investigated the performance of a CW circulating encapsulated PCM HE to extract heat from an indoor room in Indian summer conditions. With such a passive technology, it was found that the mean air temperature in the room was 6K lower with 50% less heat gained from the ambient. Additionally, the HE was more beneficial over long-term durations by ensuring a more consistent indoor air temperature. In a similar study [189], a PCM HE was experimentally tested to retrieve coolness accumulated over night to provide to a cabin for free cooling in the day. The 76kg HE cooled the cabin indoor temperature by only 2.5K, making it useful to be used in hybrid of air-conditioning units to lower energy consumption. Similarly, Rajagopal et al. [190], investigated a flat plate PCM modular HE as a source of free cooling in a room in Bangalore. The HE had the capacity to maintain the room temperature at 303K (29.85°C) for durations of up to 8 hours. In a real-scale experimental study, Rouault et al. [191], provided cooled indoor air by a horizontal shell and tube paraffin PCM HE. Based on the experiment, a numerical simulation was validated to be used in an illustrative application with an optimisation programme for single family houses in Madrid. Cano et al. [192], used a shell with a PCM and tubes with water-based HE to recover the residual energy of a hydrogen cycle to be used in air-conditioning applications. Four different PCMs with

varying water flow rates along with different operating circumstances were assessed in a sensitivity analysis based on this experiment. In a novel application, Zhu et al. [193], developed a small PCM integrated HE in a gas mask for firefighters. This device used a mixture of paraffin and graphite particles to cool hot air from 500K (226.85°C) to 313K (39.85°C) in a gas mask for a duration of about 20 minutes. Using PCM-based HEs in HP applications for HVAC are also quite common. Zhou et al. [194], devised a novel pipe circumferentially surrounded by a PCM embedded in the ground that served as a HE for cooling applications. This PCM earth-air HE was 20.24% more effective than a simple earth-air HE, comparatively lowering the temperature by a further 0.83K. Bottarelli et al. [195], analysed the performance of coupling shallow ground-source HPs with PCMs as backfill materials for long-term seasonal energy storage in a residential building in Italy. The COP of the HP was improved with the inclusion of the PCM, whilst providing a source of thermal energy all year long, even in winter. Wenju et al. [196], holistically investigated a double-spiral coiled tube HE with a PCM as the evaporator of an ASHP. A numerical model was validated based on an experimental setup for both the frosting and defrosting of the HP. Furthermore, the use of PCM-based HEs in passive solar thermal applications is also a major research area. Zipf et al. [197], developed a highly efficient screw HE used to store thermal energy for steam production in concentrated solar thermal power systems. With this novel design, the HE surface-area was decoupled to its storage capacity which enhanced the heat transfer rate and thermal conductivity of the PCM. Additionally, this HE had a self-cleaning effect that minimised fouling and efficiency losses over the long-term. Youssef et al. [198], developed a unique water flowing spiral-wired tube HE with a PCM-based outer shell coupled with an indirect solar assisted HP for hot water production. In a different application, Shon et al. [199], used a fin-tube HE filled with PCM to re-heat engine coolant by extracting the waste thermal energy, whilst a vehicle was not operating. It had the capability to store 1,300 kJ of heat and increase the coolant temperature by 56K, while being lightweight at only 4.2kg.

The holistic performance of a PCM-based HE to harness waste heat from non-industrial GW to CW considering both the melting and freezing of the PCM was a research gap. At the same time, such a HE would have heat transfer enhancement mechanisms both internally within the pipe flow and externally inside the PCM. This would uniquely increase the performance which was especially required for this high impulse

application. Since all non-industrial buildings do not have uniform GW production characteristics, the novel design methodology of this thesis can be potentially applied to any non-industrial building. Empirical relationships for the performance of a unit-volume were put forward for applicability to any sized HE within this research domain of GW heat harnessing. Additionally, the investigation of multi-cascaded PCMs with respect to both freezing and melting in this application was innovative. The practical applicability of this designed prototype to a conventional appliance has been techno-economically assessed in a typical household in the UK.

This phase of the research has the following objectives:

- A basic review of the methods to numerically model a PC-based HE outlining the reasons for selecting the unit-module method.
- A basic review of the methods to holistically assess the thermal performance of HEs outlining the reasons for selecting the method to formulate empirical correlations as the design methodology.
- Numerically establishing the thermal performance of the holistic HE.
- Investigating the performance of a multi-cascaded PCM arrangement.
- Establishing the techno-economic feasibility of the holistic HE based on usage in a typical UK household.

## **6.2. Design methodology**

The harnessing of heat from GW was not without challenges, which were tackled and integrated into the design in the three-phase research methodology outlined in Table 1-2. The most viable option for GW heat harnessing in residential appliances is extracting the heat into the incoming CW, although with PCMs, the stored GW heat can be used in many other applications. Using the three-phase research strategy, an optimum HE configuration was selected with the prescribed boundary conditions. The outcome along with the procedure for each phase is summarised in Table 6-1:

Table 6-1: Summary of the results of the three-phase research methodology to harness GW heat for usage in CW in residential appliances

	<b>Research strategy</b>	<b>Procedure</b>	<b>Outcome</b>
<b>1</b>	Heat storage – Phase 1 – Selection of the PCM	The 2-phase solution to the Stefan problem coupled with the PSO technique was used to select the best thermal parameters of the PCM within the boundary conditions.	A PCM with a melt temperature of 298K (24.85°C) and a latent storage capacity of 170 kJ/kg was selected. RT-25 manufactured by Rubitherm is a commercial product matching this criteria.
<b>2</b>	Heat extraction – Phase 2 – Internal heat transfer enhancement	Based on a literature review, corrugated pipes were selected as the best enhancement mechanism in this application. An experimental test rig was used to validate a 3D numerical model. Upon which, a parametric study was carried out to select the best configuration based on three different TPFs with the considered boundary conditions.	A corrugated copper pipe having an internal nominal diameter of 12.7mm with a rib height ‘e’ of 4.5mm and a corrugation pitch ‘p’ of 30mm was selected. This configuration has a TPF2 ratio of 3.1 for GW and 2.4 for the CW flow.
<b>3</b>	Heat transfer – Phase 3 – External heat transfer enhancement	Based on a literature review, fins were selected as the best PCM enhancement mechanism suitable for this application. Using an experimental model, a 3D numerical simulation was validated to perform a sensitivity analysis. The optimum fin configuration providing the complete PCM phase change, maximum heat transfer and GW/CW temperature differentials in the 900s time frame was the objective.	Copper fins of a 90mm height, 40mm width and 10mm pitch, with a thickness of 1mm were selected. These fins phase changed the entire PCM in its vicinity for both melting and freezing, maximising latent heat transfer. At the same time, the mass reduction of the PCM was only 6.7%, corresponding to a latent heat capacity loss of 25kJ.

To gain a thorough understanding of the thermal physics of a full-scale HE, a numerical study is more insightful compared to an experimental analysis whilst having only a minor loss in accuracy between 2-10% [200]. Additionally, CFD-based numerical simulations are known to be more economical and easier to implement, especially for the preliminary design process of a HE [201]. Amongst the five basic numerical

methods to construct and analyse a holistic HE, the most appropriate to this application was selected with the following reasoning [197,198]:

- Analysis by scale: This requires powerful computational hardware and a very large fine mesh for a CFD analysis, especially in this case to accurately capture the details of the pipe corrugations and fins, which was not feasible.
- Analysis with downscaling: This is the most common technique in automobile design whilst keeping important features in the geometry, especially for wind tunnel CFD analysis for aerodynamic applications. However, in this application, the effects of turbulence in the corrugated pipes and the visualisation of gravity-assisted natural convection in the PCM would be undermined with this approach.
- Symmetrical analysis: This simplifies the layout to a great extent and if permitted, even a 2D design can be constructed. However, in this case, due to the corrugations in the pipes, a symmetrical plane does not exist for a CFD analysis.
- Analogical methods: The important parameters of heat transfer in a non-CFD platform can be modelled using analogies with certain concepts of physics. The most common method is using the analogy of electric current and heat flow. Each element in the HE can be specified with a thermal resistance, capacitance, porous surface properties, etc. However, accurate analogies are extremely difficult to mathematically formulate without a basic CFD analysis for this complex geometry involving PCMs linked with corrugated finned pipes.
- Unit-module method: Another approach in CFD simulations is to identify a unit-module in the HE with repetitive behaviour. The HE is usually subdivided with a unit-volume length in the main flow direction modelled with iterating the input parameters between each unit-module simulation, to holistically assess the virtual serially-linked units as an entire HE in steps. This unit-wise modelling of the HE is a simple, accurate and feasible method to be used in this analysis.



A unit-volume having a piping length of 600mm was constructed in section 5.5.3, as the basis of an iterative study to numerically model the holistic performance of the HE, using Star-CCM v12.04. Based on the results of Table 6-1, an overview of this unit-volume of the optimum counter-flow HE configuration for harnessing GW into CW in appliances for a residential building, is presented in Figure 6-1:

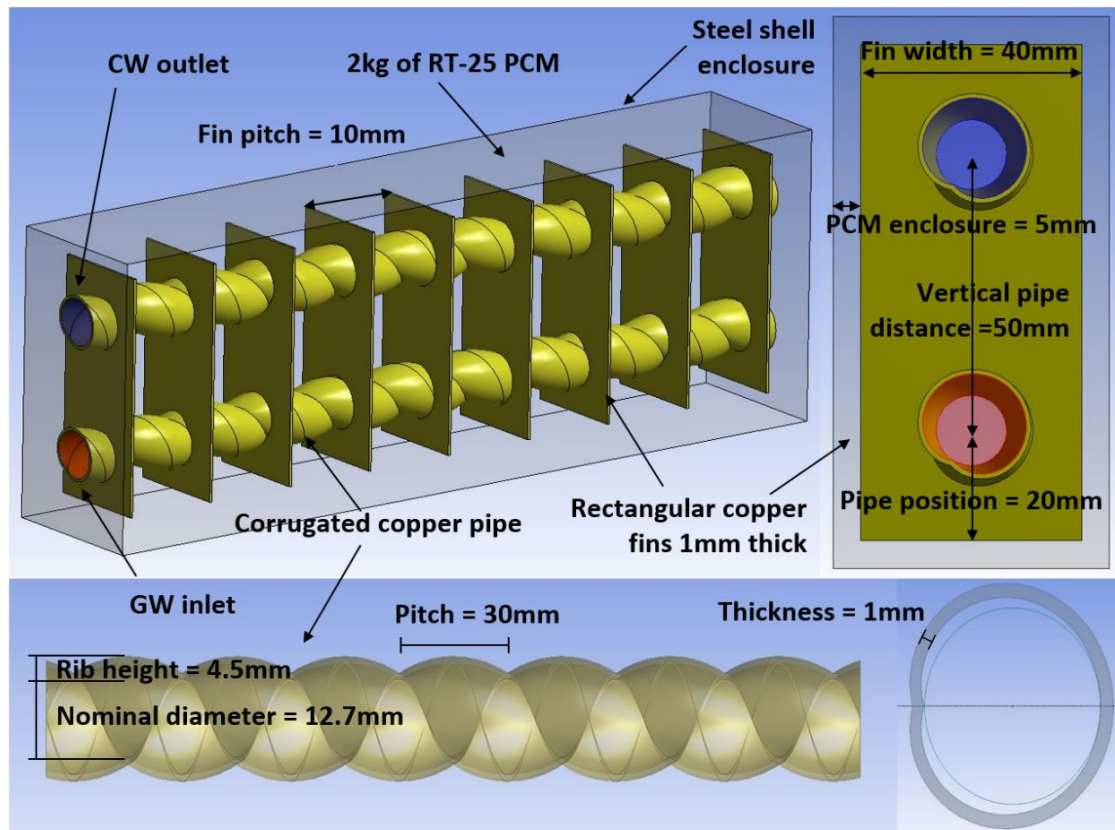


Figure 6-1: Configuration of a unit-volume of the designed HE

The mathematical solvers and mesh settings were similar to those previously conducted in section 5.5. As per the approach, the parameters of the unit-volume were periodically iterated from the output of one simulation as the input to the next. The first iterated parameter was the outlet temperature of the GW/CW flows which was eventually necessary to establish the thermal parameters of the holistic HE. Since the arrangement was counter-flow, the iteration orders were reversed for the GW and CW flows. The second parameter to be iterated was the outlet velocity profile for both GW and CW to account for the flow conditions, keeping in mind the fully developed turbulent flow. Finally, as the holistic HE models both melting (GW flow) and freezing (CW flow), the temperature profiles of the PCM and the copper pipe-fin domains were iterated from the

output of each set of simulations as the final parameter. As mentioned, the order of iterations for the GW flow and CW flow were reversed as the flow was counter-flow. In total, seven iterations each of this unit-volume were done for melting and freezing, as summarised in Figure 6-2:

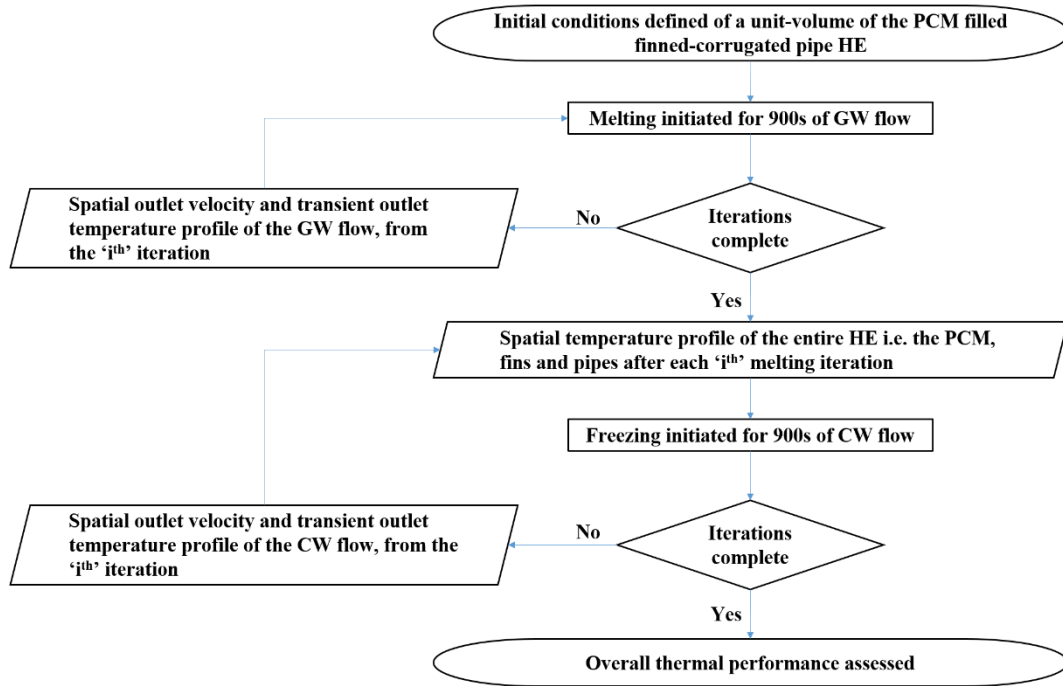


Figure 6-2: Procedure of the iterative scheme to model a holistic HE, based on a unit-volume

The seventh temperature profile of the PCM and metallic pipe-fin domains in the melting of the unit-volume was taken as the input for the first iteration in freezing and so forth. To analyse the performance of the holistic HE based on the outcomes of the CFD simulations of the unit-volume, the most common techniques along with their constraints with regard to this application [202,203], are as in Table 6-2:

Table 6-2: Adaptability of typical methods for holistic HE analysis to this application

	Technique	Overview
1	Effectiveness-Number of Transfer Units ( $\epsilon$ -NTU)	The overall performance of the HE was unknown but that of a unit-volume was known, making the applicability difficult, since these methods are sizing-based, using holistic thermal parameters. PCM phase change is a combination of convection and conduction, making it impossible to mathematically predict the U-value for both melting and freezing. The HE in this application was three-way including GW, CW and the PCM. Both methods are suitable towards sensible heat transfer and not particularly useful for latent heat storage applications.
2	Log Mean Temperature Difference (LMTD)	

		Both models assume constant thermo-physical properties of the PCM which are actually non-homogenous with non-linearity and inconsistency. As an example, the specific heat capacity of a PCM is non-linearly dependent on the incoming heat flux [150]. This application was of a transient nature, making the accuracy of these steady-state models limited. In these models, the PCM is modelled at a constant temperature although there are enthalpy variations. Both methods are more accurate for 1D simpler configurations.
3	Conduction Transfer Functions (CTF)	The CTF method is used to predict transient heat conduction, not convection in the PCM. Hence, it is more suitable to model only freezing but not melting. Using a time series method, heat fluxes are calculated based on surface temperatures. The inclusion of corrugations and fins make it impossible to determine the complete surface temperature without using an additional numerical technique. A finite element-based multiple CTF value method would be appropriate for this application but complicate things with limited accuracy.
4	Dimensionless analysis to predict correlations	Dimensionless analysis generalises basic correlations to increase their applicability in similar applications. Such design equations for specific geometries have been developed but with no single generic curve reported in the literature, especially for such applications involving finned corrugated pipes in a PCM for both melting and freezing. The complication of the geometry in this application along with the variant PCM behaviour would make the development of such correlations, very general and inaccurate. Similarly, analytical correlations for PCM HEs, especially in 3D layouts, are non-existent and imprecise to derive without numerical techniques.
5	Empirical correlations of useful parameters	Based on experimental/numerical observations, empirical relationships of important variables are developed. It is the most common approach to model PCM-HEs for novel applications. However, the validity of the equations is restricted only to the specific application.

The development of important empirical relationships relying on numerical modelling was the most suitable problem-based technique for this application, also it is the most commonly used for PCM HEs [203]. Lazaro et al. [204], developed an empirical model of the thermal performance of a real-scale PCM-air HE based on experimental results. Bie et al. [205], formulated an empirical correction model to predict the average PCM temperature with better accuracy in a 3D simulation of a HE for solar applications. Dolado et al. [206], experimentally tested a real scale air-PCM HE with different operating conditions. An empirical model based on a multi-variant linear regression analysis of the temperature increment of the air was developed as a designing tool for similar HVAC applications. Wang et al. [207], established a correlation with 92.5%

accuracy of the ‘Nu’ number and ‘f’ for different arrangements of spacing bars in a spiral-wound HE based on numerical data. In fact, many researchers even use the other methods listed in Table 6-2, including the e-NTU method in PCM applications with custom derived empirical relationships [202]. In PCMs, the thermal transmittance and heat transfer area of the phase change front are consistently changing. To tackle this, most researchers empirically model this aspect coupled with the  $\varepsilon$ -NTU method for a mean assessment. Castell et al. [208], established an empirical relationship for a coiled tube in a PCM for cold storage applications to be coupled with the  $\varepsilon$ -NTU method. The relationship defining the effectiveness of the system dependent on the mass-flow rate per unit area accurately predicted the overall thermal performance for different operating conditions validated by a case study.

### **6.3. Performance of the HE**

#### **6.3.1. Thermal performance**

Three parameters were of prime interest to establish the thermal practicality of the HE:

- PCM phase change ratios for both melting and freezing.
- Heat transfer to and from the PCM.
- Temperature variations of the CW/GW flows.

As per Table 6-1, the objective of the configuration was the complete phase change of the PCM in the unit-volume for both melting and freezing. The results of the first parameter of interest for the seven iterations are presented in Figure 6-3:

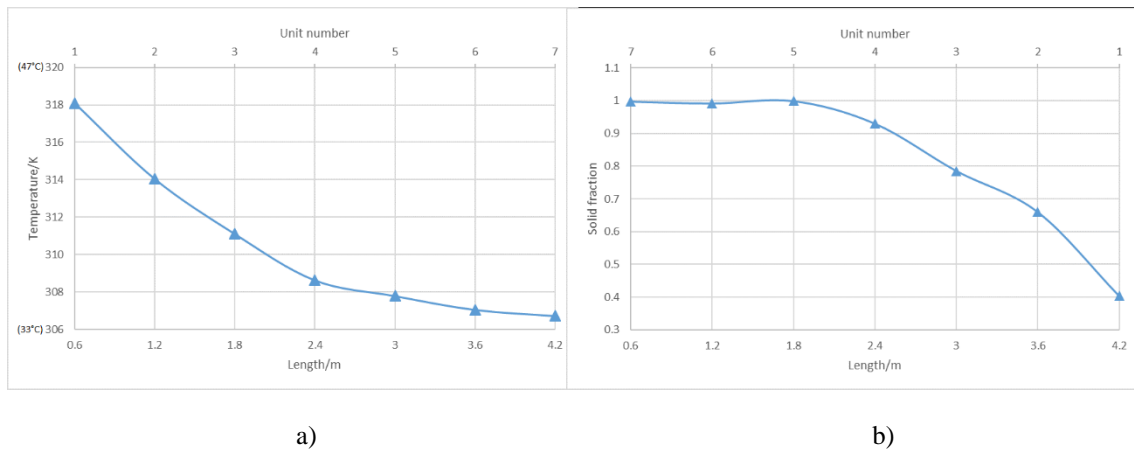
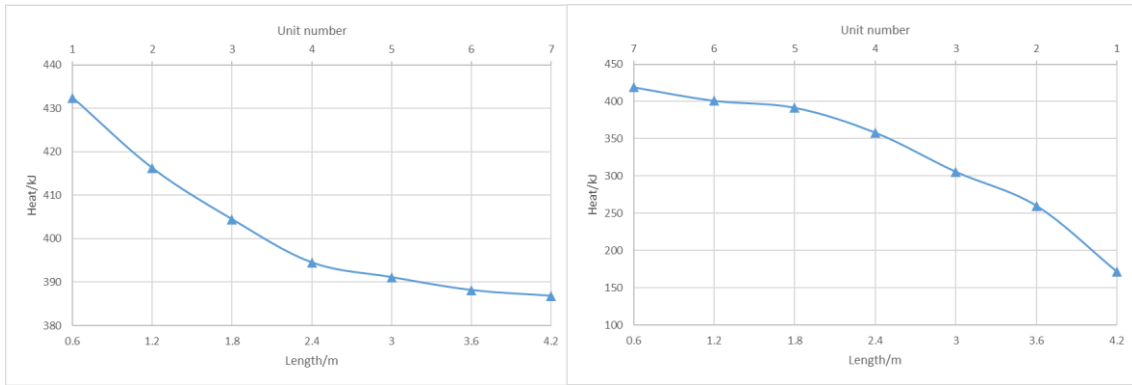


Figure 6-3: a) Average temperature of the PCM after complete melting b) Solid volume fraction of the PCM after freezing

The design of the unit-volume was established based on the bottleneck freezing case, since melting is 67% faster compared to freezing. Consequently, complete phase change occurred in all seven iterations of the melting simulations. The time at which the PCM's solid fraction completed its melting increased linearly between 339s in the first, to 594s in the final iteration. As a result, considerable sensible heat was absorbed into each unit during the melting simulations. The average temperature of the entire PCM domain after each iteration was exponentially decreasing, as presented in Figure 6-3a. For the case of freezing, complete phase change occurred only in the first three iterations, after which it dropped exponentially. The reason for this was that the development of the design was done at a CW inlet temperature of 285K (11.85°C). As the CW gained heat after every unit-volume iteration, its temperature increased, resulting in a lesser phase change fraction through the remaining iterations, with only a 0.4 solid fraction in the last one. A similar trend was observed in the heat transfer values into (GW flow) and out (CW flow) of the PCM, as in Figure 6-4:

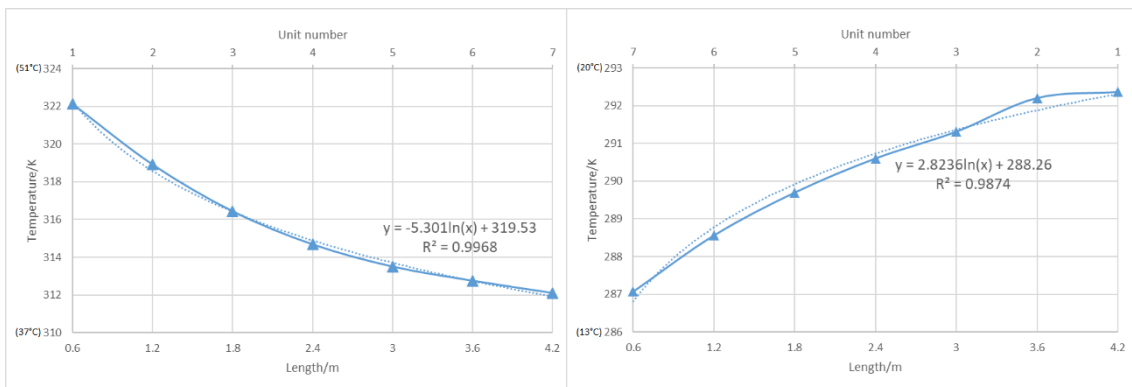


a)

b)

Figure 6-4: Heat a) absorbed into the PCM during GW flow b) released from the PCM during CW flow

As a result of the optimisation in the design process aimed at the complete melting and freezing of the unit-volume, about 95% of the thermal energy transferred into the PCM by the GW was absorbed by the CW in the first three iterations. Beyond which, the amount of heat transferred by the GW decreased only by 40kJ from the maximum. However, in the case of freezing, the absorbed energy decreased exponentially by about 50% of the initial maximum, proving that freezing was the bottleneck case in the design process. This is reflected in the temperature profiles of the GW and CW flow in Figure 6-5:



a)

b)

Figure 6-5: Temperature profiles for a) GW outlet during PCM melting b) CW outlet during PCM freezing

For the GW flow, the temperature differential was about 13K after the end of the seventh iteration from the initial 325K (51.85°C), while it was only about 7K for the CW flow from the initial 285K (11.85°C). Both plots have a logarithmic nature as is typical of fluid flows in HEs [209]. Based on these plots, empirical correlations have

been established with a high R-square value to predict the temperature profiles for a higher length of piping for this HE configuration.

### 6.3.2. Multi-cascaded PCMs

These seven iterations corresponded to a total piping length of 4.2m. In this HE length, only 54% of the heat extracted from the GW was transferred to the CW, as reflected in the temperature differentials of Figure 6-5. The leading reason for this disparity is illustrated in Figure 6-6:

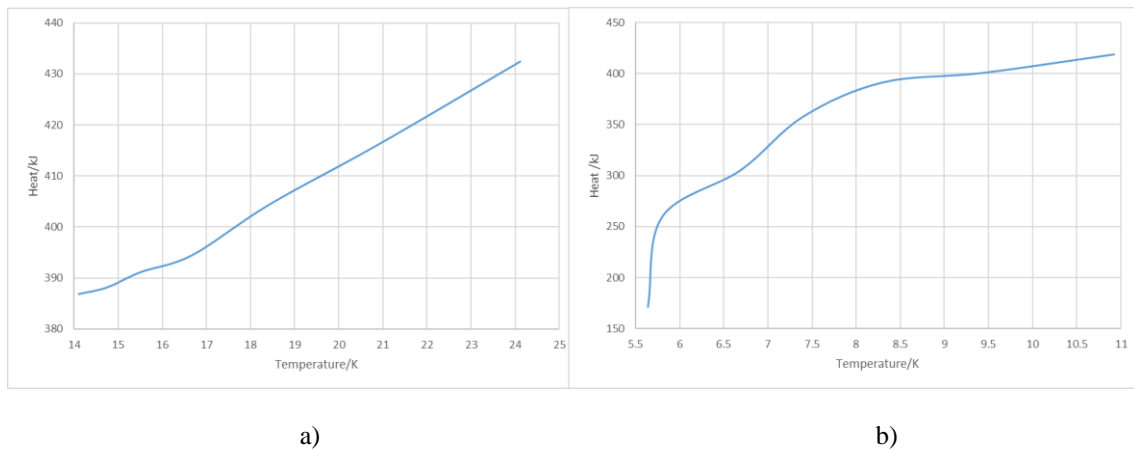


Figure 6-6: PCM a) heat absorbed vs  $\Delta(T_{GW} - T_{melt\_PCM})$  b) heat released vs  $\Delta(T_{melt\_PCM} - T_{CW})$

As per Table 6-1, the PCM used in the unit-volume iterations for both melting and freezing was RT-25, having a melt temperature of 298K (24.85°C). The temperature differential of this PCM melt temperature with the GW was relatively 2.5 times larger than that with the CW. For this reason, the heat transferred to the PCM from the GW was linear with not much variation in the values on the y-axis. For freezing however, the heat absorbed by the CW from the PCM was not linear and considerably decreased when the temperature differential decreased below 6K. Hence, it was clear that to maximise heat transfer, the temperature differential must always be kept above this minimum limit. Similar to electric circuits, the driving force of heat is the temperature differential analogous to current with voltage. Additionally, as per the first law of thermodynamics, the transfer of heat is linearly proportional to the  $\Delta T$  between the source and sink [209]. In this HE, the reduction in overall heat transfer eventually affected the outlet temperature for both the CW and GW flows. Consequently, a

relationship of the temperature increments of these fluids related to this  $\Delta T$  is presented in Figure 6-7:

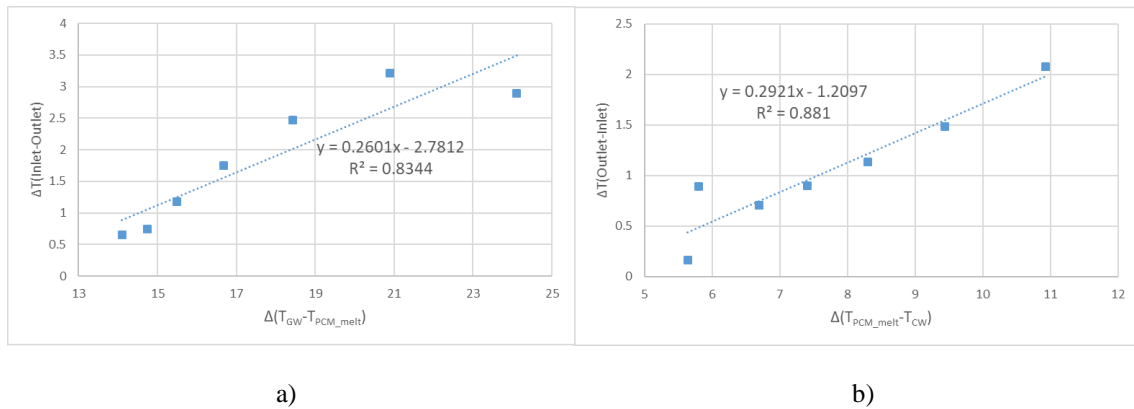
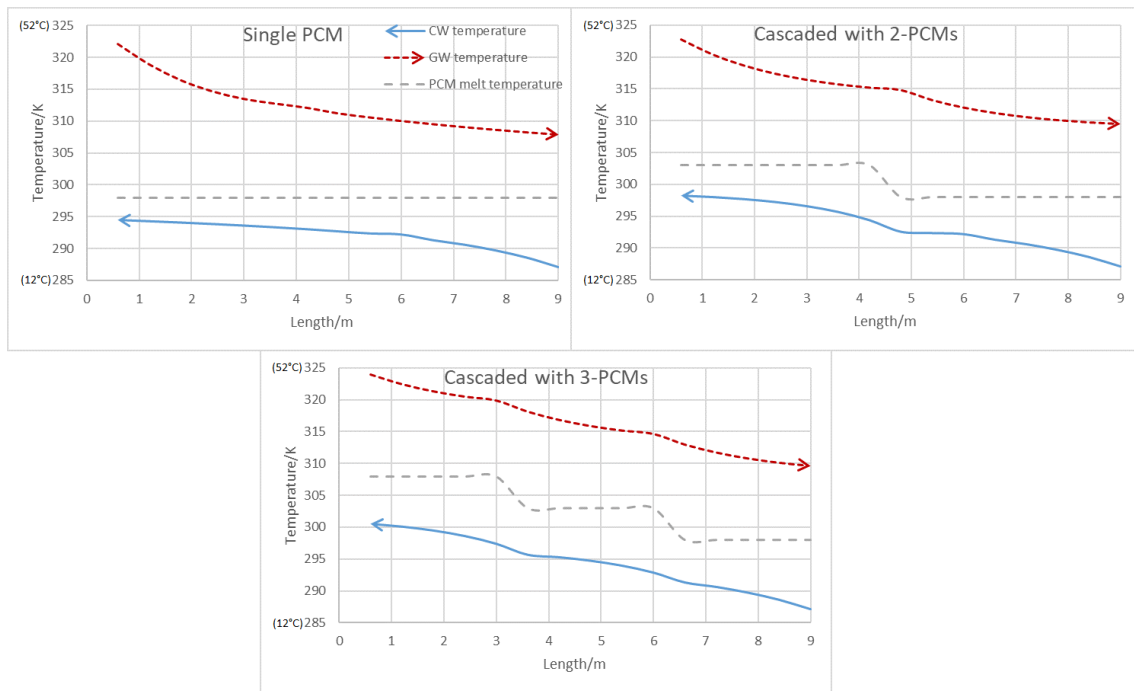


Figure 6-7: Fluid flow vs the fluid outlet-PCM, temperature differentials for a) GW b) CW flow

Both relationships were predicted with a linear empirical correlation with an acceptable R-square accuracy [209]. The increments in the GW temperature were about two times higher, since the differential with the PCM melt temperature was in the range of 24-14K. On the other hand, the increments in the CW temperature were much lower, with the temperature differential in the range of 11-6K. As a result, the GW easily transferred heat into the PCM, which could not be fully absorbed by the CW in the 900s time duration. Especially after the three initial iterations of the CW flow, this caused a huge disparity in the fluid temperature differentials which can easily be optimised. A commonly used optimisation strategy to passively enhance this heat flow between a PCM and the fluid is using multi-cascaded PCMs within a single HE [171]. Cascaded combination PCMs have sequentially decreasing melt temperatures along the longitudinal length of the GW pipe. As the CW was in a counter-flow arrangement, this would maintain a consistent  $\Delta T$  for both fluids with the PCMs, resulting in equal heat transfer values as outlined in section 5.2.3 [171]. The most commonly used number of cascaded PCMs in such arrangement is three, as enhancement benefits beyond this number decay exponentially [161]. Based on the empirical correlations of Figure 6-7, the thermal performance of a cascaded combination of two and three PCMs was investigated. The melt temperatures of the additional PCMs were selected to ensure a consistent  $\Delta T$  between the GW flow of 17-10K and the CW flow of 11-7K, as the heat transfer within this range was the maximum, as per Figure 6-6. Additionally, the usage of a single PCM was compared with the cascaded cases based on the empirical GW/CW



temperature profile equations developed in Figure 6-5. The resulting temperature profiles are presented in Figure 6-8:



a) b) c)

Figure 6-8: Temperature profiles with a) single b) three-cascaded c) two-cascaded PCMs

For uniformity, all three HE designs had a 9m length, derived as serially coupled arrangements of the unit-volume based on the simulation results. The two-cascaded option varied the PCMs after 4.5m of fluid pipe length with melt temperatures of 303K (29.85°C) and 298K (24.85°C). The three-cascaded combination varied the PCMs after every 3m with melt temperatures of 308K (34.85°C), 303K (29.85°C) and 298K (24.85°C). In both cases, these PCM melt temperatures were arranged from the GW entrance. The temperature profiles of the CW and GW exhibited typical logarithmic counter-flow behaviour as is common in the literature [202,209]. The counter-flow arrangement provided a better heat transfer between the hotter portions of the two fluids on the one hand and the colder portions at the other. The CW outlet temperature can never exceed the PCM melt temperature while the GW outlet temperature cannot go below this temperature. However the cascaded combinations sequentially varied the PCM melt temperature to provide an overall higher temperature differential for both the GW and CW. As was evident from Figure 6-8, the

cascading ensured no disparity between the fluid end-temperatures, as the push of heat from the GW was balanced by the pull of heat to the CW with minimal inefficient sensible heat transfer. Consequently, the end temperatures of the GW between each combination of Figure 6-8 increased by 1K starting from 307K (33.85°C) in the single PCM arrangement. However, the end temperature of the CW increased by 4K in the two-cascaded combination and by 6K in the three-cascaded combination from the initial value of 294K (20.85°C) with the single PCM option. Hence, based on the CW outlet temperature, the two-cascaded arrangement improved the performance by 40% while the three-cascaded arrangement improved it by 64% to a final value of 300.6K (27.45°C). In this optimum three-cascaded option, both the GW and CW had net temperature differentials of 15K which has clearly optimised the push and pull of heat from the PCM. A practical layout of this HE is presented in Figure 6-9:

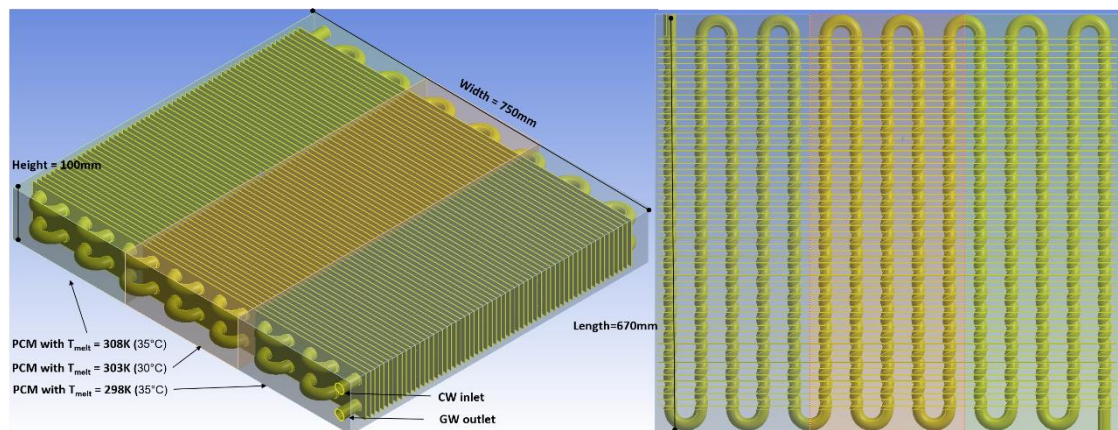


Figure 6-9: Layout of the holistic HE having three-cascaded PCMs with a piping length of 9m

The three different PCMs in this layout can be divided by a thin insulating impermeable sheet to avoid mixing. Another factor for this HE was the pressure loss, which is particularly important for GW heat harnessing. As per section 4.5.7, the selected corrugated pipe reduced pressure losses compared to a simple pipe by about 10%, due to the ability to provide a smoother helical path to the fluid. Consequently, the pressure losses for both fluid flows at a mass-flow rate of 0.1kg/s were about 700Pa/m. This corresponds to a pressure loss of only 6.4kPa for this 9m HE.

## 6.4. Case study

As previously outlined, the design of this HE was based on a mass-flow rate of 0.1kg/s with a GW inlet temperature of 325K (51.85°C) and 285K (11.85°C) for the CW. These boundary conditions resulting in the HE configuration were applicable to many typical residential appliances, as per Figure 6-10:

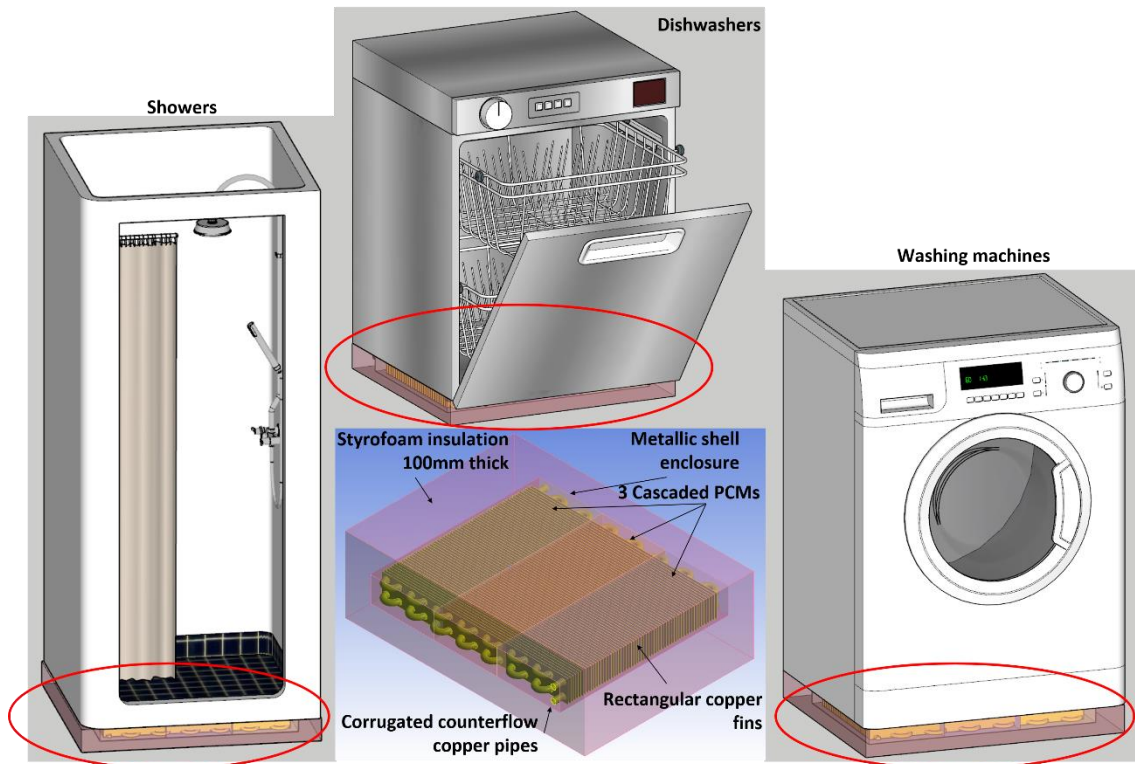


Figure 6-10: Overview of applicability of the holistic HE in typical residential appliances

In practical installations, a 100mm thick Styrofoam insulation layer with a thermal conductivity of 0.033W/(m.K) corresponds to an R-Value of 3.22. This results in a heat loss rate of only 6W to ensure that more than 99% of the heat content in the HE is retained for long-term usage, taking an ambient indoor temperature of 295K (21.85°C). Based on the UK standards of drainage and waste disposal [21], the minimum depth of a P-trap linked with typical residential appliances is between 50-75mm. Consequently, with the inclusion of this P-trap and auxiliary piping, 300mm is available for the installation of this HE adjacent to these appliances. The typical dimensions of a showering floor are 700 × 1,000mm which is easily capable of fitting a 670 × 750mm HE underneath it, and linking it with the plumbing system of the house. Similarly, there

is enough volume adjacent to dishwashers and washing machines for the adjustment of this HE.

With a 15K increment in the CW temperature, this HE can be used as a regenerator to initially heat the CW to eventually raise it to the required 323K (49.85°C) in showers, 338K (64.85°C) in washing machines and 358K (84.85°C) in dishwashers. This would save between 20-40% of the energy consumed in these residential appliances.

Additionally, it can be linked with residential basins and sinks [3]. With harnessing GW heat in commercial applications using such HE, a building can be a decentralised source of heat in smart fourth generation DH grids, as envisioned [3].

This HE has a thermal rating of 6.3kW based on the CW outlet temperature. As a comparison, a typical electric shower has a rating between 6-15kW while typical radiators in a building's central heating system have a rating between 5-20kW.

However, it should be considered that this HE is a passive technology in comparison, with no external energy consumption. An estimation of the cost of this HE derived from the experimental analysis of section 5.4 is presented in Table 6-3:

Table 6-3: Distribution of costs for the holistic HE

	<b>Description</b>	<b>Unit price</b>	<b>Quantity</b>	<b>Total price/£</b>
<b>1</b>	PCM	£7.5/kg	30kg	225
<b>2</b>	Corrugated pipes	£7/m	18m	126
<b>3</b>	Copper fins (740×90×1)mm	£8/fin	60	480
<b>4</b>	U-Bends	£2/bend	28	56
<b>5</b>	Reducers and sealing	£2/reducer	4	8
<b>6</b>	Impermeable sheets	£4/sheet	3	12
<b>7</b>	Mild steel container (750×100×1)mm	£20/container	1	20
<b>8</b>	Insulation (100mm)	£5/enclosure	1	5
<b>9</b>	Assembly and manufacturing costs	20% of material cost		186.4
			<b>Total</b>	<b>£1,118.4</b>

Based on this cost, the economic feasibility of installing this HE in a four-member household was assessed based on a saving of 15K in CW temperature addition from the

incoming mains flow. Using an estimated production of about 0.18m<sup>3</sup> of GW per day per person [3], the results are presented in Table 6-4:

Table 6-4: Economic feasibility of the HE

	<b>Description</b>	<b>Amount</b>
<b>1</b>	Daily quantity of GW saved/kg	180
<b>2</b>	Daily energy saved per person/kWh	3.15
<b>3</b>	Daily energy saved for a four-member household/kWh	12.6
<b>4</b>	Yearly energy savings/kWh	4687.2
<b>5</b>	Efficiency of a conventional gas boiler/%	80
<b>6</b>	Equivalent consumption of gas/m <sup>3</sup>	669.6
<b>7</b>	Yearly CO <sub>2</sub> savings/kg	1477.7
<b>8</b>	Yearly savings on gas consumed by boiler at a price of 4p/kWh including standing charges	234.36
<b>9</b>	Yearly savings on gas consumed by boiler at a price of 5p/kWh including standing charges	292.95
<b>10</b>	Yearly savings on gas consumed by boiler at a price of 6.3p/kWh including standing charges	369.12
<b>11</b>	Payback time in years at a gas price of 4p/kWh in 2020	4.77
<b>12</b>	Payback time in years at a gas price of 5p/kWh in 2025	3.82
<b>13</b>	Payback time in years at a gas price of 6.3p/kWh in 2030	3.03

The average gas consumption of a four-member household is about 10,000kWh, whilst the average standing charge in the UK is about £100 and the unit rate of gas is about 3p/kWh [210]. This corresponds to an average price of about 4p/kWh for domestic users. Similarly, the average increment in domestic gas prices based on figures from the last 30 years is about 4.6% per annum [210]. With this volatility in prices, an optimistic payback time of about 3.82 years in 2025 is possible for a four-member household. Similarly, if this HE was to be constructed on a commercial level with automated machinery, the unit cost would decrease drastically making the payback time even less. Since there are no moving parts, the maintenance costs are negligible. However, long-term cyclic testing of the PCM is recommended, as it might need replacement over elongated time durations.

## 6.5. Outcome

This section successfully predicted both a positive technical and economic feasibility for the developed HE. Using the unit-module method, the empirical correlations for the thermal performance of a holistic HE have been established. Consequently, the output temperatures of a HE with 9m long internal pipes are summarised in Table 6-5:

*Table 6-5: Performance results of the holistic HE*

	<b>Single-PCM</b>	<b>Two-cascaded PCMs</b>	<b>Three- cascaded PCMs</b>
<b>CW outlet temperature/K</b>	294.5 (21.35°C)	298.3 (25.15°C)	300.1 (27.15°C)
<b>GW outlet temperature/K</b>	307.9 (34.75°C)	309.4 (36.25°C)	309.6 (36.05°C)
<b>CW to GW heat transfer efficiency/%</b>	56	85	98
<b>Pressure loss/kPa</b>	6.4		

Based on the CW outlet temperature, the three-cascaded PCM-HE has a thermal rating of 6.3kW. At a laboratory scale, the fabrication of such a device costs about £1,118.4, giving a payback time of 4.77 years for a four-member household in the UK. However, manufacturing at a commercial level would lower costs intensely, whilst evident inflation in the prices of natural gas would further lower the payback time.

## Chapter 7 - Conclusion and recommendations

### 7.1. Summary

Only 10-20% of the thermal content of water is used before it is transformed into GW, in non-industrial buildings. Commercially available HEs and HPs are used for GW heat harnessing. However, both these technologies are unable to decouple the supply of GW with the demand of CW. At the same time, heat recovery and sensible heat storage are done in separate steps with these technologies. This not only minimises the energy efficiency but also limits the applications of using the harnessed heat. The usage of PCMs in a three-way HE would exploit these deficiencies in commercial technologies, to fully exploit the energy and exergy potential for GW heat harnessing. The possibility of harnessing GW heat exists at a building, sewage and waste-treatment plant level. However, simplicity in installation with the maximum exergetic potential exists for harnessing heat in appliances in residential buildings. A three-phase methodology has been put forward to design such a HE applicable to harness non-industrial GW heat. This methodology was demonstrated by applying it to harnessing GW heat into CW for residential appliances, although the harnessed heat could be used in numerous applications. Typically, GW from residential appliances has a mass-flow rate of 0.1kg/s with an average temperature of 325K (51.85°C), flowing for about 900s. Similarly, the average incoming temperature of CW is about 285K (11.85°C).

The initial step in the three-phase methodology was to select an appropriate PCM with the optimum thermal properties with regard to the boundary conditions of this application. An optimiser using the PSO algorithm coupled with the classical 2-phase analytical solution was developed to determine the thermal parameters of the PCM, with the objective to maximise the net heat transfer for both melting (GW flow) and freezing (CW flow). This algorithm could be used in the primary phase of the design process without the need of an extensive detailed design. Based on the results of this phase, the best performing PCM in this application would have a phase change temperature of 296.5K (23.35°C). It was observed that PCM melting was a relatively fast phenomenon, with freezing being the bottleneck of design process. Based on this outcome, RT-25, a

commercially available organic PCM developed by Rubitherm was selected as the most appropriate.

In the second phase of the design, the internal heat transfer within the CW and GW pipes was to be enhanced. Corrugated pipes were proposed to replace the plane pipes as a passive enhancement technique for this three-way HE. This technique had the highest heat transfer enhancement ratios with the least penalty in pressure drops along with a low vulnerability to biofilm deposits. Based on an experimental model, a numerical simulation was validated with acceptable accuracy. Following this a parametric study was developed in the numerical simulation to assess the overall flow and thermal performance of a discrete set of corrugated pipes. A configuration with a rib height of 4.5mm and a pitch length of 30mm had the finest performance to be considered the best choice for this application. This configuration provided a less turbulent, more helical flow path, with the fluid smoothly guided through the corrugations and having a higher surface area of contact. Additionally, it also nominally improved the thermal performance of the PCM external to the pipe wall.

In the third phase of the research, the external heat transfer within the PCM was to be enhanced. For this obligation, a finned design was proposed, to be radially attached to the surface of the GW and CW pipes. Amongst the various passive enhancement techniques, fins provided the greatest surface-area-to-volume ratio enhancement, were mechanically stable, had chemical steadiness in the PCM structure and were economical. A detailed experimental model was conducted with a complete counter-flow PCM-HE for both the GW and CW flow. During the experiment, a sensitivity analysis was performed with different PCMs, varying mass-flow rates and operation strategies for the HE. It was concluded that amongst the PCMs, RT-25 was indeed the optimum choice. Amongst the operation strategies, the solo-flow of both the GW and CW provided the best results at a mass-flow rate of 0.1kg/s. This outcome approved the initially laid out objective, that PCMs would decouple the demand of CW and supply of GW. Based on the experiment, a numerical simulation was validated with considerably close R-squared values between both data sets. Comparatively, the freezing of a PCM was 60-70% slower than melting in the same time duration. Hence, the layout of the fins was to be optimised based on the bottleneck case of freezing, using the validated numerical simulation. A sensitivity analysis was performed to select an optimum finned



configuration to provide complete phase change for both melting and freezing, with maximum heat transfer from the GW to the CW. A  $40 \times 90$ mm fin with 1mm thickness and a pitch of 10mm, fulfilled this optimised criteria. It was observed from the results that the heat transfer was enhanced in spite of the average velocity of the convectational currents decreasing by half compared to a non-finned arrangement. Although the fins acted as a hurdle to the free flow of convectational currents, there was an overall improvement in the net heat transfer with fins, as the rate of the initial propagation of heat via conduction was much higher.

With the outcomes of the three design phases, the numerical simulation of a unit-volume of the HE was set up. The thermal performance of a holistic HE was developed using empirical correlations based on the outcome of the numerical simulation. Additionally, the usage of a multi-cascaded PCM arrangement in the HE for harnessing GW heat in a residential appliance increased the temperature differential of the CW flow by 64%. Consequently, based on this design, a 9m piping length HE for a four-member household has the capability to save 4,687kWh of energy on an annual basis. Such a HE would cost a mere £1,118 with a rate of return of 4.77 years on the investment, based on current gas prices in the UK. At the same time, it would reduce reliance on gas to increment the share of electricity consumption in the UK energy grid, as is government policy [211].

## **7.2. Recommendations**

At the moment, this HE can be categorised as being at a TRL of 3/4. Several improvements would still be needed before practically demonstrating it in real working conditions. Based on this research, the following are recommended to commercialise this passive heat harnessing concept:

- The classical 2-phase analytical solution should be upgraded to improve the accuracy of prediction. It can easily be modified with more detailed implicit approximations within the existing algorithm for further studies. At the same

time, a basic mathematical model of convection heat transfer should be integrated.

- An analysis of using thinner corrugated pipes would be interesting, as it would give better results since the thermal resistivity of the pipe would decrease. However, practically manufacturing such pipes with soft brittle materials would be difficult, while it would be extremely energy intensive with harder materials. Recent advancements in 3D-printing would be an interesting investigation after an analysis of viable thinner pipes.
- A full-scale practical experimental setup of the holistic HE with the integrated finned-corrugated pipes should be investigated, followed by a pilot-study in real residential appliances. It is also recommended to conduct long-term loading tests to assess the chemical and thermal stability of the PCM along with the fins and the container.
- An investigation should also be carried out in terms of the safety and adaptability aspects of such a PCM-based HE in residential buildings. Also, better insulation techniques with proper sealing strategies need to be analysed [121].
- The usage of such HEs in decentralised, fourth generation DH grids has been put forward, especially for commercial buildings. The real-time modelling of such a scenario in a smart energy grid would be extremely interesting. Real-time data of the production of GW and the consumption of CW in non-industrial buildings is required for this.
- As mentioned, most GW heat harnessing devices are used as preheaters. It would be an interesting investigation to assess the usage of this PCM-based GW heat harnessing unit in cascaded combinations with conventional HPs and HEs.

Using this three-step research methodology, an appropriate PCM, an internal and an external heat transfer enhancement configuration can be selected for different applications of GW heat harnessing in non-industrial buildings. This can easily be done with variations in the boundary conditions of temperature, time and mass-flow rate of the fluid flows.

## References

- [1] International Energy Agency. Technology Roadmap: Energy Efficient Buildings, Heating and Cooling Equipment. Paris: 2011.
- [2] Christoff P. The promissory note: COP 21 and the Paris Climate Agreement. *Env Polit* 2016;25:765–87. doi:10.1080/09644016.2016.1191818.
- [3] Mazhar A, Liu S, Shukla A. A Key Review of Non-Industrial Greywater Heat Harnessing. *Energies* 2018;11:386. doi:10.3390/en11020386.
- [4] Schnieders J, Feist W, Rongen L. Passive Houses for different climate zones. *Energy Build* 2015;105:71–87. doi:10.1016/j.enbuild.2015.07.032.
- [5] Stephan A, Crawford RH, de Myttenaere K. A comprehensive assessment of the life cycle energy demand of passive houses. *Appl Energy* 2013;112:23–34. doi:10.1016/j.apenergy.2013.05.076.
- [6] Meggers F, Leibundgut H. The potential of wastewater heat and exergy : Decentralized high-temperature recovery with a heat pump. *Energy Build* 2011;43:879–86. doi:10.1016/j.enbuild.2010.12.008.
- [7] International Energy Agency. Renewable Energy : RD & D Priorities. Paris: 2006.
- [8] Yeatman EM. Energy harvesting – small scale energy production from ambient sources. *Act Passiv Smart Struct Integr Syst* 2009;7288:728802–728802–7. doi:10.1117/12.824472.
- [9] Vatansever D, Siores E, Shah T. Alternative Resources for Renewable Energy: Piezoelectric and Photovoltaic Smart Structures. *Glob Warm - Impacts Futur Perspect* 2012:263–90. doi:10.5772/50570.
- [10] Mazhar AR, Liu S, Shukla A. A state of art review on the district heating systems. *Renew Sustain Energy Rev* 2018;96. doi:10.1016/j.rser.2018.08.005.
- [11] Lund H, Werner S, Wiltshire R, Svendsen S, Eric J, Hvelplund F, et al. 4th Generation District Heating ( 4GDH ) Integrating smart thermal grids into future sustainable energy systems. *Energy* 2014;68:1–11. doi:10.1016/j.energy.2014.02.089.
- [12] Schmid F. Sewage water: interesting heat source for heat pumps and chillers. 9th Int IEA Heat Pump Conf 2008.
- [13] Gill ZM, Tierney MJ, Pegg IM, Allan N. Measured energy and water performance of an aspiring low energy/carbon affordable housing site in the UK. *Energy Build* 2011;43:117–25. doi:10.1016/j.enbuild.2010.08.025.
- [14] Energy Savings Trust. Measurement of domestic hot water consumption in dwellings. *Energy Savings Trust* 2008:1–62.
- [15] Ni L, Lau SK, Li H, Zhang T, Stansbury JS, Shi J, et al. Feasibility study of a localized residential grey water energy-recovery system. *Appl Therm Eng* 2012;39:53–62. doi:10.1016/j.applthermaleng.2012.01.031.
- [16] Wallin J, Claesson J. Analyzing the efficiency of a heat pump assisted drain water heat recovery system that uses a vertical inline heat exchanger 2014;8:109–19. doi:10.1016/j.seta.2014.08.003.
- [17] Al-Jayyousi OR. Greywater reuse: Towards sustainable water management. *Desalination* 2003;156:181–92. doi:10.1016/S0011-9164(03)00340-0.
- [18] Allen L, Christian-smith J, Palaniappan M. Overview of Greywater Reuse : The Potential of Greywater Systems to Aid Sustainable Water Management. 2010.
- [19] Alsulaili AD, Hamoda MF. Quantification and characterization of greywater from schools. *Water Sci Technol* 2015;72:1973–80. doi:10.2166/wst.2015.408.
- [20] Association of Plumbing & Heating Contractors. Understanding sanitary systems within the home. Solihull: 2017.
- [21] HM Government. The Building Regulations 2010: Drainage and waste disposal. London: 2010.
- [22] Wheatley AD, Surendran S, Services B. Greywater treatment and reuse results from a 50-person trial Office of Water Services 2014;5:187–94. doi:10.1080/15730620802013177.
- [23] National Measurement System. An Introduction To Non-Invasive Ultrasonic. Glasgow: 2017.
- [24] Du DJ, Wanner O. A mathematical model to predict the effect of heat recovery on the wastewater temperature in sewers 2013;8. doi:10.1016/j.watres.2013.10.017.
- [25] Zaloum C, Lafrance M. Drain Water Heat Recovery Characterization and Modeling. Ottawa: 2007.
- [26] Wallin J, Claesson J. Investigating the efficiency of a vertical inline drain water heat recovery heat exchanger in a system boosted with a heat pump. *Energy Build* 2014;80:7–16. doi:10.1016/j.enbuild.2014.05.003.
- [27] Corona-Nakamura MA, Ruelas R, Ojeda-Magana B, Finch DWC. Identification of domestic water consumption in a house based on fuzzy clustering algorithms. 2009 IEEE Int Conf Syst Man Cybern 2009:3751–6. doi:10.1109/ICSMC.2009.5346891.

- [28] Zaloum C, Gusdorf J, Parekh A. Performance Evaluation of Drain Water Heat Recovery Technology at the Canadian Centre for Housing Technology. Ottawa: 2007.
- [29] Eslami-nejad P, Bernier M. Impact of Grey Water heat recovery on the electrical demand of domestic hot water heaters. Proc Elev Int IBPSA Conf Glas UK, 27–30 July 2009; 2009:681–7.
- [30] Energy Saving Trust. At Home with Water. London: 2013.
- [31] Boyjoo Y, Pareek VK, Ang M. A review of greywater characteristics and treatment processes. Water Sci Technol 2013;67:1403–24. doi:10.2166/wst.2013.675.
- [32] Vavrin JL. A Quantitative Study of the Viability of Greywater Heat Recovery ( GWHR ). US Army Corps Eng 2011.
- [33] Chao S, Yiqiang J, Yang Y. A field study of a wastewater source heat pump for domestic hot water heating 2016. doi:10.1177/0143624412463571.
- [34] Nolde E. Water and energy recycling at a residential passive house. Poster Sustain Build Conf Graz, Austria 2013:1353–60.
- [35] Alnahhal S, Spremberg E. Contribution to Exemplary In-House Wastewater Heat Recovery in Berlin, Germany. Procedia CIRP 2016;40:35–40. doi:10.1016/j.procir.2016.01.046.
- [36] Seybold C. In-house waste water heat recovery. Rehva J 2013:18–21.
- [37] Dieckmann J. Drain Water Heat Recovery. ASHRAE J 2011;53:13.
- [38] Hepbasli A, Biyik E, Ekren O, Gunerhan H, Araz M. A key review of wastewater source heat pump (WWSHP) systems. Energy Convers Manag 2014;88:700–22. doi:10.1016/j.enconman.2014.08.065.
- [39] Moran M, Shapiro H. Engineering Thermodynamics. 5th ed. Chichester: John Wiley & Sons, Inc.; 2006.
- [40] Energy Saving Trust. Domestic heating by gas : boiler systems – guidance for installers and specifiers Contents. London: 2008.
- [41] Baradey Y, Hawlader MNA, Ismail AF, Hrairi M. Waste Heat Recovery in Heat Pump Systems: Solution To Reduce Global Warming. IIUM Eng J 2018;16:31–42. doi:10.31436/iiumej.v16i2.602.
- [42] Neugebauer G, Kretschmer F, Kollmann R, Narodoslowsky M, Ertl T, Stoeglehner G. Mapping Thermal Energy Resource Potentials from Wastewater Treatment Plants. Sustainability 2015;7:12988–3010. doi:10.3390/su71012988.
- [43] Kordana S. SWOT analysis of wastewater heat recovery systems application. Proc 9th Conf Interdiscip Probl Environ Prot Eng EKO-DOK 2017.
- [44] Cipolla SS, Maglionico M. Heat recovery from urban wastewater: Analysis of the variability of flow rate and temperature in the sewer of Bologna, Italy. Energy Procedia 2014;45:288–97. doi:10.1016/j.egypro.2014.01.031.
- [45] Cautley D. Drain Water Heat Recovery - A field study of commercial applications. Madison: 2013.
- [46] Słyś D, Kordana S. Financial analysis of the implementation of a Drain Water Heat Recovery unit in residential housing. Energy Build 2014;71:1–11. doi:10.1016/j.enbuild.2013.11.088.
- [47] Kimmels A. Shower Heat Recovery. Slepden: 2011.
- [48] Wavin. Showersave Product & Installation Guide. Zwolle: 2009.
- [49] Schuitema R, Sijpbeer NC, Bakker EJ. Energy performance of a drainwater heat recovery system Experimental results of drainwater heat recovery in ECN research dwellings. Eur Conf Coop Exch Sustain Energy Syst 2005.
- [50] Timea G, Rusu T, Dan V. Technological Variations for Domestic Waste Water Heat Recovery. ProEnvironment 2010;3:313–7.
- [51] Collins M, Decker G Van, Murray J. Characteristic Effectiveness Curves for Falling Film Drain Water Heat Recovery Systems. HVAC&R Res 2013;19:649–62. doi:10.1080/10789669.2013.796857.
- [52] McNabola A, Shields K. Efficient drain water heat recovery in horizontal domestic shower drains. Energy Build 2013;59:44–9. doi:10.1016/j.enbuild.2012.12.026.
- [53] Lee J, Lee D, Yang C, Chen C, Ting C. Developing the footplate for shower drain water heat recovery 2014;1:89–94.
- [54] Manouchehri R, Banister CJ, Collins MR. Impact of small tilt angles on the performance of falling film drain water heat recovery systems. Energy Build 2015;102:181–6. doi:10.1016/j.enbuild.2015.05.024.
- [55] Todoran R. Modern Management Methods for Managing the Waste Water and Recovering the Heat from Waste Water. Ann Univ Apulensis Ser Oeconomica 2010;12:11–3.
- [56] Beentjes I, Manouchehri R, Collins MR. An investigation of drain-side wetting on the performance of falling film drain water heat recovery systems. Energy Build 2014;82:660–7.

- doi:10.1016/j.enbuild.2014.07.069.
- [57] Goth J. Heat Pumps. *Energy Build Ind* 2011;9:29–32.
- [58] Chao S, Yiqiang J, Yang Y, Shiming D. Experimental performance evaluation of a novel dry-expansion evaporator with defouling function in a wastewater source heat pump. *Appl Energy* 2012;95:202–9. doi:10.1016/j.apenergy.2012.02.030.
- [59] Nyers J. COP and Economic Analysis of the Heat Recovery from Waste Water using Heat Pumps. *Acta Polytech Hungrica* 2016;13:135–54.
- [60] Hytiris N, Ninikas K, Emmanuel R, Aaen B, Younger P. Heat Energy Recovery from Waste Water in the Glasgow Subway System. *Procedia Eng* 2016;165:394–403. doi:10.1016/j.proeng.2016.11.715.
- [61] Tanha K, Fung AS, Leong WH. Investigating the performance of two types of Solar Domestic Water Heating (SDWH) systems with drain water heat recovery through computer simulation and experimental analysis. *ASHRAE Trans* 2012;118:214–21.
- [62] Liu L, Fu L, Jiang Y. Application of an exhaust heat recovery system for domestic hot water. *Energy* 2010;35:1476–81. doi:10.1016/j.energy.2009.12.004.
- [63] Dong J, Zhang Z, Yao Y, Jiang Y, Lei B. Experimental performance evaluation of a novel heat pump water heater assisted with shower drain water. *Appl Energy* 2015;154:842–50. doi:10.1016/j.apenergy.2015.05.044.
- [64] Chen W, Liang S, Guo Y, Cheng K, Gui X, Tang D. Investigation on the thermal performance and optimization of a heat pump water heater assisted by shower waste water. *Energy Build* 2013;64:172–81. doi:10.1016/j.enbuild.2013.04.021.
- [65] Dunsmore I. *Heat from Wastewater*. Manchester: 2016.
- [66] Sharma A, Tyagi V V., Chen CR, Buddhi D. Review on thermal energy storage with phase change materials and applications. *Renew Sustain Energy Rev* 2009;13:318–45. doi:10.1016/j.rser.2007.10.005.
- [67] Iten M. *Air-Multiple PCMs for the Free Cooling and Ventilation of Buildings*. Coventry: 2015.
- [68] López-Sabirón AM, Royo P, Ferreira VJ, Aranda-Usón A, Ferreira G. Carbon footprint of a thermal energy storage system using phase change materials for industrial energy recovery to reduce the fossil fuel consumption. *Appl Energy* 2014;135:616–24. doi:10.1016/j.apenergy.2014.08.038.
- [69] Yagi J, Akiyama T. Storage of thermal energy for effective use of waste heat from industries. *J Mater Process Technol* 1996;48:793–804.
- [70] Nomura T, Okinaka N, Akiyama T. Waste heat transportation system, using phase change material (PCM) from steelworks to chemical plant. *Resour Conserv Recycl* 2010;54:1000–6. doi:10.1016/j.resconrec.2010.02.007.
- [71] Beyhan B, Ahan NŞ, Paksoy HÖ. *Phase Change Material Applications for Domestic Appliances*. Cukurova Univ Turkey 2008.
- [72] Paksoy H, Yilmaz S, Ozgul G, Yilmaz MÖ, Mazma HE. *Thermal Energy Storage for More Efficient Domestic Appliances*. Balcali: 2007.
- [73] Robert L, Longardener WJL. *Phase Change Heat Exchanger*. 5220954, 1993. doi:10.1145/634067.634234.
- [74] Devaraj P, Vishnu S. Waste heat storage using PCM. *Thiagarajar Coll Eng Madurai India* 2012:35–8.
- [75] Zhang X, Yu S, Yu M, Lin Y. Experimental research on condensing heat recovery using phase change material. *Appl Therm Eng* 2011;31:3736–40. doi:10.1016/j.applthermaleng.2011.03.040.
- [76] Gu Z, Liu H, Li Y. Thermal energy recovery of air conditioning system - Heat recovery system calculation and phase change materials development. *Appl Therm Eng* 2004;24:2511–26. doi:10.1016/j.applthermaleng.2004.03.017.
- [77] Al-Abidi AA, Bin Mat S, Sopian K, Sulaiman MY, Lim CH, Th A. Review of thermal energy storage for air conditioning systems. *Renew Sustain Energy Rev* 2012;16:5802–19. doi:10.1016/j.rser.2012.05.030.
- [78] Alhando MH, Theeb MA, Golam AS. Finned double-tube PCM system as a waste heat storage. *IOP Conf Ser Mater Sci Eng* 2015;95:012033. doi:10.1088/1757-899X/95/1/012033.
- [79] Prabu SS, Asokan MA. A study of waste heat recovery from diesel engine exhaust using phase change material. *Int J ChemTech Res* 2015;8:711–7.
- [80] Klein Altstedde M, Rinderknecht F, Friedrich H. Integrating phase-change materials into automotive thermoelectric generators: An experimental examination and analysis of energetic potential through numerical simulation. *J Electron Mater* 2014;43:2134–40. doi:10.1007/s11664-014-2990-z.
- [81] Kiran CS, Reddy RM. *Experimental Analysis of a Thermal Energy Storage System-Waste Heat*

- Recovery 2015;7768–74. doi:10.15680/IJRSET.2015.0408122.
- [82] Shon J, Kim H, Lee K. Improved heat storage rate for an automobile coolant waste heat recovery system using phase-change material in a fin-tube heat exchanger. *Appl Energy* 2014;113:680–9. doi:10.1016/j.apenergy.2013.07.049.
- [83] Nagano K, Ogawa K, Mochida T, Hayashi K, Ogoshi H. Thermal characteristics of magnesium nitrate hexahydrate and magnesium chloride hexahydrate mixture as a phase change material for effective utilization of urban waste heat. *Appl Therm Eng* 2004;24:221–32. doi:10.1016/j.applthermaleng.2003.09.003.
- [84] Cipollone R, Bianchi G, Battista D Di. Experimental and numerical analyses on a plate heat exchanger with phase change for waste heat recovery at off-design conditions. *J Phys Conf Ser* 655 2015;012038. doi:10.1088/1742-6596/655/1/012038.
- [85] Azzouz K, Leducq D, Gobin D. Performance enhancement of a household refrigerator by addition of latent heat storage. *Int J Refrig* 2008;31:892–901. doi:10.1016/j.ijrefrig.2007.09.007.
- [86] Mazhar AR, Liu S, Shukla A. An optimizer using the PSO algorithm to determine thermal parameters of PCM : A case study of grey water heat harnessing. *Int J Heat Mass Transf* 2019;144:118574. doi:10.1016/j.ijheatmasstransfer.2019.118574.
- [87] Mousa H, Gujarathi AM. Modeling and analysis the productivity of solar desalination units with phase change materials. *Renew Energy* 2016;95:225–32. doi:10.1016/j.renene.2016.04.013.
- [88] Zhao J, Ji Y, Yuan Y, Zhang Z, Lu J. Energy-Saving Analysis of Solar Heating System with PCM Storage Tank. *Energies* 2018;11. doi:10.3390/en11010237.
- [89] Ihm P, Krarti M, Henze GP. Development of a thermal energy storage model for EnergyPlus. *Energy Build* 2004;36:807–14. doi:10.1016/j.enbuild.2004.01.021.
- [90] Asbik M, Ansari O, Bah A, Zari N, Mimet A, El-ghetany H. Exergy analysis of solar desalination still combined with heat storage system using phase change material ( PCM ). *DES* 2016;381:26–37. doi:10.1016/j.desal.2015.11.031.
- [91] Fadaei N, Kasaeian A, Akbarzadeh A. Experimental investigation of solar chimney with phase change material ( PCM ). *Renew Energy* 2018;123:26–35. doi:10.1016/j.renene.2018.01.122.
- [92] Arıcı M, Bilgin F, Nižetić S, Papadopoulos AM. Phase change material based cooling of photovoltaic panel: A simplified numerical model for the optimization of the phase change material layer and general economic evaluation. *J Clean Prod* 2018;189:738–45. doi:10.1016/j.jclepro.2018.04.057.
- [93] Zhao R, Gu J, Liu J. Optimization of a phase change material based internal cooling system for cylindrical Li-ion battery pack and a hybrid cooling design. *Energy* 2017;135:811–22. doi:10.1016/j.energy.2017.06.168.
- [94] Zwanzig SD, Lian Y, Brehob EG. Numerical simulation of phase change material composite wallboard in a multi-layered building envelope. *Energy Convers Manag* 2013;69:27–40. doi:10.1016/j.enconman.2013.02.003.
- [95] Virgone J, Noel J. Optimization of a phase change material wallboard for building use. *Appl Therm Eng* 2008;28:1291–8. doi:10.1016/j.applthermaleng.2007.10.012.
- [96] Annulus H, Li S, Chen Y, Sun Z. Numerical Simulation and Optimization of the Melting Process of Phase Change Material inside Horizontal Annulus. *Energies* 2017;10. doi:10.3390/en10091249.
- [97] Salyan S, Suresh S. Liquid metal gallium laden organic phase change material for energy storage: An experimental study. *Int J Hydrogen Energy* 2018;43:2469–83. doi:10.1016/j.ijhydene.2017.12.047.
- [98] Li W, Li SG, Guan S, Wang Y, Zhang X, Liu X. Numerical study on melt fraction during melting of phase change material inside a sphere. *Int J Hydrogen Energy* 2017;42:18232–9. doi:10.1016/j.ijhydene.2017.04.136.
- [99] Park S, Woo S, Shon J, Lee K. Numerical model and simulation of a vehicular heat storage system with phase-change material. *Appl Therm Eng* 2017;113:1496–504. doi:10.1016/j.applthermaleng.2016.11.162.
- [100] Bhagat K, Saha SK. Numerical analysis of latent heat thermal energy storage using encapsulated phase change material for solar thermal power plant. *Renew Energy* 2016;95:323–36. doi:10.1016/j.renene.2016.04.018.
- [101] Joulin A, Younsi Z, Zalewski L, Lassue S, Rousse DR, Cavrot J. Experimental and numerical investigation of a phase change material : Thermal-energy storage and release. *Appl Energy* 2011;88:2454–62. doi:10.1016/j.apenergy.2011.01.036.
- [102] Lamberg P, Lehtiniemi R, Henell A. Numerical and experimental investigation of melting and freezing processes in phase change material storage. *Int J Therm Sci* 2004;43:277–87. doi:10.1016/j.ijthermalsci.2003.07.001.

- [103] Dadollahi M, Mehrpooya M. Modeling and investigation of high temperature phase change materials (PCM) in different storage tank configurations. *J Clean Prod* 2017;161:831–9. doi:10.1016/j.jclepro.2017.05.171.
- [104] Gracia A De, Oró E, Farid MM, Cabeza LF. Thermal analysis of including phase change material in a domestic hot water cylinder. *Appl Therm Eng* 2011;31:3938–45. doi:10.1016/j.applthermaleng.2011.07.043.
- [105] Kanimozhi B, Harish K, Tarun BS, Sainath Reddy PS, Sujeeth PS. Charging and Discharging Processes of Thermal Energy Storage System Using Phase change materials. *IOP Conf Ser Mater Sci Eng* 2017;197. doi:10.1088/1757-899X/197/1/012040.
- [106] Thomas J, Srivatsa PVSS, S RK, Baby R. Thermal Performance Evaluation of a Phase Change Material Based Heat Sink : A Numerical Study. *Procedia Technol* 2016;25:1182–90. doi:10.1016/j.protcy.2016.08.237.
- [107] Chiong R. *Nature-Inspired Algorithms for Optimisation*. Warsaw: Springer; 2009.
- [108] Qi H, Niu CY, Gong S, Ren YT, Ruan LM. Application of the hybrid particle swarm optimization algorithms for simultaneous estimation of multi-parameters in a transient conduction-radiation problem. *Int J Heat Mass Transf* 2015;83:428–40. doi:10.1016/j.ijheatmasstransfer.2014.12.022.
- [109] Zhang B, Qi H, Sun SC, Ruan LM, Tan HP. Solving inverse problems of radiative heat transfer and phase change in semitransparent medium by using Improved Quantum Particle Swarm Optimization. *Int J Heat Mass Transf* 2015;85:300–10. doi:10.1016/j.ijheatmasstransfer.2015.01.140.
- [110] Lee KH, Kim KW. Performance comparison of particle swarm optimization and genetic algorithm for inverse surface radiation problem. *Int J Heat Mass Transf* 2015;88:330–7. doi:10.1016/j.ijheatmasstransfer.2015.04.075.
- [111] Luo X, Xie Q, Wang Y, Yang C. Estimation of heat transfer coefficients in continuous casting under large disturbance by Gaussian kernel particle swarm optimization method. *Int J Heat Mass Transf* 2017;111:1087–97. doi:10.1016/j.ijheatmasstransfer.2017.03.105.
- [112] Lee KH. Inverse estimation of various surface emissivity distributions using repulsive particle swarm optimization. *Int J Heat Mass Transf* 2019;134:1323–32. doi:10.1016/j.ijheatmasstransfer.2017.12.103.
- [113] Mamode M. Two Phase Stefan problem with boundary temperature conditions: An analytical approach. *SIAM J Appl Math* 2013;73:460–74. doi:10.1137/110852474.
- [114] Alexiades V, Solomon AD. *Mathematical Modeling of Melting and Freezing Processes*. Washington: Taylor & Francis; 1993.
- [115] Dubovsky V, Ziskind G, Letan R. An Analytical Technique of Transient Phase- Change Material Melting Calculation for Cylindrical and Tubular Containers. *Heat Transf Eng* 2018;0:1–14. doi:10.1080/01457632.2018.1457271.
- [116] Mosaffa A, Talati F, Rosen MA, Basirat TH. Phase change material solidification in a finned cylindrical shell thermal energy storage: An approximate analytical approach. *Therm Sci* 2013;17:407–18. doi:10.2298/TSCI120326207M.
- [117] Dutil Y, Rousse DR, Salah N Ben, Lassue S, Zalewski L. A review on phase-change materials: Mathematical modeling and simulations. *Renew Sustain Energy Rev* 2011;15:112–30. doi:10.1016/j.rser.2010.06.011.
- [118] Zhaochun W, Jianping L, Jingmei F. A novel algorithm for solving the classical Stefan problem. *Therm Sci* 2011;15:39–44. doi:10.2298/TSCI11S1039W.
- [119] Salvatori L, Tosi N. Stefan problem through extended finite elements: Review and further investigations. *Algorithms* 2009;2:1177–220. doi:10.3390/a2031177.
- [120] Carslaw H., Jaeger J. *Conduction of Heat in Solids*. Second. London: Oxford University Press; 1959.
- [121] Fleischer AS. *Thermal Energy Storage Using Phase Change Materials Fundamentals and Applications*. Villanova: Springer; 2015. doi:10.1007/97-3-319-20922-7.
- [122] Rubinstein L. *The Stefan Problem*. Volume 27. American Mathematical Society; 1971.
- [123] Manzano-agugliaro F, Montoya FG, Gil C, Alcayde A, Gómez J, Ba R. Optimization methods applied to renewable and sustainable energy : A review. *Renew Sustain Energy Rev* 2011;15:1753–66. doi:10.1016/j.rser.2010.12.008.
- [124] Selvi V, Umarani R. Comparative Analysis of Ant Colony and Particle Swarm Optimization Techniques. *Int J Comput Appl* 2010;5:1–6.
- [125] Pal SK, Rai C., Singh AP. Comparative Study of Firefly Algorithm and Particle Swarm Optimization for Noisy Non-Linear Optimization Problems. *Int J Intell Syst Appl* 2012;4:50–7. doi:10.5815/ijisa.2012.10.06.
- [126] Yang B. Modified Particle Swarm Optimizers and their Application to Robust Design and

- Structural Optimization. Technische Universität München, 2009.
- [127] Eberhart R, Kennedy J. A New Optimizer Using Particle Swarm Theory. *IEEE 6th Int Symp Micro Mach Hum Sci* 1995;39–43.
- [128] AlRashidi M., El-Hawary M. A Survey of Particle Swarm Optimization Applications in Electric Power Systems. *IEEE Trans Evolutionary Comput* 2009;13:913–8. doi:10.1109/TEVC.2006.880326.
- [129] Sharaf A, El-gammal A. *Computational Intelligence in Power Engineering*. Heidelberg: Springer; 2010.
- [130] Eberhart C, Shi Y. Comparing inertia weights and constriction factors in particle swarm optimization. *Proc 2000 Congr Evol Comput* 2000:84–8. doi:10.1109/CEC.2000.870711.
- [131] Rubitherm Technologies GmbH. Data Sheet RT25. Berlin: 2016.
- [132] Khan Z, Khan Z, Ghafoor A. A review of performance enhancement of PCM based latent heat storage system within the context of materials, thermal stability and compatibility. *Energy Convers Manag* 2016;115:132–58. doi:10.1016/j.enconman.2016.02.045.
- [133] Acir A, Emin Canlı M. Investigation of fin application effects on melting time in a latent thermal energy storage system with phase change material (PCM). *Appl Therm Eng* 2018;144:1071–80. doi:10.1016/j.applthermaleng.2018.09.013.
- [134] Solomon GR, Velraj R. Analysis of the heat transfer mechanisms during energy storage in a Phase Change Material filled vertical finned cylindrical unit for free cooling application. *Energy Convers Manag* 2013;75:466–73. doi:10.1016/j.enconman.2013.06.044.
- [135] Riffat S, Mempo B, Fang W. Phase change material developments: a review. *Int J Ambient Energy* 2015;36:102–15. doi:10.1080/01430750.2013.823106.
- [136] Pereira da Cunha J, Eames P. Thermal energy storage for low and medium temperature applications using phase change materials - A review. *Appl Energy* 2016;177:227–38. doi:10.1016/j.apenergy.2016.05.097.
- [137] Sheikholeslami M, Gorji-Bandpy M, Ganji DD. Review of heat transfer enhancement methods: Focus on passive methods using swirl flow devices. *Renew Sustain Energy Rev* 2015;49:444–69. doi:10.1016/j.rser.2015.04.113.
- [138] Liu S, Sakr M. A comprehensive review on passive heat transfer enhancements in pipe exchangers. *Renew Sustain Energy Rev* 2013;19:64–81. doi:10.1016/j.rser.2012.11.021.
- [139] Ji WT, Jacobi AM, He YL, Tao WQ. Summary and evaluation on single-phase heat transfer enhancement techniques of liquid laminar and turbulent pipe flow. *Int J Heat Mass Transf* 2015;88:735–54. doi:10.1016/j.ijheatmasstransfer.2015.04.008.
- [140] Maradiya C, Vadher J, Agarwal R. The heat transfer enhancement techniques and their Thermal Performance Factor. *Beni-Suef Univ J Basic Appl Sci* 2017;7:1–21. doi:10.1016/j.bjbas.2017.10.001.
- [141] Xin F, Liu Z, Zheng N, Liu P, Liu W. Numerical study on flow characteristics and heat transfer enhancement of oscillatory flow in a spirally corrugated tube. *Int J Heat Mass Transf* 2018;127:402–13. doi:10.1016/j.ijheatmasstransfer.2018.06.139.
- [142] Pethkool S, Eiamsa-ard S, Kwankaomeng S, Promvong P. Turbulent heat transfer enhancement in a heat exchanger using helically corrugated tube. *Int Commun Heat Mass Transf* 2011;38:340–7. doi:10.1016/j.icheatmasstransfer.2010.11.014.
- [143] Webb RL. *Principles of Enhanced Heat Transfer*. New York: John Wiley & Sons Inc.; 1994.
- [144] Hong Y, Du J, Wang S, Huang SM. Heat transfer and flow behaviors of a wavy corrugated tube. *Appl Therm Eng* 2017;126:151–66. doi:10.1016/j.applthermaleng.2017.07.135.
- [145] Ali S, Habchi C, Menanteau S, Lemenand T, Harion JL. Three-dimensional numerical study of heat transfer and mixing enhancement in a circular pipe using self-sustained oscillating flexible vorticity generators. *Chem Eng Sci* 2017;162:152–74. doi:10.1016/j.ces.2016.12.039.
- [146] Tan XH, Zhu DS, Zhou GY, Zeng LD. Heat transfer and pressure drop performance of twisted oval tube heat exchanger. *Appl Therm Eng* 2013;50:374–83. doi:10.1016/j.applthermaleng.2012.06.037.
- [147] Vicente PG, García A, Viedma A. Experimental investigation on heat transfer and frictional characteristics of spirally corrugated tubes in turbulent flow at different Prandtl numbers. *Int J Heat Mass Transf* 2004;47:671–81. doi:10.1016/j.ijheatmasstransfer.2003.08.005.
- [148] Kareem ZS, Abdullah S, Lazim TM, Mohd Jaafar MN, Abdul Wahid AF. Heat transfer enhancement in three-start spirally corrugated tube: Experimental and numerical study. *Chem Eng Sci* 2015;134:746–57. doi:10.1016/j.ces.2015.06.009.
- [149] Rousseau PG, Eldik M Van, Greyvenstein GP. Detailed simulation of fluted tube water heating condensers. *Int J Refrig* 2003;26:232–9.
- [150] Iten M, Liu S, Shukla A. Experimental validation of an air-PCM storage unit comparing the



- effective heat capacity and enthalpy methods through CFD simulations. *Energy* 2018;155:495–503. doi:10.1016/j.energy.2018.04.128.
- [151] SIEMENS. *Star CCM+ Documentation v12.04*. Plano: 2017.
- [152] Mohammadi B, Pironneau O. *Analysis of the K-Epsilon turbulence model*. Pris: Chichester ; Paris : Wiley ; Masson; 1994.
- [153] Sharifi N, Bergman TL, Faghri A. Enhancement of PCM melting in enclosures with horizontally-finned internal surfaces. *Int J Heat Mass Transf* 2011;54:4182–92. doi:10.1016/j.ijheatmasstransfer.2011.05.027.
- [154] Oberkampf W, Trucano T. *Verification and validation in Computational Fluid Dynamics*. New Mexico: 2002.
- [155] Merlin K, Delaunay D, Soto J, Traonvouez L. Heat transfer enhancement in latent heat thermal storage systems: Comparative study of different solutions and thermal contact investigation between the exchanger and the PCM. *Appl Energy* 2016;166:107–16. doi:10.1016/j.apenergy.2016.01.012.
- [156] Mazhar AR, Liu S, Shukla A. Experimental study on the thermal performance of a grey water heat harnessing exchanger using Phase Change Materials. *Renew Energy* 2019;146:1805–17. doi:10.1016/j.renene.2019.08.053.
- [157] Kazemi M, Hosseini MJ, Ranjbar AA, Bahrapoury R. Improvement of longitudinal fins configuration in latent heat storage systems. *Renew Energy* 2018;116:447–57. doi:10.1016/j.renene.2017.10.006.
- [158] Yilmaz M, Comkali O, Yapici S, Sara O. Performance Evaluation Criteria for Heat Exchangers Based on First Law Analysis. *J Enhanc Heat Transf* 2005;12:121–57.
- [159] Mazhar AR, Shukla A, Liu S. Numerical analysis of rectangular fins in a PCM for low-grade heat harnessing. *Int J Therm Sci* 2020;152:106306. doi:10.1016/j.ijthermalsci.2020.106306.
- [160] Liu Z, Yu Z (Jerry), Yang T, Qin D, Li S, Zhang G, et al. A review on macro-encapsulated phase change material for building envelope applications. *Build Environ* 2018;144:281–94. doi:10.1016/j.buildenv.2018.08.030.
- [161] Tao YB, He YL. A review of phase change material and performance enhancement method for latent heat storage system. *Renew Sustain Energy Rev* 2018;93:245–59. doi:10.1016/j.rser.2018.05.028.
- [162] Al-Maghalseh M, Mahkamov K. Methods of heat transfer intensification in PCM thermal storage systems: Review paper. *Renew Sustain Energy Rev* 2018;92:62–94. doi:10.1016/j.rser.2018.04.064.
- [163] Liu L, Su D, Tang Y, Fang G. Thermal conductivity enhancement of phase change materials for thermal energy storage: A review. *Renew Sustain Energy Rev* 2016;62:305–17. doi:10.1016/j.rser.2016.04.057.
- [164] Sivasamy P, Devaraju A, Harikrishnan S. Review on Heat Transfer Enhancement of Phase Change Materials (PCMs). *Mater Today Proc* 2018;5:14423–31. doi:10.1016/j.matpr.2018.03.028.
- [165] Al-Abidi A, Mat S, Sopian K, Sulaiman Y, Mohammad A. Heat Transfer Enhancement for PCM Thermal Energy Storage in Triplex Tube Heat Exchanger. *Heat Transf Eng* 2016;37:705–12. doi:10.1080/01457632.2015.1067090.
- [166] Gil A, Peiró G, Oró E, Cabeza LF. Experimental analysis of the effective thermal conductivity enhancement of PCM using finned tubes in high temperature bulk tanks. *Appl Therm Eng* 2018;142:736–44. doi:10.1016/j.applthermaleng.2018.07.029.
- [167] Laing D, Bauer T, Breidenbach N, Hachmann B, Johnson M. Development of high temperature phase-change-material storages. *Appl Energy* 2013;109:497–504. doi:10.1016/j.apenergy.2012.11.063.
- [168] Rudonja NR, Komatina MS, Živković GS, Antonijević DL. Heat transfer enhancement through pcm thermal storage by use of copper fins. *Therm Sci* 2016;20:s251–9. doi:10.2298/TSC1150729136R.
- [169] Pan C, Hoenig S, Chen CH, Neti S, Romero C, Vermaak N. Efficient modeling of phase change material solidification with multidimensional fins. *Int J Heat Mass Transf* 2017;115:897–909. doi:10.1016/j.ijheatmasstransfer.2017.07.120.
- [170] Ji C, Qin Z, Dubey S, Choo FH, Duan F. Simulation on PCM melting enhancement with double-fin length arrangements in a rectangular enclosure induced by natural convection. *Int J Heat Mass Transf* 2018;127:255–65. doi:10.1016/j.ijheatmasstransfer.2018.07.118.
- [171] Abujar CR, Jové A, Prieto C, Gallas M, Cabeza LF. Performance comparison of a group of thermal conductivity enhancement methodology in phase change material for thermal storage application. *Renew Energy* 2016;97:434–43. doi:10.1016/j.renene.2016.06.003.

- [172] Tiari S, Qiu S, Mahdavi M. Numerical study of finned heat pipe-assisted thermal energy storage system with high temperature phase change material. *Energy Convers Manag* 2015;89:833–42. doi:10.1016/j.enconman.2014.10.053.
- [173] Abdulateef AM, Mat S, Abdulateef J, Sopian K, Al-Abidi AA. Geometric and design parameters of fins employed for enhancing thermal energy storage systems: a review. *Renew Sustain Energy Rev* 2018;82:1620–35. doi:10.1016/j.rser.2017.07.009.
- [174] Madad A, Mouhib T, Mouhsen A. Phase Change Materials for Building Applications : A Thorough Review and New Perspectives. *Buildings* 2018;8. doi:10.3390/buildings8040063.
- [175] Guarino F, Dermardiros V, Chen Y, Rao J, Athienitis A, Cellura M, et al. PCM thermal energy storage in buildings: Experimental study and applications. *Energy Procedia* 2014;70:219–28. doi:10.1016/j.egypro.2015.02.118.
- [176] Kasaeian A, bahrami L, Pourfayaz F, Khodabandeh E, Yan WM. Experimental studies on the applications of PCMs and nano-PCMs in buildings: A critical review. *Energy Build* 2017;154:96–112. doi:10.1016/j.enbuild.2017.08.037.
- [177] Khodadadi JM, Fan L. Thermal conductivity enhancement of phase change materials for thermal energy storage: A review. *Renew Sustain Energy Rev* 2010;15:24–46. doi:10.1016/j.rser.2010.08.007.
- [178] Senthil R, Cheralathan M. Natural heat transfer enhancement methods in phase change material based thermal energy storage. *Int J ChemTech Res* 2016;9:563–70.
- [179] Wang C, Lin T, Li N, Zheng H. Heat transfer enhancement of phase change composite material: Copper foam/paraffin. *Renew Energy* 2016;96:960–5. doi:10.1016/j.renene.2016.04.039.
- [180] Shah KW. A review on enhancement of phase change materials - A nanomaterials perspective. *Energy Build* 2018;175:57–68. doi:10.1016/j.enbuild.2018.06.043.
- [181] Shabgard H, Allen MJ, Sharifi N, Benn SP, Faghri A, Bergman TL. Heat pipe heat exchangers and heat sinks: Opportunities, challenges, applications, analysis, and state of the art. *Int J Heat Mass Transf* 2015;89:138–58. doi:10.1016/j.ijheatmasstransfer.2015.05.020.
- [182] Robak CW, Bergman TL, Faghri A. Enhancement of latent heat energy storage using embedded heat pipes. *Int J Heat Mass Transf* 2011;54:3476–84. doi:10.1016/j.ijheatmasstransfer.2011.03.038.
- [183] Sharifi N, Bergman TL, Allen MJ, Faghri A. Melting and solidification enhancement using a combined heat pipe, foil approach. *Int J Heat Mass Transf* 2014;78:930–41. doi:10.1016/j.ijheatmasstransfer.2014.07.054.
- [184] Ambirajan A, Adoni AA, Vaidya JS, Rajendran AA, Kumar D, Dutta P. Loop heat pipes: A review of fundamentals, operation, and design. *Heat Transf Eng* 2012;33:387–405. doi:10.1080/01457632.2012.614148.
- [185] Hu BW, Wang Q, Liu ZH. Fundamental research on the gravity assisted heat pipe thermal storage unit (GAHP-TSU) with porous phase change materials (PCMs) for medium temperature applications. *Energy Convers Manag* 2015;89:376–86. doi:10.1016/j.enconman.2014.10.017.
- [186] Yogeve R, Kribus A. PCM storage system with integrated active heat pipe. *Energy Procedia* 2013;49:1061–70. doi:10.1016/j.egypro.2014.03.115.
- [187] Rubitherm Technologies GmbH. Data Sheet RT42. Berlin: 2016.
- [188] Garg H, Pandey B, Saha SK, Singh S, Banerjee R. Design and analysis of PCM based radiant heat exchanger for thermal management of buildings. *Energy Build* 2018;169:84–96. doi:10.1016/j.enbuild.2018.03.058.
- [189] Muthuvelan T, Panchabikesan K, Munisamy R, Nibhanupudi KM, Ramalingam V. Experimental investigation of free cooling using phase change material-filled air heat exchanger for energy efficiency in buildings. *Adv Build Energy Res* 2018;12:139–49. doi:10.1080/17512549.2016.1248487.
- [190] Rajagopal M, Velraj R. Experimental investigation on the phase change material-based modular heat exchanger for thermal management of a building. *Int J Green Energy* 2016;13:1109–19. doi:10.1080/15435075.2016.1181073.
- [191] Rouault F, Bruneau D, Sébastien P, Lopez J. Experimental investigation and modelling of a low temperature PCM thermal energy exchange and storage system. *Energy Build* 2014;83:96–107. doi:10.1016/j.enbuild.2014.05.026.
- [192] Cano D, Funéz C, Rodriguez L, Valverde JL, Sanchez-Silva L. Experimental investigation of a thermal storage system using phase change materials. *Appl Therm Eng* 2016;107:264–70. doi:10.1016/j.applthermaleng.2016.06.169.
- [193] Zhu Y, Xiao J, Chen T, Chen A, Zhou S, Liu Z, et al. Experimental and numerical investigation on composite phase change material (PCM) based heat exchanger for breathing air cooling. *Appl Therm Eng* 2019;155:631–6. doi:10.1016/j.applthermaleng.2019.04.014.

- [194] Zhou T, Xiao Y, Liu Y, Lin J, Huang H. Research on cooling performance of phase change material-filled earth-air heat exchanger. *Energy Convers Manag* 2018;177:210–23. doi:10.1016/j.enconman.2018.09.047.
- [195] Bottarelli M, Bortoloni M, Su Y, Yousif C, Aydın AA, Georgiev A. Numerical analysis of a novel ground heat exchanger coupled with phase change materials. *Appl Therm Eng* 2015;88:369–75. doi:10.1016/j.applthermaleng.2014.10.016.
- [196] Hu W, Song M, Jiang Y, Yao Y, Gao Y. A modeling study on the heat storage and release characteristics of a phase change material based double-spiral coiled heat exchanger in an air source heat pump for defrosting. *Appl Energy* 2019;236:877–92. doi:10.1016/j.apenergy.2018.12.057.
- [197] Zipf V, Neuhäuser A, Willert D, Nitz P, Gschwander S, Platzer W. High temperature latent heat storage with a screw heat exchanger: Design of prototype. *Appl Energy* 2013;109:462–9. doi:10.1016/j.apenergy.2012.11.044.
- [198] Youssef W, Ge YT, Tassou SA. CFD modelling development and experimental validation of a phase change material (PCM) heat exchanger with spiral-wired tubes. *Energy Convers Manag* 2018;157:498–510. doi:10.1016/j.enconman.2017.12.036.
- [199] Shon J, Kim H, Lee K. Improved heat storage rate for an automobile coolant waste heat recovery system using phase-change material in a fin-tube heat exchanger. *Appl Energy* 2014;113:680–9. doi:10.1016/j.apenergy.2013.07.049.
- [200] Aslam Bhutta MM, Hayat N, Bashir MH, Khan AR, Ahmad KN, Khan S. CFD applications in various heat exchangers design: A review. *Appl Therm Eng* 2012;32:1–12. doi:10.1016/j.applthermaleng.2011.09.001.
- [201] Sundén B. Computational fluid dynamics in research and design of heat exchangers. *Heat Transf Eng* 2007;28:898–910. doi:10.1080/01457630701421679.
- [202] Castell A, Solé C. An overview on design methodologies for liquid-solid PCM storage systems. *Renew Sustain Energy Rev* 2015;52:289–307. doi:10.1016/j.rser.2015.07.119.
- [203] de Gracia A, Cabeza LF. Numerical simulation of a PCM packed bed system: A review. *Renew Sustain Energy Rev* 2017;69:1055–63. doi:10.1016/j.rser.2016.09.092.
- [204] Lazaro A, Dolado P, Marin JM, Zalba B. PCM-air heat exchangers for free-cooling applications in buildings: Empirical model and application to design. *Energy Convers Manag* 2009;50:444–9. doi:10.1016/j.enconman.2008.11.009.
- [205] Bie Y, Li M, Chen F, Królczyk G, Yang L, Li Z, et al. A novel empirical heat transfer model for a solar thermal storage process using phase change materials. *Energy* 2019;168:222–34. doi:10.1016/j.energy.2018.11.107.
- [206] Dolado P, Lazaro A, Marin JM, Zalba B. Characterization of melting and solidification in a real-scale PCM-air heat exchanger: Experimental results and empirical model. *Renew Energy* 2011;36:2906–17. doi:10.1016/j.renene.2011.04.008.
- [207] Wang S, Jian G, Tong X, Wen J, Tu J. Effects of spacing bars on the performance of spiral-wound heat exchanger and the fitting of empirical correlations. *Appl Therm Eng* 2018;128:1351–8. doi:10.1016/j.applthermaleng.2017.09.094.
- [208] Castell A, Belusko M, Bruno F, Cabeza LF. Maximisation of heat transfer in a coil in tank PCM cold storage system. *Appl Energy* 2011;88:4120–7. doi:10.1016/j.apenergy.2011.03.046.
- [209] Shah R, Sekulic D. *Fundamentals of Heat Exchanger Design*. New Jersey: John Wiley & Sons, Inc.; 2003.
- [210] Rutherford T. *Energy Prices*. London: 2016.
- [211] Department of Energy and Climate Change UK. *The Carbon Plan: Delivering our low carbon future*. London: 2011.

# Appendix A – Data sheets of PCMs

## Data sheet



### RT25



RUBITHERM® RT is a pure PCM, this heat storage material utilising the processes of phase change between solid and liquid (melting and congealing) to store and release large quantities of thermal energy at nearly constant temperature. The RUBITHERM® phase change materials (PCM's) provide a very effective means for storing heat and cold, even when limited volumes and low differences in operating temperature are applicable.

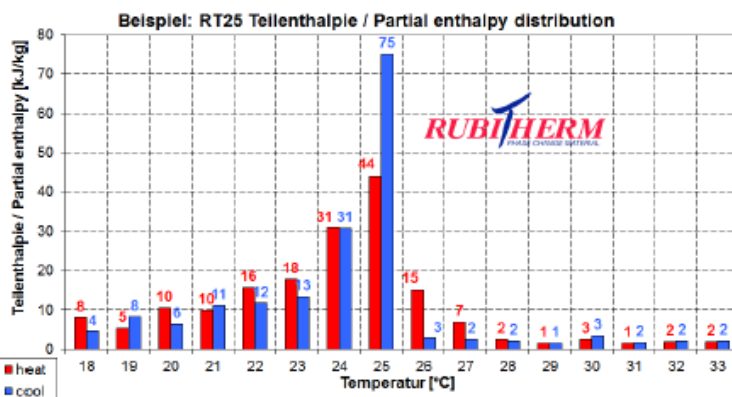
We look forward to discussing your particular questions, needs and interests with you.

**Properties:**

- high thermal energy storage capacity
- heat storage and release take place at relatively constant temperatures
- no supercooling effect, chemically inert
- long life product, with stable performance through the phase change cycles
- melting temperature range between -4 °C and 100 °C

**The most important data:**

	Typical Values	
<b>Melting area</b>	<b>22-26</b>	[°C]
	main peak: 25	
<b>Congeeing area</b>	<b>26-22</b>	[°C]
	main peak: 25	
<b>Heat storage capacity ± 7,5%</b>	<b>170</b>	[kJ/kg]*
Combination of latent and sensible heat in a temperatur range of 16°C to 31°C.	<b>48</b>	[Wh/kg]*
<b>Specific heat capacity</b>	<b>2</b>	[kJ/kg·K]
<b>Density solid</b> at 15 °C	<b>0,88</b>	[kg/l]
<b>Density liquid</b> at 40 °C	<b>0,76</b>	[kg/l]
<b>Heat conductivity (both phases)</b>	<b>0,2</b>	[W/(m·K)]
<b>Volume expansion</b>	<b>14</b>	[%]
<b>Flash point</b>	<b>143</b>	[°C]
<b>Max. operation temperature</b>	<b>55</b>	[°C]



Rubitherm Technologies GmbH  
 Sperenberger Str. 5a  
 D-12277 Berlin  
 Tel: +49 30 720004-62  
 Fax: +49 30 720004-99  
 E-Mail: info@rubitherm.com  
 Internet: www.rubitherm.com

The product information given is a non-binding planning aid, subject to technical changes without notice. Version: 01.03.2016

\*Measured with 3-layer-calorimeter.

# RT42



RUBITHERM® RT is a pure PCM, this heat storage material utilising the processes of phase change between solid and liquid (melting and congealing) to store and release large quantities of thermal energy at nearly constant temperature. The RUBITHERM® phase change materials (PCM's) provide a very effective means for storing heat and cold, even when limited volumes and low differences in operating temperature are applicable.

We look forward to discussing your particular questions, needs and interests with you.

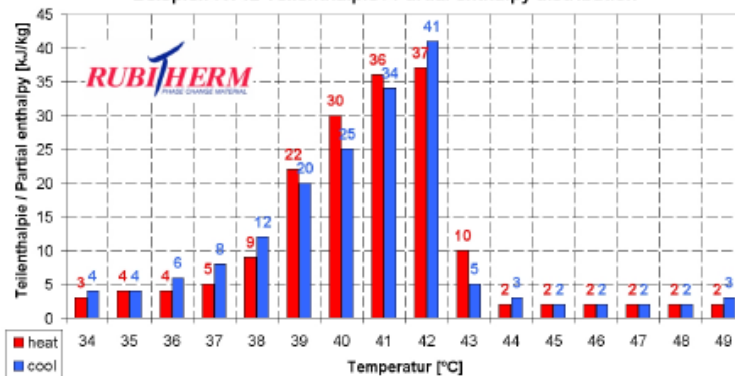
**Properties:**

- high thermal energy storage capacity
- heat storage and release take place at relatively constant temperatures
- no supercooling effect, chemically inert
- long life product, with stable performance through the phase change cycles
- melting temperature range between -4 °C and 100 °C

**The most important data:**

	Typical Values	
<b>Melting area</b>	<b>38-43</b>	<b>[°C]</b>
	main peak: 41	
<b>Congeealing area</b>	<b>43-37</b>	<b>[°C]</b>
	main peak: 42	
<b>Heat storage capacity ± 7,5%</b>	<b>165</b>	<b>[kJ/kg]*</b>
Combination of latent and sensible heat in a temperatur range of 35°C to 50°C.	<b>48</b>	<b>[Wh/kg]*</b>
<b>Specific heat capacity</b>	<b>2</b>	<b>[kJ/kg·K]</b>
<b>Density solid</b> at 15 °C	<b>0,88</b>	<b>[kg/l]</b>
<b>Density liquid</b> at 80 °C	<b>0,76</b>	<b>[kg/l]</b>
<b>Heat conductivity (both phases)</b>	<b>0,2</b>	<b>[W/(m·K)]</b>
<b>Volume expansion</b>	<b>12,5</b>	<b>[%]</b>
<b>Flash point</b>	<b>186</b>	<b>[°C]</b>
<b>Max. operation temperature</b>	<b>72</b>	<b>[°C]</b>

Beispiel: RT42 Teilenthalpie / Partial enthalpy distribution



\*Measured with 3-layer-calorimeter.

Rubitherm Technologies GmbH  
 Sperenberger Str. 5a  
 D-12277 Berlin  
 Tel: +49 30 720004-62  
 Fax: +49 30 720004-99  
 E-Mail: info@rubitherm.com  
 Internet: www.rubitherm.com

The product information given is a non-binding planning aid, subject to technical changes without notice. Version: 09.05.2016

## Appendix B – Experimental results of all thermocouples in the finned heat exchanger of section 5.4.3

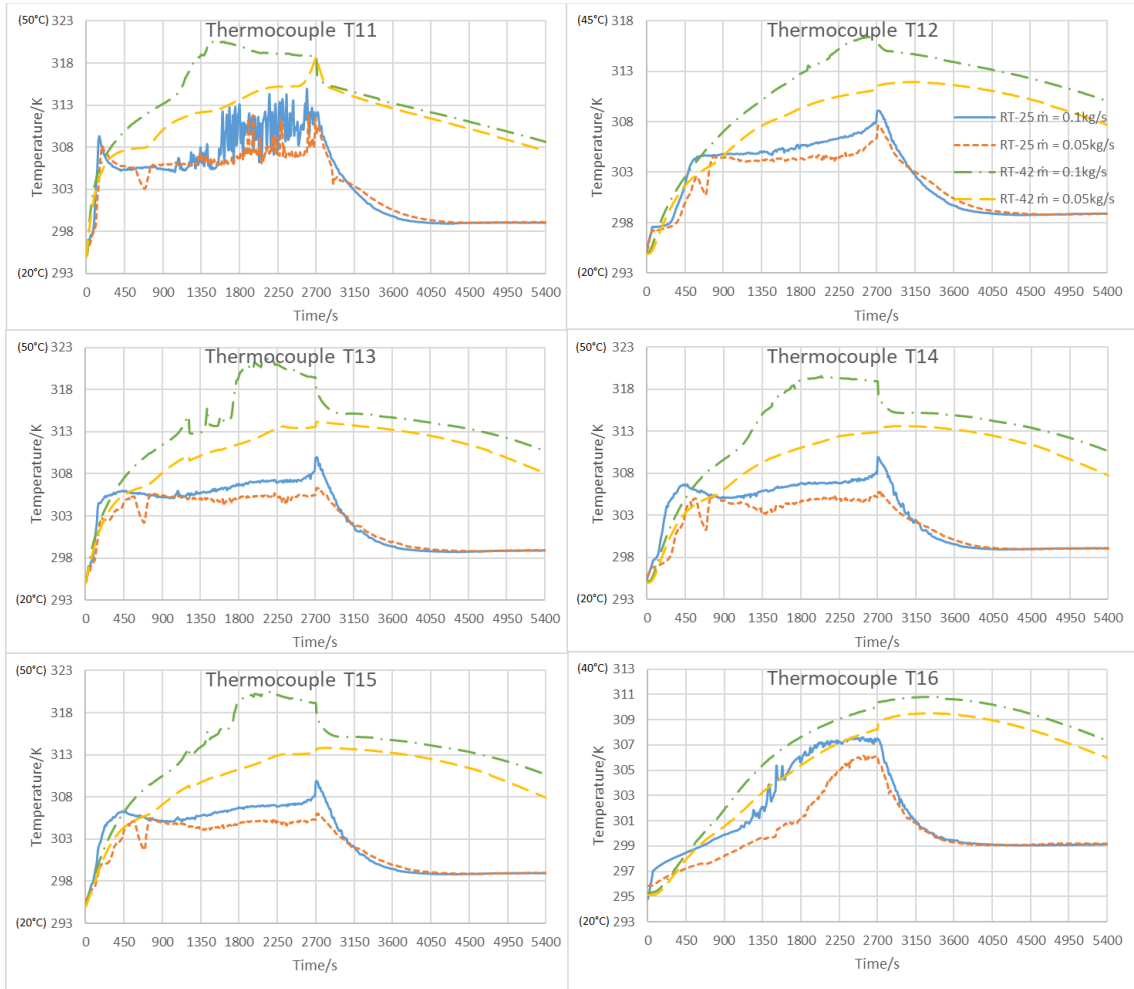


Figure B-1: Temperature variations for the lower tier of thermocouples in the solo-flow strategy

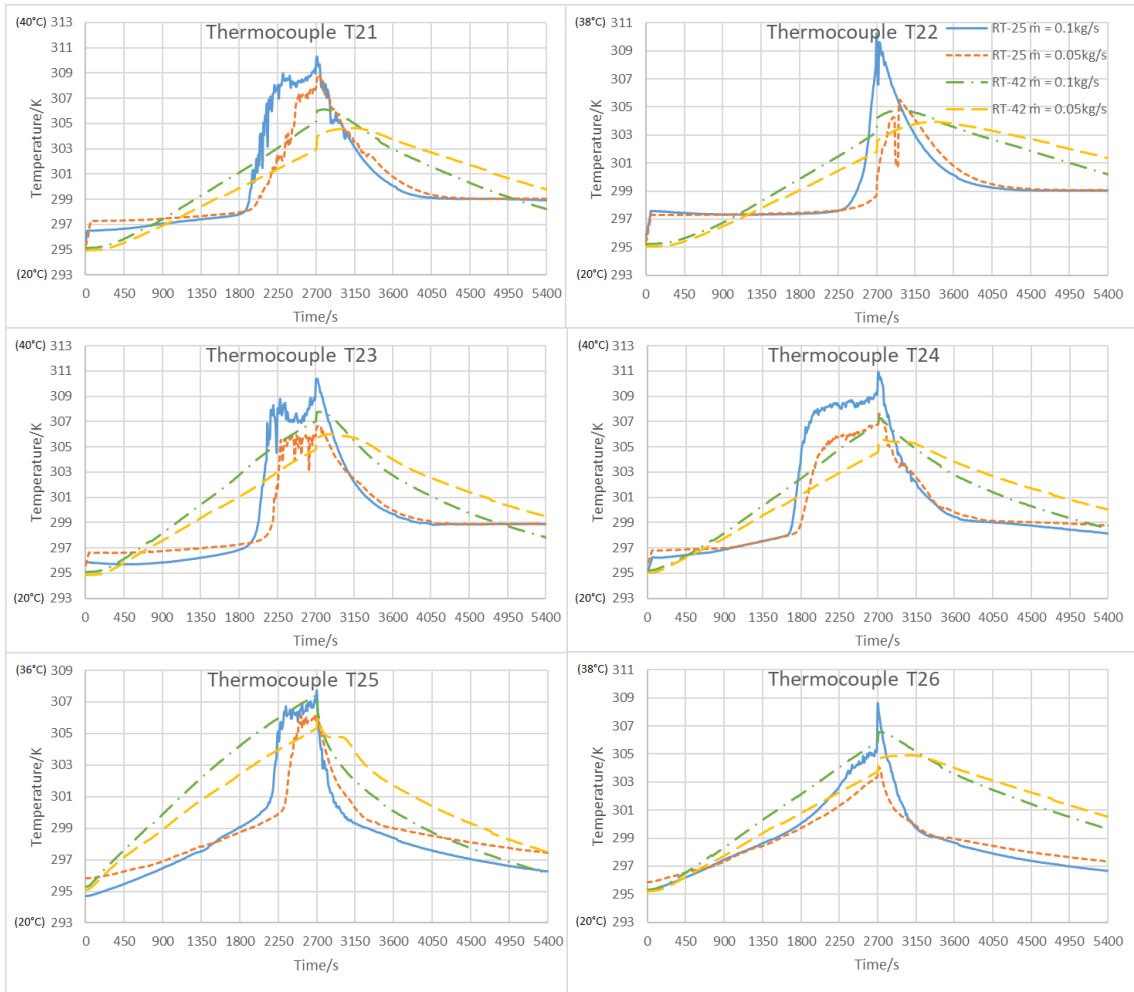


Figure B-2: Temperature variations for the middle tier of thermocouples in the solo-flow strategy



Figure B-3: Temperature variations for the upper tier of thermocouples in the solo-flow strategy



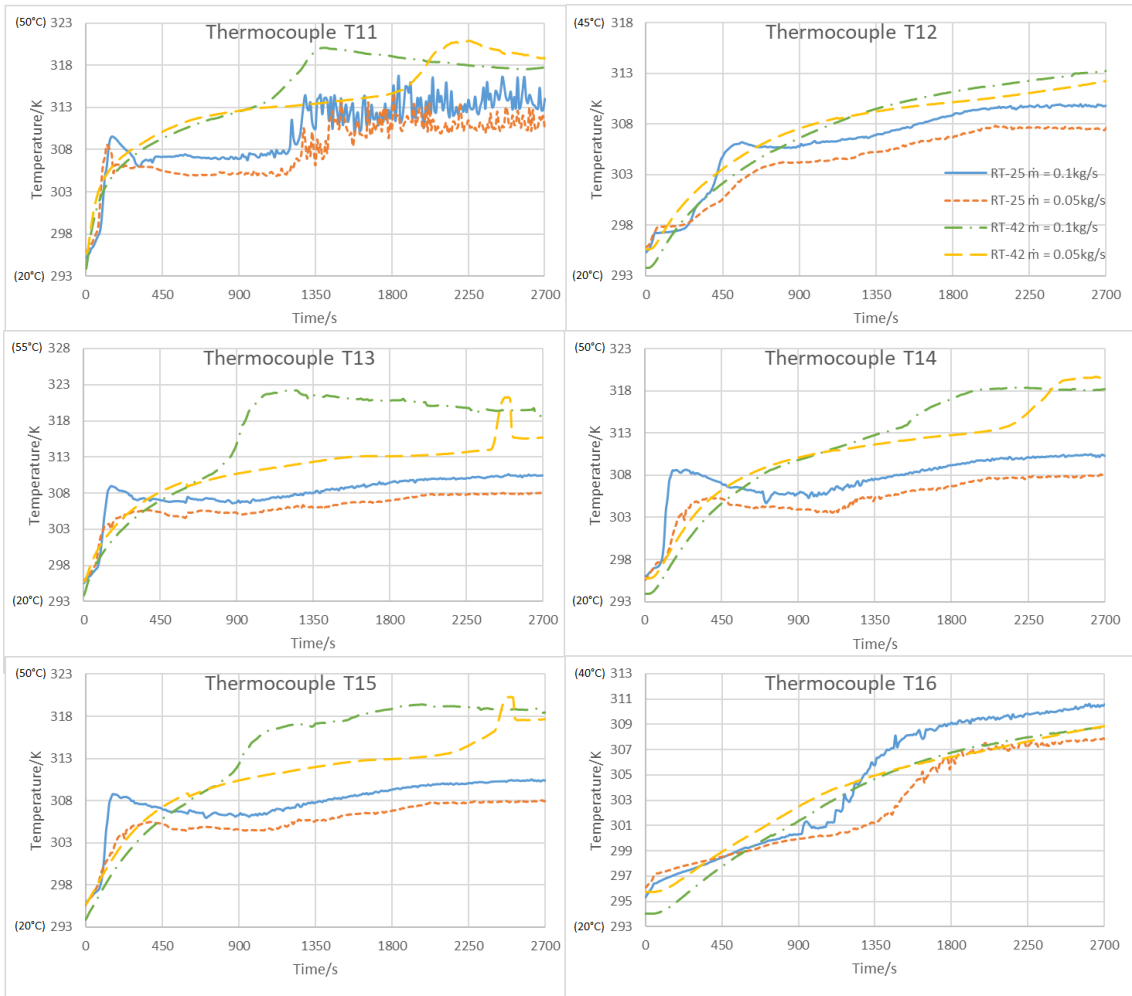


Figure B-4: Temperature variations for the lower tier of thermocouples in the dual-flow strategy

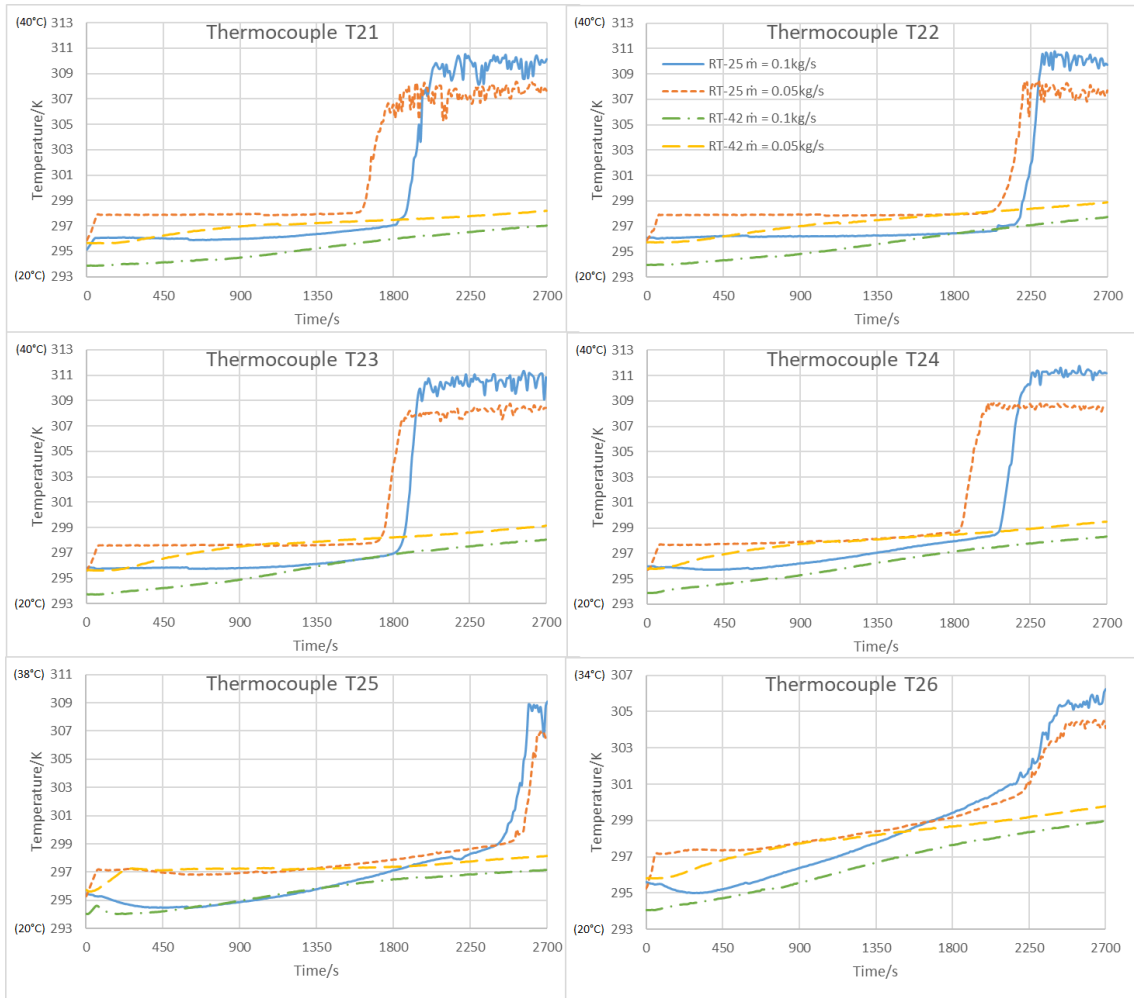


Figure B-5: Temperature variations for the middle tier of thermocouples in the dual-flow strategy

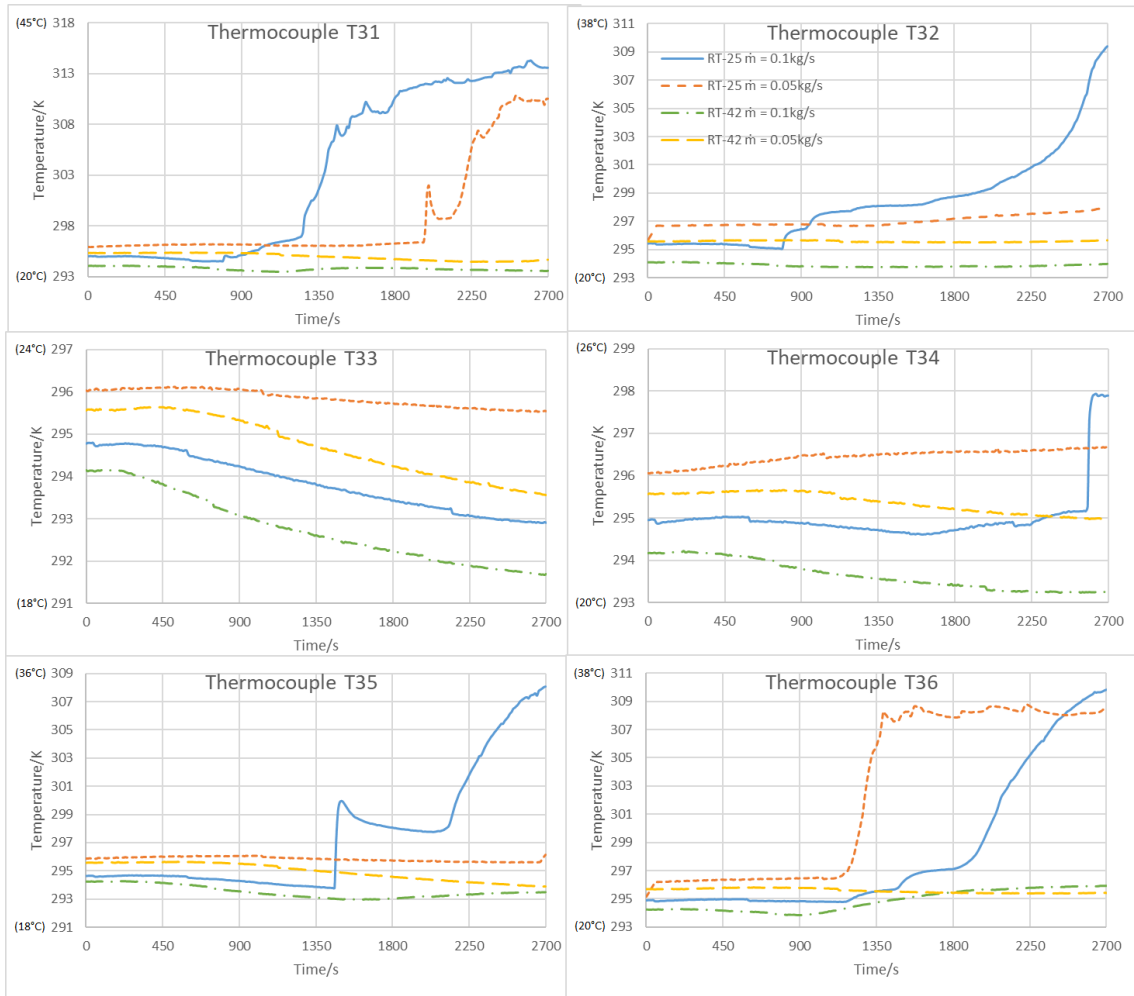


Figure B-6: Temperature variations for the upper tier of thermocouples in the dual-flow strategy

## Appendix C – Publications

<b>Journal papers</b>	
1.	Mazhar, A., Liu, S., and Shukla, A. (2020) ‘Numerical analysis of rectangular fins for low-grade heat harnessing’. <i>International Journal of Thermal Sciences</i> , doi: 10.1016/j.ijthermalsci.2020.106306
2.	Mazhar, A., Liu, S., and Shukla, A. (2019) ‘An Optimizer Using the PSO algorithm to determine thermal parameters of PCM: A case study of grey water heat harnessing’. <i>International Journal of Heat and Mass Transfer</i> , doi: 10.1016/j.ijheatmasstransfer.2019.118574
3.	Mazhar, A., Liu, S., and Shukla, A. (2019) ‘Experimental study on the thermal performance of a grey water heat harnessing exchanger using PCMs’. <i>Renewable Energy</i> , doi: 10.1016/j.renene.2019.08.053
4.	Mazhar, A., Liu, S., and Shukla, A. (2018) ‘A state of art review on the district heating systems’. <i>Renewable and Sustainable Energy Reviews</i> , doi: 10.1016/j.rser.2018.08.005.
5.	Mazhar, A., Liu, S., and Shukla, A. (2018) ‘A key review of non-industrial greywater heat harnessing’. <i>Energies</i> , doi: 10.3390/en11020386
6.	Mazhar, A., Liu, S., and Shukla, A. (2020) ‘Numerical investigation of the heat transfer enhancement of corrugated pipes in grey water harnessing using a Phase Change Material’. <i>International Journal of Energy Research</i> , Under Review
7.	Mazhar, A., Liu, S., and Shukla, A. (2020) ‘Building heating demand reduction with a PCM-based grey water heat harnessing exchanger’. <i>Energy and Buildings</i> , Under Review
<b>Book chapter</b>	
8.	Mazhar, A., Liu, S., and Shukla, A. (2020) ‘Comprehensive Study of District Heating (DH) in the UK: techno-economic aspects, policy support and trends’. <i>Low Carbon Energy Supply Technologies and Systems</i> , CRC Press Taylor & Francis Group LLC, ISBN: 978-0-367-37340-5
<b>Conference proceedings</b>	
9.	Mazhar, A., Liu, S., and Shukla, A. (2019) ‘Experimental validation of a numerical model of a corrugated pipe-phase change material (PCM) based heat exchanger to harness grey water heat’. <i>Conference proceedings (Springer) UKHTC-2019 Nottingham</i>